SANDIA REPORT

SAND95–2364 • UC–906
Unlimited Release
Printed January 1996

On the Convergence of the Phase Gradient Autofocus Algorithm for Synthetic Aperture Radar Imaging

Mary Jane Hicks

Prepared by
Sandia National Laboratories
Albuquerque, New Mexico 87185 and Livermore, California 94550
for the United States Department of Energy
under Contract DE-AC04-94AL85000

Approved for public release; distribution is unlimited.

SF2900Q(8-81)

Issued by Sandia National Laboratories, operated for the United States Department of Energy by Sandia Corporation.

Available to DOE and DOE contractors from
Office of Scientific and Technical Information
PO Box 62
Oak Ridge, TN 37831

Prices available from (615) 576-8401, FTS 626-8401

Available to the public from
National Technical Information Service
US Department of Commerce
5285 Port Royal Rd
Springfield, VA 22161

NTIS price codes
Printed copy: A13
Microfiche copy: A01

SAND 95-2364
Unlimited Release
Printed January 1996

Distribution
Category UC-906

ON THE CONVERGENCE OF THE PHASE GRADIENT AUTOFOCUS ALGORITHM FOR SYNTHETIC APERTURE RADAR IMAGING

Mary Jane Hicks
International Projects Department I, 5821
Sandia National Laboratories
Albuquerque, NM 87185-0765

ABSTRACT

Synthetic Aperture Radar (SAR) imaging is a class of coherent range and Doppler signal processing techniques applied to remote sensing. The aperture is synthesized by recording and processing coherent signals at known positions along the flight path. Demands for greater image resolution put an extreme burden on requirements for inertial measurement units that are used to maintain accurate pulse-to-pulse position information. The recently developed Phase Gradient Autofocus algorithm relieves this burden by taking a data-driven digital signal processing approach to estimating the range-invariant phase aberrations due to either uncompensated motions of the SAR platform or to atmospheric turbulence. Although the performance of this four-step algorithm has been demonstrated, its convergence has not been modeled mathematically. A new sensitivity study of algorithm performance is a necessary step towards this model. Insights that are significant to the application of this algorithm to both SAR and to other coherent imaging applications are developed. New details on algorithm implementation identify an easily avoided biased phase estimate. A new algorithm for defining support of the point spread function is proposed, which promises to reduce the number of iterations required even for rural scenes with low signal-to-clutter ratios.

Preface

What follows is the full manuscript of the dissertation submitted by the author to the University of New Mexico, Albuquerque, New Mexico, in partial fulfillment of the requirements for the degree of Doctor of Philosophy in Engineering. Only the title, abstract and distribution pages have been modified to conform to the standards for publication of SAND documents. The research reported herein was supported by the In-House Dissertation Program at Sandia National Laboratories. The dissertation has been reproduced as this SAND document to maximize distribution of this work support by our tax dollars.

Readers familiar with synthetic aperture radar (SAR) image formation and the Phase Gradient Autofocus (PGA) algorithm my wish to read only Chapters 1 and 6. Readers are also advised that an important reference, inadvertently omitted from the selected bibliography, is US Patent NO. 4,924,229 dated May 8, 1990.

This dissertation was produced under Contract DE-AC04-94AL85000 between
Sandia Corporation and the U. S. Department of Energy.

to

Larry

Acknowledgements

Without the full support of a number of people completion of this degree would not have been possible. Course work was completed through the educational assistance programs at Sandia National Laboratories. This dissertation was completed through Sandia's In-House Dissertation program administrated by Ruth Brooks. Participation in this program was made possible through my manager, Dr. James D. Williams, and my director, Dr. Dennis C. Miyoshi. Without their support this degree would not have been completed.

My faculty advisor and dissertation chairman, Dr. Neeraj Magotra, provided sound technical guidance and willingly accommodated my needs as a non-traditional student. Thanks go also to the other members of my committee Dr. Nasir Ahmad and Dr. Gregory Donohoe of the University; and, in particular, Dr. Dennis C. Ghiglia of Sandia National Laboratories, who listened patiently as I formulated my ideas. Technical discussions with my Sandia colleagues Dr. J. Thomas Cordaro and Dr. Mark Snell were greatly appreciated.

Last, but certainly not least, thanks go to my family, friends and colleagues for their kind and frequent words and deeds of support and encouragement.

Table of Contents

List of Figures

List of Tables

Chapter 1

Introduction

This introductory chapter is divided into five sections. The first section presents an overview of the area of research and a summary of the original contributions made here. The second section provides a very general overview of the principles of Synthetic Aperture Radar (SAR) imaging sufficient to motivate the need for autofocus. The third section introduces the contribution made by the Phase Gradient Autofocus (PGA) algorithm to the problem of high-resolution SAR imaging. The fourth section reviews five areas of investigation into the functioning of the PGA algorithm. These investigations are a necessary step in the development of a convergence model for this very significant algorithm, and they constitute the original research documented here. The fifth and final section provides a chapter outline.

1.1 Research Summary

The Phase Gradient Autofocus (PGA) algorithm for Synthetic Aperture Radar (SAR) imaging takes a non-parametric approach to estimating and correcting for phase errors in the SAR data. These phase errors arise from uncompensated changes in signal path length, which are, in turn, due either to uncompensated SAR platform motion or changes

in signal path length due to random propagation delays introduced by atmospheric turbulence. The data-driven PGA algorithm was first introduced in the literature in 1989, by Eichel, Ghiglia and Jakowatz [18]. Its gradient estimation kernel is based on optimal estimation theory. The PGA algorithm has been regarded as an enabling technology for SAR image formation. However, the convergence behavior of this algorithm has not been modeled mathematically. Such a model could be used to further optimize algorithm implementation in SAR imaging and would facilitate the application of PGA to other coherent imaging processes.

This research presents analyses critical to the development of a convergence model. The problem is partitioned into five areas of investigation. Both theoretical and numerical analyses are used to probe these five areas. The principles of Fast Fourier Transforms (FFTs) (used in SAR image processing to map received signals to the image plane), and random angle modulation (the manifestation of uncompensated changes in signal path length) are fundamental to this research.

Both theoretical and numerical methods of analyses are used here to address issues not found in the literature. The tools of theoretical analyses applied here are derivations of Cramér-Rao lower bounds and Taylor series expansion of the phase gradient estimator. The numerical analyses presented here are the results of a systematic study of the sensitivity of PGA algorithm performance to both synthesized and real SAR data for three classes of aberrating phase errors. The detail and depth of these numerical analyses exceed published methods and results.

This research has identified an inherent gradient-dependent bias in the gradient estimator. Another larger estimator bias is also identified. However, it is shown that this larger bias can be easily eliminated by not using zero-padded FFTs to interpolate data in the alternate domain, a commonly used digital signal processing practice. This research also identifies the limited representation of real SAR data by the current data model. Finally, a more robust alternative to a current heuristically defined subprocess of the PGA algorithm is proposed. This alternative offers better performance for images with lower signal-to-clutter ratios, such as rural scenes, and promises to require fewer iterations of the PGA algorithm to achieve near diffraction-limited image focus.

This introductory chapter provides an overview of the principles of SAR, briefly introduces autofocus and in particular the Phase Gradient Autofocus algorithm, identifies the five areas of investigation pertaining to that algorithm that are the subject of this research, and closes with a chapter outline. Greater detail on the problem statement follows in Chapters 2 and 3.

1.2 Principles of SAR

A very general review of the principles of Synthetic Aperture Radar (SAR) imaging is presented here to support the review of the objectives of this research which follows.

The power of the received radar echo, P_R, is a function of the power of the transmitted pulse, P_T, the gain of the transmitting and receiving antennas, G_T and G_R, the range to the

reflector or target, R, transmitted wavelength, λ, and the radar reflectivity or radar cross section, σ, of that target. This relationship is defined by the well known radar equation,

$$P_R = \frac{P_T G_T G_R \lambda^2 \sigma}{(4\pi)^3 R^4} . \qquad (1\text{-}1)$$

The relationship between received power and transmitted power, antenna gains and range losses is not critical to understanding the aspects of radar imaging addressed by this research. What is critical to understanding this discussion of radar imaging is the concept that different materials (both natural and man-made) have different radar cross sections and that radar cross section for any single material can vary as a function of both radar frequency and angle of illumination. Thus, received power is determined by radar cross section. Radar imaging displays these differences in received power as a function of echo position in two-dimensional space to the extent that the return signals can be resolved within that space.[1]

Range is estimated from the measured round-trip delay between the transmitted signal and the received echo. Range resolution, the ability to distinguish between the relative delay between adjacent echo sources, is a function of the effective width of the

---

[1] Echo sources are interchangeably referred to as targets or scatters. Clutter is just a collection of scatters that are considered indistinguishable because their radar cross sections are statistically identical but independent.

transmitted pulse; the narrower the pulse the greater the resolution;

$$\text{range resolution [m]} = \frac{\text{velocity of propagation [m/s]} \times \text{effective pulse width [s]}}{2}. \quad (1\text{-}2)$$

Using the inverse relationship between effective signal pulse width and signal frequency or bandwidth, the principle of radar range resolution can be alternately stated as

$$\text{range resolution [m]} = \frac{\text{velocity of propagation [m/s]}}{2 \text{ bandwidth [1/s]}}; \quad (1\text{-}3)$$

that is, the greater the bandwidth the greater the resolution. While *range* resolution is achieved with a wide-bandwidth signal, *azimuth* or cross-range resolution is achieved with a narrow-beam antenna. If the wavelength, λ, is much less than the antenna or aperture dimension, D, beamwidth, θ_B, is defined by the ratio of wavelength to antenna dimension,

$$\theta_B = \lambda / D \text{ [rads]}. \quad (1\text{-}4)$$

SAR — Synthetic Aperture Radar — is a method of using a single, physically small antenna with a wide beam to synthesize a long, linear antenna array. The synthesized linear array has a narrow beam in the dimension of the array and the beamwidth is inversely proportional to the length of the synthesized array. A distinguishing feature of synthesized arrays is that resolution is independent of range to target and is proportional to the physical length of the antenna. SAR geometry is illustrated in Figure 1-1. The diagram in the upper portion of Figure 1-1 illustrates range resolution in the plane normal to the flight path. Range resolution is proportional to the effective pulse width. The diagram in the lower portion of Figure 1-1 illustrates the synthesis of the array by the platform flight path. The patch of terrain to be imaged must be within the wide beam of

the single, physically small antenna at each point along the aperture. Points along the aperture are illustrated in the figure by the dots along the flight path.

While SAR range resolution is proportional to pulsewidth, SAR cross range or azimuth resolution requires accurate knowledge of the pulse-to-pulse position of the SAR platform to within a fraction of a wavelength. One approach to correcting for deviations in antenna phase center across the aperture is to use information from an inertial measurement unit to estimate and compensate for platform motion. However, increasing standoff ranges and aperture lengths place an extreme burden on the motion

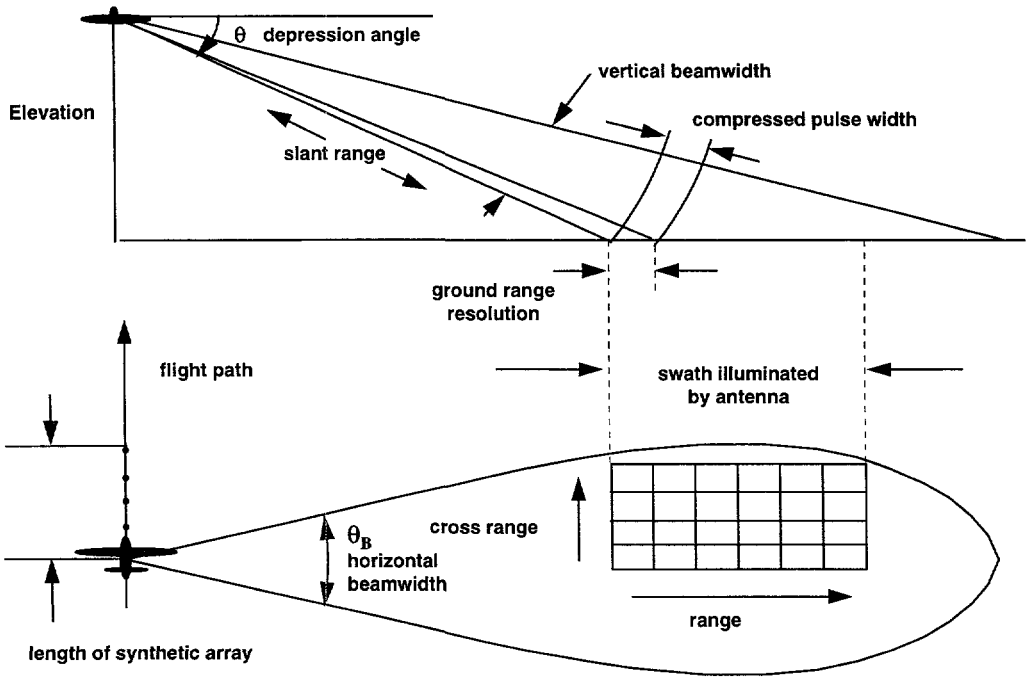

Figure 1-1. SAR geometry illustrated in plane normal to flight path and projected onto horizontal plane. Grid indicates patch imaged. Dots along the flight path indicate points at which pulses are transmitted to synthesize an array.

compensation system. Uncorrected deviations of the antenna phase center appear in the data as phase modulations which blur the detected image. Atmospheric turbulence can induce random propagation delays, which alter the pulse-to-pulse path length. These errors produce a similar effect on image quality as does uncompensated platform motion. Clearly, platform motion compensation techniques are of no use in correcting for the effects of atmospheric turbulence. The effect of phase modulation is illustrated in Figure 1-2 where a focused and defocused image are displayed along with the associated point spread functions and image peak responses. The point spread function is a measure of aperture response. While the theoretical point response is a delta function, the realized point response exhibits multiple sidelobes due to the finite size of the aperture. The image peak response shows the detected squared magnitude in the azimuth dimension of a bright pixel[2] in the scene and the adjacent pixels. The plots in Figure 1-2 show the adjacent 128 pixels.

1.3 Autofocus — An Alternative to Motion Compensation

In the early 1970's researchers began looking for data-driven digital alternatives to motion compensation systems.[3] Work in focusing of stellar optical images was motivated by phase aberrations introduced by atmospheric turbulence. Work in radar image

---

[2] A target is a pixel with large radar cross section.

[3] A summary of the literature chronicling the development of autofocus algorithms is provided in Appendix A.

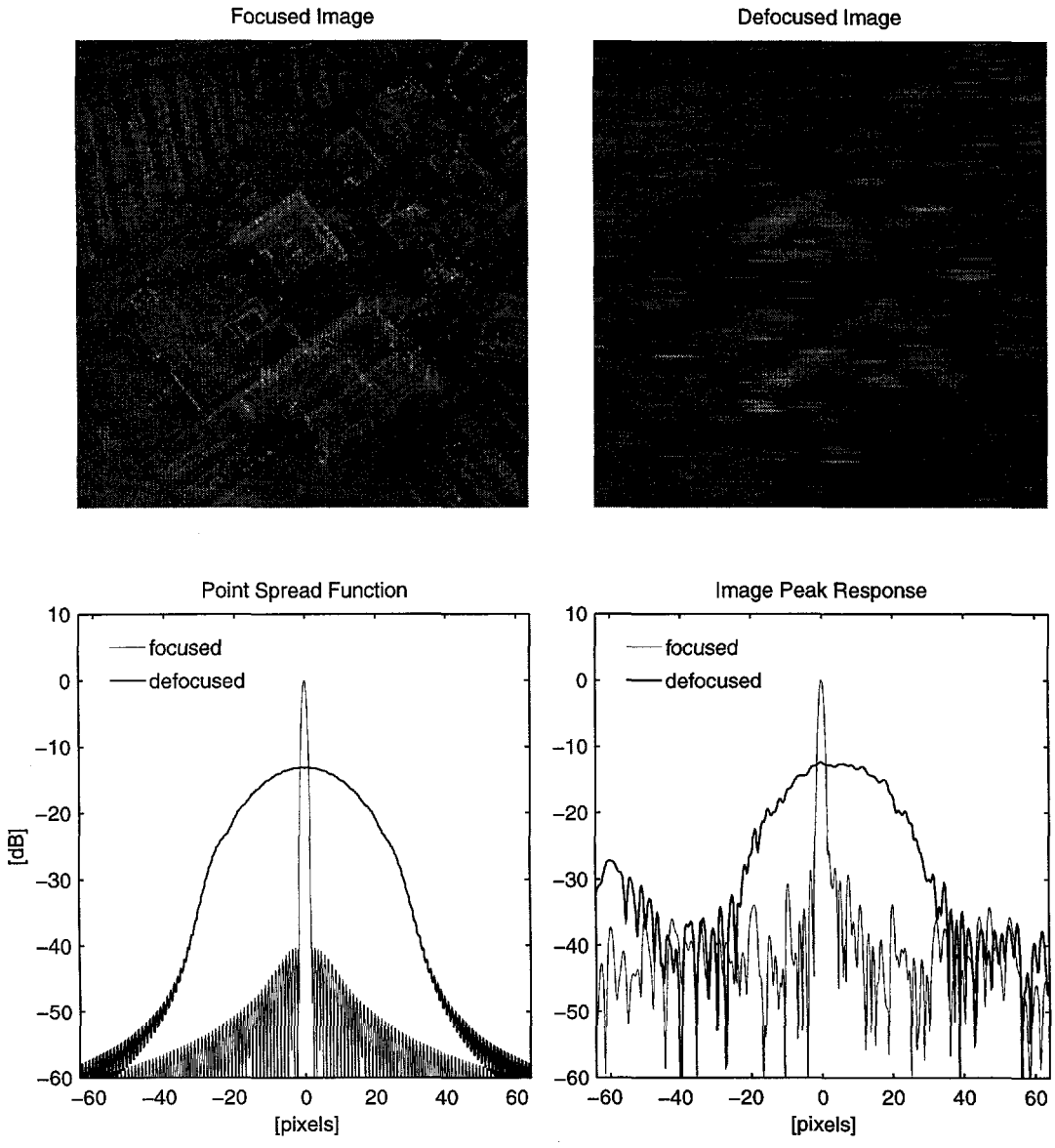

Figure 1-2 Illustration of focused and defocused images and associated point spread functions and image responses at a bright point.

formation was motivated by aberrations introduced by platform motion. Early SAR autofocus algorithms took a parametric or order-based approach to phase estimation. Early optical autofocus algorithms approached the problem as one of deconvolving the phase modulation transfer function from the aberrated diffraction-limited point response of the optical system. Both approaches require an isolated bright object in the scene that is equivalent to a point source.

In 1989, a four step approach to SAR autofocus, later to be called the Phase Gradient Autofocus (PGA) algorithm, appeared in the literature [18]. Unlike previous approaches, this non-parametric algorithm works well in the absence of isolated bright objects in the scene. A block diagram of the PGA algorithm is shown in Figure 1-3. This algorithm, considered an enabling technology, is relevant not only to SAR but to all coherent array imaging processes. The PGA is a four step algorithm:

1) circularly shift brightest points;

2) window (limit support of the point spread function);

3) estimate and remove phase; and

4) iterate.

What sets the PGA algorithm apart from similar algorithms employing some but not all of the four steps, is the demonstrated necessity of all four steps [65]. In 1993 a maximum likelihood (ML) phase-gradient estimation kernel replaced the original linear unbiased minimum variance (LUMV) estimation kernel and performance of the ML estimator was compared to the theoretical Cramér-Rao lower bound [33].

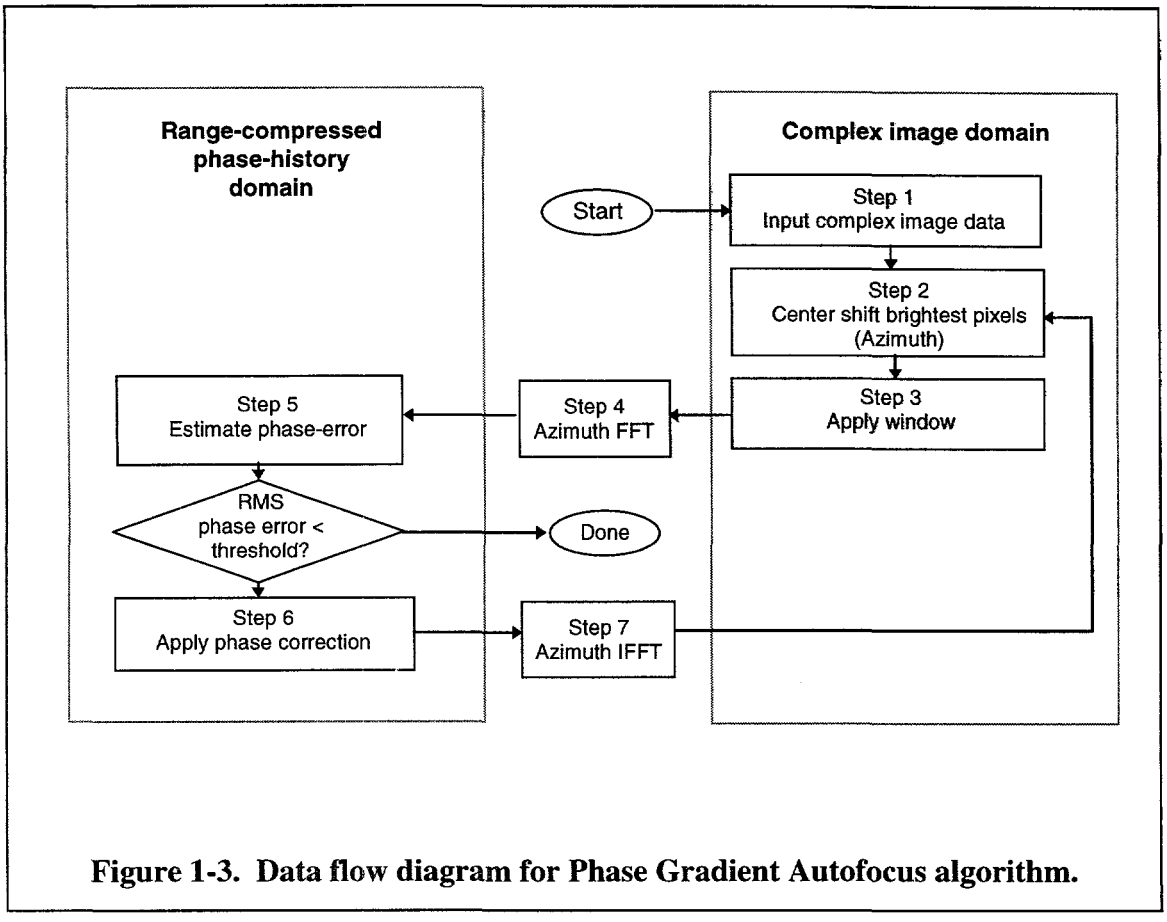

Figure 1-3. Data flow diagram for Phase Gradient Autofocus algorithm.

1.4 The Five Objectives of this Research

While much has been demonstrated about the PGA algorithm, there are still a number of open issues. Five areas of investigation are identified here and are the object of this research. These five areas include: significant details of algorithm implementation not addressed in the literature, the accuracy with which real SAR data are represented by the current data model (the data model from which the Cramér-Rao lower bound has been derived), and the heuristically defined threshold for estimating the required support of the

point spread function. The new work presented here compares results of numerical sensitivity analyses using both synthesized and real SAR data to each other and to theoretical Cramér-Rao lower bounds. The five areas of investigation, the methods of analyses and the results are summarized in the following paragraphs.

1.4.1 Method of Interpolating and Integrating Phase-Gradient Estimates

The first area of consideration is not at Step 1 of the algorithm but is the process immediately following Step 5 of the PGA algorithm, (see Figure 1-3) the optimal estimation kernel. At this point, prior to applying the phase correction, estimates of phase error across the full aperture must be computed from bandlimited estimates of phase gradients. This subprocess is at the core of the algorithm but it is not explicitly indicated in Figure 1-3 nor has it been addressed in the literature. Four candidate algorithms to accomplish this subprocess are considered here. Interpolation of phase gradients prior to integration is shown to be optimal. The commonly used technique of zero padding of FFTs to interpolate data in the phase-history domain is shown to actually correlate the noise, resulting in biased estimates of phase gradients. This conclusion is supported by a Taylor series expansion of the gradient estimator.

1.4.2 Improvement with Iteration

The next steps in the PGA algorithm are phase correction then iteration. Improvement with iteration for real SAR data has been demonstrated by Wahl, Eichel, Ghiglia and Jakowatz in [65]. In [51] Snarski suggests that the elimination of errors in the shifting of

the brightest points accounts for improvement with iteration. Here, it is shown that there is improvement with iteration using synthesized data even with no shifting errors. This result is also supported by the Taylor series expansion of the gradient estimator discussed in the previous step. That expansion indicates a small estimation bias even when the noise is uncorrelated.

1.4.3 Differences Between Synthesized and Real SAR Data

Iteration returns the process back to Step 1, the beginning of the PGA algorithm. The CRLB derived in [33] is predicated on the model for SAR phase-history data. While the robustness of algorithm performance has been demonstrated [65], a systematic sensitivity analysis has not been conducted, nor has the validity of the data model in [33] been verified. A systematic sensitivity analysis is presented here. This analysis begins with a comparison of expected PGA performance calculated using the CRLB from [33] to numerical results using synthesized and real SAR data (without any errors in the shifting of the brightest points). There are notable differences between the results using synthesized and real SAR data, particularly for low signal-to-noise ratios. These results indicate a need to expand the data model to explicitly represent the modulation of clutter by the aberrating phase.

1.4.4 Effect of Shift Errors on Estimator Performance

The next step in the sensitivity study considers the effect of errors in center shifting of the brightest points at Step 2 of the PGA algorithm. This issue is explored both theoretically

and numerically. If shift errors are appended to the current data model as multiplicative noise, then the resulting Cramér-Rao lower bound indicates that shift errors effect a loss in signal-to-noise ratio. Numerical results, however, do not support this theoretical result. Numerical results indicate that shifting errors increase the required width of the support of the point spread function. These findings indicate that the data model should be further expanded to include the transfer function of the support of the point spread function.

1.4.5 Definition of the Support of the Point Spread Function

The final area investigated is Step 3 of the PGA algorithm, windowing, which requires estimation of the width of the support for the point spread function. Current practice for scenes with high SNR is to use 1.5 times the -10 dB width of the computed point spread function. Current practice for scenes with low SNR is to set the window to the maximum expected width for the first iteration and to successively narrow the window by 20% with each iteration [65]. A robust alternative to the current thresholding scheme is presented here. This new method is compared to current practice. The advantage of the new method is that it performs equally well for scenes with both high and low SNR.

Investigation into area 1 identifies best practices and potential pitfalls in the mechanics of algorithm implementation. Investigation into Area 5 identifies a "hands-off" alternative to estimation of the support of the point spread function that is demonstrated to be robust even for rural scenes with low signal-to-clutter ratios.

Investigation into Areas 2, 3, and 4 provide significant insights necessary to understanding algorithm performance within the construct of SAR image formation. These insights are significant to the understanding of the modeling necessary to apply the PGA algorithm to other image formation processes using coherent detection.

In summary, results presented here fall into two categories: process controls that improve algorithm performance and process responses that provide insights but may be beyond the control of the current implementation.

1.5 Chapter Outline

Whenever full discussion or derivation of process or full inclusion of data would interrupt the flow of the main thought, those discussions, derivations or data will be presented in summary in the main body with the details relegated to the appendices. Considerable emphasis is placed on data visualization.

The problem statement outlined in this introduction is fully developed in Chapters 2 and 3.

Chapter 2 provides an overview of the SAR image formation process. The level of detail is sufficient to understand the need for autofocus and the implementation of the PGA algorithm.

Chapter 3 reviews the implementation of the PGA algorithm in greater detail. This review is supported by examples and the five areas of investigation are reiterated as questions.

In Chapters 2 and 3, the necessary background in the area of application (SAR image formation) and the area of investigation (convergence behavior of the Phase Gradient Autofocus algorithm) is developed. In Chapter 4, the phase and image data are presented and in Chapter 5 the theoretical and numerical methods that applied to this research are developed.

The two parts of **Chapter 4** review the phase and image data used for this research. The first section on aberrating phases begins with a review of the principles of deterministic angle modulation. This review provides a basis for the discussion of the applicable theory of random angle modulation which follows. The aberrating phase error functions and associated metrics used in this research are then presented. In the second section of Chapter 4 the SAR image data used here are presented and the method used to synthesize image data is discussed. Results of exploratory analysis of the real and synthesized SAR image data are summarized. The most interesting finding is a significant difference in the distribution of clutter between real and synthesized SAR data. (The full results of this exploratory analysis are contained in Appendix B.)

The two parts of **Chapter 5** present the theoretical and numerical methods of analysis employed. Some preliminary results are presented to provide the background and

constraints for the results developed in chapter 6.

In part one of **Chapter 5**, the principal tool for the theoretical analyses used here, the Cramér-Rao lower bound, is discussed. The equations for the Cramér-Rao lower bound for unbiased and biased estimators are presented. Some details, significant to the computation of Cramér-Rao lower bounds for the non-linear problem of phase-gradient estimation, are explored. Computation of Cramér-Rao lower bounds can be algebraically tedious. Therefore, to avoid excursions from the significant facts, all derivations of Cramér-Rao lower bounds will be given in the appendices. Only results will be presented in the body of this work.

In part two of **Chapter 5** the two numerical methods of analyses used here are developed. Synthesized SAR data with near infinite signal-to-clutter ratio is used to develop numerical lower bounds on estimation error for the phases of interest. These bounds are expressed as a function of the width of the support of the point spread function. Theoretical Cramér-Rao lower bounds are mapped from a function of signal-to-noise ratio to functions of scene signal-to-clutter ratio and width of support of the point spread function. This provides an opportunity to introduce a format for data-display that will be used extensively throughout Chapter 6. Chapter 5 concludes with discussion of a menu of eleven metrics of residual phase error and image quality used in the sensitivity studies upon which the results in Chapter 6 are based.

In **Chapter 6**, the five identified areas of investigation are addressed in detail. Results are supported by numerous examples. Chapter 6 contains the original contributions of this research. Those results have already been summarized in Section 4.1 of this chapter.

Conclusions and recommendations are summarized in **Chapter 7**.

Appendix A offers an historical summary of the literature on non-parametric SAR autofocus algorithms.

Appendix B contains all plots used for exploratory analysis of real SAR data and comparisons of synthesized to real SAR data.

Appendix C contains the derivation of Cramér-Rao lower bound for the data model used by Jakowatz and Wahl in [33].

In **Appendix D** Taylor series expansions are used to evaluate the expected value of the gradient estimator. The data model is expanded to include correlated noise and the Cramér-Rao lower bound for unbiased estimates using data with correlated noise is derived.

In **Appendix E** the data model is expanded to include shift errors as multiplicative noise and the associated Cramér-Rao lower bound is derived.

Chapter 2

Background

Principles of SAR Image Formation

This research investigates two areas pertaining to the implementation of the Phase Gradient Autofocus (PGA) algorithm to SAR imaging and three areas pertaining to the modeling of the performance of that algorithm. In order to understand the context of the problem and the assumptions inherent in the PGA algorithm, it is useful to understand the principles of SAR image formation. There are a number of references that cover this topic in detail. In this chapter the topic is covered at a level of detail sufficient to support the subsequent investigation into the implementation and modeling of the PGA algorithm. References include Eaves and Reedy [17], Elachi [20], Fitch [22], Hovanessian [30], Mensa [40] and [41], Stimpson [53], and Jakowatz, Wahl, Eichel, Ghiglia and Thompson [32]. Here, the discussion is divided into three major topics: 1) Antennas, Arrays and Synthesized Arrays; 2) SAR Data Collection and Image Formation; and 3) Approaches to Autofocus. The first section addresses the relative resolution attained with antennas, real arrays and synthesized arrays. The resolution of synthesized arrays is shown to be twice that of real arrays. In the second section, the principles of SAR data collection and image formation are presented at a level of detail

sufficient to understand the problem addressed by the PGA algorithm. The key concepts presented in this second section are: 1) resolution attained by compression of a chirped pulse; 2) a replica of the transmitted chirp is all that is required for range pulse compression; but, 3) precise information on the relative position of the antenna phase center (to within a fraction of a wavelength) along the entire platform trajectory (or SAR aperture) is required for accurate azimuth data compression. Errors in the azimuth reference result in image blur in the azimuth dimension. A final topic, that of aperture taper, is covered in this second section. The principal point is that a Taylor window with -40 dB sidelobes and $\bar{n} = 6$ was used to taper the aperture for all results reported here. The third and final section of this chapter provides a brief overview of approaches to SAR autofocus.

2.1 Antennas, Arrays and Synthetic Arrays

2.1.1 Real Antennas

The beamwidth, θ_B, of a real antenna is proportional to the transmitter wavelength, λ, and inversely proportional to the antenna diameter, D. This relationship is illustrated in Figure 2-1(a) and is expressed mathematically as $\theta_B = \lambda / D$ [rads].

As illustrated for a parabolic antenna, the angle from the center or boresight of the antenna at which the change in round trip delay ($2\Delta R$) at the edges of the antenna equals half a wavelength, $\lambda/2$, is the angle at which the signals received at opposite edges of the

antenna are π radians out of phase. Resolution is then a function of antenna beamwidth, θ_B, and range to target, R; that is, resolution = $R\theta_B$. To achieve 3m resolution at a range of 1000 m at a frequency of 30 GHz (wavelength λ = 1 cm) requires $R\theta_B = R\lambda / D = 3\text{m}$ or $D = 3.3\text{m}$.

2.1.2 Array Antennas

As illustrated in Figure 2-1(b), the function of a single real antenna can be realized by an array of small-aperture, wide-beam antennas with overall array dimension equal to that of the real antenna. The narrow beam is achieved by adjusting the phase relationships between the array elements such that the signals received at all elements are in phase for a plane wave normal to the array, hence the name "phased array" antenna. Assuming that

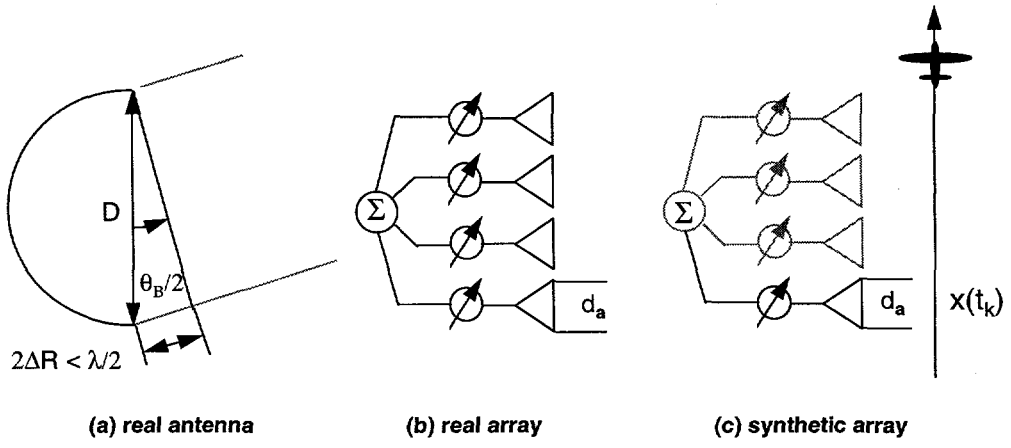

Figure 2-1. Illustration of relationships between real antenna, real array and synthetic array.

all elements transmit and receive simultaneously, then the beamwidth of the phased array is the same as that of the single narrow-beam antenna of the same size and the resolution is, likewise, range dependent. The beam can be steered by adjusting the relative phases of the elements. Beam focusing and steering can be achieved using either analog or digital signal processing. The bounds on the maximum steering angle are a function of the array geometry, a topic beyond the scope of this dissertation.

2.1.3 Synthetic Arrays

The functionality of a real array can be approximated by a synthetic array as illustrated in Figure 2-1(c). An array is synthesized in time and space by sequentially positioning a single small array element at the positions that would be occupied by real array elements. In concept, at each element position, a single pulse is transmitted and received before repositioning the element. In order to process the sequentially received data, the sequence of element positions must be known precisely. In practice, the array is synthesized by a platform moving along a known path at a known velocity. Synthesized array lengths can be orders of magnitude greater than real array lengths. There are two significant differences between real and synthetic arrays. The theoretical resolution achievable with a synthetic array, d_x, is one half the diameter, d_a, of the single array element and secondly, resolution is independent of range!

The following development of the azimuth resolution of synthetic arrays is based on that of Hovanessian [30], Mensa [41] and Stimpson [53]. First, consider the beamwidth of a

real array, which has both a one-way and a two-way antenna pattern. Consider the one-way pattern. All elements of the array receive a plane wave from an emitter at some point along the boresight of the antenna. Now rotate the emitter about the center of the array. The angle at which the phase at the far element is π radians greater than the phase of the near element is the half beam angle. This change in signal path length is illustrated in Figure 2-1(a). The one-way pattern has the form $\sin Nx / \sin x$, where N is the number of array elements and x is proportional to the product of sine of the angle, θ, off the boresight and the ratio of array separation, d, to signal wavelength, λ; that is; $x = 2\pi \frac{d}{\lambda} \sin\theta$. The two-way pattern is then $(\sin Nx / \sin x)^2$. However, a synthetic array has no one-way pattern. Since each element of a synthesized array receives only its own transmitted signal, there is no cross-coupling between array elements. The two-way pattern is determined by the round-trip phase delays to the synthesized array elements relative to the center of the synthesized array. Thus, the two-way antenna pattern of synthesized array is equivalent to the one-way antenna pattern of a real array of twice the length. That is; the two-way pattern of a synthetic array is $\sin 2Nx / \sin 2x$. For a uniformly illuminated real array of length L, the one-way 3-dB beamwidth is $0.88\frac{\lambda}{L}$, thus the two-way 3-dB beamwidth of a synthetic array is $0.44\frac{\lambda}{L}$. The commonly used 4-dB beamwidth of the two-way antenna pattern for synthetic arrays is conveniently $\theta_{4dB} = \frac{\lambda}{2L}$ radians. The azimuth resolution, d_x at range, R, is then $R\frac{1}{2}\theta_{4dB}$; thus

$$d_x = \frac{\lambda}{2L} R. \tag{2-1}$$

The object of interest must be in the beam of the real antenna of the synthetic array for the full length of the array. Thus the synthetic array length is limited by the beamwidth of the real antenna,

$$L_{\max} = \frac{\lambda}{d_a} R, \tag{2-2}$$

where d_a is the length of the real antenna. Substituting L_{max} from (2-1) for L in (2-2) produces the stated azimuth resolution $d_x = \frac{1}{2} d_a$. Even this limitation on resolution can be removed by using "spotlight" mode SAR, where the beam on the real antenna is kept continuously pointed on the area being mapped rather than sweeping over that area.

2.2 SAR Data Collection and Image Formation

Having established the fundamentals of synthetic array formation, the discussion now proceeds to the fundamentals of SAR data collection and image formation. The geometry of a SAR platform represented by an aircraft (flying into the page) with a side-looking antenna was illustrated in Chapter 1 in Figure 1-1. At each position along the synthesized array a pulse is transmitted. Range resolution is inversely proportional to the bandwidth of the transmitted signal. Typically a chirped pulse is used to achieve a wide bandwidth and hence fine range resolution (after pulse compression). The duration of the chirped pulse is on the order of 10 to 100 microseconds, while the duration of the aperture formation is on the order of 1 to 10 seconds!

2.2.1 Range Compression

Range compression is illustrated in Figure 2-2. Although the slope of the chirp is arbitrary, a negative chirp is illustrated. For each pulse transmitted, an ensemble of replicas of that pulse are received with time delays proportional to the ranges of the reflectors. The received signal for a single pulse is the sum of these delayed and attenuated echoes. While echo delay is proportional to the round-trip delay from the transmitter to the source of the echo, the echo power of interest here is proportional to the radar cross section of the echo source[1]. This sum is dechirped or deramped by mixing it with a copy of the transmitted pulse. The result is the sum of signals with frequencies proportional to range and amplitude proportional to the reflectivity (radar cross section) of the ensemble of reflectors at the associated range. The received, deramped signals are then passed through a bank of bandpass filters, thus sorting the data by range. If the deramped data are digitized, then the filter bank can be realized using Fourier transforms. The duration of the chirped pulse is on the order of tens of microseconds. The round trip delay varies from 70 μs for airborne SAR platforms at ranges on the order of 10 km to 3

---

[1] The term target is often used to refer to an echo source. The terms: point source, point scatterer, specular source or point target all refer to distinguishable features in the scene being imaged that have a radar cross section that is significantly larger than that of adjacent echo sources.

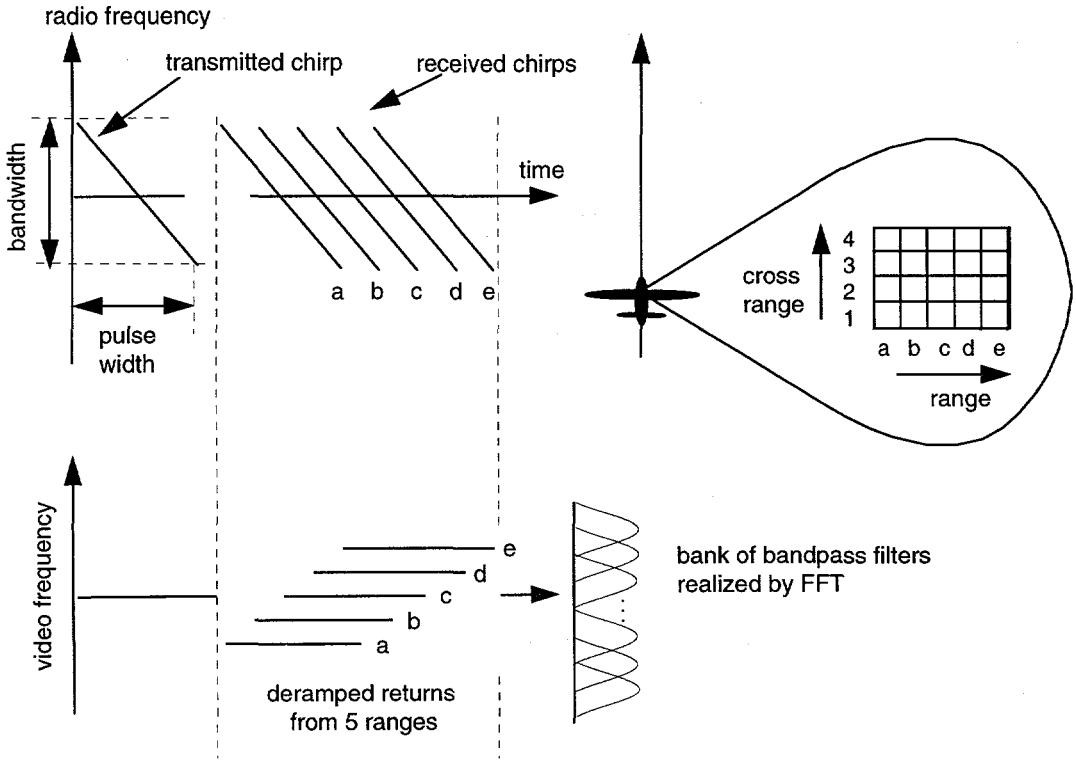

Figure 2-2. Illustration of SAR range resolution achieved through pulse compression.

ms for spaceborne platforms at ranges on the order of 500 km. For each pulse transmitted the ensemble of received pulses is processed on a pulse-by-pulse basis. This process is called pulse compression.

Pulse compression is expressed mathematically as follows: Let the transmitted pulse be expressed as

$$s_T(t) = \sin\left(2\pi f_o t + \frac{\pi B}{T} t^2\right) \qquad |t| \le \frac{T}{2}$$

$$= \sin\left(2\pi f_o t + \pi \dot{f}\ t^2\right) \tag{2-3}$$

where

f_o is the carrier frequency,

B is the chirp bandwidth,

t is the time index within the pulse,

T is the pulse duration, and

$\frac{B}{T} = \dot{f}$, the chirp rate [Hz/s].

Although the actual received signal is the continuous-time integration of echoes, for simplicity we will represent it by the discrete-time summation of delayed versions of the transmitted signal.

$$s_R(t) = \sum_{k=1}^{N_{range}} \sin\left(2\pi f_o (t-\tau_k) + \pi \dot{f}(t-\tau_k)^2\right) \tag{2-4}$$

where τ_k is the round-trip delay to the k^{th} resolvable range and N_{range} is the number of resolvable ranges in the summation.

The received signal is coherently detected. That is, both the in-phase and quadrature components are detected, thus preserving the received magnitude, frequency and phase. This process is illustrated in Figure 2-3.

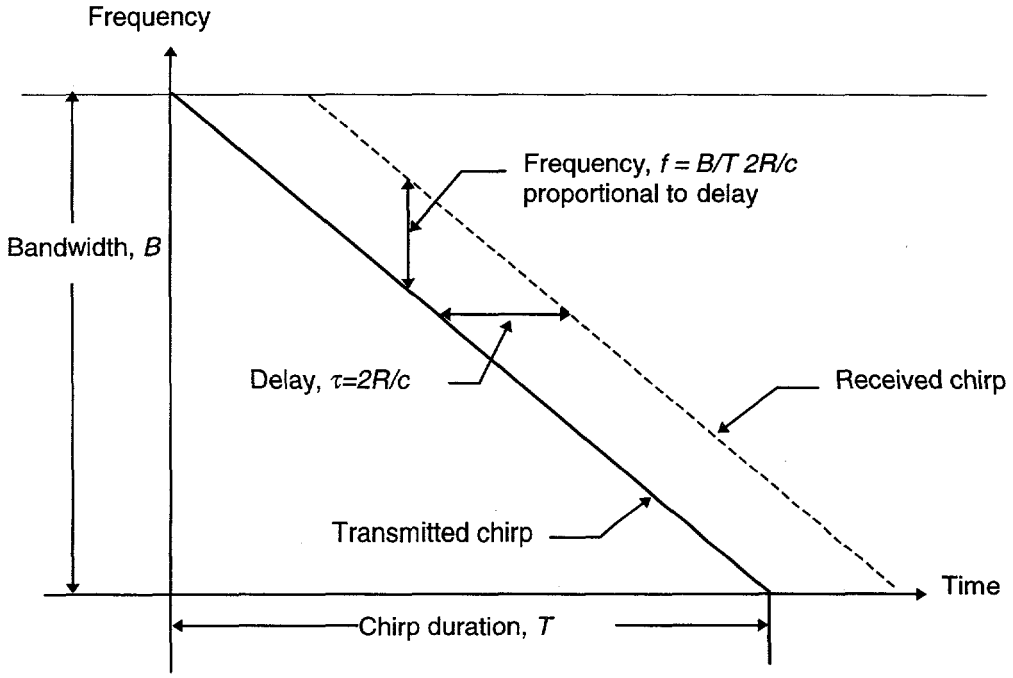

Figure 2-3. Detail of transmitted and received chirps.

The output of the mixer (which is synonymous with demodulator or deramper) for a single term of the discrete summation in equation (2-4) is

$$x_k(t) = \cos\left(2\pi \dot{f}\tau_k t + 2\pi f_o \tau_i - \pi \dot{f}\,\tau_k^{\,2}\right). \tag{2-5}$$

Substituting $2R/c$ for time delay, τ, in (2-5), where $2R$ is the round-trip range and c is the velocity of light, results in

$$x_k(t) = a_k \cos\left(2\pi\ \dot{f}\ 2R_k / ct + 4\pi f_o\ R_k / c - \pi \dot{f}\left(2R_k / c\right)^2\right) \tag{2-6}$$

where the first term, $4\pi\ \dot{f}\ R_k / c$, is the range-dependent frequency term, the second term, $4\pi f_o\ R_k / c$, is the range-dependent phase term, and the third term, $\pi \dot{f}\left(2R_k / c\right)^2$, is approximately zero if the maximum round-trip delay, $2R_{\max} / c$, is much greater than T, where T is the chirp duration.

The first term, the range-dependent frequency term, is the mathematical expression for the data that are passed through the bank of narrowband filters that are realized with a discrete Fourier transform. The signal power at each Fourier frequency is proportional to the coherent signal returns from all scatters within the associated range resolution cell.

The data are now in what is called range-compressed phase-history (Doppler) domain. The second term, the range-dependent phase term, is used to achieve cross-range or azimuth resolution. Note that the reference used to deramp the received chirped pulses is just a replica of the transmitter chirp. The stability of the reference is predicated on the stability of the radar electronics.

2.2.2 Azimuth Compression

The mathematics of azimuth compression are similar to the mathematics of range compression. However, unlike the range compression reference signal, which is just a replica of the transmitted pulse, generation of the reference for azimuth compression requires accurate knowledge of the SAR platform trajectory. This information is typically acquired by inertial measurement units. The principles of SAR azimuth compression are developed and illustrated in this subsection.

The relationship between position in the aperture and slant ranges to a pair of reflectors (targets) over the length of the synthetic aperture are illustrated in Figure 2-4. As the platform approaches the target, range decreases; as it moves away from the target, range increases. This change in range causes a pulse-to-pulse shift in phase. The time rate of change of this phase is called Doppler frequency.

The signal processing of Doppler histories across the aperture is illustrated in Figure 2-5. As can be seen from the figure, each range-compressed pulse contains the sum of Doppler shifted returns from the ensemble of reflectors (targets) within the specified range bin. While the Doppler histories are illustrated as continuous-time data, they are actually discrete-time data with sample intervals equal to the pulse repetition period. In a manner similar to range pulse compression, the Doppler phase histories are deramped by mixing them with a digital Doppler reference. This deramping is called focusing, and is not to be

confused with autofocusing. If the Doppler histories are not deramped they are unfocused, and clearly the image resolution is severely limited.

The slope of the Doppler reference is determined by the measured velocity of the SAR platform over the length of the synthetic aperture. In a manner similar to range compression, the deramped Doppler phase histories are passed through a bank of bandpass filters that are realized with a discrete Fourier transform.

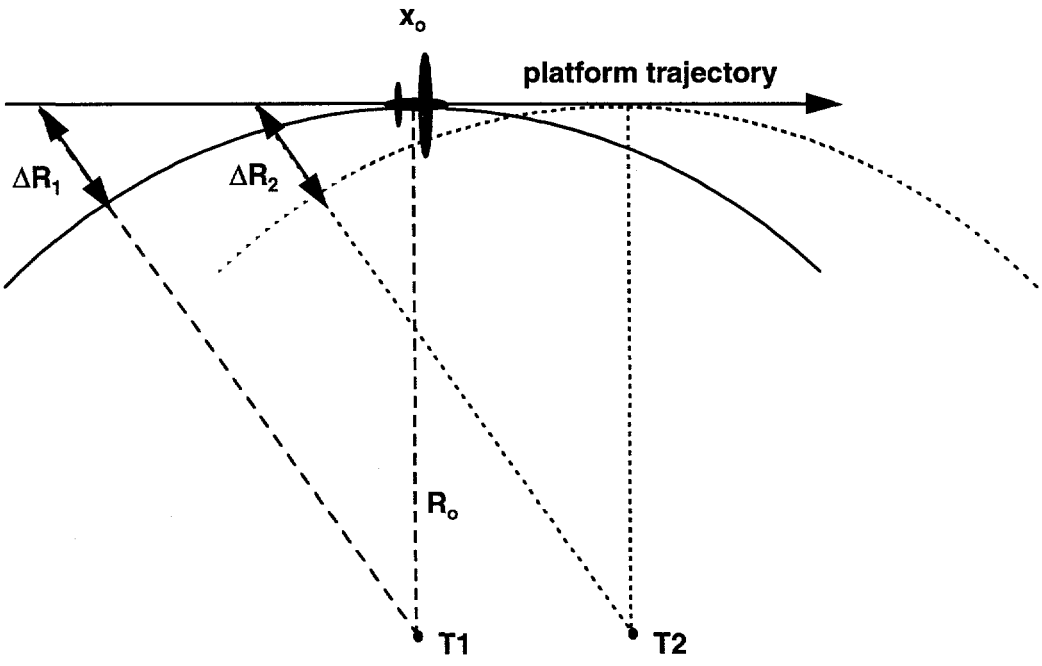

Figure 2-4. Illustration of change in range to a point target.

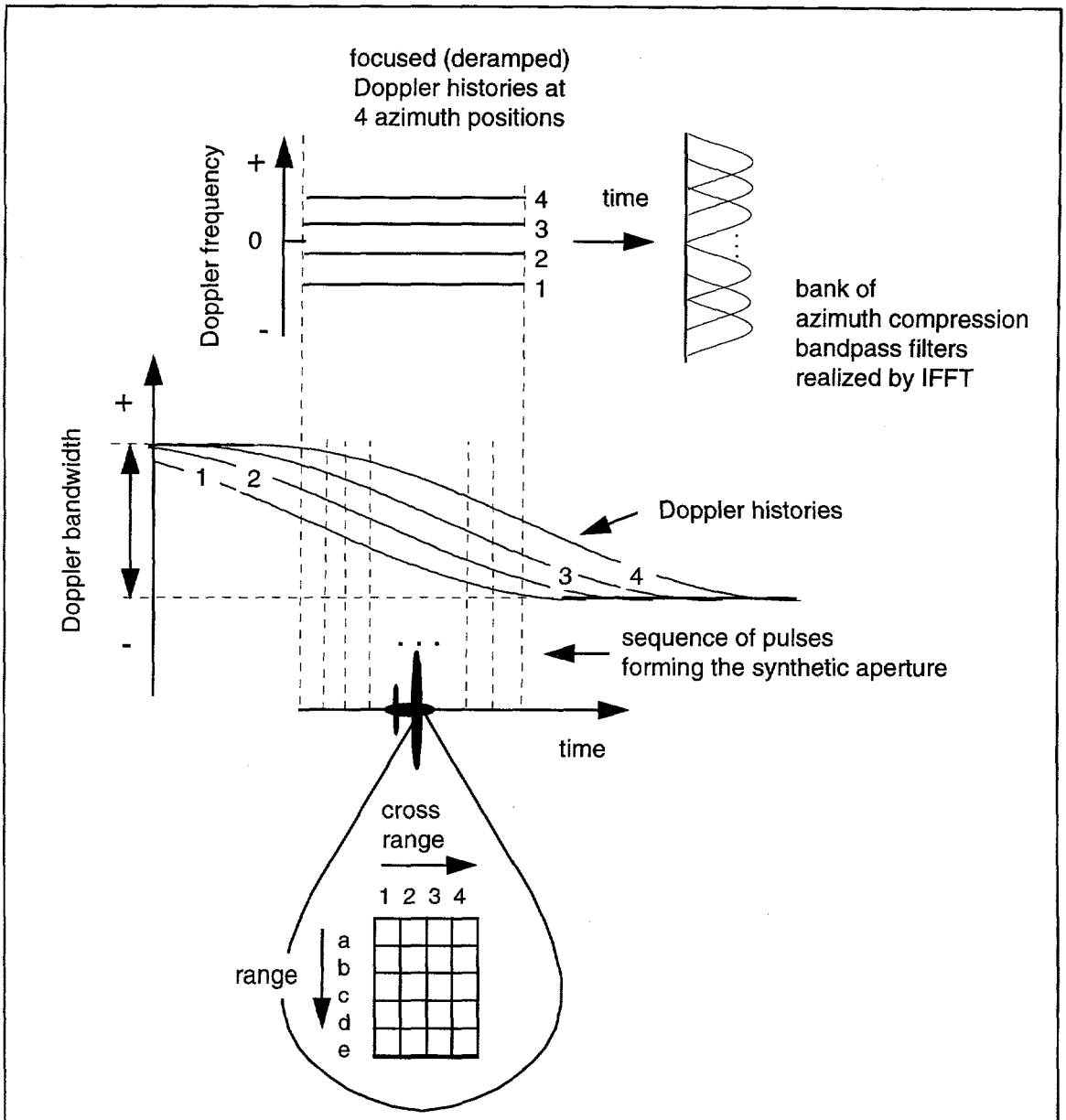

Figure 2-5. Illustration of SAR azimuth resolution achieved through compression of Doppler phase histories.

The process of azimuth deramping is expressed mathematically as follows. Recall that the range-dependent phase term in (2-6) is the expression of interest; that is,

$$\phi = 4\pi f_o R_k / c. \tag{2-7}$$

For slant range from the trajectory to the scene center, R_o, that is much greater than the aperture length, the instantaneous slant range can be approximated by

$$R(t_m) = R_o + \frac{\left[x(t_m) - x_o\right]^2}{2R_o}, \tag{2-8}$$

where $x(t_m)$ is the platform position along the aperture at the m^{th} pulse and x_o the platform position at the center of the aperture. Substituting (2-8) into (2-7) and replacing $x(t_m)$ with $V(t)\, t_m$ where $V(t)$ is the instantaneous along-track platform velocity and noting that $\lambda = c / f_o$ produces

$$\phi(t) = \frac{2\pi}{R_o \lambda}\left(V(t)t_m - x_o\right)^2 \tag{2-9}$$

with the time dependence of the phase shown explicitly in the notation. The instantaneous frequency is the time derivative of the instantaneous phase; that is,

$$\omega_d(t) = 2\pi \frac{2V(t)}{R_o \lambda}\left(V(t)t_m - x_o\right)\frac{dV(t)}{dt} \quad \text{[rads / s]}. \tag{2-10}$$

Equation (2-10) is the expression for the Doppler reference signal.

The difference between the references for range and azimuth (Doppler) compression merits emphasis. The reference for range compression is the transmitted signal and is internal to the radar. The reference for azimuth compression is the estimated rate of change of range (or path length) to a nominal point in the patch illuminated by the antenna.

A simple example serves to illustrate the effect of using an incorrect reference to deramp the azimuth data. Consider the case of underestimated platform velocity as illustrated in Figure 2-6(a). The frequency error in Figure 2-6(a) is linear, thus the phase error is quadratic.

In Figure 2-6(b) the ideal single target spectrum called the diffraction limited point response is compared to the spectrum due to demodulation using our erroneous reference.

A note about phase errors. A constant phase error has no effect on image quality. A linear phase error shifts the image but does not spread or split the point spread function. Quadratic phase error blurs the point spread function as illustrated.

Two types of perturbations can cause the rate of change of phase (and the associated phase slope) to deviate from the nominal: 1) perturbations in the radial velocity of the platform with respect to the nominal reference point, and 2) perturbations in the radial path length due to changes in the refraction index of the air caused by atmospheric turbulence. While the former may be corrected with a high resolution inertial measurement unit on the SAR platform, the latter must be estimated and corrected using data-dependent methods. Data dependent algorithms for estimating and correcting for errors in the Doppler reference are called autofocus algorithms.

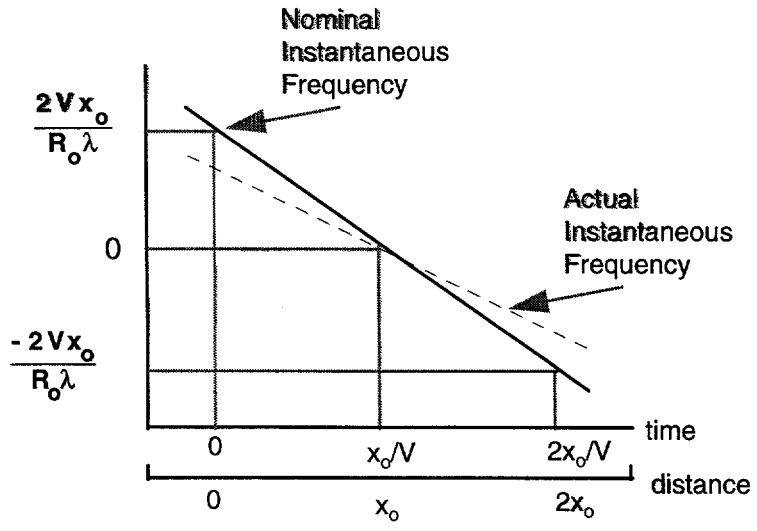

(a) Illustration of error in slope of Doppler reference.

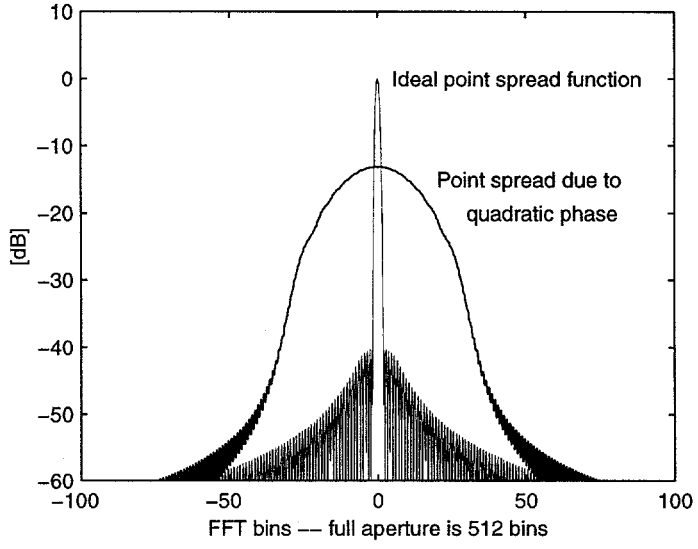

(b) Comparison of diffraction limited point spread function to point spread function aberrated by quadratic phase error due to error in slope of Doppler reference.

Figure 2-6. Illustration of phase rate error and resultant image blur.

Although there is a third possible cause of change in path length, target motion, it is not considered here. What is considered here is that the function of autofocus is to estimate and correct for path length changes common to all ranges.

2.2.3 Resolution & Aperture Taper

A brief discussion of image resolution, aperture taper and image sidelobe levels is appropriate. Consider the point response to a single isolated bright scatterer. In the range-compressed phase-history domain this single scatterer would be represented by discrete samples with a constant phase slope over the duration of the aperture. In the image domain the point response would be represented not by a delta function but by a sinc function due to the finite length of the aperture centered at the constant frequency. This is also true for range resolution. It is well known that the peak sidelobe level of a sinc function is 13 dB below the mainlobe. Generally accepted criteria for high quality imagery are peak sidelobe levels of at least 25 dB below the main lobe [30]. This lower sidelobe level is achieved at the cost of slightly increased mainlobe width by applying an amplitude tapering function to the data in the range-compressed phase-history domain. Harris [28] provides a thorough discussion of windowing functions and their application. For the examples in Figure 2-6(b), a Taylor window with a peak sidelobe level of -40 dB and parameter $\bar{n} = 6$ was used. The defining equation, as stated by Cook and Bernfeld in [15] is

$$W(t) = 1 + 2\sum_{m=1}^{\bar{n}-1} F_m \cos\frac{(2\pi mt)}{\Delta t} \tag{2-11}$$

where

$$F_m = \frac{0.5(-1)^{m+1}}{\prod_{p=1,p\neq m}^{\bar{n}-1}\left(1-\frac{m^2}{p^2}\right)}\prod_{n-1}^{\bar{n}-1}\left[1-\frac{\sigma_p^{-2}m^2}{A^2+(n-\frac{1}{2})^2}\right], \tag{2-12}$$

$$\sigma_p = \frac{\bar{n}}{\left(A^2+(\bar{n}-\frac{1}{2})^2\right)^{1/2}}, \text{ and} \tag{2-13}$$

$$A = \frac{1}{\pi}\cosh^{-1}\left(10^{PSLR/20}\right). \tag{2-14}$$

PSLR is the peak-to-sidelobe ratio in dB. The parameter $\bar{n}$ governs the extent over which sidelobe levels are constant in the vicinity of the mainlobe. The Taylor window is an approximation to the Dolph-Chebyshev window discussed by Harris in [28]. The Taylor window is the aperture taper of choice for this dissertation.

2.3 Approaches to Autofocus

Approaches to autofocus fall into two main categories: parametric and non-parametric.

Parametric approaches assume some maximum order for a polynomial fit to the phase error of interest. The full aperture is divided into adjacent subapertures with the number of subapertures equal to the order of the polynomial. The map drift (linear shift in scene content between subaperture pairs) is used to estimate piecewise linear phase error (phase slope) between subaperture pairs. Various curve fitting techniques are then used to estimate the phase function. These parametric approaches are widely referred to as map drift, mean frequency or subaperture autofocusing. They only work for up to about fourth-order polynomial-type phase errors [21].

Prior to PGA, prominent-point autofocus was the non-parametric approach to autofocus. This approach estimates the phase by deconvolving the complex point spread function of the system from the measured complex point spread function of an identifiable strong point-like reflector in the scene. While this approach does not require any a priori assumptions about the structure of the phase, the disadvantage is obvious. It requires a strong point-like reflector in the scene, a condition not always met in practical applications of SAR imaging.

The PGA algorithm takes a signal processing approach to the problem of autofocus. It recognizes that the phase errors due to SAR platform motion or atmospheric turbulence have nearly the same affect at every pixel and at every range. It takes advantage of this redundancy of information. The process can be likened to coherently summing phase-gradient vectors across ranges. The coherent gain in signal-to-noise ratio is then approximately equal to the number of ranges in the sum.

Chapter 3

Background

The Phase Gradient Autofocus Algorithm

In Chapter 1, five areas of investigation regarding the PGA algorithm were identified as the object of this research. That chapter identified the issues and the current state of knowledge, then summarized the original results that are presented in Chapter 6. In Chapter 2, the principles of SAR image formation were reviewed and the need for data-driven autofocus was developed. In this chapter the functions of the PGA algorithm are reviewed in detail. This review begins with Step 1, Input the Complex Image. Areas of investigation are restated as questions as the steps of the algorithm are reviewed. The block diagram of the PGA algorithm was shown in Chapter 1 in Figure 1-3 on page 10. Here, the questions raised are summarized in the expanded data flow diagram in Figure 3-4 on page 50 at the end of this chapter.

3.1 Review of the Phase Gradient Autofocus Algorithm

Step 1. Input the Complex Image

We begin with the data model assumed by Jakowatz, Eichel and Ghiglia in [34] and [18] and by Jakowatz and Wahl in [33]. Although this data model is defined in the phase-

history domain, it defines related assumptions in the image domain. It is, therefore, appropriate to introduce the data model at the first step of our review of the PGA algorithm. In [33], the m^{th} phase-history data sample at the k^{th} range is defined as

$$x_{k,m} = a_k e^{j\phi_m} + n_{k,m} \tag{3-1}$$

where

$a_k = |a_k| e^{j\theta_k}$ is the complex envelope of the signal at the k^{th} range. The expected value of the magnitude squared of a_k, $E\{|a_k|^2\} = \sigma_a^2$ and $|a_k|$ are assumed to be independent and identically distributed across ranges, but invariant across azimuth at any single range. Similarly θ_k, a target-dependent phase at the k^{th} range, is assumed to be independent and identically and uniformly distributed across ranges, but invariant across azimuth at any single range.

ϕ_m is the aberrating phase of interest at the m^{th} azimuth sample and is assumed to be invariant across ranges for any given azimuth index.

$n_{k,m}$ is complex circularly Gaussian noise, assumed to be independent and identically distributed for all range samples indexed by k and all azimuth samples indexed by m. Noise power is defined as $E\{|n_{k,m}|^2\} = \sigma_n^2$.

This data model is predicated on the assumption that clutter in the image domain is also complex circularly Gaussian, independent and identically distributed for all range samples indexed by k and all azimuth samples indexed by m. It is further predicated on

the assumption that signal is also complex circularly Gaussian and independent and identically distributed for all ranges with only one signal per range. These assumptions are stated explicitly by Jakowatz and Wahl in [33]. The relationship between the assumptions in the phase-history domain and those made in the complex image domain is a consequence of the fact that the discrete Fourier transform is a unitary linear transform. The adequacy of this data model to represent real SAR data is identified as Area 3 .

Step 2. Circularly Shift the Brightest Points

Recall from Chapter 2, that for both map drift and prominent point autofocus algorithms, the brightest point at each range is regarded as signal. The mathematical model for the unaberrated brightest point at the k^{th} range is

$$w_{k,m} = a_k e^{j\omega_{d_k} m\Delta t} + n_{k,m} \tag{3-2}$$

where

a_k and $n_{k,m}$ are as defined above for equation (3-1),

ω_{d_k} is the radian Doppler frequency associated with the brightest point at the k^{th} range, and

Δt is the sample interval in the azimuth dimension.

The mathematical model for the aberrated brightest point at the k^{th} range is

$$w_{k,m} = a_k e^{j\phi_m} e^{j\omega_{d_k} m\Delta t} + n_{k,m}. \tag{3-3}$$

Shifting the brightest points in the complex image domain to the index corresponding to the center of the scene is equivalent to demodulating the data in the phase-history domain; that is,

$$x_{k,m} = w_{k,m} e^{-j\omega_{d_k} m\Delta t} . \tag{3-4}$$

The shifting process is illustrated in Figure 3-1(a), (b) and (c). Figure 3-1(a) shows a gray-scale plot of the magnitude squared of a synthesized SAR image. There is a single bright scatterer at each range with signal-to-clutter ratio of 26 dB. Since there is no structure to this synthesized SAR scene, it appears noise-like. To clarify the display, only one quarter of the 512 by 512 pixel scene is shown. Figure 3-1(b) shows the same SAR scene defocused in azimuth by a quadratic phase error with full extent of the point spread equal to 1/8 of the azimuth aperture. Figure 3-1(c) shows the center portion of the shifted version of Figure 3-1(b). For this example there were no shift errors present. The loci of the brightest points were determined and center shifted prior to defocusing. In practice, however, the radial Doppler frequencies, ω_{d_k}, are unknown and must, therefore, be estimated. The effect of errors in estimation of ω_{d_k}, referred to here as shift errors and expressed in the notation as $\omega_{s_k} = \omega_{d_k} - \hat{\omega}_{d_k}$, where $\hat{\omega}_{d_k}$ is the estimated value and ω_{s_k} is the estimation error, will appear as Area 4 in the list of areas to be investigated.

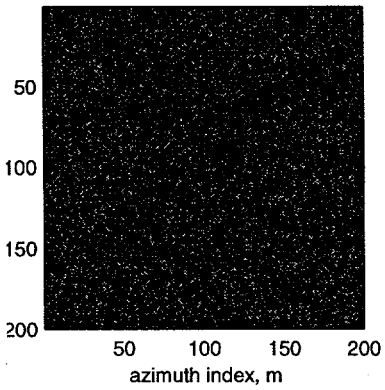

(a) Unaberrated synthesized SAR image with a single bright point at each range. Amplitudes and azimuth positions of the bright points are random and independent. Mean signal-to-clutter ratio = 26 dB.

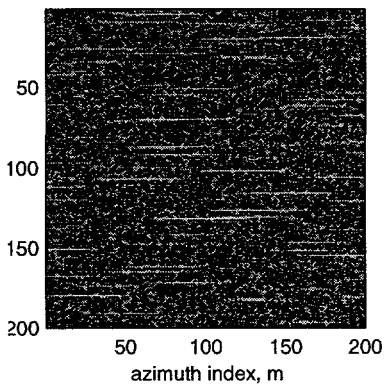

(b) Synthesized SAR image defocused by quadratic phase error with a 50 radian deviation at the edge of the aperture. Full extent of the point spread = 1/8 of the aperture.
Full extent of the point spread = 1/8 of the aperture.
Taylor window with -40 dB peak sidelobes and $\bar{n}$ = 6 was used to taper the range-compressed phase-history aperture.

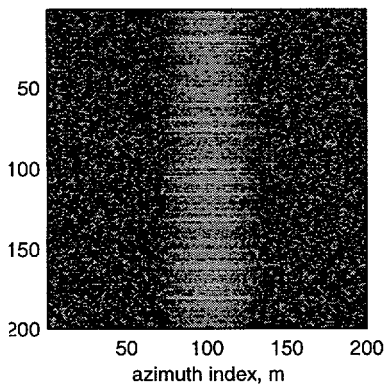

(c) Circularly shifted defocused SAR image.

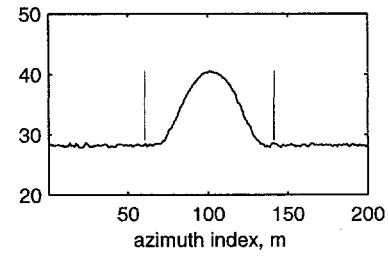

(d) Non-coherent sum, across ranges, of magnitude squared of defocused, shifted SAR image.
Vertical lines mark 1.5 x's the minus 10 dB width.

Figure 3-1. Shifting, summing and windowing processes illustrated.

Step 3. Apply Window to Limit the Support of the Point Spread Function

The purpose of limiting the support of the point spread function is to minimize the noise power in the alternate domain, the phase-history domain. This maximizes the SNR into the ML phase-gradient estimator. In order to develop the data from which to estimate the required support (or window) of the point spread function, the shifted, squared-magnitude data are summed across ranges. The sum at the m^{th} azimuth sample is defined in the image domain as [65]

$$S_m = \sum_{k=1}^{N_{ranges}} \left| X_k(\omega_m) \right|^2 \tag{3-5}$$

where

$X_k(\omega_m)$ is the Fourier transform of the range-compressed phase history, x_k, and because of the shifting process, the maximum of S_m is at $\omega_m = 0$.

If the data are as modeled in equation (3-1) then the windowed or bandlimited noise power in the phase-history domain $= \frac{N_{window}}{N_{az}} \sigma_n^2$, where N_{window} is the size of the window and N_{az} is the total number of azimuth samples across the aperture. Current practice with the PGA algorithm is to use a rectangular window of width = 1.5 × (-10 dB width). The sum and point-spread support are illustrated in Figure 3-1(d). Current practice has been shown to be effective for scenes with high contrast (high signal-to-clutter ratios) such as urban scenes. For scenes with low contrast, as is the case for many rural scenes, current

practice is to start with the width of the support equal to the maximum expected width and to then decrease the width of the window by 20% with each iteration.

An alternative algorithm for estimating the required point spread support will be offered in Chapter 6. The method of defining the required support for the point spread function is identified as Area 5.

Step 4. FFT

At this point the windowed complex image data are transformed back to the phase-history domain. How this is done is part of Area 1, which is discussed as part of Step 6.

Step 5. Phase Gradient Estimation

Two phase-gradient estimator kernels have been proposed for the PGA algorithm. The more recent, maximum likelihood (ML) estimator, which replaced the earlier linear unbiased minimum variance (LUMV) estimator is the only estimator that will be considered here.

The model of the data into the estimator has already been given in equation (3-1). The ML estimator itself is an eigenfilter, which is the stochastic equivalent to matched filters for deterministic signals [29]. In [33] Jakowatz and Wahl developed the theory for the general eigenfilter for phase gradients of length M and derived the Cramér-Rao lower

bound[1] (CRLB) for the general case. They demonstrated estimator performance for M = 64 and for $M = 2$. Within the context of the PGA algorithm, M is the number of azimuth data samples simultaneously processed to estimate M-1 phase gradients. Thus, M is also the dimension of the covariance matrix of the data into the estimator.

Here, we will consider only the case for the minimum dimension of $M = 2$; that is, pair-wise estimates of phase gradients. The relative mathematical intractability for the case of $M > 2$ as opposed to the case of $M = 2$ argues strongly for using the simplest possible form to gain insights. Results for $M = 2$ are expected to extrapolate to the mathematically more complex implementation with $M > 2$.

The phase gradient estimator for $M = 2$ is defined as

$$\hat{\psi}_{n,m} = \angle \sum_{k=1}^{N_{ranges}} x_{k,n} x_{k,m}^{*} . \tag{3-6}$$

This estimator can be visualized as the angle defined by the coherent sum of vector products. This concept is illustrated in Figure 3-2. Figure 3-2(a) shows a vector pair for

---

[1] The Cramér-Rao lower bound (CRLB) provides a measure of the variance of an efficient estimator without requiring the specification or even the existence of that estimator [B12.21]. It provides a figure of merit against which to measure performance of candidate estimator algorithms. Details of the CRLB will be covered in Chapter 5, Appendix C, and applied in Chapter 6.

a single range. The angle, ψ, between the two vectors is the only parameter that is constant over range. It is considered to be non-random but unknown. Figure 3-2(b) illustrates the coherent sum of vector products.

In [33] Jakowatz and Wahl have shown that, for the assumption of the data model stated in equation (3-1), the Cramér-Rao lower bound for estimates of gradients between M pairs of angles is

$$\sigma_{\psi}^2 = \frac{1+M\beta}{N_{ranges} M\beta^2}. \tag{3-7}$$

For the problems addressed here, for $M = 2$; thus, equation (3-7) reduces to

$$\sigma_{\psi}^2 = \frac{1+2\beta}{2N_{ranges}\beta^2} \tag{3-8}$$

where $\beta = \frac{\sigma_a^2}{\sigma_n^2}$ is the signal-to-noise ratio in the phase-history domain.

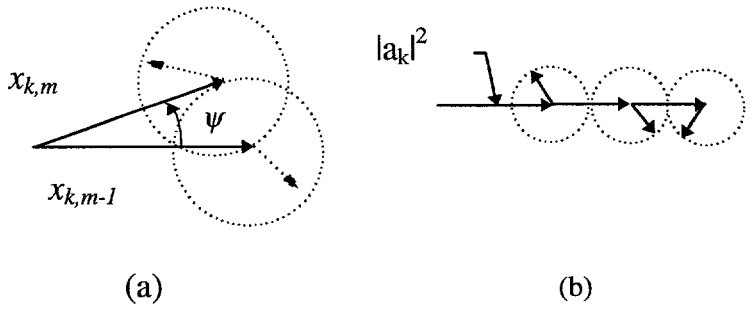

Figure 3-2. Phasor diagrams illustrating the ML phase-gradient estimator. (a) Only the difference angle, ψ, is constant across ranges. (b) The vector products sum coherently across ranges.

Equation (3-8) is shown in the plot in Figure 3-3 along with the output from Monte-Carlo trials. The data used from these trials were simulated in the phase-history domain using the data model of equation (3-1). Note that the theoretical CRLB and the results of Monte-Carlo trials show only the mean square of the principal value of phase-gradient errors for in-band data. Neither the model nor the simulations consider the effects of a too-narrow support of the point spread.

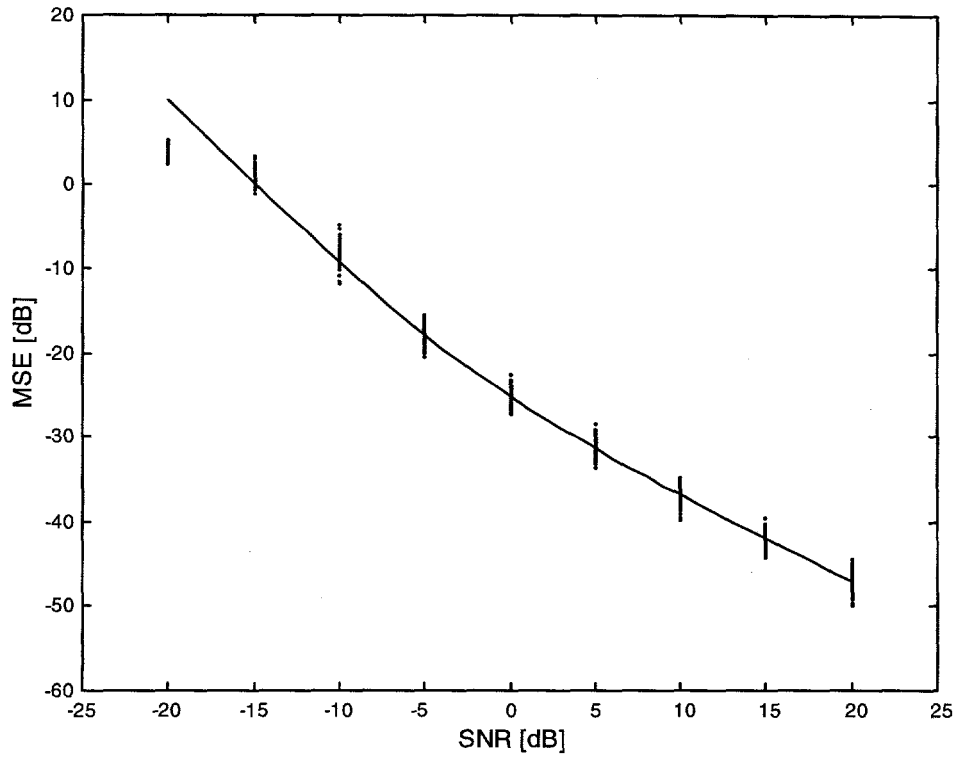

Figure 3-3. Theoretical Cramér-Rao lower bound for $M = 2$ (solid line) and scattergram of MSE across the aperture of principal values of estimated phase gradient. Estimates are shown for 121 Monte-Carlo trials using simulated phase histories. Data from Monte-Carlo trials are so tightly clustered that the scattergrams appear as vertical lines.

Step 6. Apply Phase Correction

There is a critical step in the implementation of PGA that is neither illustrated explicitly in the data flow-diagram nor addressed in the literature. Between Step 4 (the FFT back to the phase-history domain) and Step 6 (application of the phase correction), bandlimited data must be up-sampled to estimate the phase error for each aperture sample. This implied step requires digital integration of phase gradients and interpolation of bandlimited data, though not necessarily in that order. Implementation of this data transformation subprocess between Step 4 and Step 6 is identified as Area 1.

Step 7. IFFT and Iteration

Experience shows that residual phase error can be further reduced by repeating the entire process [65] and [51]. One explanation offered for this phenonenon is that as the point spread support is narrowed with each iteration, the bandwidth of the residual phase gradient is reduced and thus the signal-to-noise ratio improves. Improvement in phase-gradient estimation is attributed to this improvement in signal-to-noise ratio. An alternative hypothesis is posed in Snarski in [51]. Snarski, who implements three of the four critical steps of PGA, omitting Step 2, the windowing of the point spread function, has hypothesized that the need for iteration is driven by shift errors. The root cause of the demonstrated improvement with iteration is identified as Area 2.

3.2 Summary of the Five Areas of Investigation

The five areas of investigation are reiterated here in the order in which they will be addressed. The positions of these areas within the context of the PGA algorithm are illustrated in Figure 3-4.

1. What is the best method to transition from bandlimited estimates of phase gradients to phase estimates interpolated across the full aperture?
2. If the PGA ML kernel is an optimal estimator, then what drives the observed improvement with iteration?
3. Is the current data model adequate to describe PGA performance for real SAR data in the absence of shift errors?
4. How do shift errors affect PGA performance?
5. Is there an alternative to the current approach of estimating the support of the point spread function?

In order to address these questions, SAR and aberrating phase data need to be selected and theoretical and numerical methods of analyses need to be identified. In the next chapter, Chapter 4, the theory of deterministic and random angle modulation are reviewed, three classes of phase errors used for this research are identified, and associated metrics are reviewed. Five sets of SAR image data are analyzed and data with similar signal-to-clutter ratios are synthesized. Then in Chapter 5, the theoretical and numerical methods of analyses that will be used are reviewed. Finally, in Chapter 6 the five areas are addressed in the order just identified.

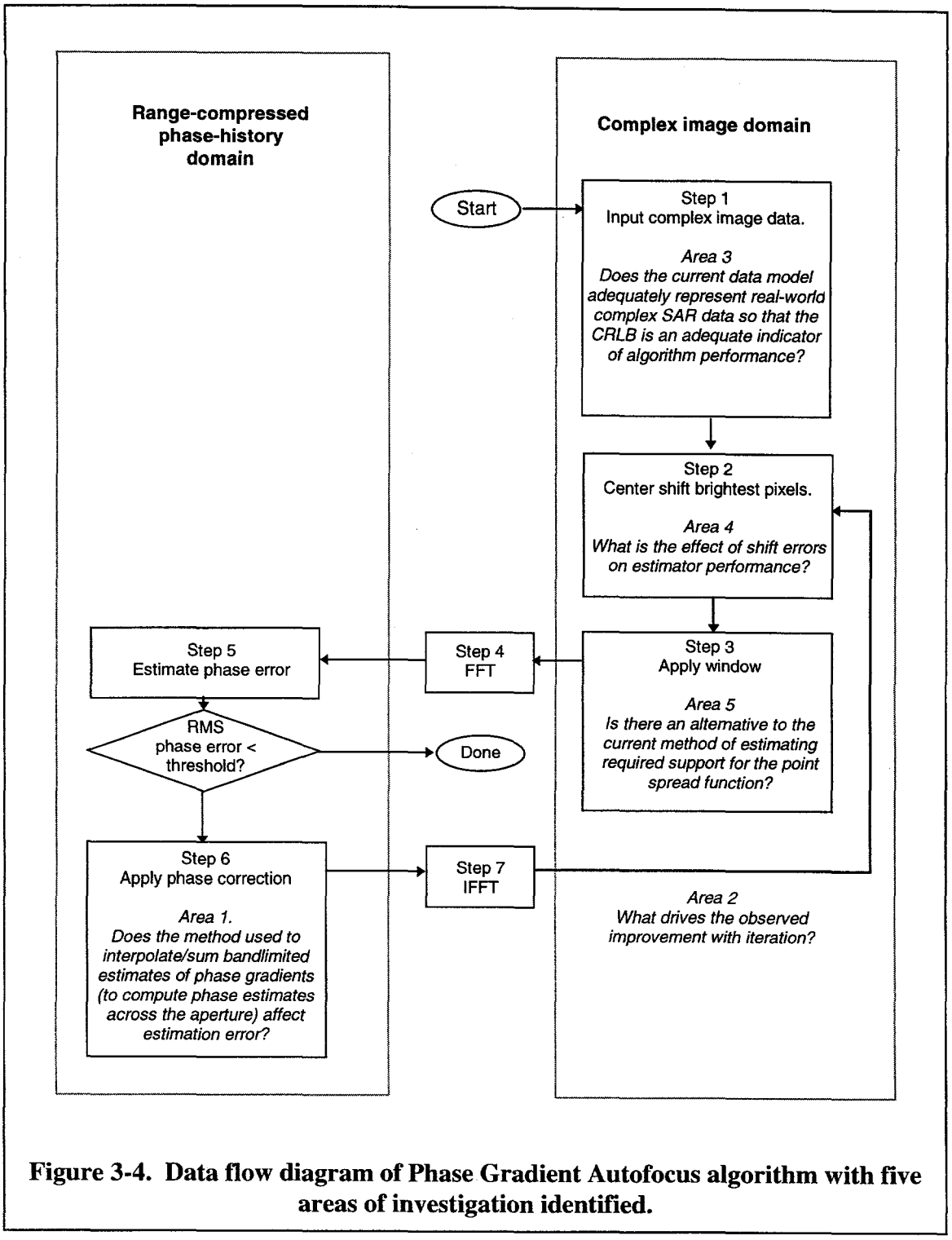

Figure 3-4. Data flow diagram of Phase Gradient Autofocus algorithm with five areas of investigation identified.

Chapter 4

Background

Phase and Scene Statistics

In this chapter, the phase error functions and the real SAR image data used for this research are presented. Phase error statistics and SAR image data statistics are independent, thus, these two topics are treated independently in the two main sections of this chapter. Significant findings are summarized at the end of each of the two main sections. The first section on angle modulation and phase statistics begins with a general discussion of the theory of deterministic angle modulation. This is followed by a discussion of metrics of random angle modulation. The first section concludes with the presentation of the sample realizations of the three classes of aberrating phase function used in this research. Metrics of random phase modulation (rms frequency deviation, the rms bandwidth and the modulation index, which is a function of the first two) provide general guidance to the properties of the aberrating phase but are not specific enough to provide detailed information on the resultant image quality. In the second section on SAR image data, five sets of SAR image data are introduced, the method of synthesizing SAR data is reviewed, and the results of exploratory and comparative analysis of the real and synthesized data are summarized. By design, the clutter of the synthesized SAR data

are independent but identically distributed with circularly Gaussian statistics. This is consistent with the assumptions of the data model given in equation (3-1) in Chapter 3. An analysis comparing real to synthesized SAR data indicates that the clutter distribution for real SAR data does not meet these same criteria of homogeneity. This is explored in greater detail in Chapter 6 where recommendations are made.

4.1 Angle Modulation and Phase Statistics

Although the SAR autofocus problem addressed here is one of estimating and correcting for stochastic wideband angle modulation, an understanding of wideband and narrowband single-frequency angle modulation is useful. References for this development are, Brown [12], Gardner [23], Papoulis [47], Schwartz [50], Stremler [55], and Tzannes [60],

4.1.1 Properties of Deterministic Angle Modulation

Phase and frequency modulation are more generally referred to as angle modulation. The complex carrier, $a\exp(j\omega_o t)$, is phase modulated by the function $\phi(t)$ to produce the signal

$$x(t) = a\exp[j\omega_o t + j\phi(t)], \tag{4-1}$$

where a is the real valued signal amplitude and $x(t)$ has an instantaneous frequency $\omega_o + \psi(t) = \frac{d}{dt}[\omega_o t + \phi(t)]$. The distinction between phase and frequency modulation is in the definition of the modulating signal. If $\phi(t)$ is the modulating signal then the process is phase modulated. If $\psi(t)$ is the signal of interest then

$x(t) = a\exp\left[j\omega_o t + j\int_0^t \psi(t)dt\right]$ is said to be frequency modulated. By omitting the carrier frequency and considering only the modulating portion of $x(t)$ and by substituting a single frequency for the modulating signal, $\int_0^t \psi(t)dt = \beta_M \sin\omega_m t$, (4-1) simplifies to

$$x(t) = a\exp[\beta_M \sin\omega_m t] = \sum_{n=-\infty}^{+\infty} J_n(\beta_M)\exp(n\omega_m t). \tag{4-2}$$

For a single modulating frequency, ω_m, the parameter $\beta_M = \Delta\omega/\omega_m$, is called the modulation index where $\Delta\omega$ is the maximum excursion of instantaneous frequency about the carrier frequency, ω_o. Equation (4-2), which is often called the Bessel-Jacobi equation (see Tzannes [60], p. 151), shows us that single-tone angle modulation produces a signal that is the weighted sum of the fundamental frequency and its harmonics. The coefficients of the fundamental and its harmonics,

$$J_n(\beta_M) = \frac{1}{2\pi}\int_{-\pi}^{\pi} e^{j(\beta\sin x - nx)}dx$$

are Bessel functions of the first kind. These functions cannot be evaluated in closed form but have been extensively calculated and tabulated for various arguments, β_M, and orders, n. Bessel functions have the property that for n > β_M+1, the magnitude $J_n(\beta_M)$ is small. A rule commonly used is that if $|J_n(\beta_M)| \le 0.01$, the harmonic is insignificant [55]. This corresponds to a harmonic 40 dB down from peak power.

If β is small, the modulation is narrowband and the higher order coefficients, $J_n(\beta_M)$; that is, for $|n| > 0$, are insignificant. The power spectrum of narrowband FM is not distinguishable from that of AM (amplitude modulation), appearing as a pair of spectral

lines centered about the carrier and with amplitude determined by the carrier amplitude. The power spectra for narrowband and wideband FM are illustrated in Figure 4-1. The data shown in the figures were generated using 512 samples with $\omega_m = \pi/8$ [rads] and $\beta_M = 0.01$ (narrowband modulation), 0.1 and 1.0 (wideband modulation).

The purpose of this discussion of single-tone angle modulation has been to gain insight into the spectral properties of angle modulated signals and to develop definitions of wideband and narrowband angle modulation. Although, the case of autofocusing a SAR image aberrated by single frequency angle modulation is not considered in this research, this discussion has demonstrated the impact to wideband angle modulation of the point spread function and has exposed the non-linearity of the problem of autofocus.

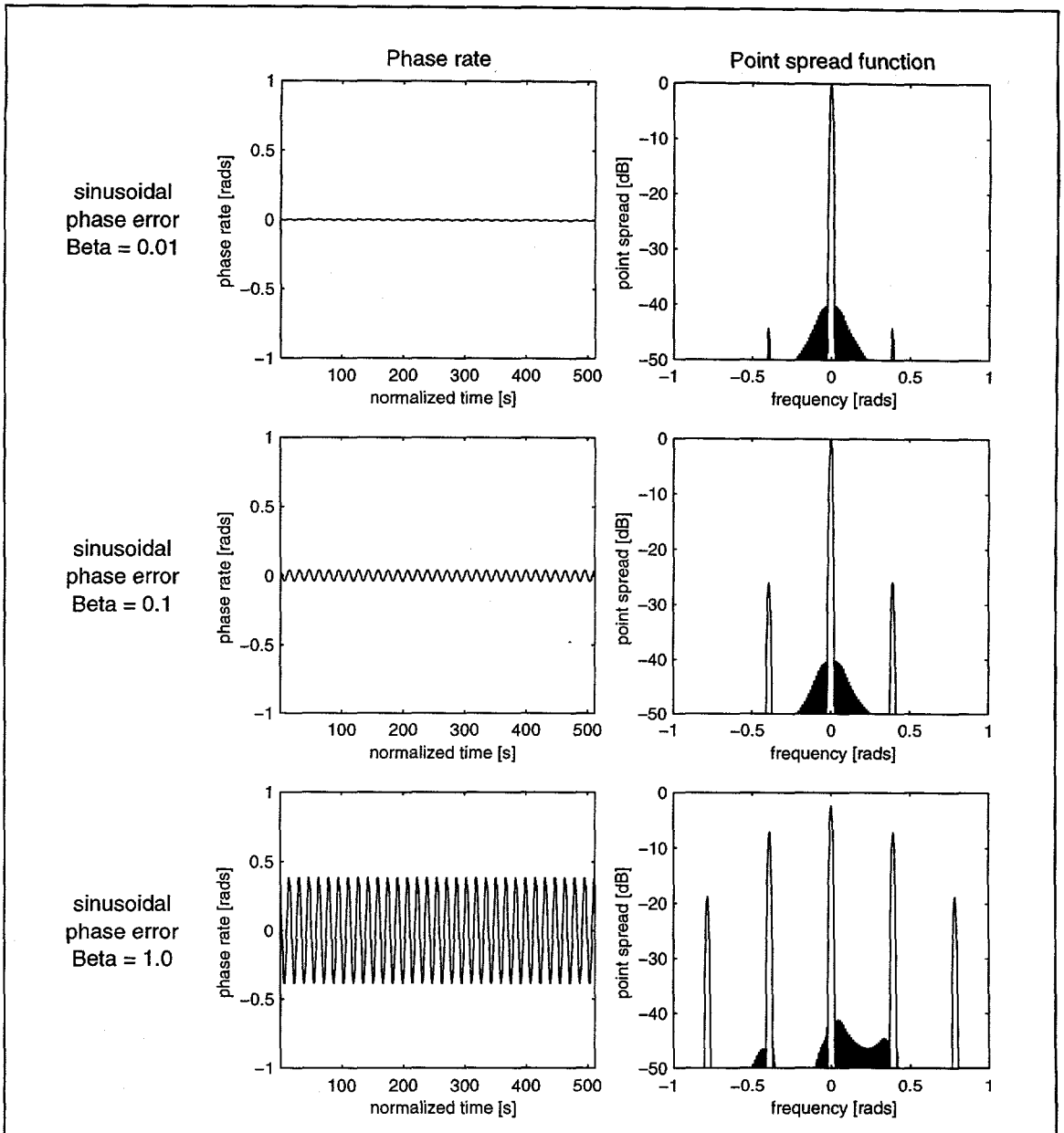

Figure 4-1. Illustration of single-tone narrowband and wideband modulation.

Plots in the left column show the frequency modulating signal (phase rate). Plots in the right column show the power spectra for the associated angle modulation. Note how the sidelobe levels increase as the amplitude of the frequency modulating signal increases.

4.1.2 Metrics of Random Angle Modulation

Closed form expressions for the spectra of multi-tone wideband modulation are not easily obtained [47]. There are, however, some useful metrics and relationships to describe wideband random angle modulation.

For random angle modulation, Gardner [23] defines the modulation index as $\beta_M = \Delta\omega / B_\psi$, the ratio of the rms frequency deviation, $\Delta\omega$, to bandwidth, B_ψ, of the phase rate. The rms frequency deviation

$$\Delta\omega = \sqrt{R_\psi(0)} = \left[\int_{-\infty}^{\infty} S_\psi(\omega) d\omega\right]^{1/2} \tag{4-3}$$

where, $R_\psi(0)$ is the autocorrelation of the phase rate, $\psi(t)$, at zero lag and $S_\psi(\omega)$ is the power sprectrum of $\psi(t)$. Bandwidth

$$B_\psi = \left[\int_{-\infty}^{\infty} \omega^2 S_\psi(\omega) d\omega\right]^{1/2} \Big/ \left[\int_{-\infty}^{\infty} S_\psi(\omega) d\omega\right]^{1/2}. \tag{4-4}$$

Using the well known relationship for function differentiation in the Fourier domain

$$S_\psi(\omega) = \omega^2 S_\phi(\omega), \tag{4-5}$$

and by substituting (4-5) into (4-3) and (4-4) it can be shown that

$$\beta_M^2 = R_\phi(0)\left(B_\phi / B_\psi\right)^2.$$

Finally using the Schwarz inequality it can be shown that

$$\left(B_\phi / B_\psi\right)^2 \le 1 \tag{4-6}$$

and consequently

$$\beta_M^2 \leq R_\phi(0). \tag{4-7}$$

Thus modulation index, β_M, provides a coarse discriminate between zero-mean narrowband and wideband angle modulation. If $R_\phi(0) \ll 1$ then $\beta_M \ll 1$, and the modulation is narrowband. Similarly, if $R_\phi(0) \gg 1$ then $\beta_M \gg 1$, and the modulation is wideband.

Mean squared frequency deviation or mean squared error of the phase gradient (MSE), rms frequency and modulation index are reported here as metrics of residual phase-gradient error at the output of the ML estimator. They were computed as follows.

The rms frequency deviation,

$$(\Delta\omega)^2 = R_\psi(0) = \frac{1}{N-1}\sum_{n=2}^{N} \varepsilon_n{}^2, \tag{4-8}$$

where the error $\varepsilon_n = \hat{\psi}_n - \psi_n$, is the difference between the estimated phase gradient and truth, and the true gradient, $\psi_n = \phi_n - \phi_{n-1}$, is the first difference of the phase.

Computation of the rms bandwidth as defined in (4-4) used the following well known identity $R_{\dot{\psi}}(0) = \int_{-\infty}^{\infty} (\omega)^2 S_\psi(\omega) d\omega$ where

$$R_{\dot{\psi}}(0) = \frac{1}{N-2}\sum_{n=1}^{N-2} (\psi_{n+1} - \psi_n)^2. \tag{4-9}$$

Using, (4-9), (4-8) and (4-3) in (4-4) results in

$$\beta = \frac{R_\psi(0)}{\sqrt{R_{\dot{\psi}}(0)}}, \tag{4-10}$$

the equation used to compute modulation index for results reported here.

Unlike the case of single-tone modulation, where $|J_n(\beta_M)| < 0.01$ provides a useful measure of bandwidth, the problem of determining the spectra due to random angle modulation is, in general, difficult. In [47] Papoulis addresses three special cases that lead to reasonable results. One of those results is Woodward's theorem. As summarized on page 255 of Gardner [23], Woodward's theorem shows that, for wideband modulation, the shape of the spectrum of the modulated signal, $e^{j\phi(t)}$, is determined not by the spectrum of the modulating signal, $\psi(t)$, but rather by the probability density of the modulating signal, $p_\psi(\psi(t))$. The usefulness of this theorem and the three metrics of angle modulation; that is, rms frequency deviation, bandwidth and modulation index are considered in the next section where the phase functions used in this research are discussed.

4.1.3 Analysis of Quadratic, Low Order and Power Law Phase Functions

The three aberrating phase functions considered were quadratic, low order and power law. The last two are the phase functions in the data set offered by Wahl et. al. in [65]. While the quadratic function is non-random, it provides a useful baseline. The low order and power law phase functions are sample realizations of random processes with spectral content dominated by low frequency and broadband components, respectively. The quadratic error is a single low frequency focus error. The low order phase error is representative of the type of phase error expected after motion compensation, although the maximum frequency deviation of the sample function used here is somewhat severe. The power law phase error is representative of phase errors induced by propagation

through a turbulent ionosphere or troposphere; see, for example, Brown [13]. The functions and their first differences, or phase rate functions, are shown in Figure 4-2.

The sample distributions of phase rate and the energy spectra of the modulated signal, $e^{j\phi(t)}$, or the point spread functions are shown in Figure 4-3. The point spread function is defined as $\left| FT\left(W(t)\times e^{j\phi(t)}\right)\right|^2$ where FT is the Fourier transform and $W(t)$ is an aperture taper or windowing function. For this figure, $W(t) = 1$ for all t, and spectra are displayed in units of normalized power. In SAR imaging, the spectrum of $e^{j\phi(t)}$, referred to as the point spread function, shows the spread of energy, due to aberrating phase, from a single pixel into adjacent pixels. Metrics of point spread are introduced in Chapter 5. Note that the rms values of the three phases shown in Figure 4-2 differ considerably while the rms values of the three phase rates shown in Figure 4-3 are nearly equal. Note also the general similarities between the sample distributions of phase rate and the sample spectra as suggested by Woodward's theorem. In Figure 4-4, the point spread functions are shown in units of dB across the full bandwidth or extent of the image. The -40 dB Taylor window was used here. The figure in the first row shows the diffraction limited point spread function for the Taylor windowed aperture, the point spread function due to the quadratic phase error with the Taylor window, and the wide, flat point spread function due to the quadratic phase error without the Taylor window. Note that without the Taylor windowing, there would be considerable opportunity for error in locating the peak of the point spread function due to quadratic phase error. Finally, in Figure 4-5, the frequency distributions of the phase rates are shown and the bandwidths of the phase rate functions

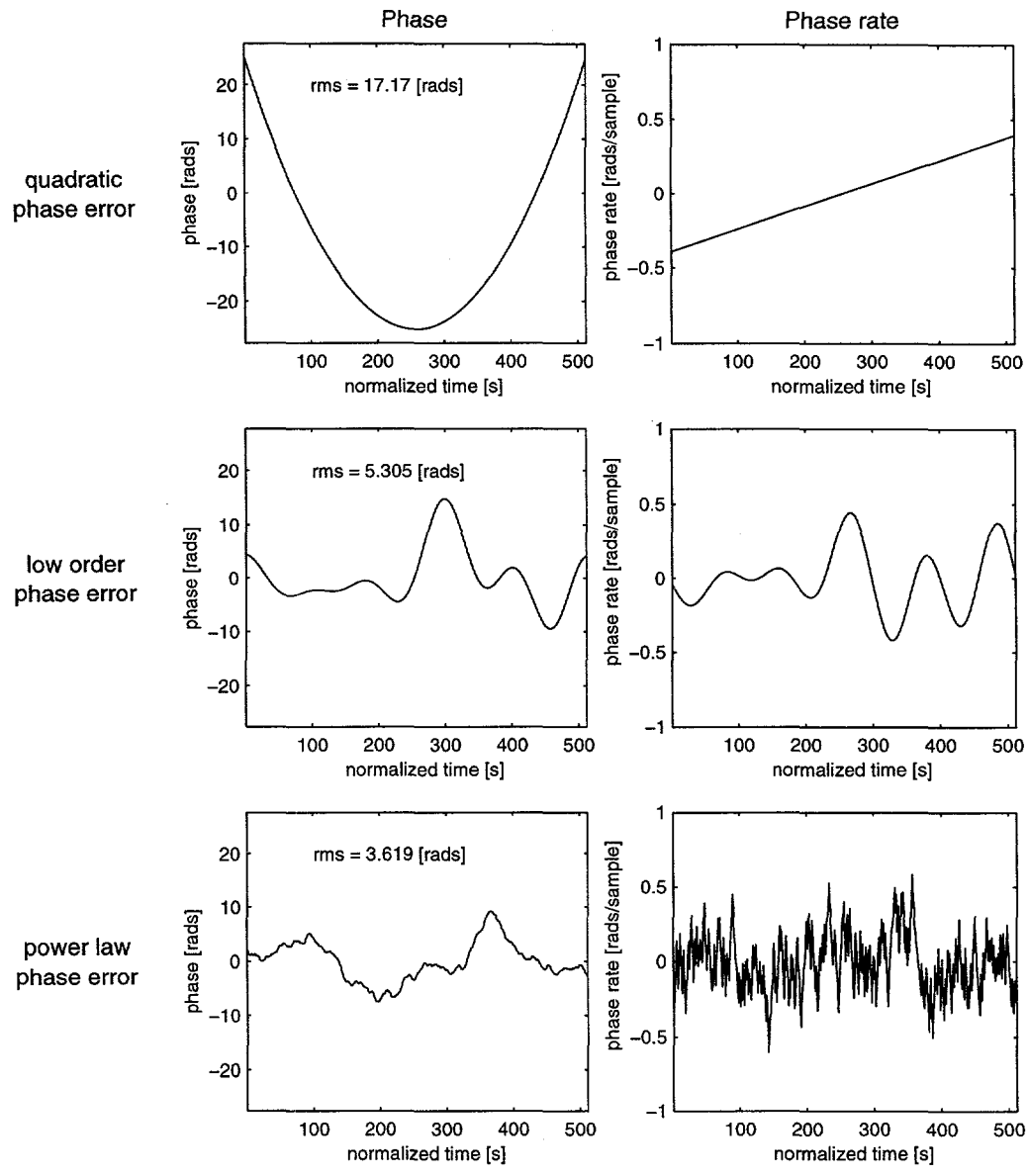

Figure 4-2. Phases and phase rates.

These are the three phase functions in this research used to aberrate SAR images. The quadratic phase provides a useful reference. The low order phase is representative of the type of phase error residual after motion compensation. The power law phase error is representative of phase errors due to propagation through turbulent ionosphere or troposphere.

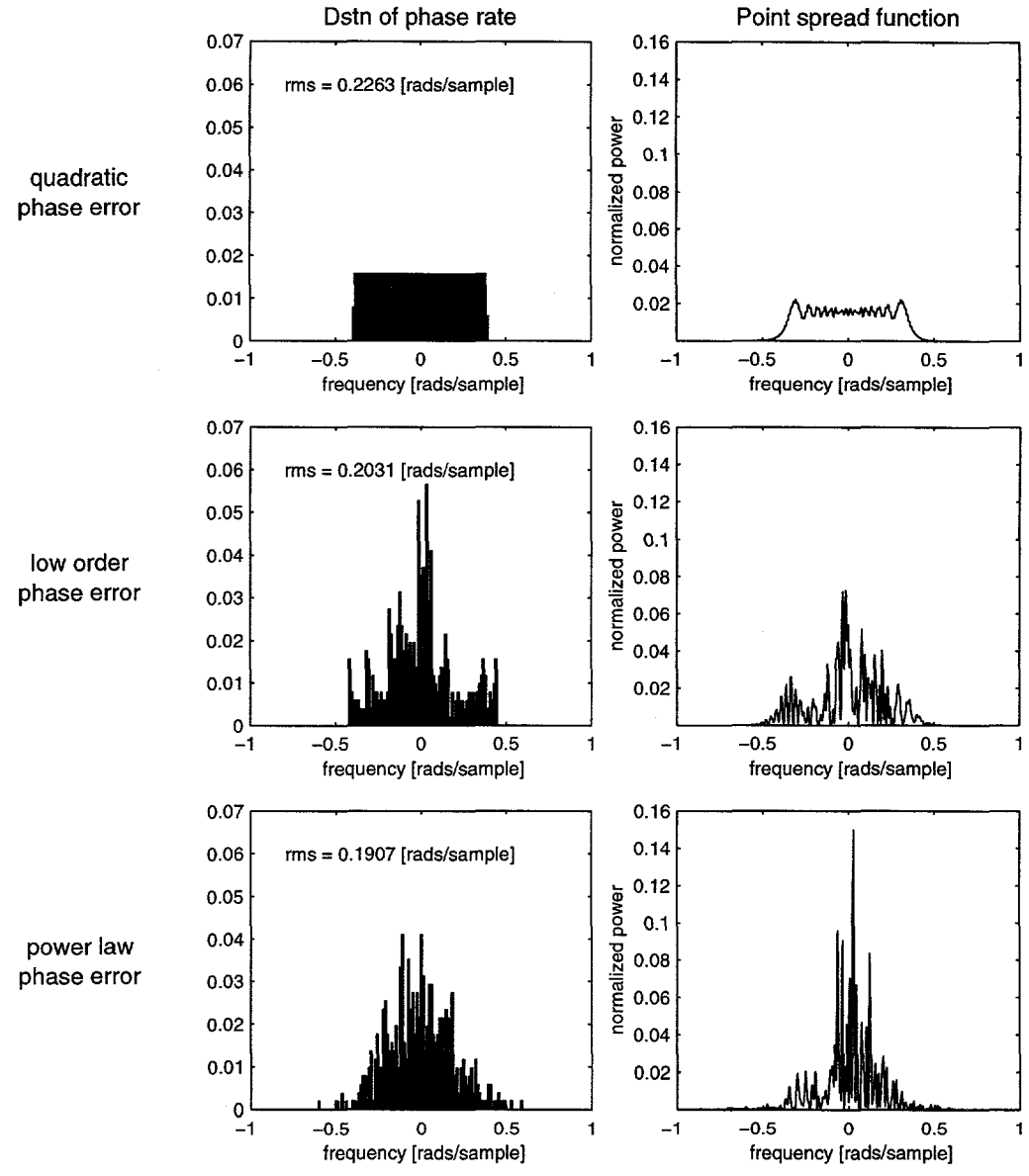

Figure 4-3. Distributions of 1st differences of phase (or phase rate) and point spread functions.

According to Woodward's theorem, note the gross similarity between the distributions of phase rates in the plots in the left column and the associated power spectra (point spread functions) shown in the plots in the right column.

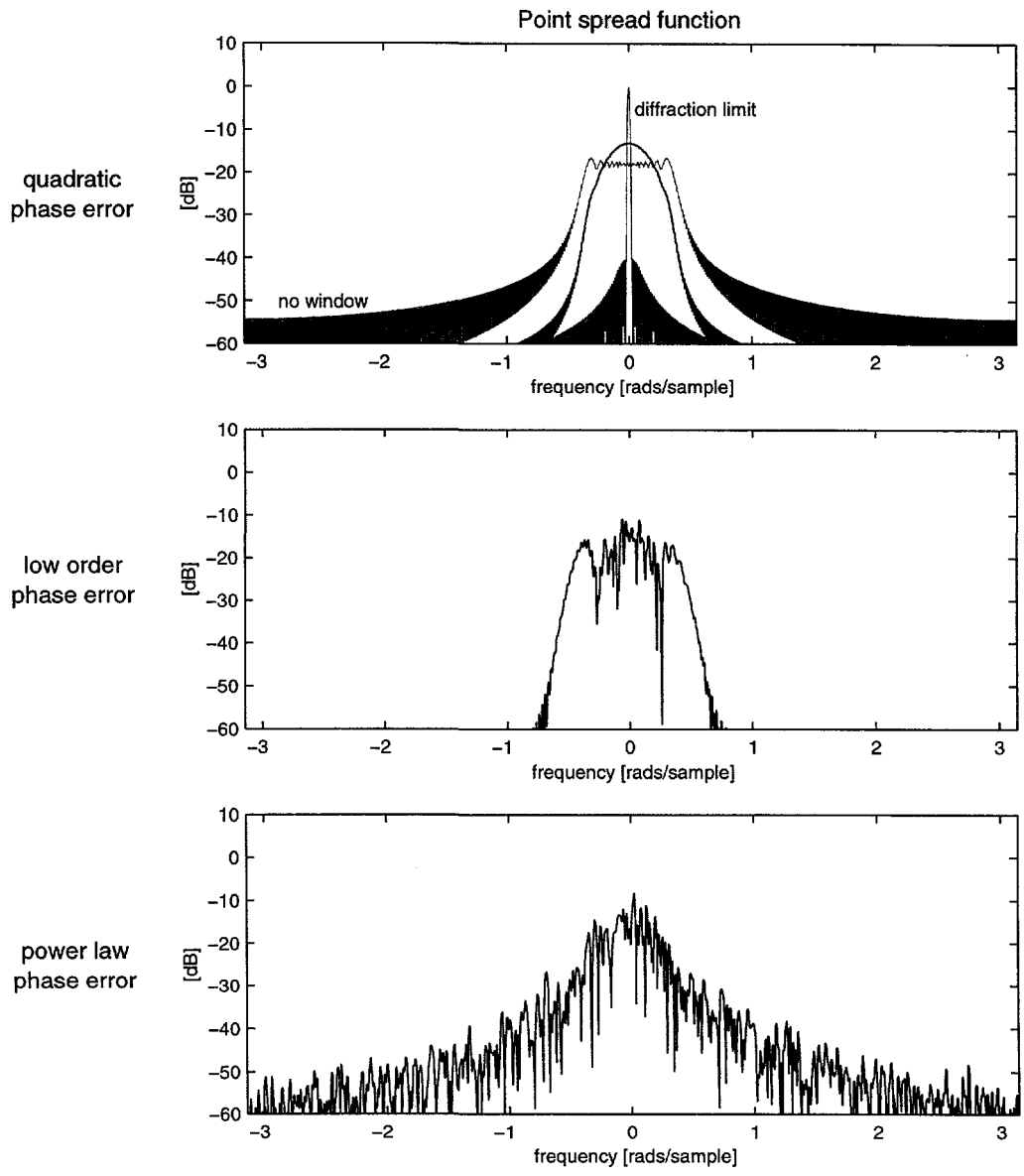

Figure 4-4. Full extent of point spread functions.

The point spread due to the quadratic phase error is shown with and without Taylor windowing and is compared to the diffraction limit. The point spread for the low order phase error requires only limited support. However, the support required for the power law phase will depend on the maximum allowable residual sidelobe level.

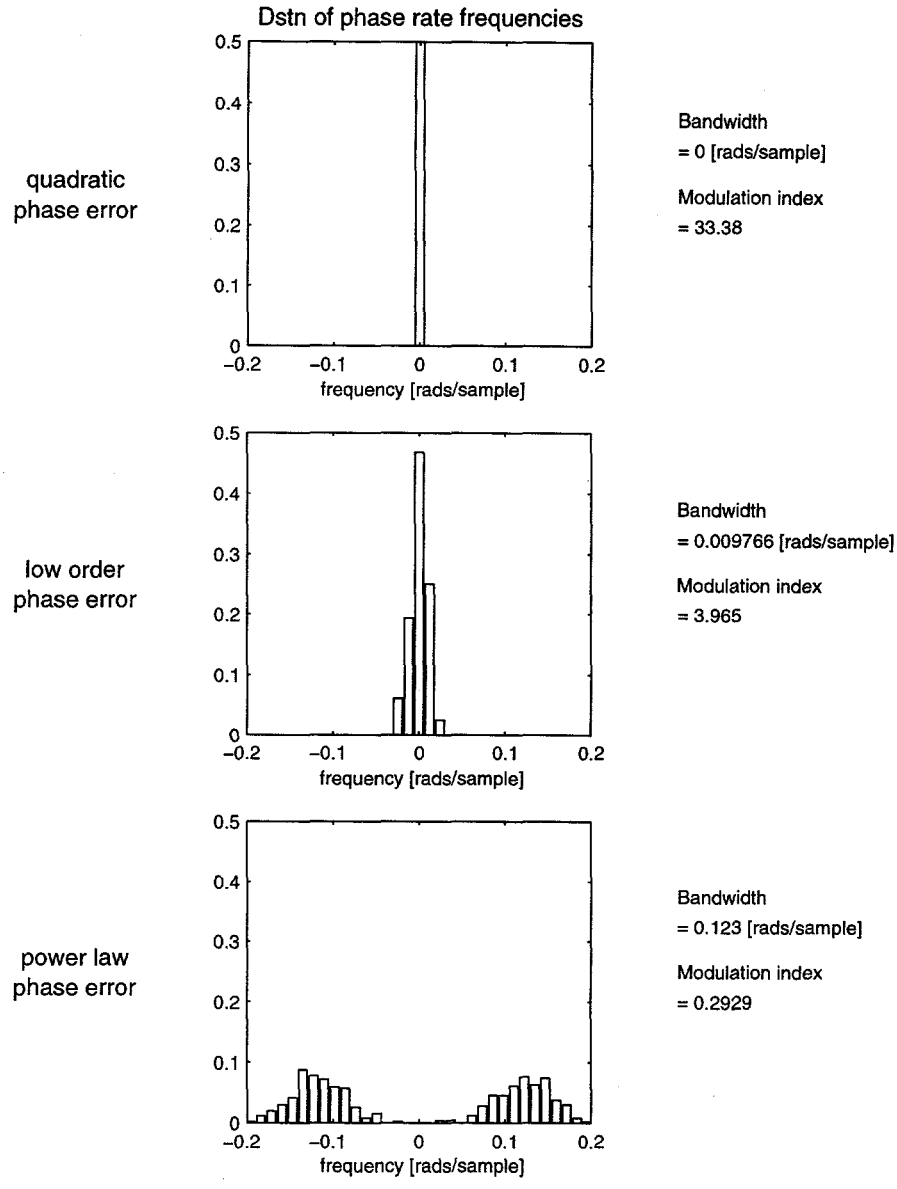

Figure 4-5. Distributions of 2nd differences of phase or frequencies of phase.

These distributions of phase rate frequencies are consistent with the spectral spread of the point spread functions shown in Figure 4-4.

and the modulation indices are listed. The notable difference in the spectral spreads between the low order phase rate and the power law phase rate is evident in these distributions.

4.1.4 Summary of Discussion on Angle Modulation

This discussion on angle modulation has shown the non-linearity of the relationship between the aberrating phase to be estimated and removed and the manifestation of that phase in the point spread function. Three measures of phase error: 1) root mean squared (rms) or mean squared (ms) phase rate (or gradient), 2) bandwidth of phase rate and 3) associated modulation index, provide some relative but no absolute guidance. In Chapter 6, Woodward's theorem will provide some guidance to understanding the relationship between observed PGA performance and properties of the residual phase rate.

4.2 SAR Image Data

The five complex SAR imagery data sets used here are the three rural and two urban scenes offered to researchers by Wahl et. al. in [65]. A sixth data set of Rayleigh noise was also used as a benchmark. These six images are shown in Figure 4-6. The Rayleigh noise, of course, appears as a random pattern of dots. The two urban scenes have at least one bright point at a number of ranges. In contrast there are no visibly dominant bright points in the three rural scenes. These scenes are assumed to represent the upper (urban) and lower (rural) bounds of scene signal-to-clutter ratios for SAR image formation problems. The mean signal-to-clutter ratios are approximately 27 dB and 15 dB respectively.

Measures and models of radar cross section for a variety of targets and conditions of illumination are readily available in the many works of F. T. Ulaby and his colleagues. This application required establishing the range of scene signal-to-clutter ratios and identifying any suggested dependence of signal and clutter statistics on scene structure. A series of data distributions were generated to meet the following two objectives.

1. Development of a basis for synthesizing SAR data with SNR comparable to the real SAR data, and
2. Identification of those properties of the real SAR data that deviate from the assumptions used by Jakowatz and Wahl [33] for the data model expressed here in equation (3-1) and used to derive the current CRLB.

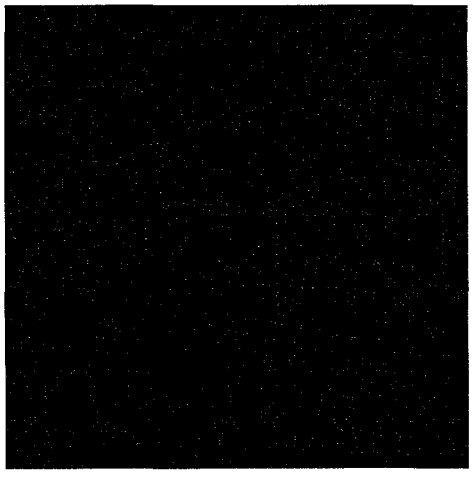

(a) synthesized Rayleigh image

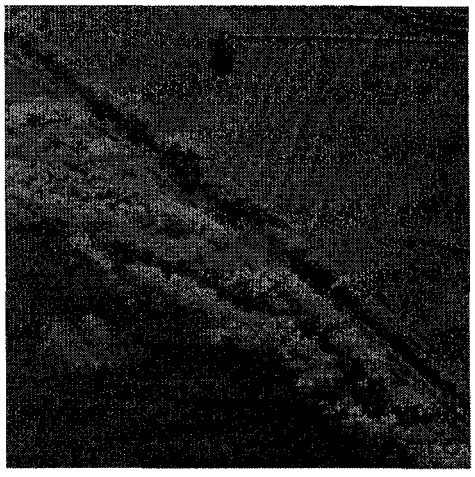

(b) Rural–1

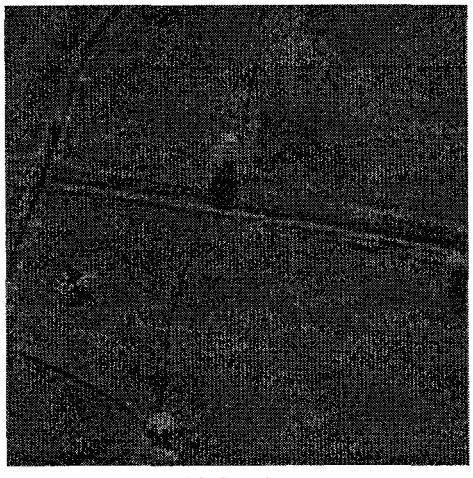

(c) Rural–2

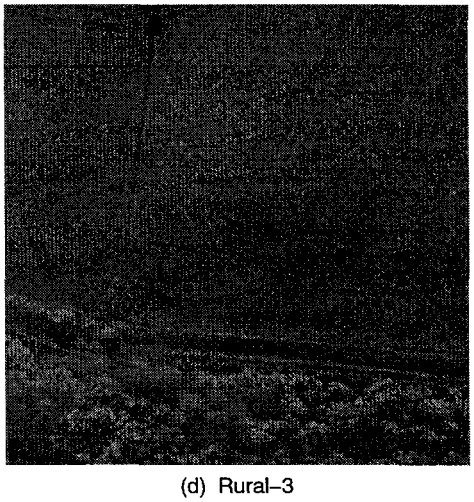

(d) Rural–3

(e) Urban–1

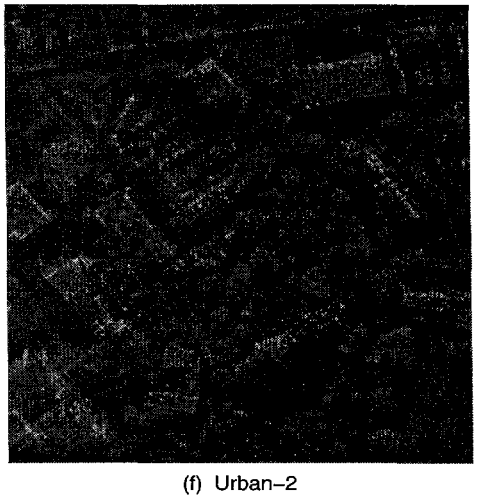

(f) Urban–2

Figure 4-6. Six SAR scenes.

4.2.1 Synthesized SAR Data

All SAR data sets used here, both real and synthesized, were 512 by 512 pixels. Signal-to-mean clutter ratios for synthesized SAR data were determined by random draws from the sample distributions of signal-to-mean clutter ratios for the real SAR data. The data in the sample distributions were the ratios of signal-to-mean clutter for the 512 ranges. Signal was defined as the sum of the power in the seven pixels centered on the brightest point at each range. The argument for choosing seven rather than one pixel to compute signal is presented later in this chapter in Section 4.2.2 and in greater detail in Appendix B. Mean clutter was defined as the arithmetic average of the power in the 128 pixels surrounding the seven signal points. To synthesize the SAR data, mean complex noise power was normalized to one and complex signal power at a given range was set to the signal-to-clutter ratio (SCR) determined by the random draw. The phase of complex data at each pixel was drawn from a uniform random distribution between $\pm\pi$. The result is a scene with a single bright point at each range surrounded by homogeneous clutter; that is, clutter that is independent and identically distributed. The azimuth positions of the bright points were determined by a draw from a uniform distribution. The sample distributions of signal-to-mean clutter ratios for the scene called Urban-1, the associated cumulative distribution from which data were synthesized and the sample distribution of signal-to-mean clutter ratios for the synthesized SAR data set are shown in Figure 4-7.

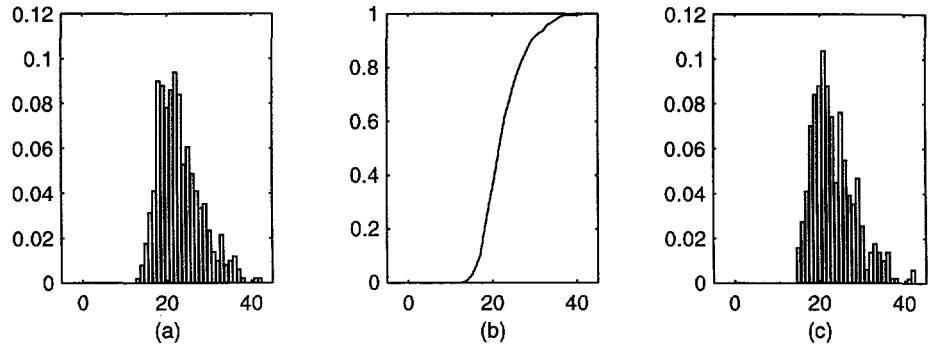

Figure 4-7. Sample distributions of signal-to-mean clutter ratios.

(a) sample distribution from Urban-1;
(b) cumulative sample distribution from Urban-1 used to synthesize data; and
(c) sample distribution of synthesized data.

4.2.2 Exploratory Analyses of Real SAR Data

Before proceeding to the catalogue of exploratory data analyses, let us consider some of the problems of dealing with real SAR data where truth is not known but is assumed to be closely approximated by the data. Although the complex image data sets were 512 by 512 pixels, examination of the range-compressed phase histories reveal stop bands, or bands of data with very low total power, at the beginning and end of the phase histories. Among the five images, these stop bands vary in width from 30 to 50 pixels on each side. These stop bands suggest that the original phase histories were either zero padded to achieve 512 azimuth pixels in the image, or were severely attenuated at the edges of the aperture. There is also an obvious but unknown taper across the aperture. The stop band

and the aperture taper indicate that azimuth resolution is somewhat greater than a single FFT bin or pixel. Examination of isolated bright points in the data (see Appendix B for details) and later experience with the data indicate that the total power in the seven pixels centered at the brightest point renders a reasonable estimation of signal power. It can be argued that if seven points are too many, then the contribution to total power from the outer pixels is insignificant.

Consider next a comparison of the non-coherent sum of brightest points across ranges; that is, the process used in Step 3 of the PGA algorithm to determine the width of the support for the point spread function. This process is illustrated in Figure 4-8 using the unaberrated Urban-1 data and its synthesized counterpart with similar signal-to-clutter ratio. The horizontal line marks the average value of the non-coherent sum; that is, the average taken over the azimuth dimension of the data. For the synthesized data, the clutter sum is flat beyond the extent of the point spread function. For the real SAR data, the clutter sum beyond the extent of the point spread function shows a modest decrease from the knees of the curve to the outer edges. This suggests that the signal-to-mean clutter ratio for real SAR data may depend on the width of the support of the point spread function.

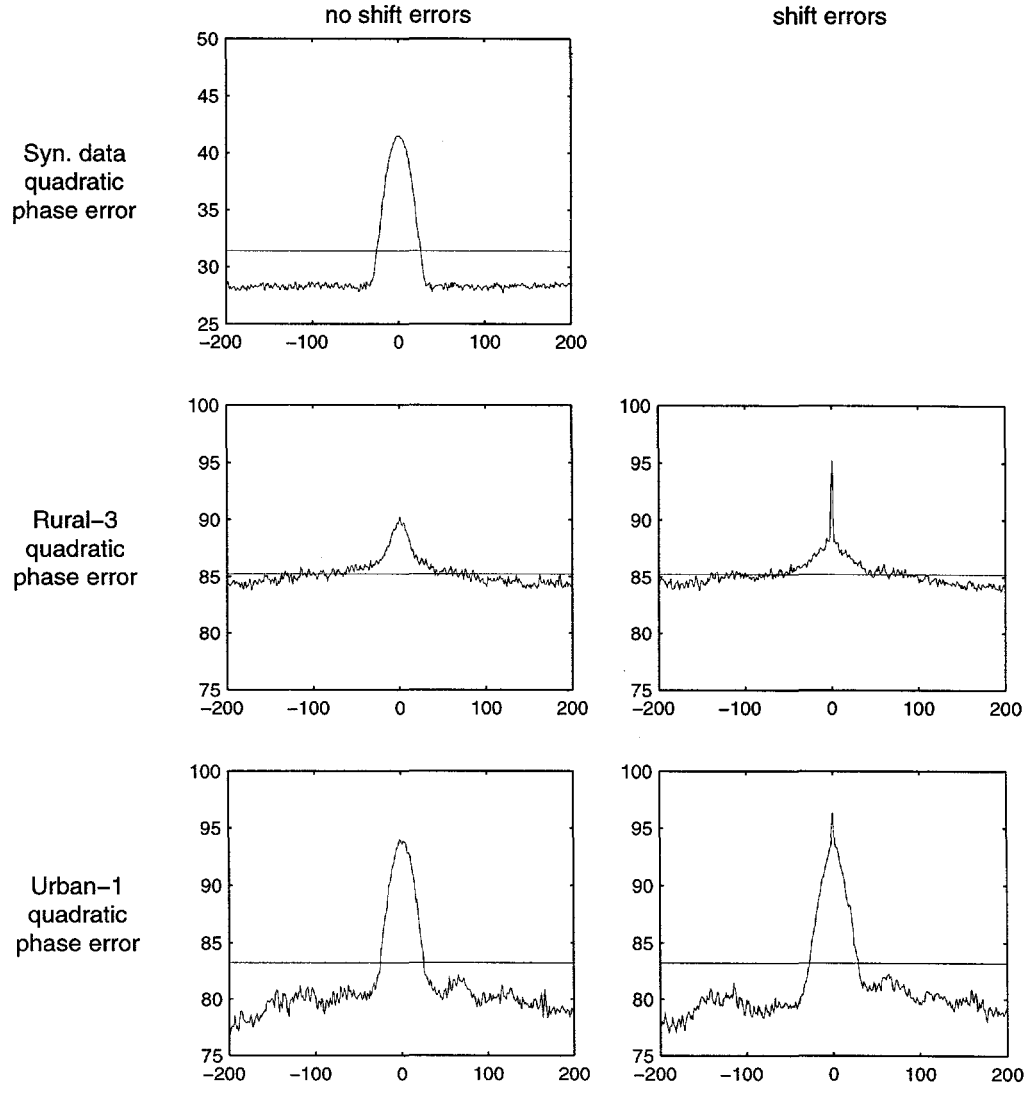

Figure 4-8. Comparison of non-coherent sums of brightest points.

The horizontal lines indicate the arithmetic mean of the non-coherent sum. Synthesized SAR data have only one signal at each range; therefore, shift errors were not considered for these data. Note the difference between the level clutter sum of the synthesized data and the slope of the clutter sum of the real SAR data. This suggests that clutter in the real SAR data may not be identically distributed as assumed in the data model.

We turn now to the catalogue of exploratory data analyses of the SAR data. The purpose of these analyses was to identify potentially significant differences between the real and synthesized SAR data, differences that might have an impact on the validity of the current data model.

Because the comparison of non-coherent sums shown in Figure 4-8 suggest differences in clutter statistics that may be a function of the support of the point spread function, all of the remaining analyses were repeated using the clutter data in the 1/4, 1/8, 1/16 of the remaining image pixels surrounding the signal. The following were considered:

Distributions of:

1. Signal-to-mean, -median, and -maximum clutter ratios.
2. Position of maximum clutter pixel relative to signal pixel.

Correlation between:

1. Position of maximum clutter and signal-to-clutter ratios.
2. Position of maximum clutter and maximum-clutter-to-mean-clutter ratios.
3. Signal-to-maximum clutter ratio and signal-to-mean clutter ratio.
4. Maximum-to-mean clutter ratio and signal-to-mean clutter ratio.

The data were visually inspected and the findings are summarized in Table 4-1. These findings are illustrated in Figure 4-9 through Figure 4-12 where distributions and scattergrams for Rural-3 and Urban-1, respectively, are compared to distributions and scattergrams for the data synthesized from their respective SCR distributions. The full ensemble of data are included in Appendix B.

Table 4-1. Summary of exploratory analyses of real and synthesized SAR data.

Distributions	Real SAR data	Synthesized SAR data
1. Signal-to-mean -median and -maximum clutter ratios.	The range of values is consistent with measured RCS reported in the literature. Monotonic increase in SCR with increase in width of support. Calculation of SNR for a given width of support of the point spread function may require special numerical handling.	No change in SCR as a function of width of the support. $SNR = SCR/N_{support}$
2. Maximum clutter position relative to signal.	Slightly less than uniform. May be significant to data model.	Uniformly distributed.
Correlations		
3. Maximum clutter position and signal-to-clutter ratios.	Uncorrelated.	Uncorrelated.
4. Maximum clutter position and maximum-clutter-to-mean-clutter ratios.	Uncorrelated.	Uncorrelated.
5. Signal-to-maximum clutter ratio and signal-to-mean-clutter ratio.	Linearly correlated. Y-intercept is significantly less than for synthesized data than for real SAR data.	Linearly correlated.
6. Maximum-to-mean clutter ratio and signal-to-mean clutter ratio.	May be correlated and significant to data model.	Uncorrelated.

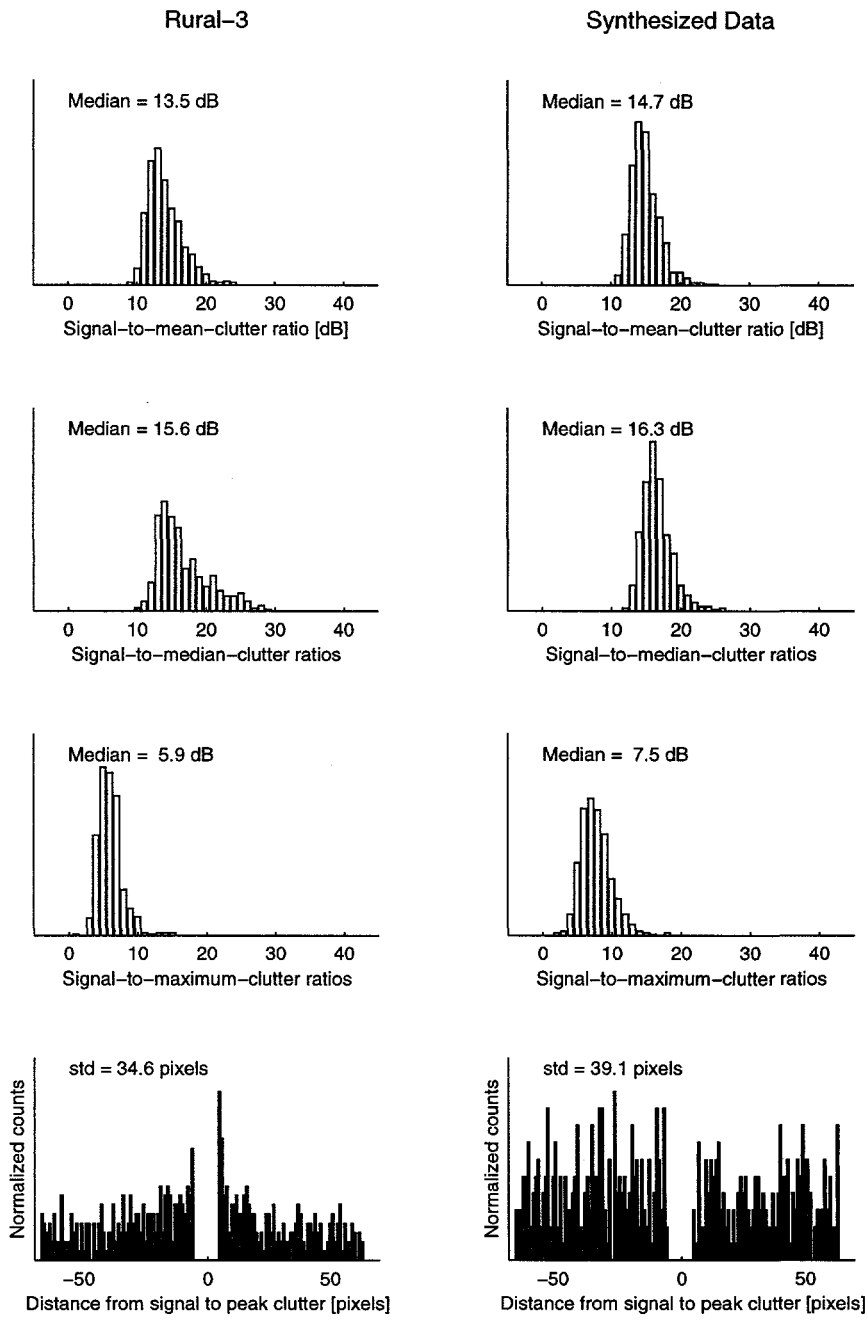

Figure 4-9. Comparison of metrics of Rural-3 and synthesized SAR data.

The differences in the distributions of signal-to-maximum clutter and the position of maximum clutter relative to signal suggest differences between the real and synthesized SAR data.

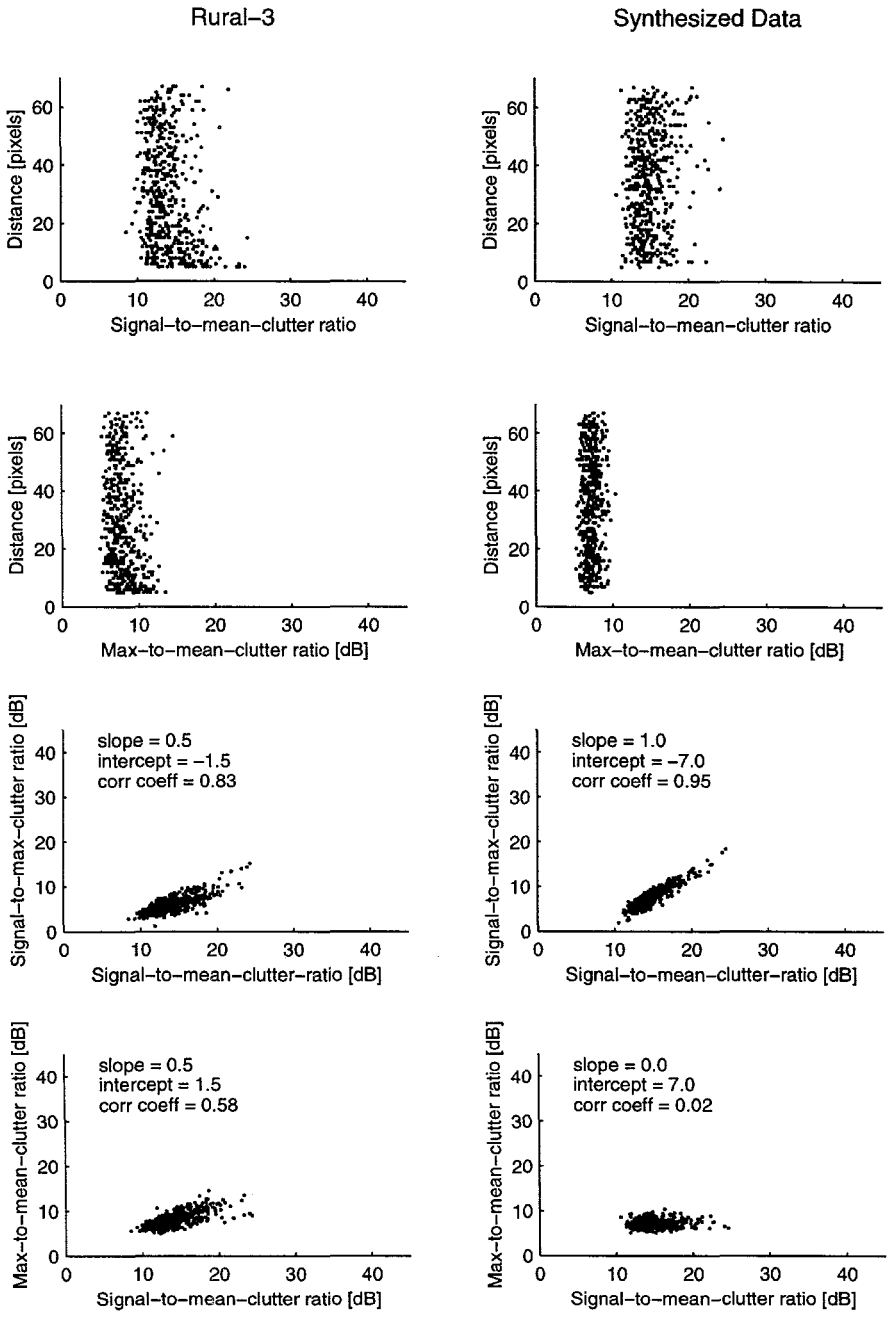

Figure 4-10. Comparison of metrics of Rural-1 and synthesized SAR data.

The four upper scattergrams show no correlation between signal-to-clutter ratio and signal-to-clutter position. The four lower scattergrams indicate some differences in clutter distributions between real and synthesized SAR data.

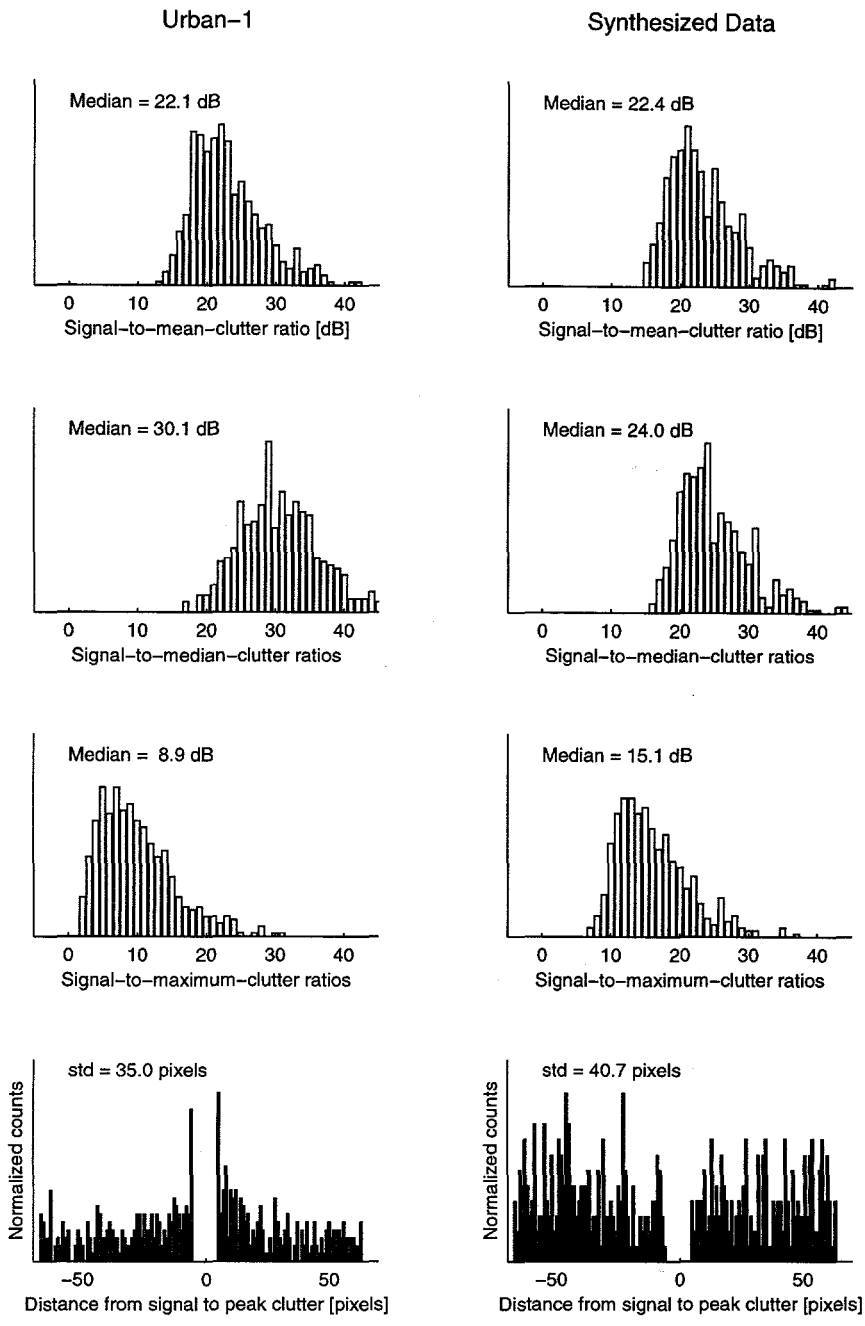

Figure 4-11. Comparison of metrics of Urban-1 and synthesized SAR data.

The differences in the distributions of signal-to-maximum clutter and the position of maximum clutter relative to signal suggest differences between the real and synthesized SAR data.

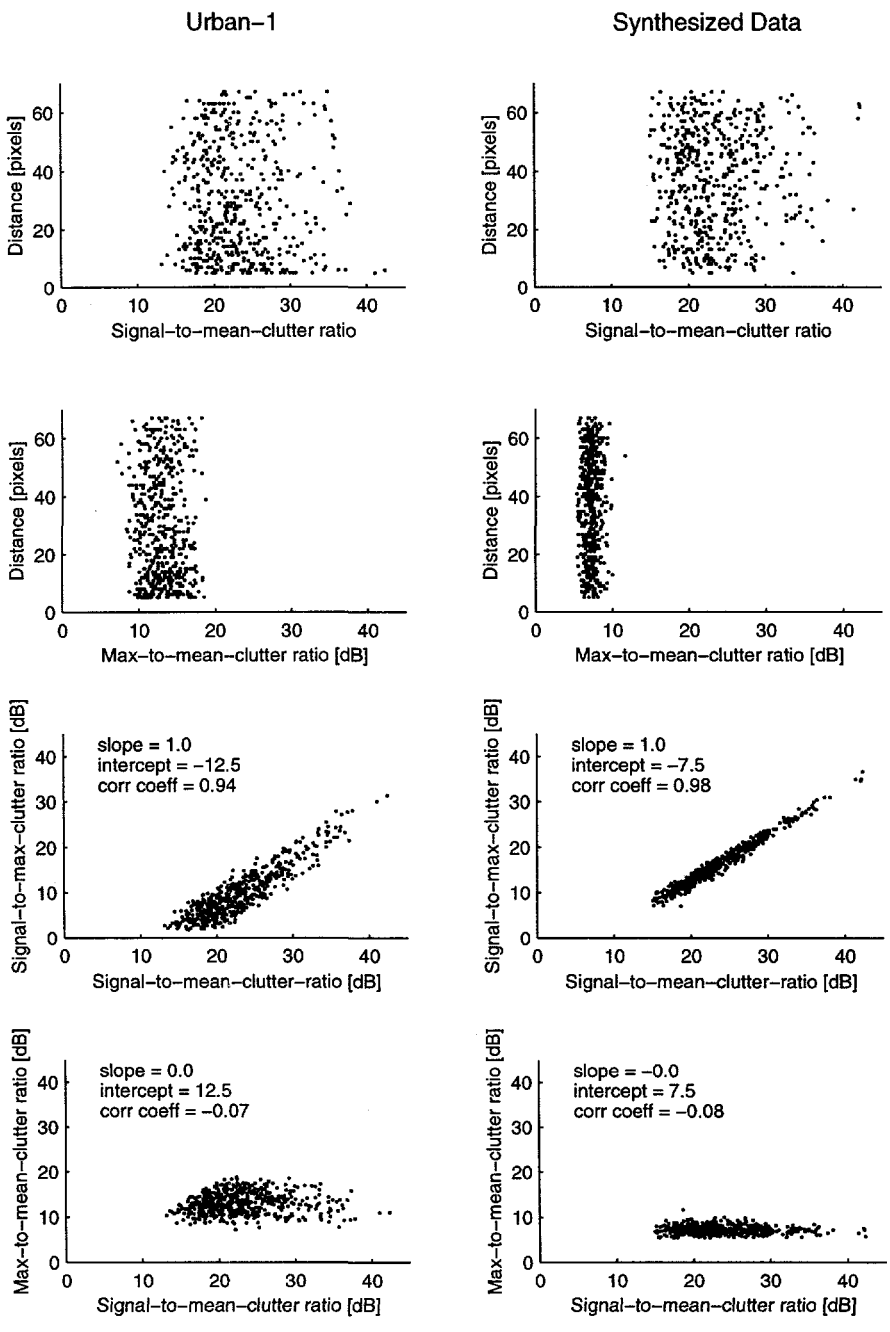

Figure 4-12. Comparison of metrics of Urban-1 and synthesized SAR data.

The four upper scattergrams show no correlation between signal-to-clutter ratio and signal-to-clutter position. The four lower scattergrams indicate some differences in clutter distributions between real and synthesized SAR data.

Let us review the data shown in Figure 4-9 through Figure 4-12. These figures only show data computed over 1/4 of the SAR image surrounding the brightest point. The first column of plots in each of the figures show the data for the real SAR images, the second column show the same distributions or scattergrams for the synthesized SAR data. The first rows of Figure 4-9 and Figure 4-11 show the sample distributions of signal-to-clutter ratios. These should agree because the synthesized data were generated using the SCR distributions of the real SAR data. The second row shows the sample distributions of signal-to-median-clutter ratios and the third row shows the sample distributions of signal-to-maximum-clutter ratios. For both Rural-3 and Urban-1 we note some differences between the real and synthesized SAR data in shape, extent and central tendency of the distributions. The fourth row shows the distribution of the position of the maximum clutter pixel relative to the signal pixel. As expected, these positions are uniformly distributed for the synthesized SAR data but show a slightly less than uniform distribution for the real SAR data. Figure 4-10 and Figure 4-12 show four pairs of scattergrams for Rural-1 and Urban-1 data respectively. The first row shows the position of maximum clutter versus the ratio of signal to mean clutter, the second row shows position of maximum clutter versus the ratio of maximum to mean clutter. There is no indication of correlation in either of these two figure pairs. The third row shows the ratio of signal to maximum clutter versus the ratio of signal to mean clutter. The strong linear trend is expected. What is notably different are the y-axis intercepts of the linear trends. In the real SAR data the ratio of signal to maximum clutter often approaches 0 dB, while the same ratio for synthesized data does not appear to go below about 7 dB. The fourth

row shows the ratio of maximum to mean clutter to the ratio of signal to mean clutter. Again there are notable differences between the real and synthesized SAR data. The plots in the fourth row are just an alternative view of the data shown in the third row. While the synthesized data show no correlation, the scattergram (and metrics of correlation) indicate that the real SAR data are correlated, particularly for Rural-3.

4.2.3 Summary of Differences Between Synthesized and Real SAR Data

The differences noted between the real and the synthesized SAR data indicate that the distribution of clutter, which is not part of the data model used by Jakowatz in [33], *may* play a significant role in the performance of the optimal ML phase-gradient estimator. This will be explored further in Chapter 6 where performance of the PGA algorithm for controlled input conditions is compared using the real and synthesized SAR data. The differences in synthesized data among the three rural scenes were negligible, as were the differences in synthesized data between the two urban scenes.

Chapter 5

Background

Methods of Analysis and Metrics of

Performance

This chapter is divided into three major sections covering 1) methods of theoretical analysis, 2) methods of numerical analysis and 3) metrics of residual phase error and associated image quality. This chapter concludes the review of background information and the development of methods required to support the original results presented in the next chapter, Chapter 6.

The first section on theoretical analysis covers six major topics:

1. the general form of the Cramér-Rao lower bound (CRLB) for *unbiased* estimates;
2. the general form of the CRLB for *biased* estimates;
3. the equivalent expressions for the Fisher information matrix;
4. the general form for computing the CRLB of *functions* of the basic parameters;

5. the influence of the formulation of the probability model on the range of signal-to-noise ratios (SNRs) for which the computed CRLB is valid; and
6. the numerical computation of CRLBs for the synthesized and real SAR data.

While the general expression for the Cramér-Rao lower bound is straightforward, computation for this non-linear estimation problem is non-trivial. In the discussion, the importance of the probability model is illustrated. In Chapter 6, shift errors are modeled as multiplicative noise. The non-linearity of the data model limits the range of signal-to-noise ratios over which the probability model is valid. The equivalent expressions of the Fisher information matrix are used to identify the range of signal-to-noise ratios over which the derived Cramér-Rao lower bound is valid. This is an important procedure for this non-linear estimation problem.

The second section covers two methods of numerical analyses.

1. modeling entirely in the phase-history domain;
2. processing of synthesized and real SAR data through single iterations of the full PGA process.

The discussion points out the assumptions made for the phase-history domain model that are not necessarily supported by the full PGA process or by the statistics of the real SAR data.

In the third section, five metrics of residual phase error and six metrics of associated image quality are defined and illustrated. The graphical presentation of these metrics represent the output of a new study of the sensitivity of the PGA autofocus algorithm to

three control variables: 1) SAR scene signal-to-clutter ratio, 2) class of aberrating phase error, and 3) width of the support of the point spread function.

5.1 Theoretical Analysis

In Chapter 3 the Cramér-Rao lower bound (CRLB) was identified as a tool for determining the best possible estimate of a parameter for a given data model *without actually defining the estimator*. Here the CRLB is considered in greater detail. Details significant to the application of this tool to the non-linear problem of phase-gradient estimation are considered. As stated in Chapter 1, derivations of CRLBs are provided in the appendices. Only results are presented in this section. References used for this discussion of the CRLB are Theil [58] p. 386, Nahi [45] p. 249-250, Van Trees [61] p.52-86, and Melsa & Cohen [40] p. 231-237.

5.1.1 CRLB for Unbiased Estimators

The bound generally attributed to Cramér and Rao was first stated by Fisher and proved by Duqué [40]. First, consider the most general of the Fisher information matrix. The elements of the Fisher information matrix are defined as

$$J_{i,j} = -E\left\{\frac{\partial^2 \ln p(\mathbf{x}|\Psi)}{\partial\psi_i \partial\psi_j}\right\}, \tag{5-1}$$

where $\mathbf{J}$ is a square matrix with dimension determined by the dimension of the parameter vector, Ψ, $\mathbf{x}$ is the matrix of observations, and $E\{\bullet\}$ denotes expected value. For an

unbiased estimator, the diagonal elements of the conditional covariance matrix of the estimates $\hat{\Psi}$, $\mathrm{var}\left\{\hat{\Psi}|\mathbf{x}\right\}$, are greater than or equal to the corresponding elements of $\mathbf{J}^{-1}$, the inverse of the Fisher information matrix. For the problem of pair-wise estimation of phase gradients, ψ, where ψ is a non-random but unknown scalar, $\mathbf{J}$ reduces to a scalar and the observation vector

$$\mathbf{x} = \begin{bmatrix} x_{1,m-n} & x_{2,m-n} & \cdots & x_{k,m-n} \\ x_{1,m} & x_{2,m} & \cdots & x_{k,m} \end{bmatrix}, \tag{5-2}$$

where k is the range index and m-n and m are the indices to the azimuth interval and position, respectively, over which the gradient is estimated. Thus, the Cramér-Rao lower bound for the conditional variance of a regular *unbiased* estimate of the phase gradient is defined as

$$E\left\{\left(\hat{\psi}-\psi\right)^2|\mathbf{x}\right\} \geq \left[-E\left\{\frac{\partial^2 \ln p(\mathbf{x}|\psi)}{\partial\psi^2}\right\}\right]^{-1} \tag{5-3}$$

assuming that $\frac{\partial p(\mathbf{x}|\psi)}{\partial\psi}$ and $\frac{\partial^2 p(\mathbf{x}|\psi)}{\partial\psi^2}$ exist and are absolutely integrable. This inequality establishes the lower bound on the expected square estimation error in terms of the statistics of the observations as defined by the joint probability density function $p(\mathbf{x}|\psi)$. If an estimator is unbiased and satisfies (5-3) with equality, then that estimator is said to be *efficient*.

5.1.2 CRLB for Biased Estimators

For a defined scalar estimator, $\hat{\psi} = f(\mathbf{x})$, the conditional expected value of the estimate $E\{\hat{\psi}|\mathbf{x}\} = \psi + \vartheta(\psi)$, where $\vartheta(\psi)$ is the estimator bias. If the estimator is biased, then $\frac{\partial E\{\hat{\psi}|\}}{\partial \psi} = 1 + \frac{\partial \vartheta(\psi)}{\partial \psi}$ and the Cramér-Rao inequality as stated by Nahi in [45] is

$$E\left\{(\hat{\psi} - \psi)^2 | \mathbf{x}\right\} \geq \frac{\left[\frac{\partial E\{\hat{\psi}|\}}{\partial \psi}\right]^2}{-E\left\{\frac{\partial^2 \ln p(\mathbf{x}|\psi)}{\partial \psi^2}\right\}}. \tag{5-4}$$

Calculation of the denominator of this expression does not require definition of the estimator. However, calculation of the numerator does require that the estimator be defined and it is not easily determined for non-linear estimators such as the phase-gradient estimator.

5.1.3 Equivalent Forms of the Unbiased Bound on the Conditional Variance

The $\ln p(\mathbf{x}|\psi)$ is called the log-likelihood function. It can be shown that the elements of the Fisher information matrix can be computed in either of two ways:

$$-E\left\{\frac{\partial^2 \ln p(\mathbf{x}|\psi)}{\partial \psi_i \partial \psi_j}\right\} = E\left\{\frac{\partial \ln p(\mathbf{x}|\psi)}{\partial \psi_i}\frac{\partial \ln p(\mathbf{x}|\psi)}{\partial \psi_j}\right\}. \tag{5-5}$$

While the left-hand side of (5-5) is typically easy to compute, the right-hand side can be algebraically tedious. Because our parameter of interest, ψ, is represented non-linearly in the observations, we will find it necessary to compare the results from both the left- and right-hand sides of (5-5) to establish the region over which results are valid. We will

refer to the left hand side of (5-5) as Method 1, the second derivative method, and the right-hand side as Method 2, the derivative squared method.

5.1.4 CRLB for Functions of Basic Parameters

On page 83 in [61] Van Trees provides the following general form for determining the CRLB for an unbiased estimator of functions, $g(\mathbf{A})$, of the basic parameters, $\mathbf{A}$.

$$E\left\{\left(\hat{g}(\mathbf{A})-g(\mathbf{A})\right)^2|\mathbf{x}\right\} \geq \left[\nabla\left(g^H(\mathbf{A})\right)\right]^H \mathbf{J}^{-1}\left[\nabla\left(g^H(\mathbf{A})\right)\right] \tag{5-6}$$

where **x** is the observation vector,

A is the vector of basic parameters,

g(**A**) is a column vector of the functions of **A** that are of interest,

∇ is the gradient operator,

the superscript H is the Hermitian or complex conjugate transpose, and

J is the Fisher information matrix.

This method is used in the next subsection where the importance of the probability model is illustrated.

5.1.5 Importance of the Probability Model

Formulation of the data model as a function of the parameters of interest affects the form of the probability model, $p(\mathbf{x}|\psi)$. Swerling [56] has emphasized the importance of the data model and has illustrated how model formulation affects the range of SNR over which the results of (5-1) are valid.

As an example, consider the significance of the probability model as it applies to the estimation of phase gradients. The data model, as stated in equation (3-1), is

$$x_{k,m} = a_k e^{j\phi_m} + n_{k,m}$$

where $x_{k,m}$ are assumed to be complex, zero mean, circularly Gaussian and independently and identically distributed across ranges indexed by *k*. The log-likelihood function for zero mean, complex circularly Gaussian data pairs is

$$\sum_{k=1}^{N_{ranges}} \ln p(\mathbf{x}_k|\psi) = -\left(\sum_{k=1}^{N_{ranges}} \ln\left[\pi^2|\mathbf{C}_k|\right] + \mathbf{x}_k^H \mathbf{C}_k^{-1} \mathbf{x}_k \right) \text{ [33]} \qquad (5\text{-}7)$$

where, for our problem, $\mathbf{x}_k = \left[x_{k,m-1}\ x_{k,m}\right]^T$, and $\mathbf{C}_k$ is the covariance matrix, which, for the assumptions made by Jakowatz and Wahl [33], is the same for all *k*. The associated CRLB, as stated in equation (3-8) is

$$\sigma_{\hat{\psi}}^2 \geq \frac{1+2\beta}{2N_{ranges}\beta^2} \qquad (5\text{-}8)$$

where $\beta = SNR$.

If the data are not zero mean, complex circularly Gaussian but the noise is zero mean, complex circularly Gaussian, then the log-likelihood function is

$$\sum_{k=1}^{N_{ranges}} \ln p(\mathbf{x}_k|\phi, a_k) = -\left(\sum_{k=1}^{N_{ranges}} \ln\left[\pi^2|\mathbf{C}_k|\right] + \left(\mathbf{x}_k^H - \mu_{\mathbf{x}_k}^*\right)\mathbf{C}^{-1}\left(\mathbf{x}_k - \mu_{\mathbf{x}_k}\right) \right) \qquad (5\text{-}9)$$

where $\mu_{x_{k,m}} = a_k e^{j\phi_m}$. Using (5-6) to calculate the CRLB for $\hat{\psi} = \hat{\phi}_m - \hat{\phi}_{m-n}$, where the parameter of interest, ψ, is a function of the basic parameters, ϕ_m and ϕ_{m-n}, the CRLB is expressed as

$$\sigma^2_{\hat{\psi}} \geq \frac{1}{N_{ranges}\beta} \tag{5-10}$$

which is equal to equation (5-8) for large signal-to-noise ratios, β, but which underestimates the MSE of phase gradients for small β. Derivations of (5-8) and (5-10) are provided in Appendix C. Numerical values are compared in Figure 5-1. Note that the CRLBs for the two probability models diverge for $\beta < 0$ dB, illustrating the importance of the probability model.

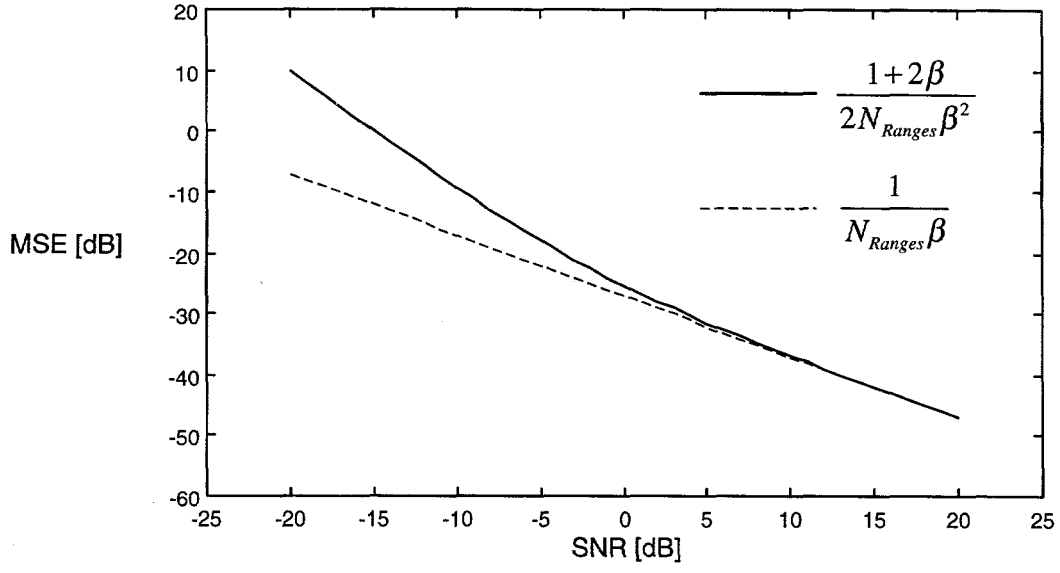

Figure 5-1. Illustration of the influence of data model on computed CRLB.

The solid line is the CRLB computed using the zero-mean data model used by Jakowatz and Wahl in [33]. The dashed line is the CRLB computed using the non-zero mean data model expressed here in the log-likelihood function in equation (5-9). Data from numerical simulations agree with the CRLB for the zero-mean data model (see Chapter 3, Figure 3-4).

5.1.6 Numerical Computation of CRLBs for Synthesized and Real SAR Data

In the previous section the CRLB was expressed as a function of SNR. In order to determine the CRLB for SAR image data it is necessary to map the scene signal-to-clutter ratio (SCR) to SNR. For the synthesized SAR data where mean clutter level is constant (see Chapter 4, Figure 4-8), the SNR was computed as

$$\beta = SCR / N_{\text{support}} \tag{5-11}$$

where $N_{support}$ is the width of the support of the point spread function. The CRLB was then computed using equation (5-8).

Figure 4-8 in Chapter 4, however, indicates that the mean clutter level for real SAR data is not constant, but may decrease as the width of the support of the point spread function increases. For this reason, the CRLB for the real SAR data was computed using

$$\sigma_{\hat{\psi}}^2 \geq \sum_{k=1}^{N_{range}} \frac{1+2\beta_k}{2\beta_k^2}, \tag{5-12}$$

where, for a given value of $N = N_{\text{support}}$, β_k, the signal-to-noise ratio at the k^{th} range was determined numerically using the following equation

$$\beta_k = \frac{\sum_{n=-N/2}^{N/2-1} S_{k,n}}{\sum_{n=-N/2}^{N/2-1} C_{k,n}} \tag{5-13}$$

where $S_{k,n}$ is the squared magnitude of the defocused signal at the n^{th} pixel of the k^{th} range and $C_{k,n}$ is the squared magnitude of defocused clutter at the n^{th} pixel of the k^{th}

range. At each range, the sums in (5-13) were centered about the brightest pixel determined from the unaberrated image. The squared magnitude of the seven pixels centered about the brightest pixel are removed from the image (see Chapter 4, Section 4.2.2 and Appendix B for details). Both the separated signal and the remaining complex clutter were defocused separately. The CRLBs computed for synthesized SAR data with 15 dB and 27 dB SCR are shown in Figure 5-2.

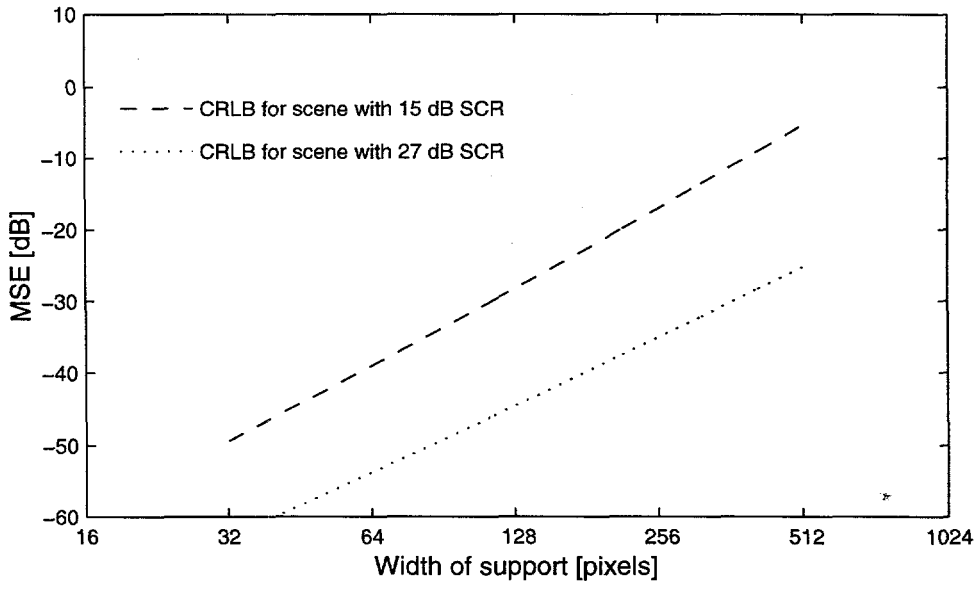

Figure 5-2. Illustration of CRLBs for synthesized SAR scenes with 15 and 27 dB SCR mapped to functions of the width of the support of the point spread function.

The units along the x axis are image pixels and the scale is log base 2. 15 dB and 27 dB represent the lower and upper bounds of mean SCR computed from the rural and urban SAR data respectively. The region between these two curves represents a mapping of real SAR data to the CRLB. Note that calculations for these curves account only for the noise due to scene clutter included in the width of the support of the point spread function. They do not account for bandlimiting effects due to the limited width of that support.

5.2 Numerical Modeling and Processing

Two approaches to numerical modeling and data processing have been used here.

1. Modeling and processing entirely in the phase-history domain using synthesized data.
2. Processing of synthesized and real SAR image data through the full PGA process as illustrated in Figure 1-1 in Chapter 1.

Modeling in the phase-history domain establishes theoretical bounds on performance due to signal-to-noise ratio. Processing of synthesized SAR data through the full PGA algorithm is used to establish performance bounds determined by the properties of the phase-error function.

5.2.1 Data Modeling and Processing in the Phase-History Domain

As previously noted, assumptions in the data model initially expressed here in Chapter 3, equation (3-1), are not necessarily supported by the full PGA process or by the statistics of the real SAR data. Modeling entirely in the phase-history domain does produce some useful results. The limitations of the assumptions and the model results are discussed in this subsection.

5.2.1.1 Data Models in the Phase-History Domain

Both signal and noise were each modeled in the phase-history domain as independent, identically distributed and complex circularly Gaussian. The normalized complex noise power $\sigma_n^2 = 1$, and the normalized complex signal power $\sigma_a^2 = SNR$. Sample phase histories of signal plus noise were synthesized for 512 ranges and 64 samples across azimuth. The 512 phase histories were then defocused by $e^{i\phi_m}$ where ϕ_m was one of the three aberrating phases, quadratic, low order or power law, introduced in Chapter 4. The phase index m ranged from 1 to 512 in increments of 8, making a total of 64 samples of phase. Note that this resampling of the phase data without filtering can introduce aliasing; that is, the bandlimiting of the data implemented in the full PGA algorithm was not incorporated into this model. Thus, results from this model must be interpreted with caution. This model is, nonetheless, very useful for identifying limits and for verifying derived CRLBs.

5.2.1.2 Processing of Data in the Phase-History Domain

Phase gradients were estimated using equation (3-6) from Chapter 3. The constant term was estimated and then removed from the estimated gradients. (This is equivalent to removing the linear term from the estimated phase. Linear phase errors shift the image but do not blur it. We are interested here only in the MSE of phase gradients that degrade image quality.) The resultant error was computed as estimated gradients minus the first differences of the resampled input phase. Truth is $\psi_m = \phi_m - \phi_{m-n}$, where $n = 8$ in this

case. Error is $\varepsilon_m = \hat{\psi}_m - \psi_m$. The MSE for a given trial was computed as the arithmetic average of the squared error of the 63 estimates across the aperture; that is, $MSE = \frac{1}{63}\sum_{n=1}^{63}\left(\hat{\psi}_{8n+1} - \psi_{8n+1}\right)$. Thus, each trial using 512 ranges with 64 azimuth samples at each range produced a single estimate of MSE. A total of 121 Monte-Carlo trials were conducted for each condition of interest.

This numerical model is used to identify the point where the *variation* of estimated MSE begins to diverge from the theoretical CRLB. The results are shown in Figure 5-3, which shows data for unwrapped phase-gradient estimation errors. This is similar to Figure 3-4 in Chapter 3. However, in Figure 3-4 only the principal values for this same data set were shown. The solid line in Figure 5-3 is the theoretical Cramér-Rao lower bound from equation (5-8). The data from the Monte Carlo trials are indicated by dots. From the figure we see that the unwrapped error begins to diverge when the single-range SNR is -11 dB for 512 range samples. The associated theoretical MSE is -7.5 dB. Note that this measure is relative to the bandwidth of the data, not to the aperture. To normalize this measure to the bandwidth of the aperture we must scale it by $\left(N_{\text{support}} / N_{az}\right)^2$, where N_{support} is the number of samples in the support of the point spread function, 64 in this case, and N_{az} is the total number of azimuth data samples across the full aperture, which is 512 for the data used throughout this research.

At times it will be useful to show this -11 dB SNR point on plots displaying the results of numerical analysis. This is illustrated in Figure 5-4, where the bold line shows the MSE

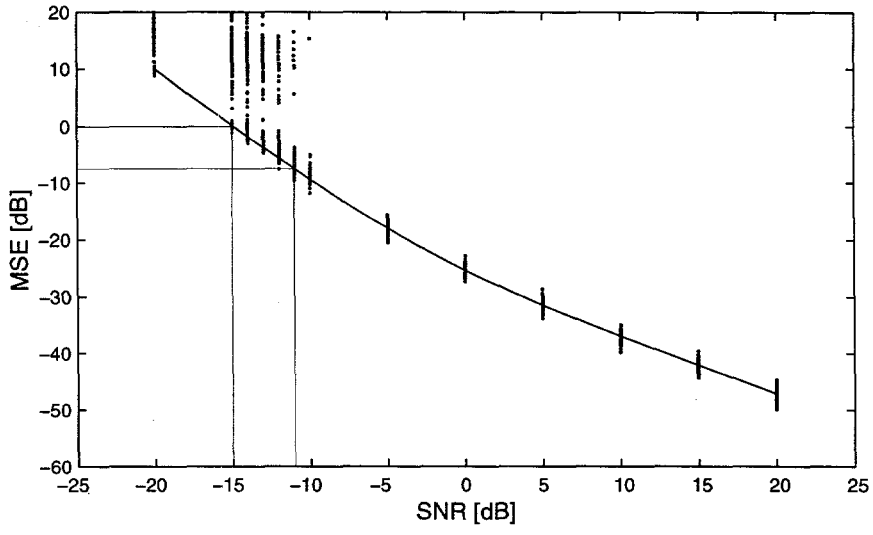

Figure 5-3. Illustration of dispersion of estimator variance using data from Monte-Carlo trails in the phase-history domain.

The estimator begins to break down at -11 dB SNR and has become completely unreliable by -15 dB SNR. These values of SNR correspond to MSE of phase gradients determined by the CRLB of -7.5 and 0 dB respectively.

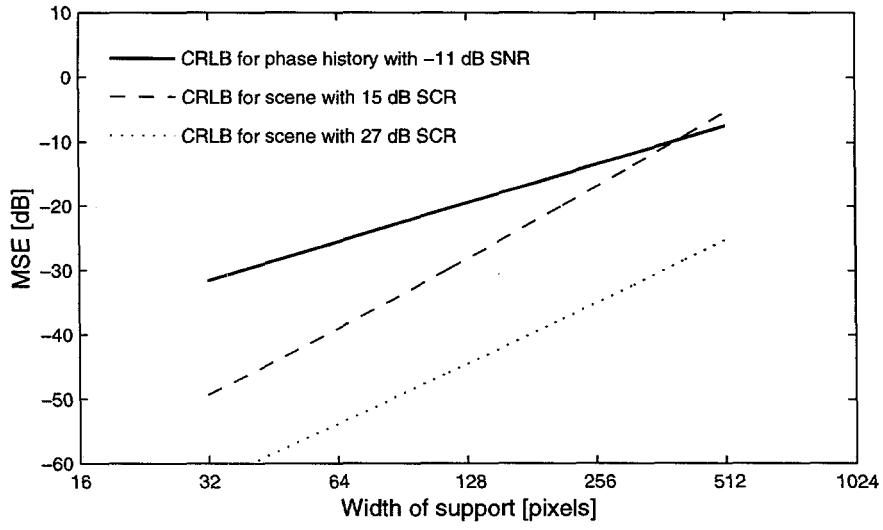

Figure 5-4. Illustration of -11 dB SNR threshold and the CRLBs for 15 and 27 dB SCR scenes versus width of the support of the point spread function.

for -11 dB single-range SNR scaled to the full aperture versus width of the support of the point spread function. Also shown on the plot are the CRLBs for scenes with homogeneous clutter and mean SCR of 15 dB and 26 dB. These bounds were calculated using equation (5-8) and (5-11). A 15 dB SCR is a good approximation for the three rural scenes introduced in Chapter 4. A 26 dB SCR is a good approximation for the two urban scenes. This plot introduces a format that will be used frequently in Chapter 6, showing MSE [dB] or other metrics versus the width of the support of the point spread function. The units of the abscissa (width of the support of the point spread function) are pixels; the scale is log base 2. Note that CRLBs show MSE as a function of SNR only, with no inclusion of the effects of bandlimiting on MSE.

5.2.2 Processing of Real and Synthesized SAR Data Through the PGA Algorithm.

Both real and synthesized SAR data were systematically processed through the PGA algorithm in order to study the sensitivity of algorithm performance to the following three control variables: 1) scene, 2) aberrating phase, and 3) width of the support of the point spread function. The width of the support of the point spread function was changed in increments of four pixels. The initial and final values for the first iteration of PGA were 32 and 512. The initial and final values for second and third iterations of PGA were 8

and 256.[1] This processor allowed shifting of the brightest points to be implemented in one of two ways: 1) circularly shift the brightest points prior to defocusing, thus eliminating shift errors; and 2) full PGA implementation with the brightest points located in the defocused image data, then circularly shifted. This processor, used to study the sensitivity of the PGA algorithms to variations in inputs and process, is illustrated in Figure 5-5. The output metrics shown in the figure are defined and illustrated in Section 5.3 of this chapter. The areas of new investigation were first identified in Chapter 1 and were reiterated as questions in Chapter 3. Original results are presented in Chapter 6.

For each image-phase combination and each iteration, the performance metrics listed below were plotted versus the width of the support of the point spread function. These metrics fall into two categories:

- Metrics of residual phase error:
    1. MSE of the residual phase gradients averaged across the aperture;
    2. rms bandwidth of the residual phase gradients;
    3. modulation index, which is a function of the first two;
- Metrics of image quality:
    4. Strehl ratio;
    5. ISLR (integrated sidelobe ratio);

---

[1] These simulations required a significant amount of computer time. Initial and final values were selected to minimize the computation of meaningless data.

6. PSLR (peak sidelobe ratio);

7. relative position of the peak sidelobe;

8. PSLR outside the support of the point spread function; and,

9. -3, -6,-18 dB width of the point spread function.

The first three metrics were introduced in Chapter 4 as part of the discussion of the properties of random angle modulation. The remainder of the metrics will be defined in the third section of this chapter where examples are introduced.

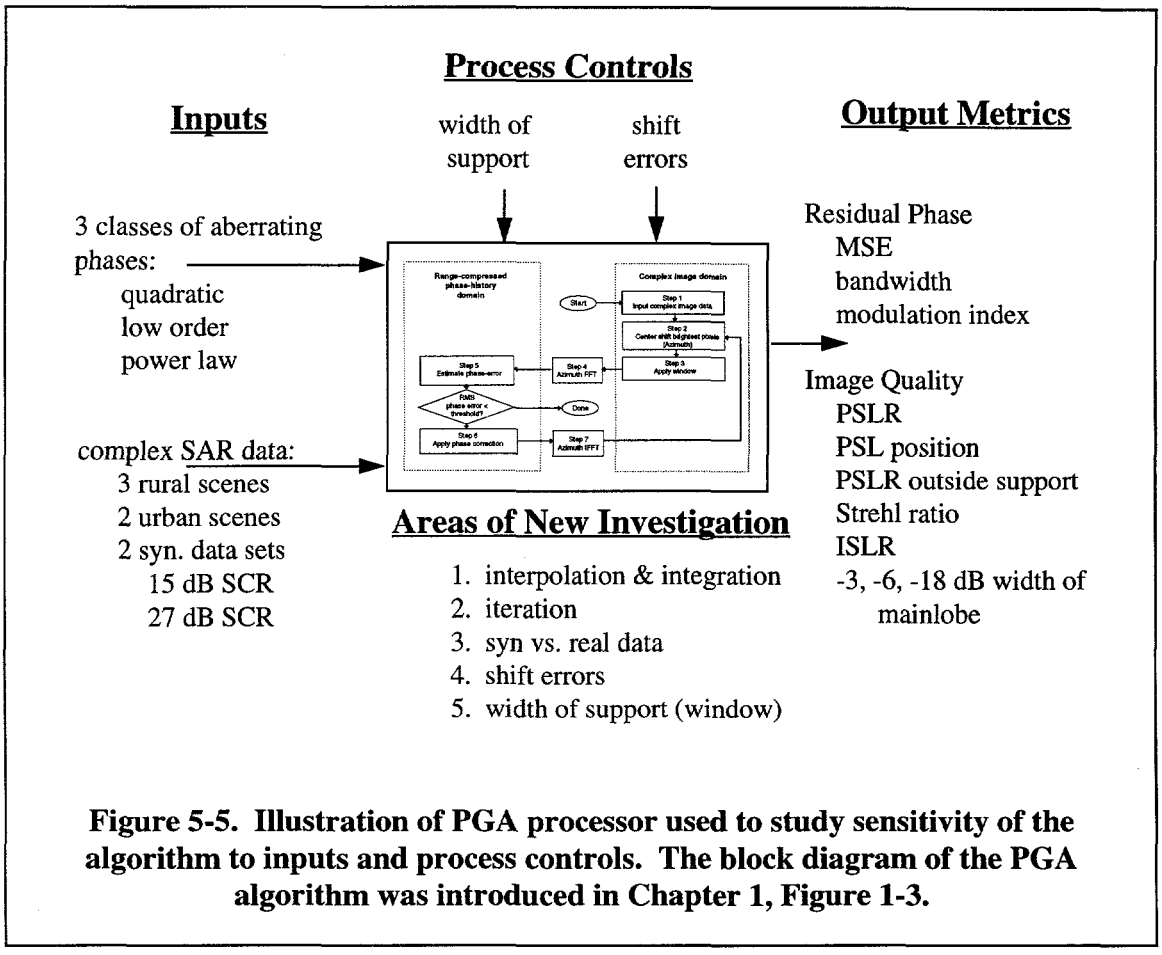

Figure 5-5. Illustration of PGA processor used to study sensitivity of the algorithm to inputs and process controls. The block diagram of the PGA algorithm was introduced in Chapter 1, Figure 1-3.

There is an important difference between the way MSE was computed for these sensitivity studies and the way MSE was computed for the phase-history domain data processing. Here, truth was defined as the first differences between *adjacent* pairs of the aberrating phase error across the full aperture; that is, $\psi_m = \phi_m - \phi_{m-n}$, with n = 1 resulting in 511 data points. Recall that n = 8 for the phase-history domain modeling, resulting in 63 data points. Gradient estimates were computed as the first differences between adjacent pairs of the estimated phase error across the full aperture $\hat{\psi}_m = \hat{\phi}_m - \hat{\phi}_{m-1}$. Estimated phase error is defined as the output of the processing where estimates of phase gradients are integrated and interpolated (but not necessarily in that order). This is the phase correction applied to the aberrated image. Gradient error was computed as the difference between truth and estimates, $\varepsilon_m = \hat{\psi}_m - \psi_m$. MSE was computed as the arithmetic average of the square of those differences; that is $MSE = \frac{1}{511}\sum_{m=2}^{512}(\hat{\psi}_m - \psi_m)^2$. Thus, unlike the MSE measured for phase-history domain simulation, here the error due to too-narrow support of the point spread function is reflected in the MSE.

A few final remarks on the computation of MSE. As noted in Chapter 4, the phase-history data of the five sets of real SAR data each had a stop band at the beginning and at the end of the data in the azimuth dimension. The width of these stop bands varied from scene to scene. The maximum width was 50 samples at each end of the data. To avoid

surreptitious errors due to the very low SNR in the stop bands, only the phase-gradient estimation error between the first 50 and last 50 samples was used to compute MSE.

5.2.3 MSE Due to Bandlimiting, Combined Lower Bounds and Associated Point Spread Functions

In this subsection the PGA processor is used to compute bounds MSE due to bandlimiting of $e^{j\phi(t)}$. These computed bounds are dependent on the aberrating phase error but are independent of SNR. By virtue of this independence, these bounds can be added to the bounds due to SNR to produce a set of combined lower bounds. Finally the point spread functions associated with the combined lower bounds for the three phase errors considered here are compared. The point spread functions reveal a great deal about resultant image quality. This comparison of point spread functions illustrates the limited information available from the residual mean squared phase-gradient error (MSE).

5.2.3.1 MSE Due to Bandlimiting

Synthesized SAR data with nearly infinite SNR (300 dB), and aberrated in turn by each of the three phases considered here, were processed through one iteration of this PGA processor. Results are shown in Figure 5-6. These data are the numerically-determined best estimates for specified pairs of phase error and width of support of the point spread function. As the width of the support decreases below the extent of the point spread

function, mean squared error of phase-gradient estimates increases because the phase gradients cannot be correctly estimated!

5.2.3.2 Combined Lower Bounds

It is reasonable to assume that the MSE due to phase-window pairs is independent of the MSE due to SNR and that the computed MSE due to windowing or bandlimiting can therefore be added to the MSE from the CRLB to produce a combined lower bound for image-phase pairs as a function of width of the window; that is, the width of the support of the point spread function. These combined lower bounds (bandlimiting and SNR), are displayed in Figure 5-7 along with the -11 dB SNR upper threshold.

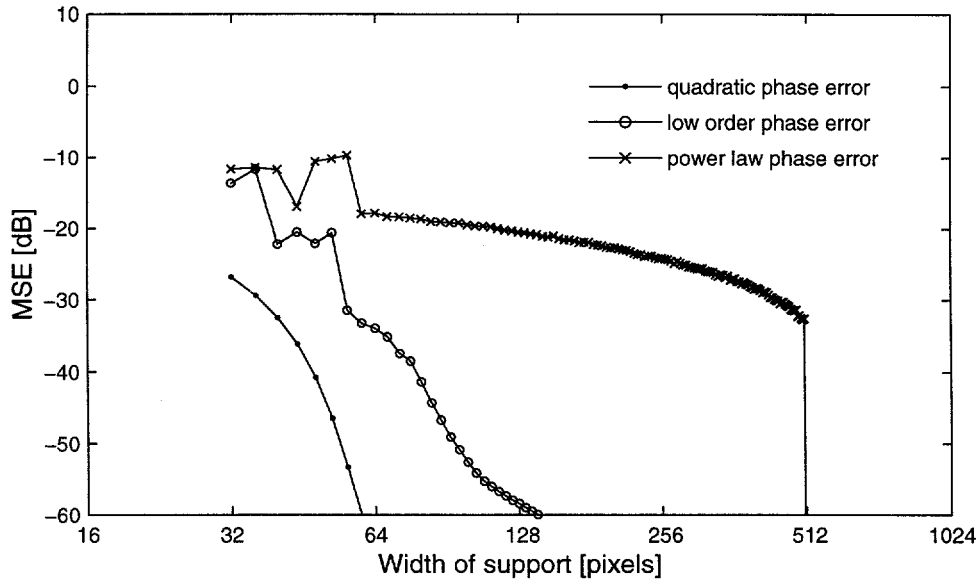

Figure 5-6. Numerically determined lower bounds due to the bandlimiting effect of the support of the point spread function.

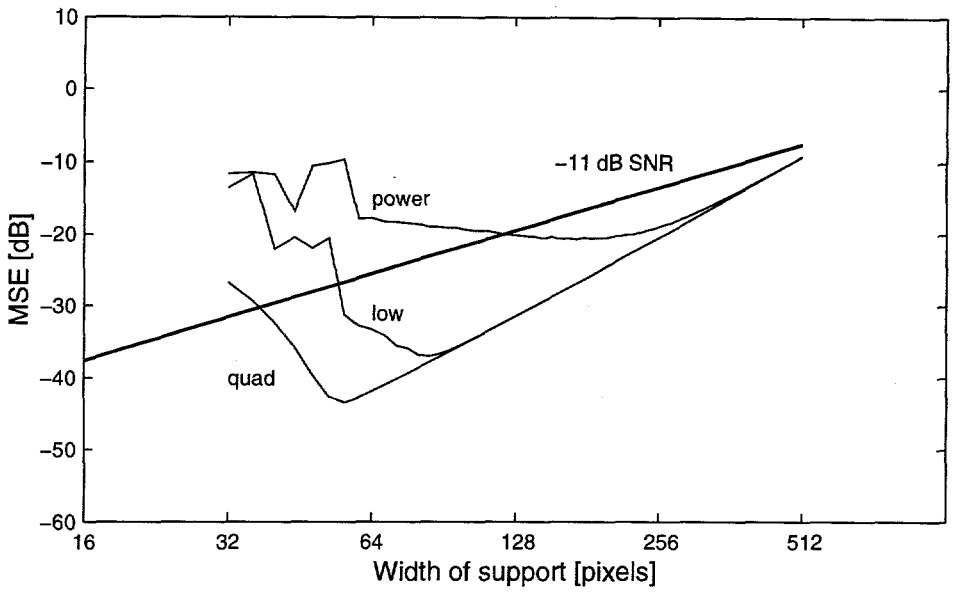

Figure 5-7. Illustration of -11 dB SNR threshold and combined lower bounds for three phases and scene with 17 dB SCR.

To the left of the knee of each curve, the MSE is governed by the bandlimiting of the phase modulated signal, $e^{j\phi(t)}$. This portion of the curve was determined numerically using ~ infinite SCR. To the right of the knee of each curve, the MSE is governed by SNR. This portion of the curve was determined theoretically using the CRLB.

In Figure 5-8 the combined bounds from Figure 5-7 are repeated (solid lines) and numerical results from processed synthesized data are added. This example shows very close agreement between the combined lower bound and the data. The agreement

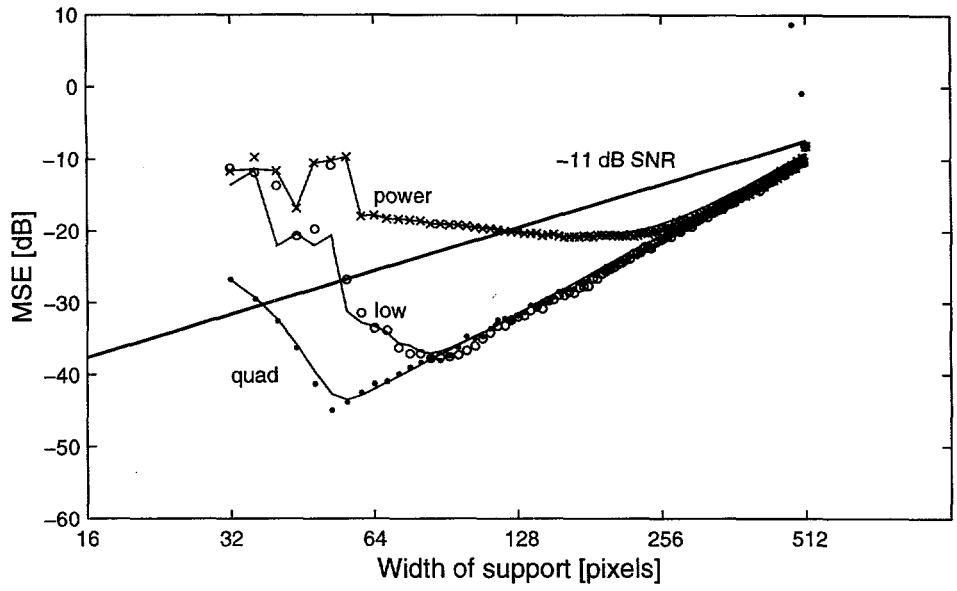

Figure 5-8. Comparison of -11 dB threshold and lower bounds from Figure 5-7 with output of PGA processor using synthesized SAR data with 17 dB SCR and homogeneous clutter.

between the numerical results using synthesized data and the model indicate that the data are well represented by the model.

While these data give a good indication of agreement with the model, they give us no information about the spectral distribution of these phase errors and consequently no information about resultant image quality. We will close this chapter with a discussion of appropriate interpretations of plots of MSE versus support width such as shown in Figure 5-8. This is done by first considering the point spread functions for $N_{support} = 64$, and then

by reviewing an ensemble of plots that provide a compressed display of residual phase error and associated image quality for the full range of $N_{support}$.

For $N_{support}$ = 64, Figure 5-8 shows MSEs of -41 dB, -34 dB and -18 dB for the quadratic, low order and power law phase errors respectively. We have already noted that the numerical data agree with the theoretical lower bound but that these data give us no information about the spectral distribution of these phase errors and consequently no information about resultant image quality. However, we should expect that deviations of the data from the model should be reflected in deviations in the data from the CRLB.

5.2.3.3 Associated Point Spread Functions

The point spread function is defined as $\left| FT\left(W(t) \times e^{j\phi(t)}\right)\right|^2$ where the operator $FT(\bullet)$ is the Fourier transform and the function *W(t)* is an aperture tapering or window function. Here the -40 dB Taylor window is used for the aperture taper. Although the data are only 512 points in length, the point spread function is always displayed here using a 4096 point FFT (Fast Fourier Transform) to interpolate the data by a factor of eight. Let us consider plots of the point spread functions for the three residual phase errors at $N_{support}$ = 64 shown in Figure 5-9. Clearly the spectral distributions of the residual phase error differ significantly for the three initial aberrating phases. The synthesized data under consideration has a mean signal-to-clutter ratio of 17 dB, and a maximum signal-to-clutter ratio of 23 dB, which is indicated by the fine horizontal line on the plots.

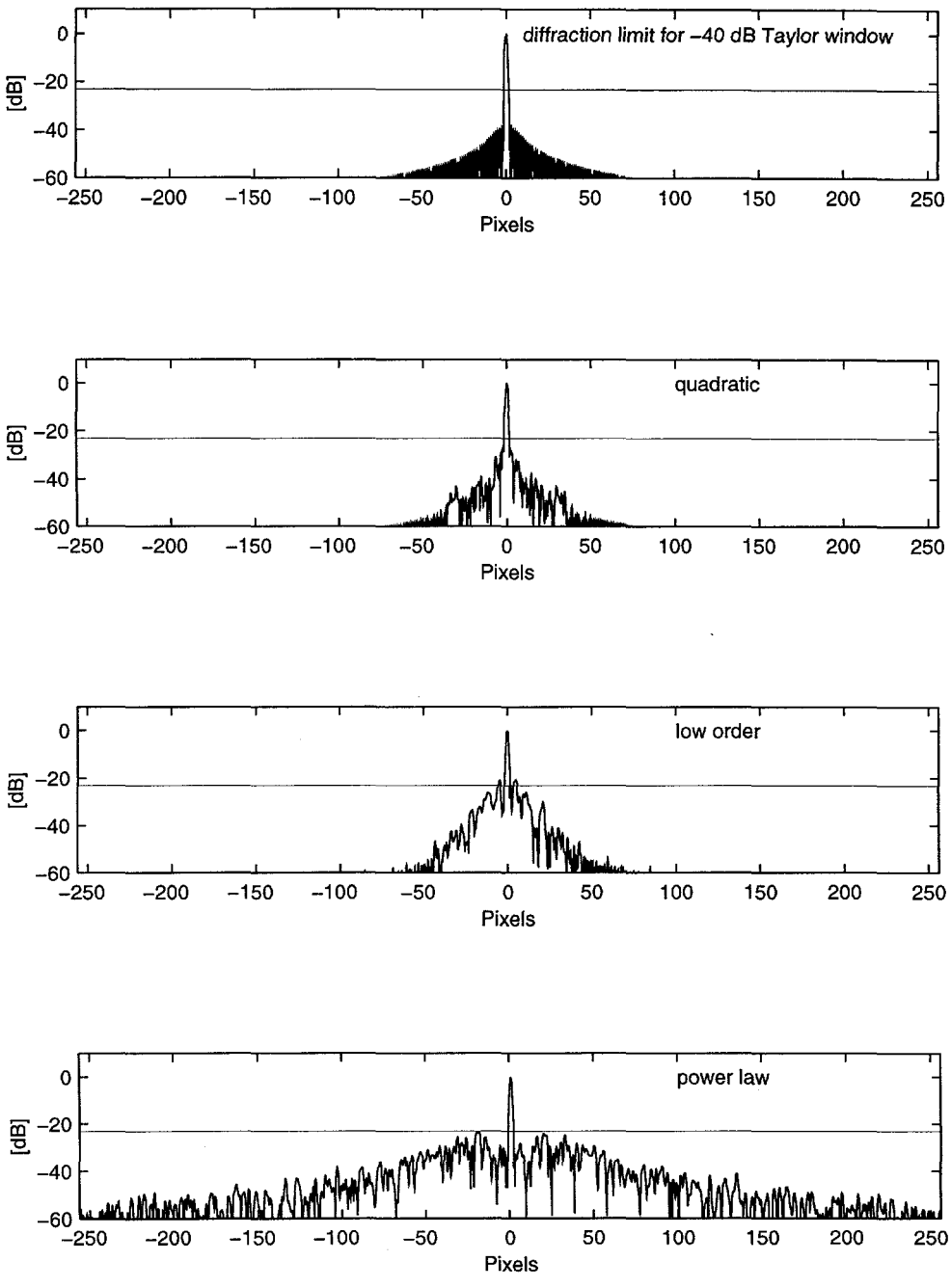

Figure 5-9. Comparison of point spread functions due to residual phase errors for 64 pixel-wide support of the point spread function.

5.3 Metrics of Residual Phase Error and Image Quality

A menu of three metrics of residual phase-gradient error and eight metrics of associated image quality was listed in Section 5.2.2. In this section, those metrics are defined and illustrated as a function of the width of the support of the point spread function.

5.3.1 Compressed Displays of Metrics

Figure 5-10, Figure 5-11, and Figure 5-12 display the menu of the metrics listed on page 94 for the data shown in Figure 5-8; that is, for the synthesized SAR data with 17 dB SCR and aberrated by the quadratic, low order and power law phase errors, respectively. Almost the same information shown in plots of point spread functions can be gathered from these plots. Unlike a point spread function which show data for single value of $N_{support}$, these plots show data compressed over the full range of values of $N_{support}$. The vertical lines and cross hairs mark the data for the single case of $N_{support} = 64$. Unfortunately, ease of interpretability is sacrificed when the data are condensed; therefore, final confidence in algorithm performance is best displayed with the resultant point spread function. Nonetheless, this ensemble of plots prove useful in revealing trends and range of support widths over which some measure of image quality remains relatively constant. They will be used in Chapter 6 when the alternative algorithms for determining the width of the support of the point spread function are presented and, therefore, merit explanation. Two pages are required to display the full ensemble of metrics for one image-phase combination. They are defined in order of appearance.

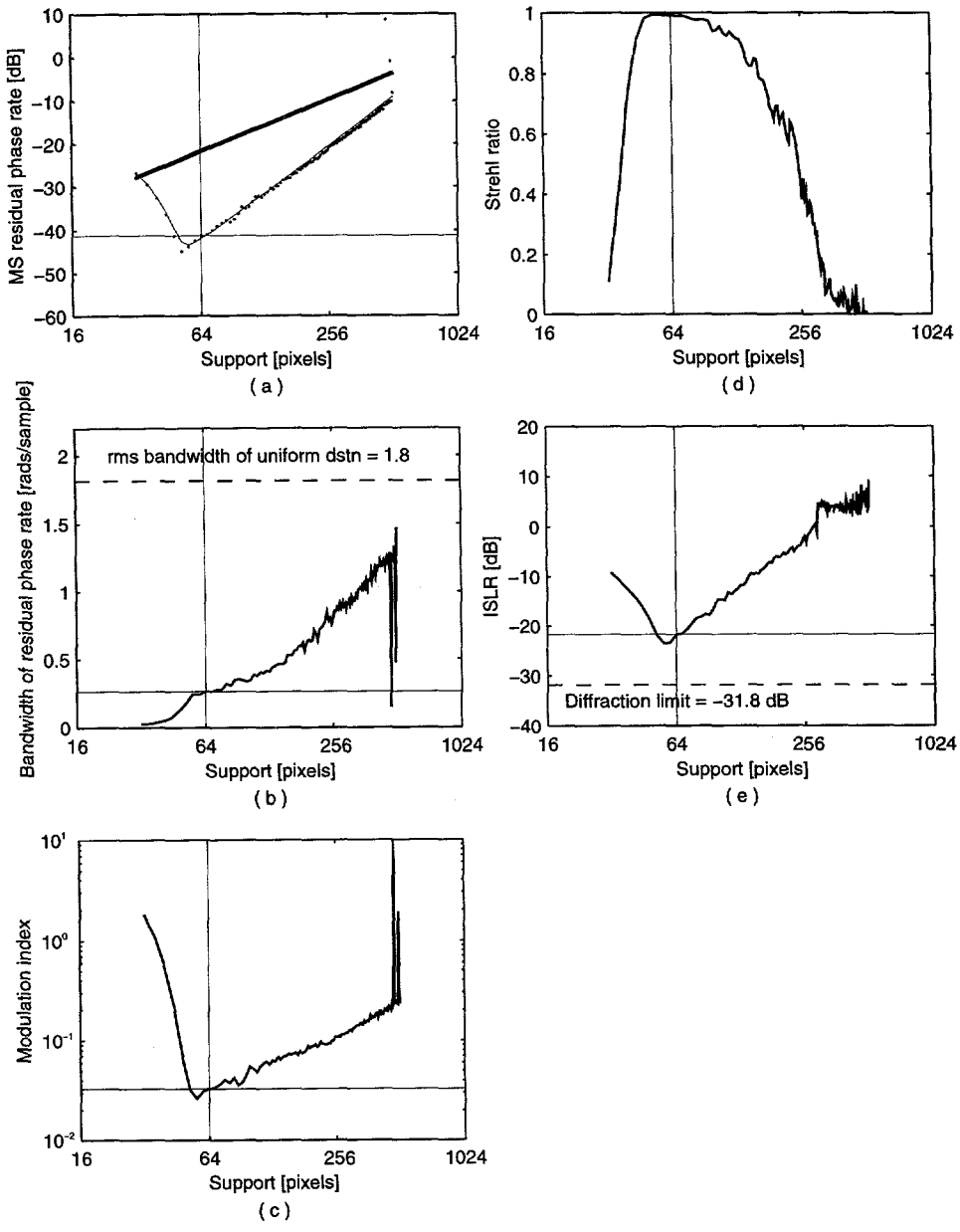

1st Iteration

Synthesized SAR data with random SCR modeled after Rural–1
no shift errors
1.0 x quadratic phase
Part 1

Figure 5-10. Metrics for quadratic phase error and 17 dB SCR.

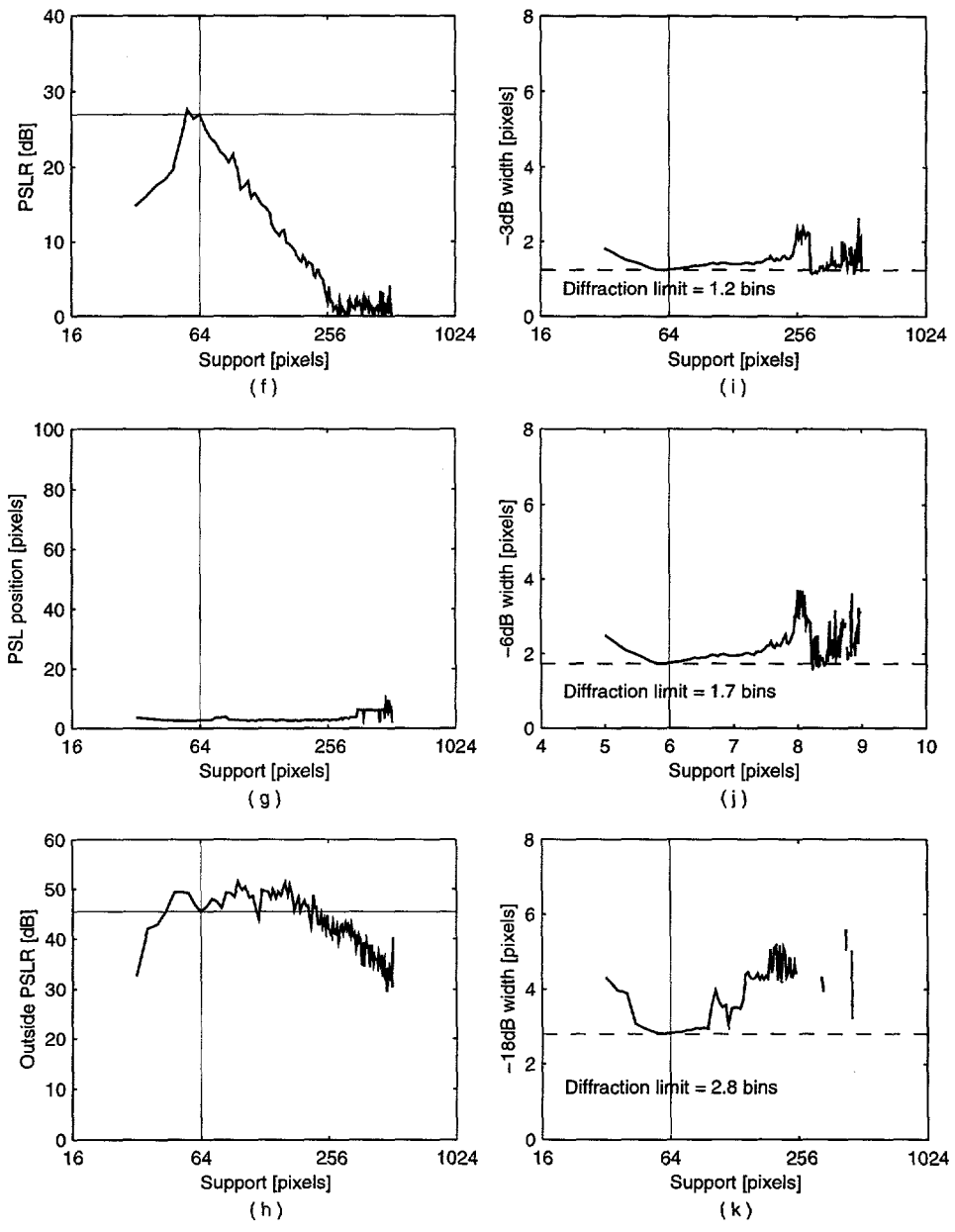

1st Iteration

Synthesized SAR data with random SCR modeled after Rural–1
no shift errors
1.0 x quadratic phase
Part 2

Figure 5-10 (con't). Metrics for quadratic phase error and 17 dB SCR.

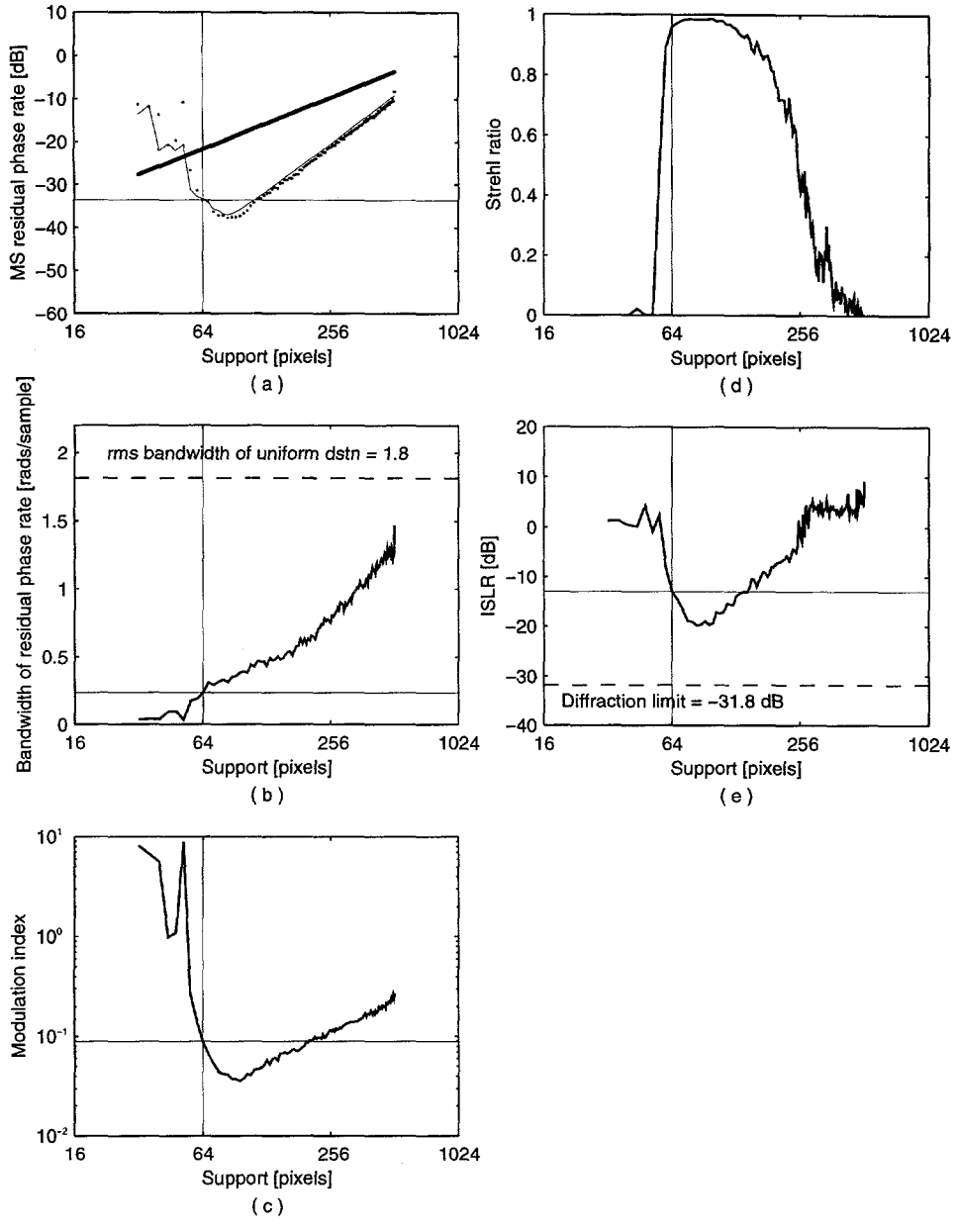

1st Iteration

Synthesized SAR data with random SCR modeled after Rural–1
no shift errors
1.0 x low order phase
Part 1

Figure 5-11. Metrics for low order phase error and 17 dB SCR.

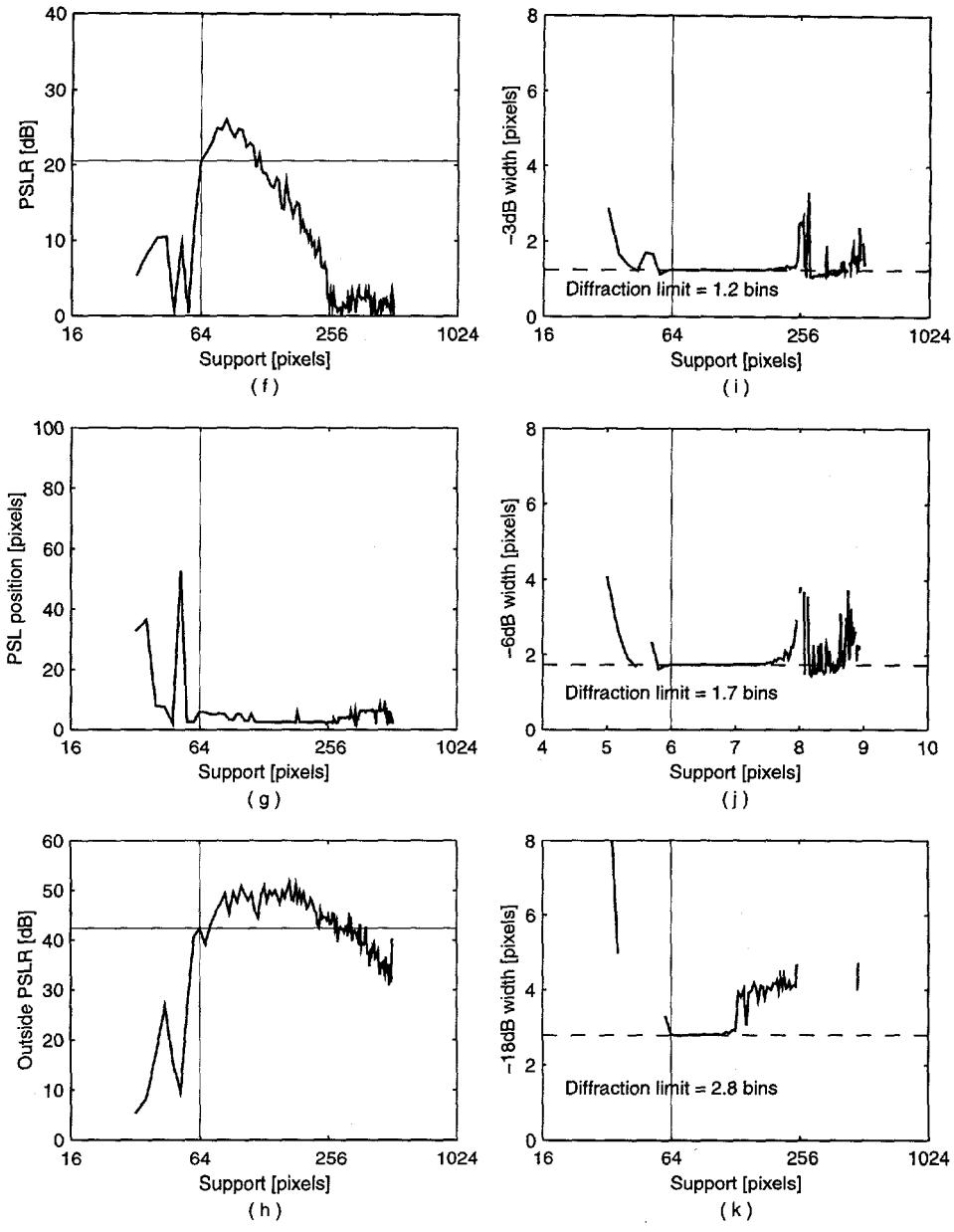

Figure 5-11 (con't). Metrics for low order phase error and 17 dB SCR.

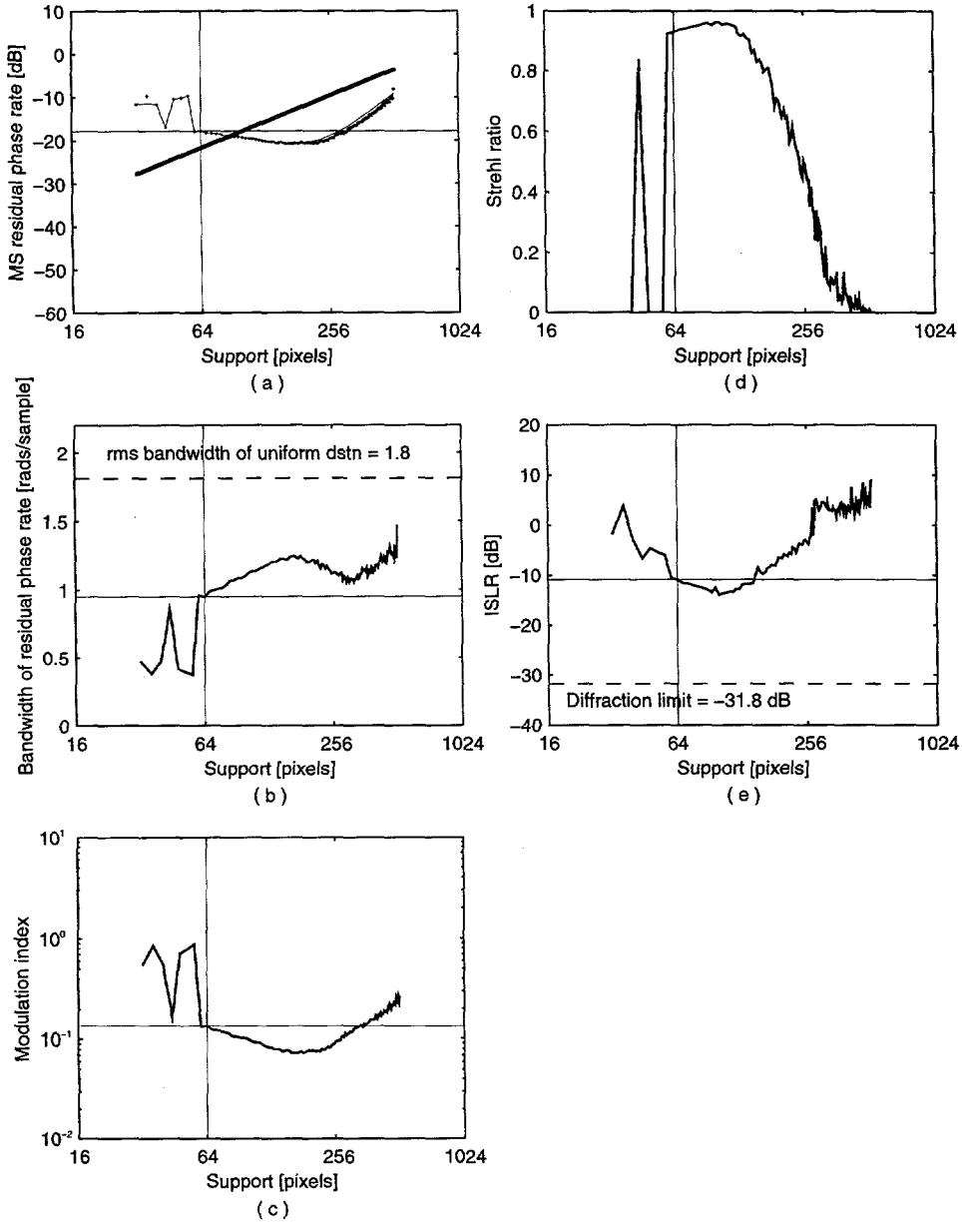

Figure 5-12. Metrics for power law phase error and 17 dB SCR.

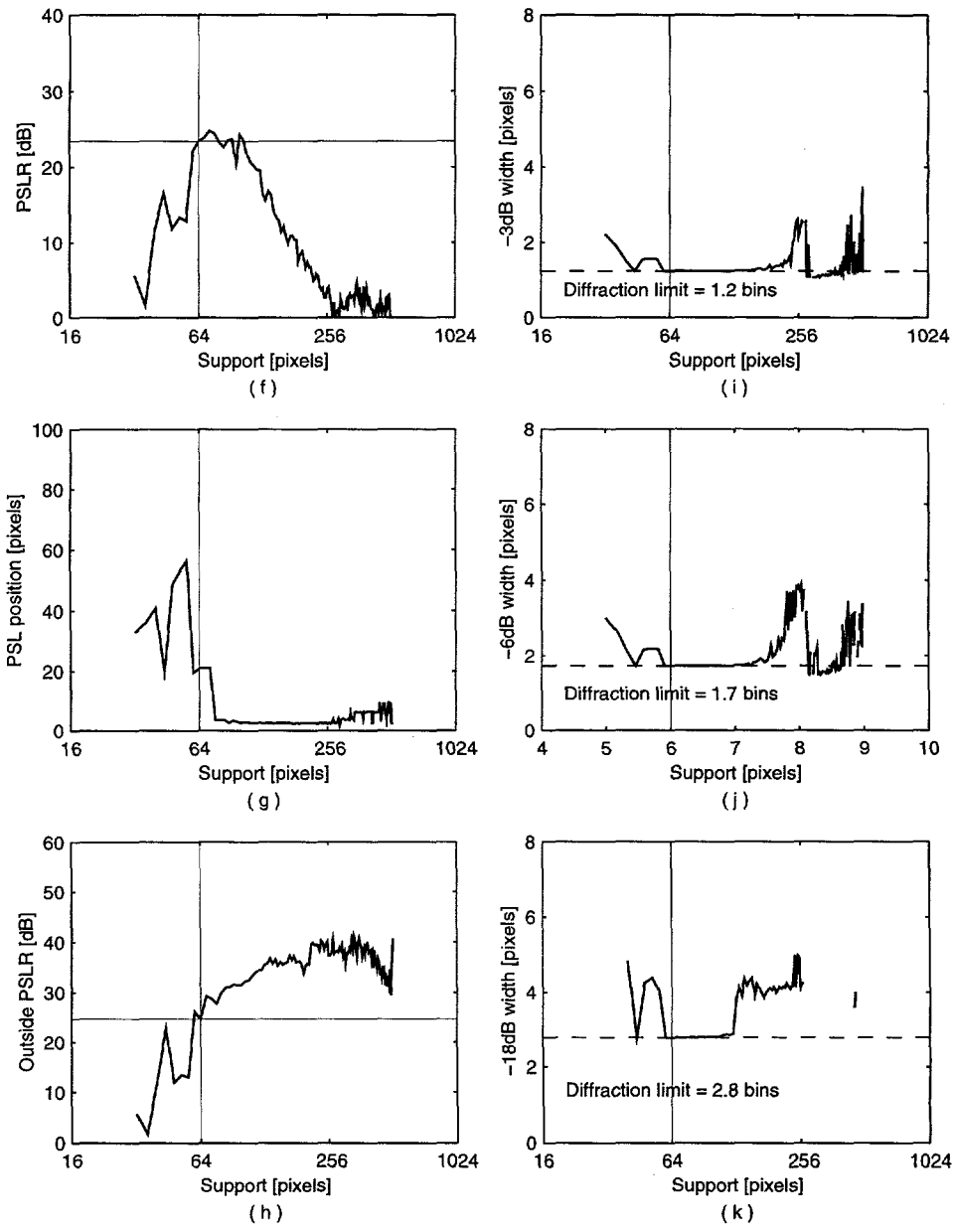

1st Iteration

Synthesized SAR data with random SCR modeled after Rural–1
no shift errors
1.0 x power law phase
Part 2

Figure 5-12 (con't). Metrics for power law phase error and 17 dB SCR.

5.3.1.1 Metrics of Residual Phase Gradients

(The letter identifiers below correspond to the letter identifiers of the graph in the figures.)

(a) MSE. These plots of residual mean squared phase-gradient error (MSE) have already been introduced in Figure 5-8.

(b) RMS Bandwidth, $B_{\psi'}$. These plots show the rms bandwidth of the residual phase gradient as defined by equation (4-4). It is a measure of the distribution of the MSE shown in the figure in position 1. Consistent with the point spread functions shown in Figure 5-9, comparison of the rms bandwidth for the three phase errors are approximately 0.25, 0.2 and 1 radian for the quadratic, low order and power law phase errors respectively.

(c) Modulation Index, β. These plots show the modulation index as defined by equation (4-10). It is not clear whether this metric will provide any additional information for this application.

5.3.1.2 Metrics of Image Quality

(d) Strehl ratio. Strehl ratio is a measure borrowed from optical imaging terminology. In optics, it is the ratio of aberrated object intensity to unaberrated object intensity.

Optical object intensity is equivalent to the square of detected magnitude in the SAR image domain. A widely used empirical approximation for Strehl ratio is of the form

$$S \cong \exp\left(-\sigma_\phi^2\right) \tag{5-14}$$

where σ_ϕ^2 is the variance of the phase aberration across the aperture (e.g., see ten Brummelaar and Bagnuolo [57]). A similar measure appears in the radar imaging literature as loss in processing gain (LPG), which is described in [17] as the loss in signal-to-noise performance due to the use of a mismatched filter in the receiver, and defined as $10 \times \log_{10} \frac{\text{pulse compression ratio}}{\text{peak response (unaberrated)}}$. Computed Strehl ratios reported here are calculated according to Equation (5-14). The peak response is assumed to be that of the Taylor window previously discussed.

While the relative value of Strehl ratios for the aberrating phase is consistent with the relative value of MSE, this is another metric of questionable value for this application.

(e) Integrated Sidelobe Ratio (ISLR). Integrated sidelobe ratio (ISLR) is defined as the integral over the synthetic aperture of the mean squared residual phase error after the linear and quadratic components have been removed. It corresponds approximately to the ratio of the energy in the sidelobes to the area under the mainlobe of the point-spread function, see Brown and Cable[12] p. 91. For numerical results reported here ISLR is calculated using the approximation based on energy ratios and is reported in units of dB. The integrated sidelobe ratio is also a metric of questionable value. The three measures

of mainlobe width coupled with rms bandwidth provide clearer insight into the distribution of residual phase error.

(f), (g), (h) PSLR, PSL position and outside PSLR. Peak-to-sidelobe ratio (PSLR) and the position of the peak sidelobe relative to the mainlobe are measures of image contrast. In a highly cultural scene with areas of strong contrast, such as Urban-1 and Urban-2, a peak sidelobe, adjacent to and 20 dB down from the mainlobe, may appear in the image as a slight blurring of the mainlobe. If that same peak sidelobe due to aberrating phase is well removed from the mainlobe, it will cause a ghost image to appear shifted by the separation between the peak sidelobe and the mainlobe. This ghost will be noticeable in areas of low clutter. Finally, when examining the effect of window width, it may be useful to record the peak sidelobe level outside the window due to residual phase error after applying the optimal ML estimator of PGA.

(I), (j), (k) Mainlobe widths. The -3 dB, -6 dB, and -18 dB widths of the mainlobe are indicators of the amount of residual quadratic phase error. These measures are reported in numbers of image pixels or FFT resolution bins. Here, a resolution bin refers to a single discrete Fourier transform bin, which is proportional to the inverse of the observation time of the data stream transformed. For normalized data, a single resolution bin in the Fourier domain has a width of $2\pi/L$, where L is the length of the transformed data stream or, equivalently, the length of the synthesized array. The practice of reporting mainlobe width in units of resolution bins follows that of Harris [28]. For the real SAR data, the stop bands with very low SNR are equivalent to zero padded data in the phase-

history domain, which results in data interpolation in the image domain. Consequently, an image pixel is narrower than an FFT resolution bin. No adjustments were made here to account for this.

The -3 dB width is the classical criterion for resolution at the half-power point. However, for two reflectors of equal amplitude to be resolvable, the total power at the crossover points must be 3 dB less than the power of either one. Thus the crossover point must occur at a separation greater than the -6 dB width. The -18 dB width is a commonly used additional measure of image resolution.

For numerical results reported here, these three measures of mainlobe width are reported only if they occur before the first nulls. The software search for nulls starts at the peak of the mainlobe and moves outward in both directions. First nulls are at the first occurrence of change in the sign of the slope of the point spread function. A chirp-z algorithm was used to interpolate the loci of the first nulls to 1% of an FFT pixel.

5.2.4 Comments on the Data Shown in Figure 5-10, Figure 5-11, and Figure 5-12.

These figures provide a methodology for visually comparing large amounts of data over a matrix of control parameters. Consider the data in plot (a) of the three figures. We have already seen this data in Figure 5-8 and remarked on the considerable difference in MSE of phase gradients for the three aberrating phase errors. We have also seen the resultant point spread functions for the 64 pixel-wide support in Figure 5-9. Plot (b) in the three

figures shows the bandwidth of the residual phase gradients. Note the difference in residual bandwidth for the 64 pixel-wide support. Bandwidth is about 0.25 radians/sample for the quadratic and low order phase error, but is nearly 1 radian/sample for the power law phase error. The lower Strehl ratio for the power law phase error shown in plot (d) reflects the associated higher MSE. The higher integrated sidelobe ratio (ISLR) for the power law phase error shown in plot (e) reflects the spectral spread of the residual phase gradients, consistent with the wider bandwidth. Peak-sidelobe ratio, (PSLR), peak-sidelobe position and PSLR outside the window also reflect the relative spectral spreads of the residual phase errors. The plots of -3, -6 and -18 dB widths of the mainlobe are indicators of the range of widths of the support of the point spread function over which the resulting mainlobe widths approach the diffraction limit.

5.4 Chapter Summary

This chapter covers the theoretical and numerical methods of analysis applied to the five areas of investigation into the performance of the PGA algorithm that are addressed in this dissertation.

The calculation of the Cramér-Rao lower bound (CRLB)was discussed Section 5.1. The CRLB is a measure of best performance against which performance of specific algorithms can be compared. However, if a particular estimator does not meet the CRLB with equality, the shortcoming is not necessarily rooted in the estimator. Swerling [56] has cited the importance of deriving the CRLB from a properly formulated data model, and

the effect of the data model on the derived CRLB has been illustrated here. The equivalent formulas for the elements of the Fisher information matrix have been emphasized here. Comparison of results using these two formulas identifies the region of validity of the derived CRLB. Specific application of these two formulas is cited in Chapter 6, Section 6.4 and detailed in Appendix E.

Numerical models were discussed in Section 5.2. Limited modeling was conducted entirely in the phase-history domain using synthesized data. The value of this model is constrained by: 1) the use of synthesized data only, and 2) the omission of the transfer function of the support of the point spread function from the data model. A sensitivity study of the full PGA algorithm was conducted using both synthesized and real SAR data. Control parameters for this study were: 1) SAR data type (synthesized or real); 2) the signal-to-clutter ratio (SCR) of the SAR data (15 dB or 27 dB); 3) the type of aberrating phase error (quadratic, low order or power law); 4) shift errors or no shift error; and, 5) the width of the support of the point spread function.

Definition and graphical presentation of a menu of performance metrics were covered in Section 5.3. This form of graphical presentation of data provides a methodology to visually inspect large amounts of data over the matrix of control parameters.

Chapter 6

Results

In Chapter 4, we introduced the aberrating phase data and the synthesized and real SAR data used for this research.

In Chapter 5, we reviewed theoretical and numerical methods of analyses. That chapter concluded with the examples and definitions of a menu of performance metrics used for exploratory analysis of PGA sensitivity to three control variables: scene, aberrating phase and width of support.

We now proceed to use that data and those methods of analyses in various combinations to address our five areas of investigation:

1. method of interpolating and integrating phase-gradient estimates;
2. improvement with iteration;
3. differences between synthesized and real SAR data;
4. effect of shift errors on estimator performance; and
5. definition of the support of the point spread function.

6.1 Method of Interpolating and Integrating Phase-Gradient Estimates

The first issue addressed is the method of interpolating and integrating phase-gradient estimates. This process is not identified in detail in the block diagram of the PGA algorithm. In Figure 6-1, those PGA algorithm steps involved in this discussion are enclosed by a dashed line.

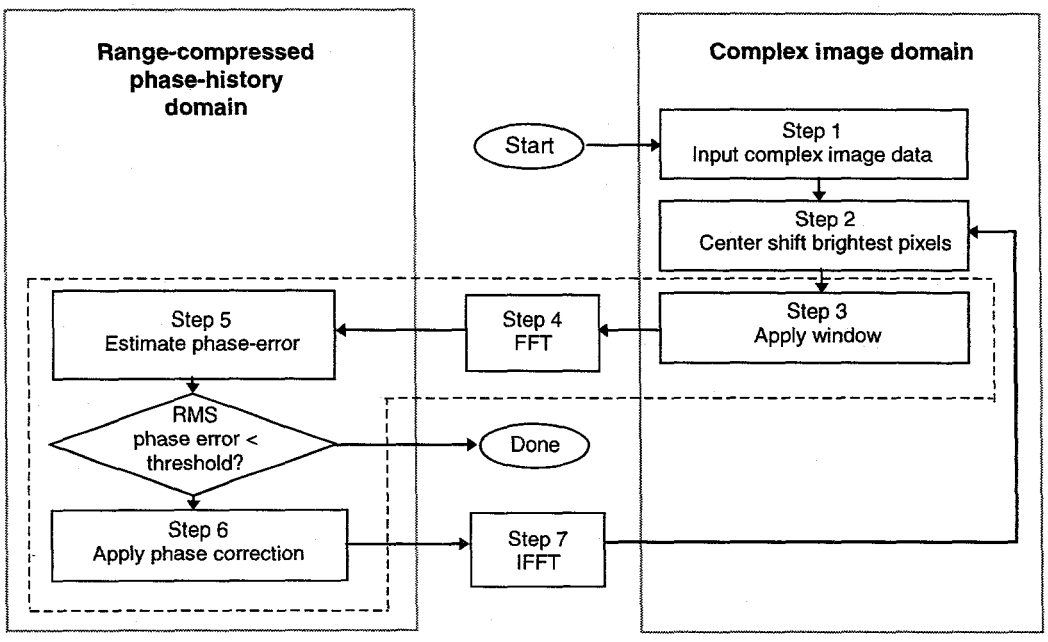

Figure 6-1. Data flow diagram for Phase Gradient Autofocus algorithm.The dashed line encloses those algorithm steps involved in making the transition from support limited data to estimates of phase error interpolated across the full aperture.

6.1.1 Four Methods Considered

Four methods of making the transition from support-limited data in the complex image domain through the ML phase-gradient estimator, to estimates of phase error across the full aperture were tested. Those methods, as shown in Figure 6-2, are

1. Zero pad to full FFT, with implicit interpolation of complex phase history;
2. Zero pad to power of 2 (partial interpolation of complex phase history), with phase interpolation to full aperture;
3. DFT with phase interpolation; and
4. DFT with interpolation of the phase gradient.

6.1.2 Experimental Results

Figure 6-3 shows the mean squared phase-gradient errors after one iteration of the PGA algorithm using these four methods. These data were produced using synthesized data with a large (27 dB) SCR and were aberrated by the low order phase error function. With the exception of Method 4 (DFT with interpolation of the phase gradient), performance on both sides of the knee of the combined bound is degraded. Degradations in performance due to changes in SNR would affect only the performance to the right of the knee. Degradation in performance due to changes in width of the support of the point spread function would only affect performance to the left of the knee. Clearly, results using Method 4, DFT with interpolation of the phase gradient, are superior to those of the other three methods. Method 4 produces results that agree with the combined lower bound.

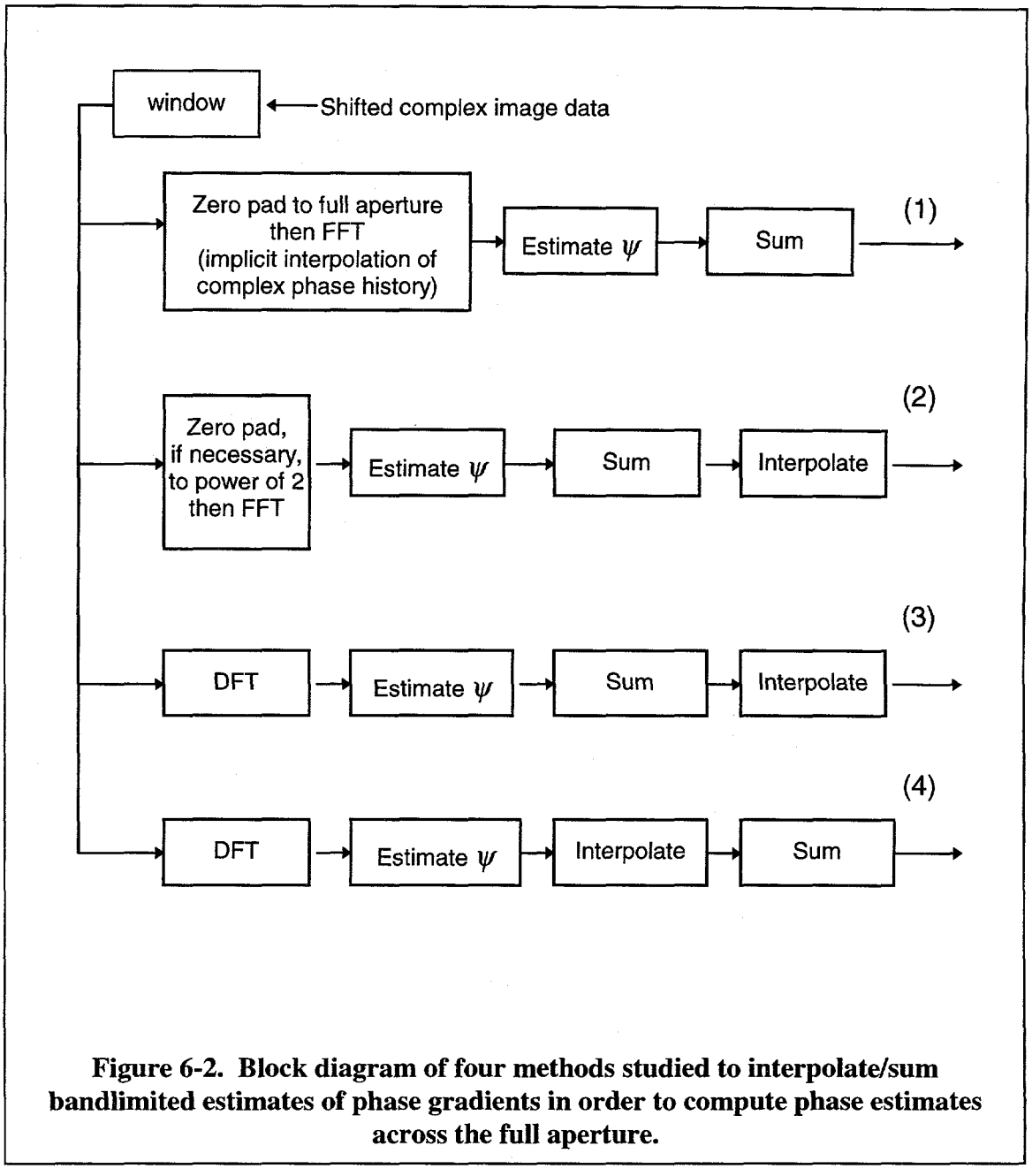

Figure 6-2. Block diagram of four methods studied to interpolate/sum bandlimited estimates of phase gradients in order to compute phase estimates across the full aperture.

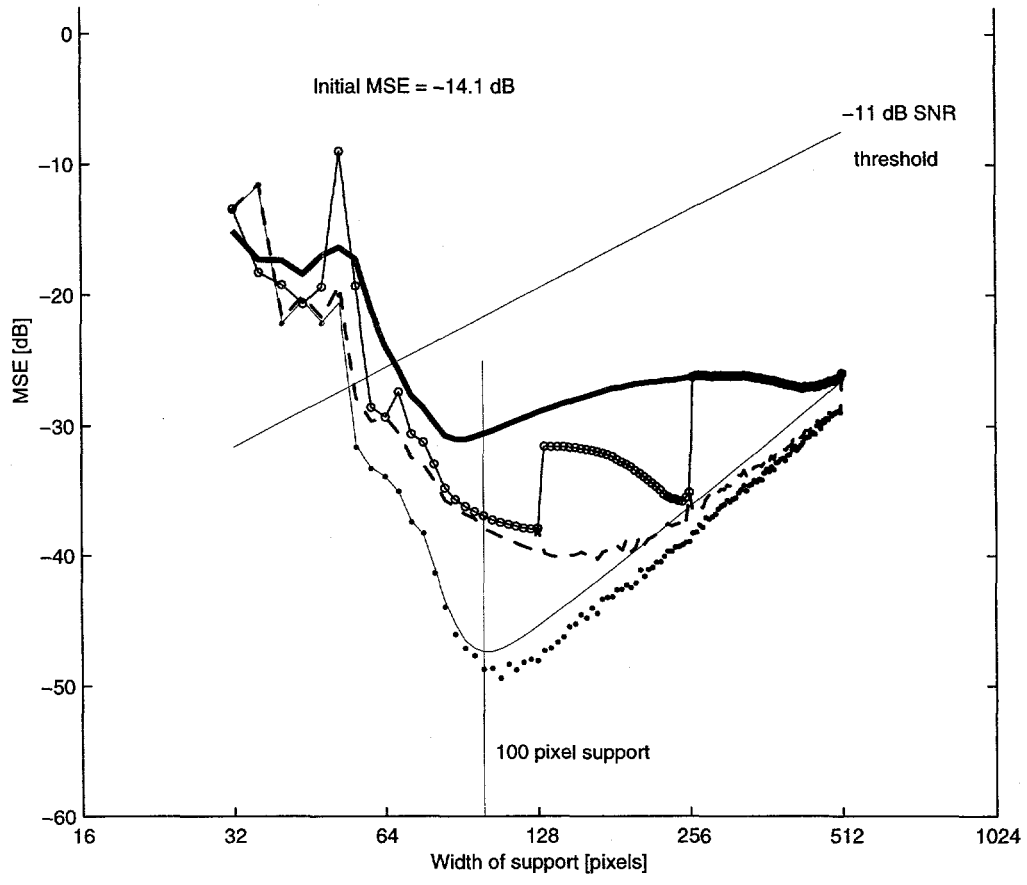

KEY

(1) Full aperture FFT–interpolation of real & imaginary parts.

(2) FFT zero padded to nearest power of 2 >= window; phase interpolation.

(3) DFT set by window; phase interpolation.

(4) DFT set by window; phase rate interpolation.

Combined lower bound.

Figure 6-3. Comparison of estimation errors for four methods of interpolating/summing phase gradients to compute and remove estimated phase error across the aperture. Also shown is combined lower bound due to bandlimiting and estimation errors for SCR = 27 dB.

6.1.3 Theoretical Explanation for Performance of Methods 1 and 2

We will show that zero padding the windowed data prior to Fourier transforming back to the phase-history domain (Methods 1 and 2) correlates the sampled noise and results in a biased estimate of the phase gradient.

The maximum likelihood phase-gradient estimator, which is the phase-gradient estimation kernel of the PGA algorithm for pairwise estimates ($M = 2$), is defined as

$$\hat{\psi}_{m,n} = \angle \sum_{k=1}^{N} x_{k,m} x^*_{k,m-n}, \tag{6-1}$$

where $x_{k,m} = a_k e^{j\phi_m} + n_{k,m}$ is an element of a two dimensional array of data with k as the range index and m as the azimuth index. The index n indicates relative separation between the two data samples with respect to the full aperture. a_k is a complex amplitude with real-valued variance, σ_a^2. ϕ_m is the modulating phase of interest at the m^{th} sample point, which is assumed to be non-random but unknown. $n_{k,m}$ is complex Gaussian noise with zero mean, uncorrelated real and imaginary parts, and real-valued variance, σ_n^2. a_k and $n_{k,m}$ are assumed to be uncorrelated. The asterisk superscript denotes complex conjugation. Consider the expected value of the summation in (6-1). By expanding the terms of (6-1) the argument of the summation becomes

$$x_{k,m} x^*_{k,m-n} = \left(a_k e^{j\phi_m} a^*_k e^{-j\phi_{m-n}} + a_k e^{j\phi_m} n^*_{k,m-n} + a^*_k e^{-j\phi_{m-n}} n_{k,m} + n_{k,m} n^*_{k,m-n} \right). \tag{6-2}$$

If the noise, $n_{k,m}$, is uncorrelated for n ≠ 0, then the expected value of (6-2) reduces to $E\left\{ |a_k|^2 e^{j\phi_m - \phi_{m-n}} \right\} = \sigma_a^2 e^{j\psi_m}$, a complex number. The phase gradient, $\psi_{m,n} = \phi_m - \phi_{m-n}$, is

the angle of that complex number. If the noise $n_{k,m}$ is correlated for n ≠ 0, then $E\{n_{k,m}n^*_{k,m-n}\} = \rho_n\sigma_n^2$ with $-1 < \rho_n < 1$, and the expected value of (6-2) becomes $\sigma_a^2 e^{j\psi_{m,n}} + \rho_n\sigma_n^2$. Using a Taylor series expansion (see Appendix D for details) it can be shown that for large N, the number of ranges used in the estimate,

$$E\{\hat{\psi}_{m,n}\} \cong \angle E\{x_{k,m}x^*_{k,m-n}\} = \arctan\left(\frac{\sigma_a^2 \sin\psi_{m,n}}{\rho_n\sigma_n^2 + \sigma_a^2\cos\psi_{m,n}}\right). \quad (6\text{-}3)$$

Thus, if the noise is correlated, the gradient, which is estimated in the phase-history domain, is biased.

In the application of PGA to SAR image processing, noise in the phase-history domain is attributed to clutter in the scene imaged. We have thus far assumed that clutter is uncorrelated and will continue to do so. The noise correlation coefficient becomes non-zero if the length of the FFT, N_{FFT}, from the image to the phase-history domain is greater than the length of the support of the point spread function, $M_{support}$, and the remaining values are zero padded. This is shown as follows.

The autocorrelation function of the sampled phase history, $R_{xx}(t_m)$, is the discrete Fourier transform of the sampled spectrum, $S_{xx}(\omega_m)$. Because the signal and clutter in the image domain are considered to be uncorrelated and the clutter is considered to be independent and identically distributed, we can consider the noise autocorrelation function independently. The normalized noise spectrum $S_{nn}(\omega_m) = 1$ for $|m| < M_{support}/2$ and $= 0$ otherwise. Therefore, the associated autocorrelation function, $R_{nn}(t_m)$, is a sinc function

with first zero crossing at $m = 1/M_{support}$ and first sample at $1/N_{FFT}$. Thus, it is easily shown that the noise correlation coefficient $\rho_n = \text{sinc}(\pi\, nx)$ where x is the ratio of the support for the point spread, $M_{support}$, to the length of the zero padded FFT, N_{FFT}; that is $x = M_{support}/N_{FFT}$.

Unless the data are undersampled, $\rho_n \geq 0$. σ_n^2 is always positive and real; therefore, the magnitude of the estimated phase gradient, $\hat{\psi}_{m,n}$, is biased downward. This bias is a function of the value of the true phase gradient, $\psi_{m,n}$, and the noise correlation coefficient, ρ_n, as indicated by equation (6-3).

6.1.4 Examples Illustrating Theoretical Explanation

Examples of biased and unbiased estimates are shown in Figure 6-4. In Figure 6-3, a vertical line intercepts the plots of mean squared estimation error for a 100 pixel-wide support of the point spread function.

The plots in Figure 6-4 show estimation error across the aperture for Methods 2 and 4 with the 100 pixel-wide support of the point spread function. Using Method 2, data were zero padded out to 128 points then FFTed to the phase history domain, producing the biased estimate ($\rho_1 = 0.26$). Using Method 4, the 100 point DFT to the phase-history domain produces a nearly unbiased estimate. The heavy, smooth dashed line shows the theoretical deviation of the biased estimate from truth. The light line shows the actual deviation of a biased estimate from truth. The heavy, rough solid line shows the actual

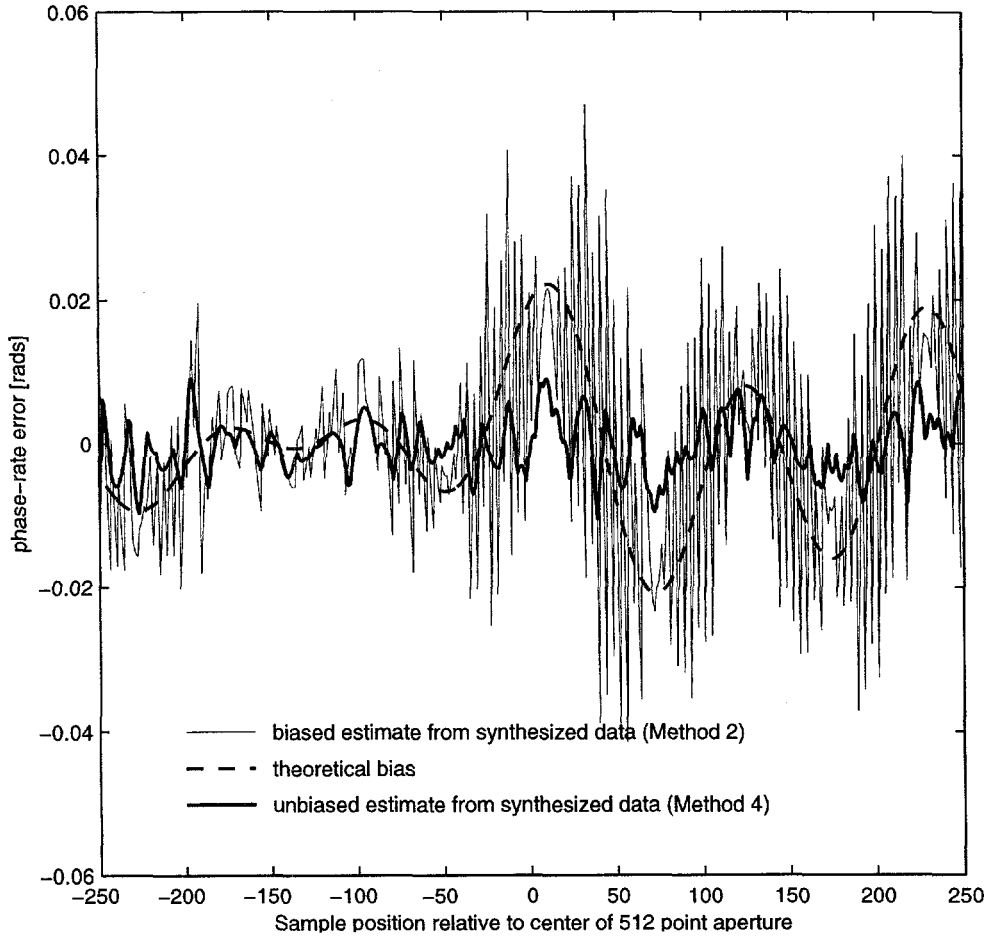

Figure 6-4. Residual phase gradients for biased and unbiased estimators using 27 dB SCR synthesized data.

deviation of an unbiased estimate from truth. Results are similar with the real SAR data.

In SAR autofocus applications of the ML phase-gradient estimator, it is easy to avoid the biased estimate by avoiding zero padding. Zero padding can be avoided by either using a DFT of length $M_{support}$ or by using all the data out to N_{FFT}. From Figure 6-3 it is clear that the increase in MSE error due to increasing the width of the support is minimal when compared to the significant loss in performance introduced by zero padding. It is, nonetheless, very important to recognize the possibility of a biased estimate and its affect on autofocus performance.

6.1.5 Explanation of Inferior Performance of Method 3 to Method 4

Next we consider the effect of phase interpolation (Method 3) versus phase-rate interpolation (Method 4). In Chapter 4 we cited Woodward's theorem which states that the power spectrum associated with phase modulation is approximately proportional to the probability density function of the phase rate. Linear interpolation of phase produces constant phase rate between the estimated data points. The resulting error in phase gradients will have a saw-tooth component due to the difference between continuous truth and the zero-order hold estimates. The frequency of this sawtooth waveform is determined by the width of the support of the point spread function. Residual phase rates from Method 3 (phase interpolation) and Method 4 (phase-rate interpolation), are compared in Figure 6-5 using the data from the same 100 pixel-wide support of the point spread function. The associated distributions of phase rates and phase-rate frequencies

for the two interpolation methods are shown in Figure 6-6. A spectral spread associated with Method 3 (phase interpolation) is evident.

Finally, the point spread functions associated with the residual phase-rate errors just discussed are shown in Figure 6-7. Residual phase error is the difference between integrated/interpolated phase-gradient estimates and truth. Recall that the point spread function is defined as $\left| FT\left(W(t)e^{j\phi(t)}\right)\right|^2$ where FT is the Fourier transform, $W(t)$ is an aperture taper and $\phi(t)$ is the aberrating phase function. The initial point spread function is illustrated in Chapter 4 in the second row of Figure 4-2(c). Rows (1) through (4) in Figure 6-7 show the point spread functions due to the residual phase associated with the four interpolation methods. Row (5) shows the point spread function that results if the window is increased to the next higher power of 2, that is, to 128 pixels. A -40 dB Taylor window with $\bar{n} = 6$ was applied to these data. The mainlobes in row (1) and row (2) are significantly wider than those of the other three rows. Comparison of row (2), 100 pixel-window zero padded out to 128 point for the FFT, to row (5) clearly illustrates the loss in performance due to zero padding compared to a small, unnoticeable loss in performance due to the increase in SNR associated with a wider support. Note that the phase interpolation used in Methods 2 and 3 introduces pairs of sidelobes at plus and minus the width of the support of the point spread function.

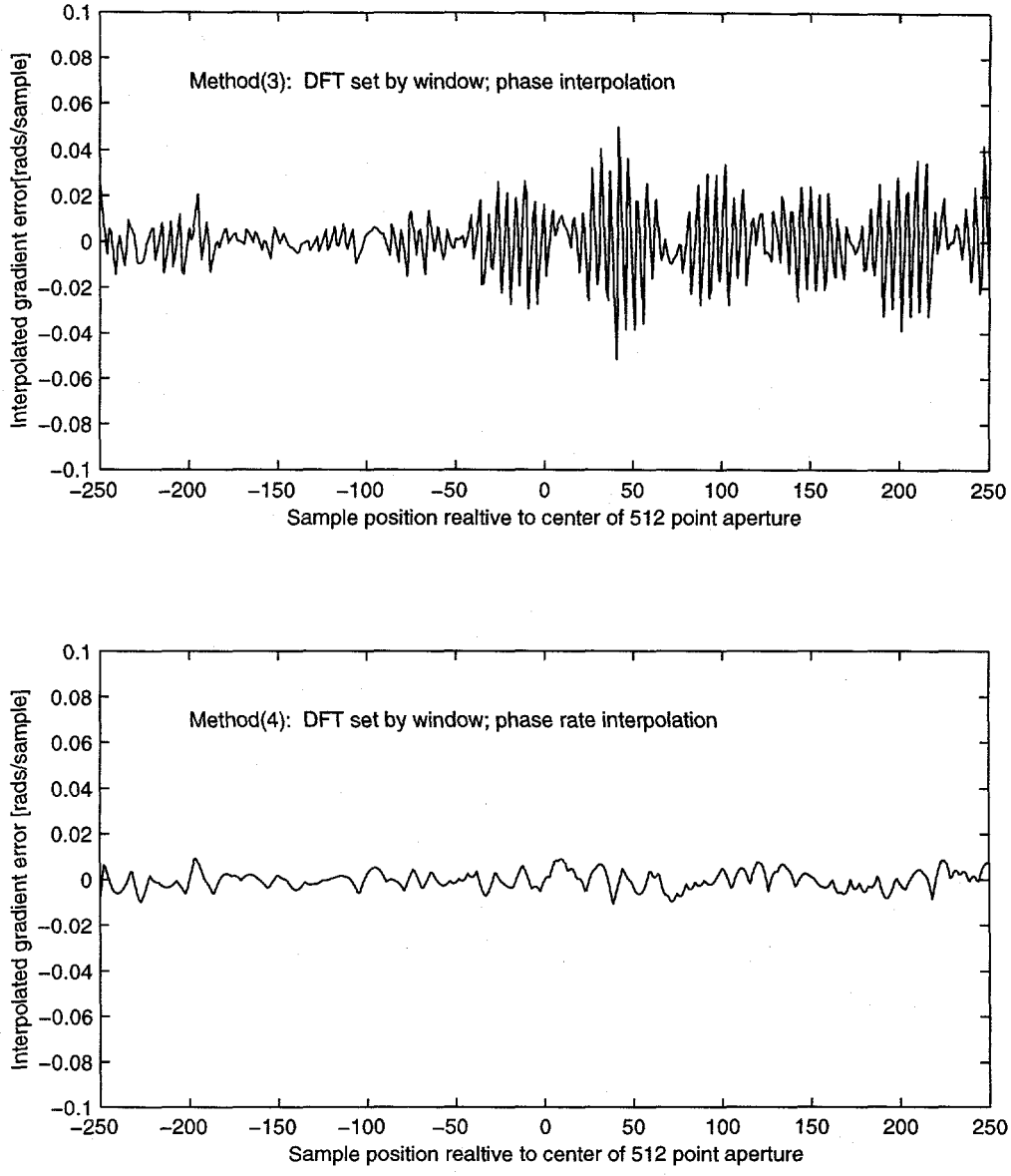

Figure 6-5. Comparison of residual phase gradients for Methods 3 and 4; phase and phase-rate interpolation respectively using 27 dB SCR synthesized data.

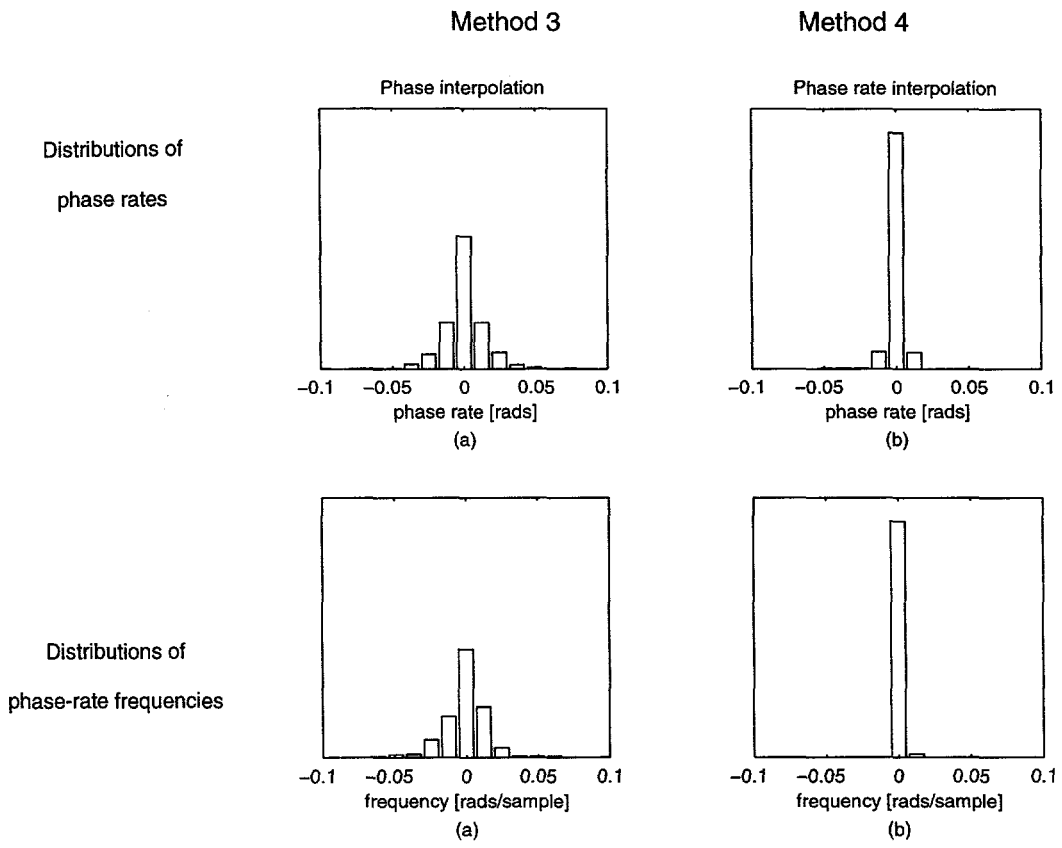

Figure 6-6. Comparison of sample distributions of residual phase rate and phase-rate bandwidth for two interpolation methods: phase interpolation and phase-rate interpolation.

Experiment used synthesized SAR data with 27 dB SCR aberrated by the low order phase. Support of the point spread function was 100 pixels for these residuals.

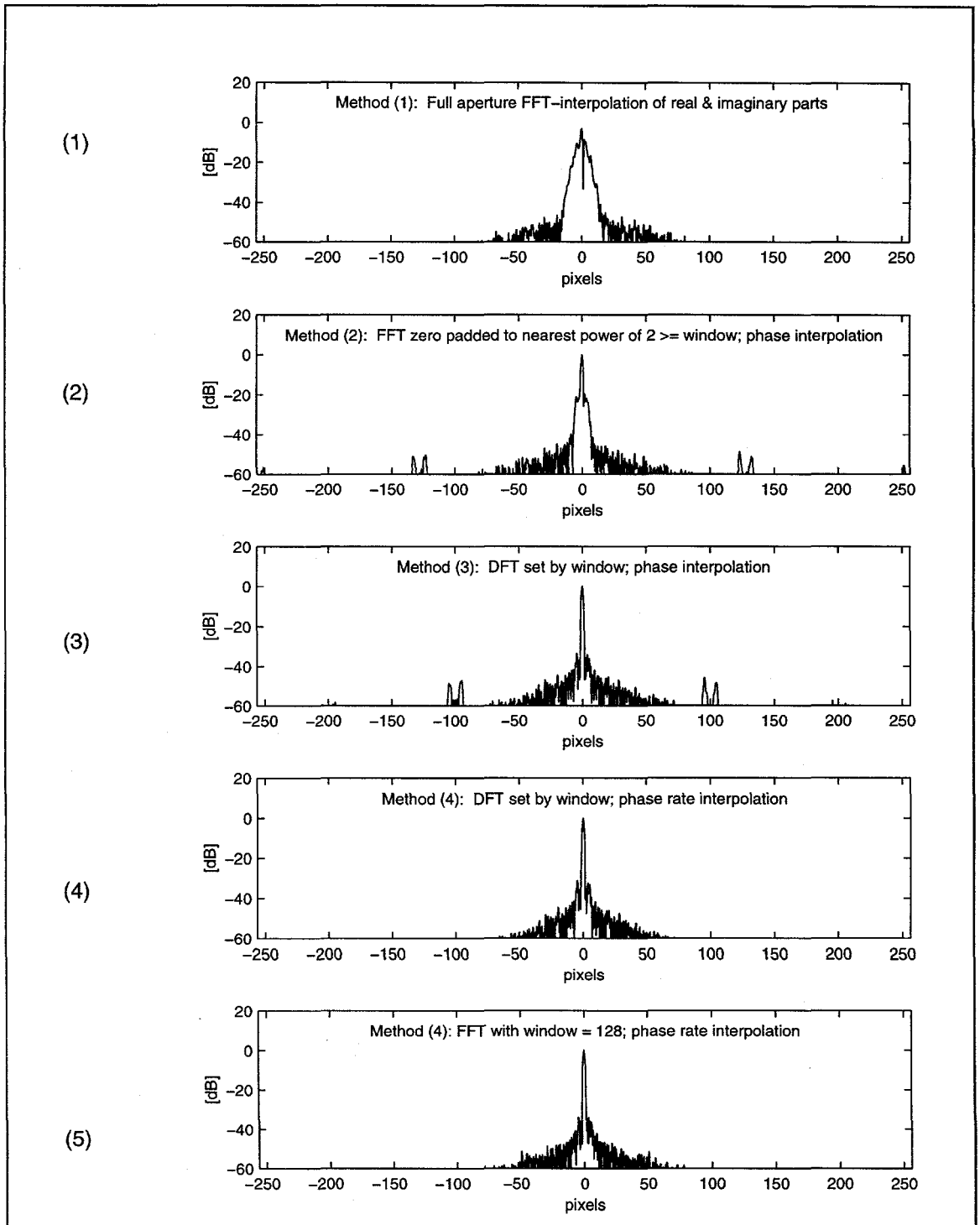

Figure 6-7. Point spread functions due to residual phase for 27 dB SCR synthesized SAR scene aberrated by the low order phase and support of the point spread function set at 100 pixels.

Figure 6-3 through Figure 6-7 showed results for synthesized data with 27 dB SCR. Figure 6-8 through Figure 6-12 show the same types of data for synthesized data with 15 dB SCR.

Having examined the point spread functions, let us return to Figure 6-6 and Figure 6-11, the distributions of phase rate and phase rate frequencies and reconsider the usefulness of Woodward's theorem for our application. While these distributions, or mean squared values of these distributions[1], provide relative measures of performance, they do not provide the clear measures of resultant image quality available from the point spread functions.

6.1.6 Summary, Conclusions and Recommendations

A subprocess of the PGA algorithm not addressed in the literature has been examined here in detail. Four implementations of this subprocess were considered. Only one of the four implementations, Method 4 (DFT with phase-rate interpolation), produces results that equal the combined lower bound. For applications where the increased computational burden of DFTs is unacceptable and FFTs must be used, we have shown that increasing the width of the support to the next highest power of two is preferable to zero padding. Only Method 4 is used for the remainder of the analyses presented here.

---

[1] bandwidth = rms value of phase rate frequencies

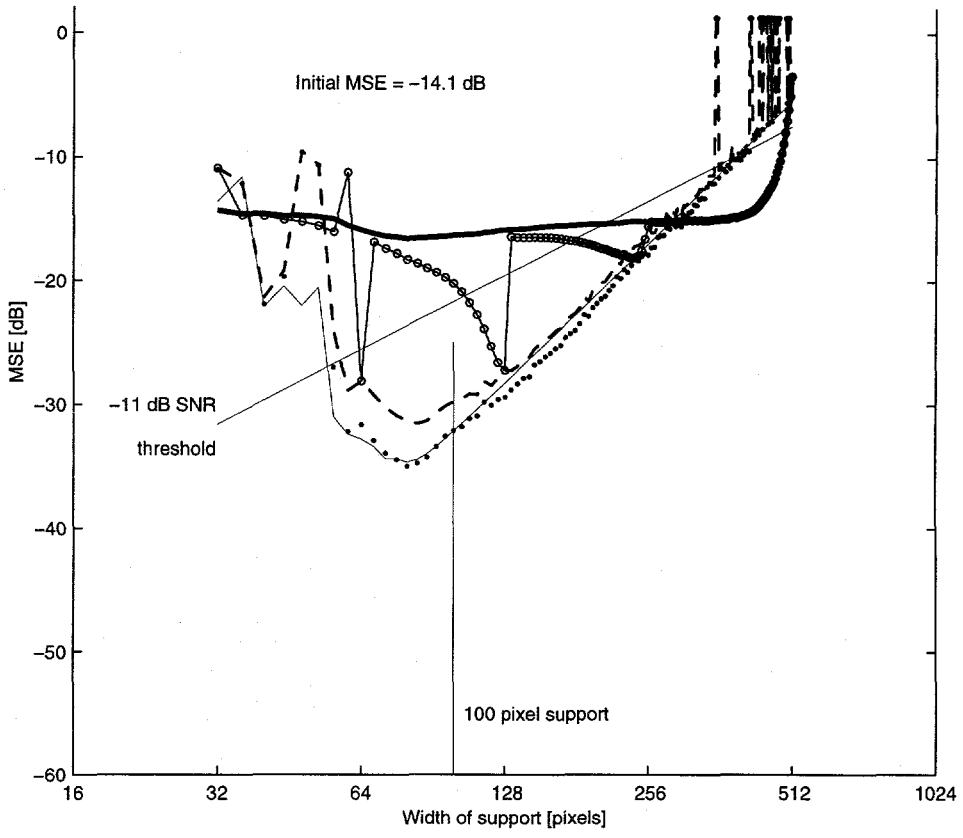

KEY

(1) Full aperture FFT–interpolation of real & imaginary parts.

(2) FFT zero padded to nearest power of 2 >= window; phase interpolation.

(3) DFT set by window; phase interpolation.

(4) DFT set by window; phase rate interpolation.

Combined lower bound.

Figure 6-8. Comparison of estimation errors for four methods of interpolating/summing phase gradients to compute and remove estimated phase error across the aperture. Also shown is combined lower bound due to bandlimiting and estimation errors for SCR = 15 dB.

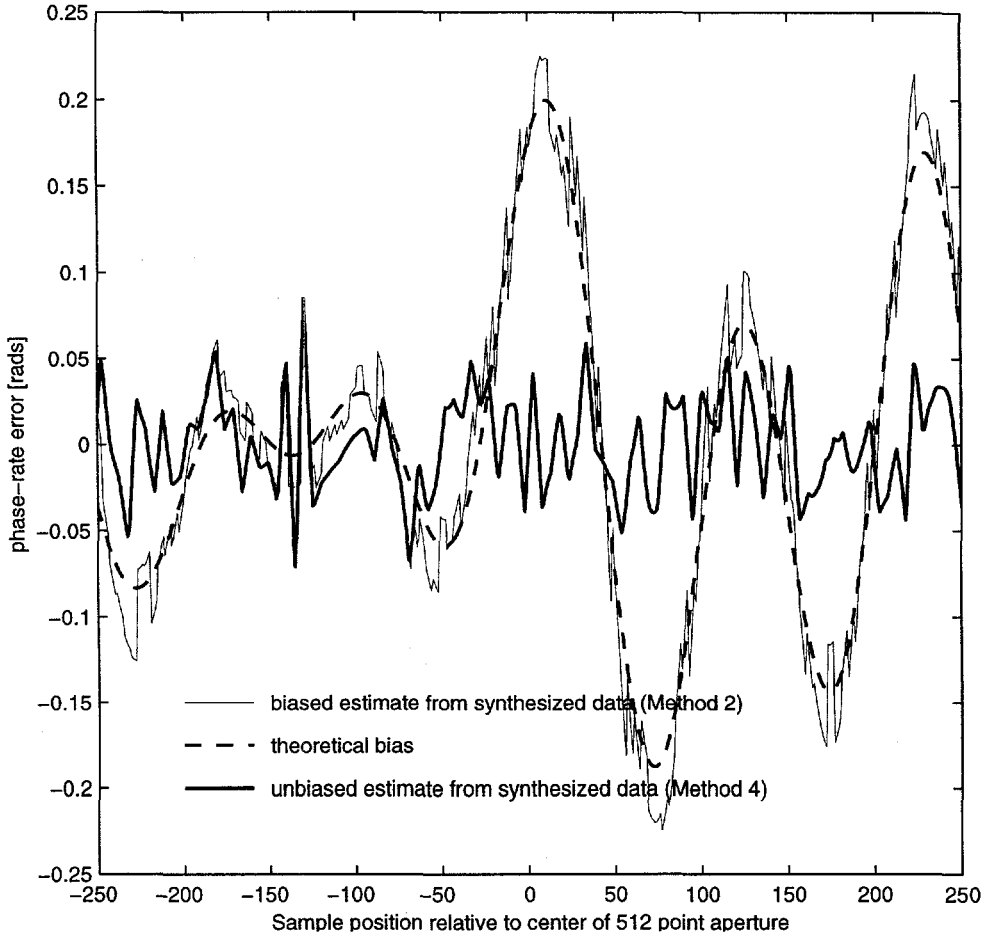

Figure 6-9. Residual phase gradients for biased and unbiased estimators using 15 dB SCR synthesized data.

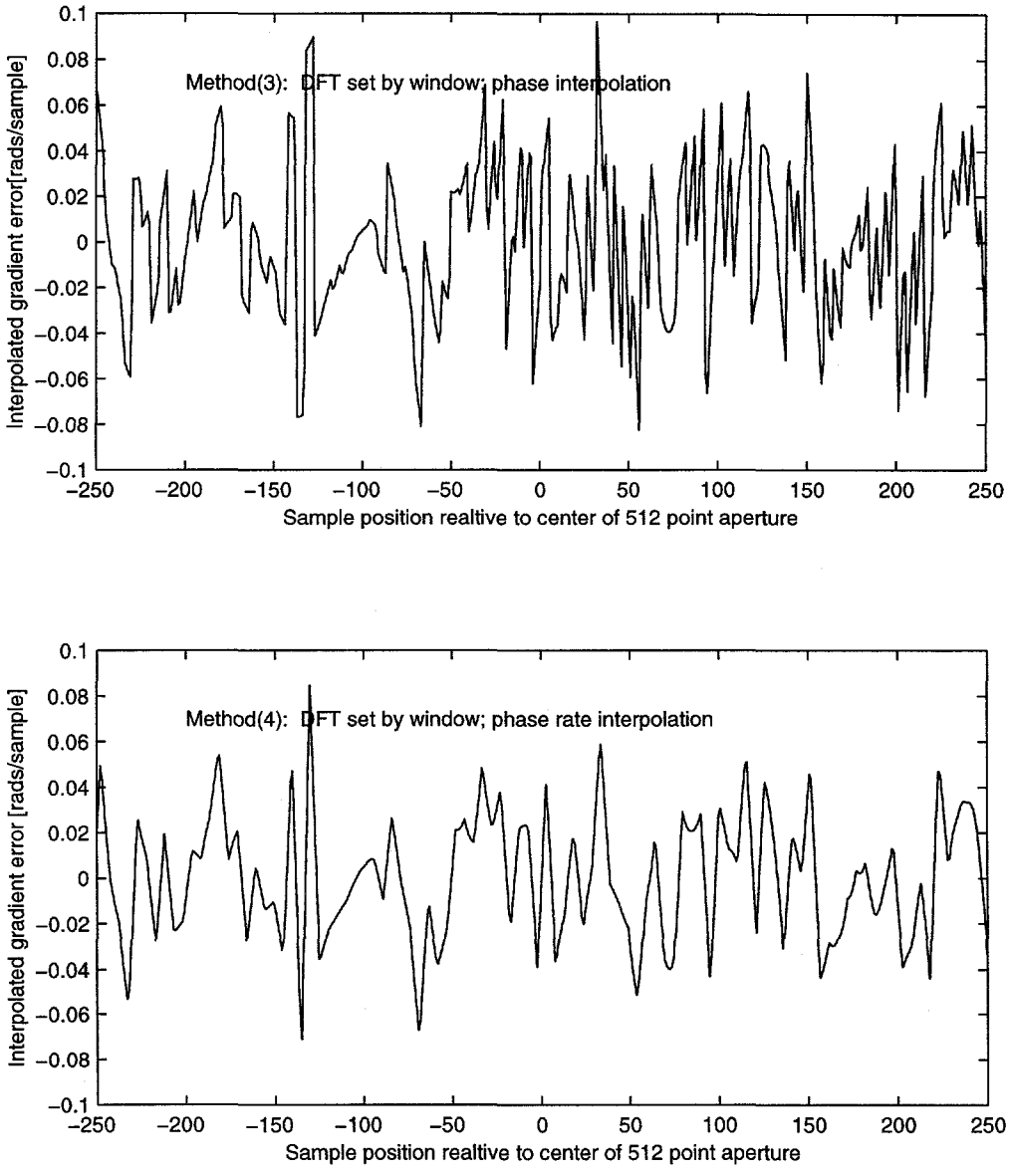

Figure 6-10. Comparison of residual phase gradients for Methods 3 and 4; phase and phase-rate interpolation respectively using 15 dB SCR synthesized data.

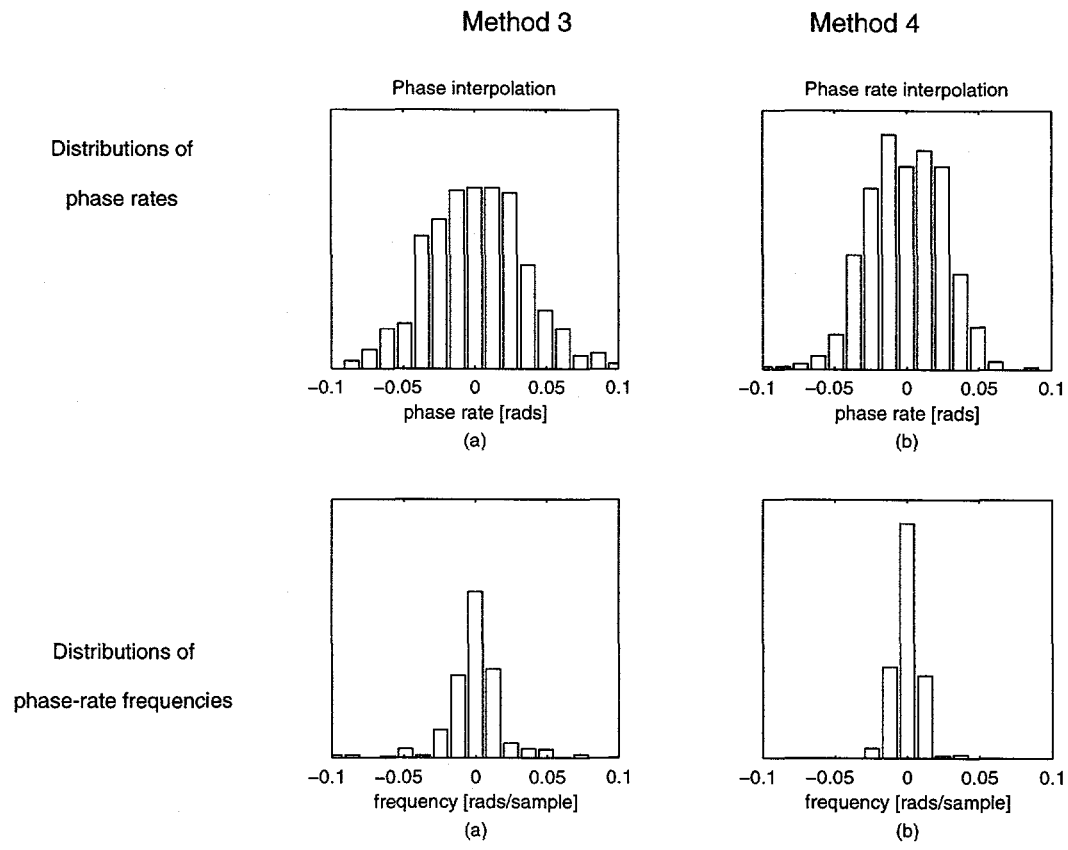

Figure 6-11. Comparison of sample distributions of residual phase rate and phase-rate bandwidth for two interpolation methods: phase interpolation and phase-rate interpolation. Experiment used synthesized SAR data with 15 dB SCR aberrated by the low order phase. Support of the point spread function was 100 pixels for these residuals.

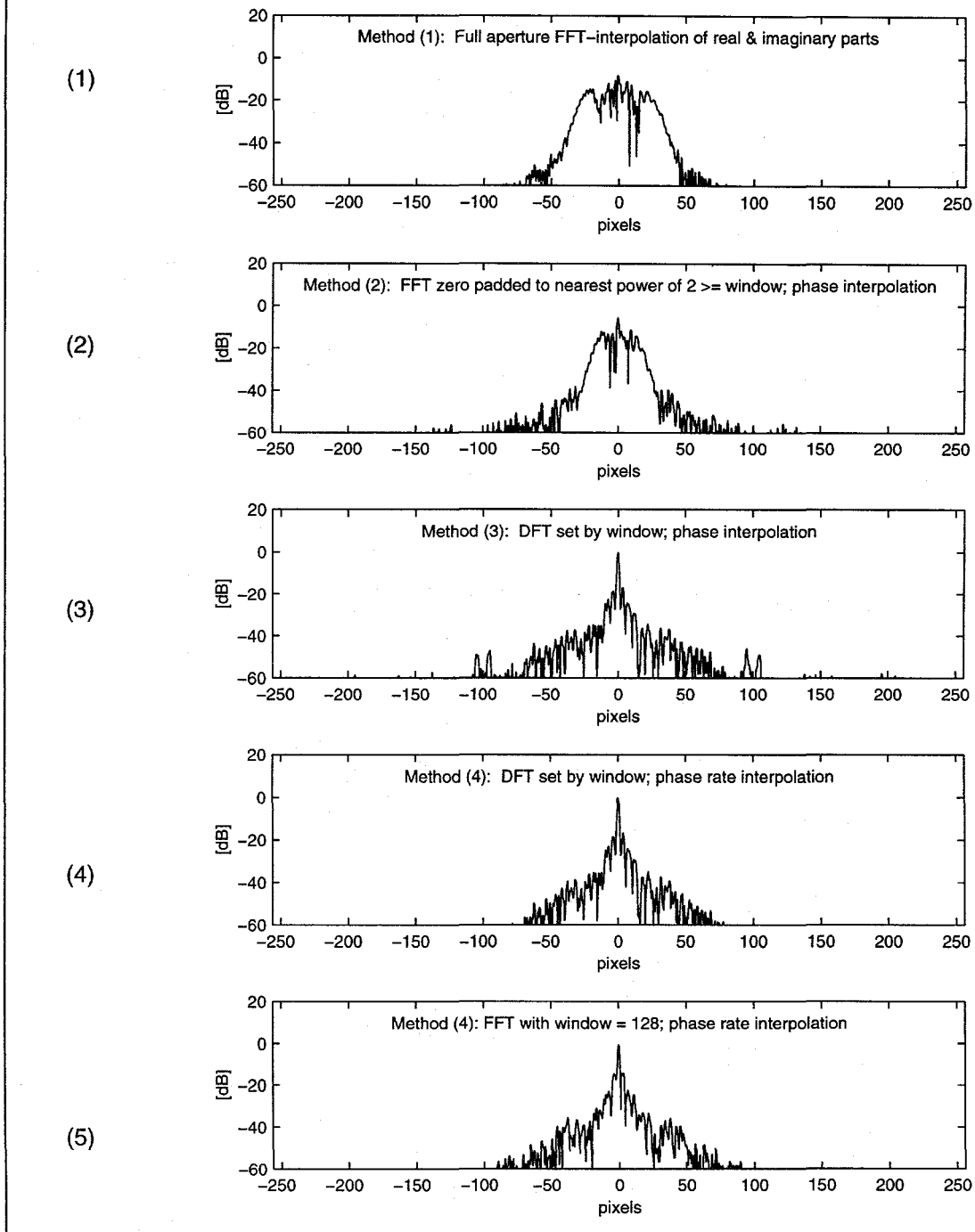

Figure 6-12. Point spread functions due to residual phase for 15 dB SCR synthesized SAR scene aberrated by the low order phase and support of the point spread function set at 100 pixels.

6.2 Improvement with Iteration

The derivation of the ML phase-gradient estimator is based on optimal estimation theory. Yet application of the PGA algorithm has demonstrated improvement with iteration. Snarski [51] has suggested that the improved focus after the first iteration reduces shift errors, and reductions in shifting errors improve gradient estimations. During discussions with the authors of [18] it was suggested that, as the support of the point spread function decreases with each iteration, the SNR into the ML estimator increases. Thus the estimation error is reduced with iteration.

6.2.1 Theoretical Analysis

We note that, while the ML estimator for the complex covariance is an unbiased optimal estimator, (see discussion following equation (6-2) on page 121), the estimate of the argument (angle) of that complex covariance is only asymtotically unbiased. This was mentioned in the previous section and is shown in the development of the Taylor series in Appendix D. Equation (D-23) in Appendix D shows

$$E\left\{\hat{\psi}\right\} = \psi + \varepsilon \tag{6-4}$$

where

$$\varepsilon = \frac{\sin 2\psi}{2N}\left(\frac{2}{\beta} + \frac{1}{\beta^2}\right) \tag{6-5}$$

where X and Y are the real and imaginary parts of $\frac{1}{N_{ranges}} \sum_{k=1}^{N_{ranges}} x_{k,m} x_{k,m-n}^{*}$. This angle-

dependent bias suggests that residual phase error is not random, but rather that it has some structure proportional to the initial phase error.

6.2.2 Simulation Results

We consider two cases for simulation. Case 1: the residual phase error at the start of the second iteration is that associated with the minimum MSE as illustrated in Figure 6-13 for the 15 dB SCR data and in Figure 6-14 for the 27 dB SCR data. Case 2: the residual phase error at the start of the second iteration is that associated with 1.4 times the width of the support of the point spread function at the minimum MSE, as illustrated in Figure 6-15 for the 15 dB SCR data and in Figure 6-16 for the 27 dB SCR data. The four plots in each of these four figures show the following: the first column of plots shows results after one iteration; the second column shows results after two iterations. The first row shows residual MSE of the estimated phase gradient versus the width of the support of the point spread function. The solid line indicates the combined lower bound. Recall that the units of the support are pixels while the scale is log base 2. For synthesized data with homogeneous clutter, the SNR into the ML estimator decreases by 3 dB with each factor of 2 increase in support along the horizontal axis. The vertical line marks the selected width of support of the point spread function. The resultant point spread functions and diffraction-limited point spread functions are shown in the second row. The two horizontal lines mark the mean and maximum values of single-range single-signal ratios of (CSR) average clutter to signal. These are measures of mean and maximum scene contrast. Sidelobes near the mean CSR line will appear in a good part of the image.

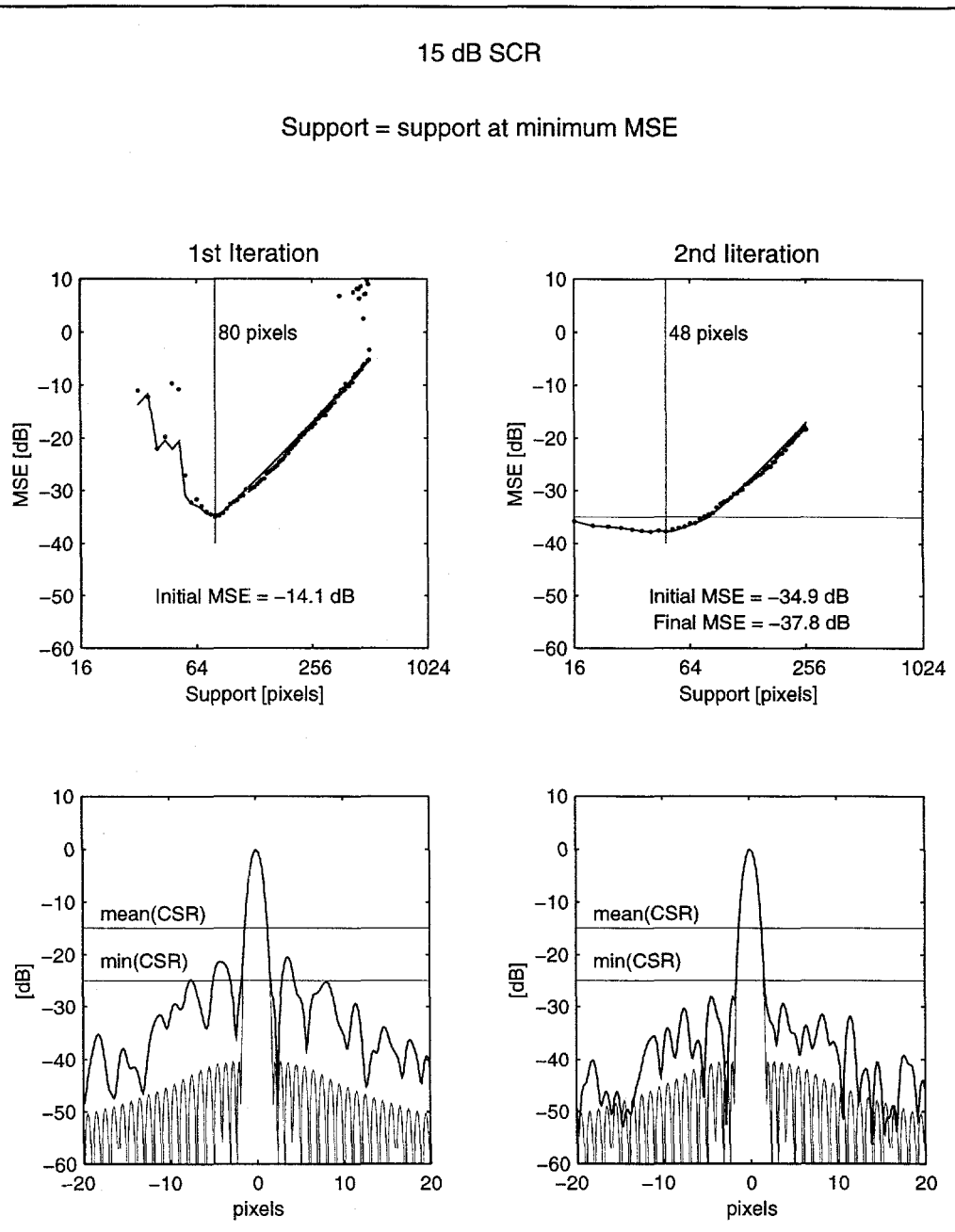

Figure 6-13. Residual mean squared phase gradients and point spread functions associated with minimum MSE.

Data are shown for two iterations of PGA using synthesized SAR data with 15 dB SCR aberrated by the low order phase function.

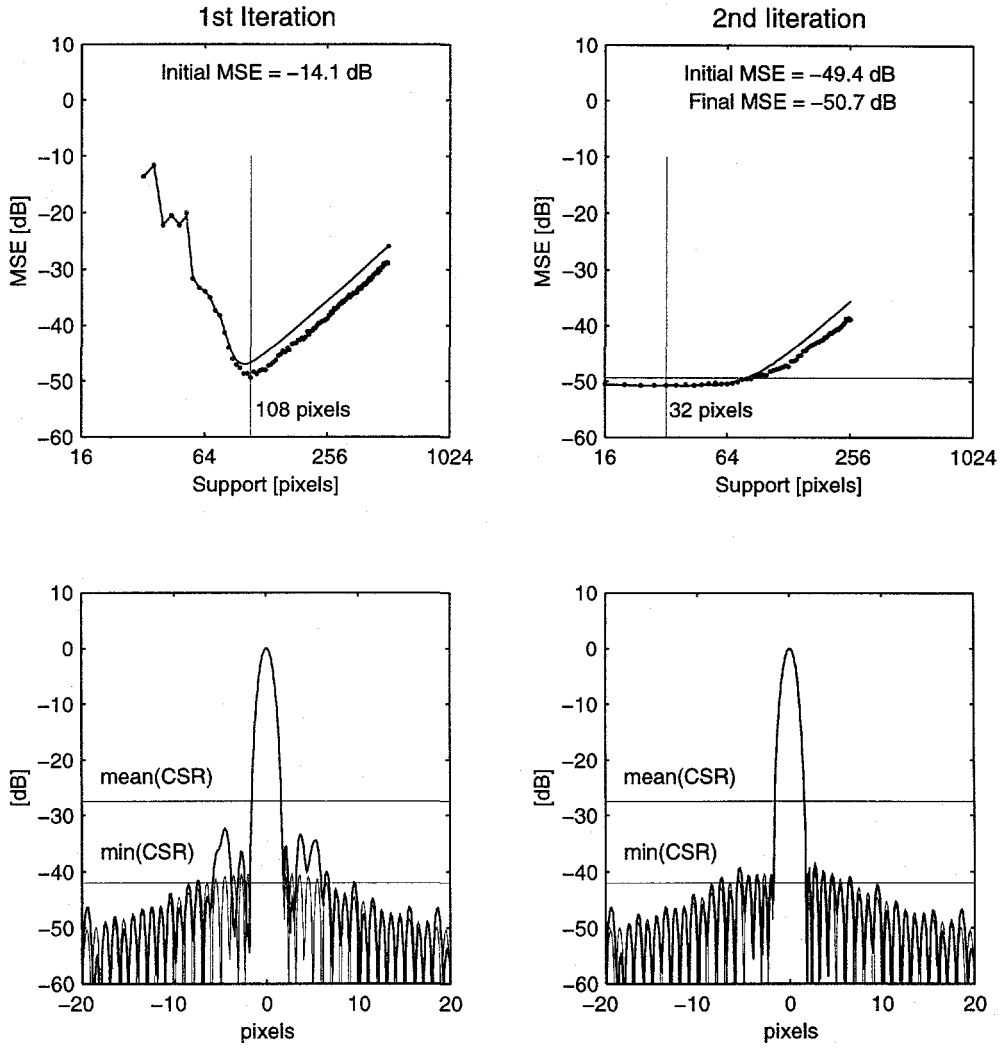

Figure 6-14. Residual mean squared phase gradients and point spread functions associated with minimum MSE.

Data are shown for two iterations of PGA using synthesized SAR data with 27 dB SCR aberrated by the low order phase function.

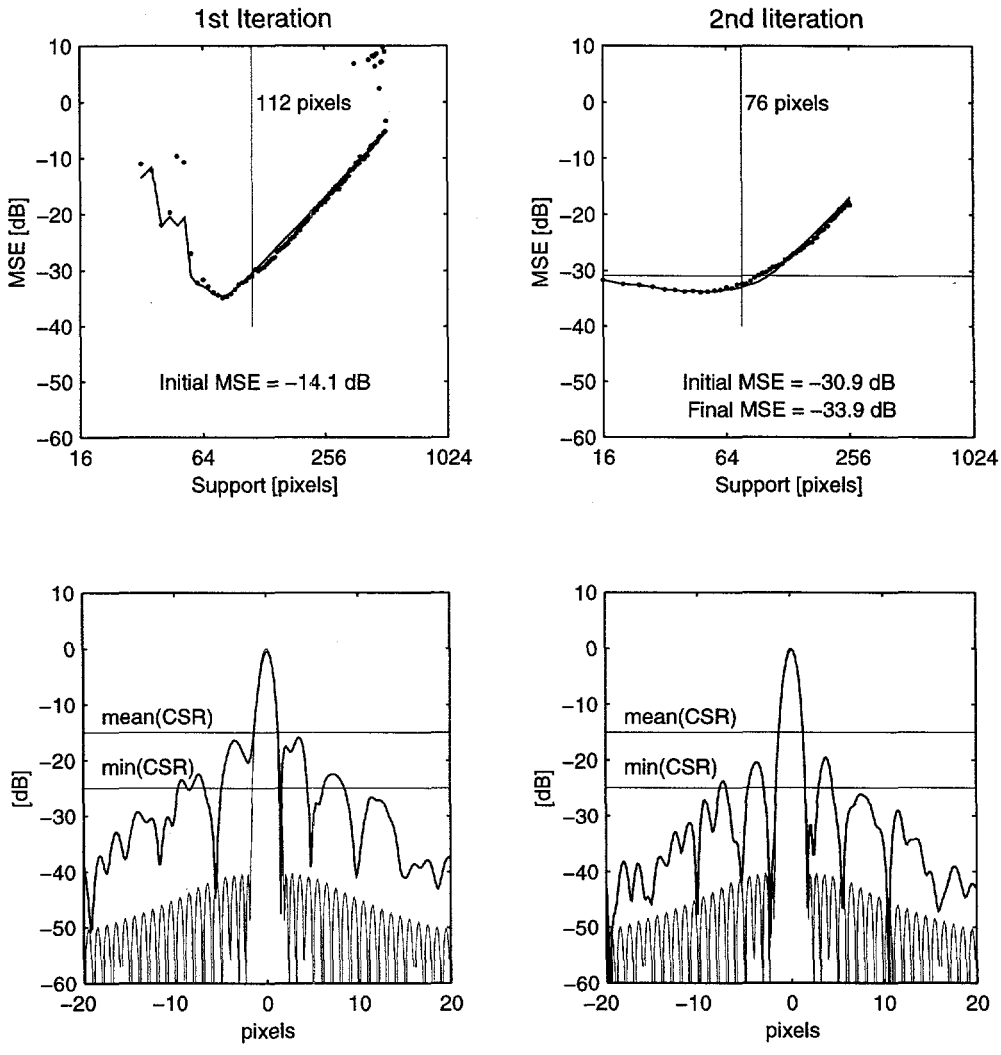

Figure 6-15. Residual mean squared phase gradients and point spread functions associated with support = 1.4 x support at minimum MSE.

Data are shown for two iterations of PGA using synthesized SAR data with 15 dB SCR aberrated by the low order phase function.

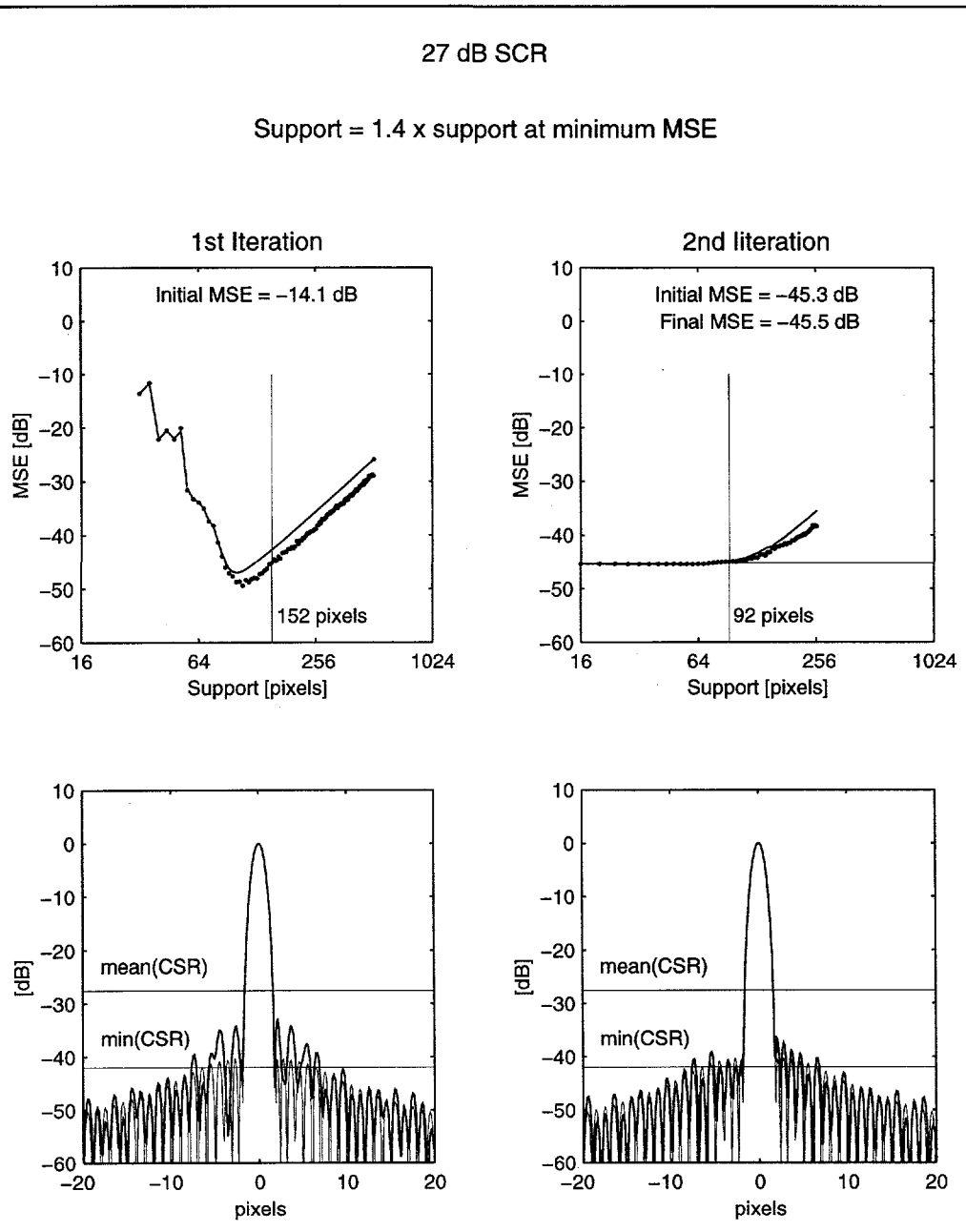

Figure 6-16. Residual mean squared phase gradients and point spread functions associated with support = 1.4 x support at minimum MSE.

Data are shown for two iterations of PGA using synthesized SAR data with 27 dB SCR aberrated by the low order phase function.

Sidelobes well below the mean CSR but above the maximum CSR will appear in at least one range of the image. The improvement for the 15 dB SCR data is about 3 dB while the improvement for the 27 dB SCR data is about 1 dB. We note that the maximum SCR for the 27 dB SCR data is 42 dB. This is 2 dB greater than the peak-sidelobe ratio of the 40 dB Taylor window.

6.2.3 Summary, Conclusions and Recommendations

The Taylor series expansion shows an angle-dependent bias inherent in the phase-gradient estimator. The magnitude of this bias is shown in Appendix D to be inversely proportional to the number of data samples used in the estimate. The experimental results show that there is improvement with iteration. There are no indications that this improvement can be realized without decreasing the width of the support of the point spread function. For improvement to occur, the residual phase gradient after the first iteration must have some detectable low pass structure with bandwidth less than the bandwidth associated with the support used on the first iteration. In order to use the expression for estimator bias to develop a full convergence model, we require a well-defined relationship between scene SCR, point spread, and selected support of the point spread.

6.3 Differences Between Synthesized and Real SAR Data

In Chapter 4 we introduced the real SAR image data used here and explored a number of metrics to establish distinctions between the synthesized data and the real SAR data. We now compare algorithm performance between the real and synthesized SAR data. We will consider SAR scenes Rural-3 and Urban-1 and their synthesized counterparts with 15 dB and 27 dB SCR respectively. We will consider all three aberrating phase errors. These comparisons are between data with no shifting errors. That is, the brightest points at each range in the scene were determined prior to defocusing, then circularly shifted to the center of the scene after defocusing.

6.3.1 Comparison of Actual and Theoretical MSE

MSE versus width of the support of the point spread function are shown for the 15 dB and 27 dB synthesized data in Figure 6-17. The combined lower bound, indicated by a dashed line was computed using equations (5-8) and (5-11). That is, the mean clutter level was assumed to be constant across the scene and $SNR = SCR/N_{support}$. The vertical line marks the MSE for the 128 pixel-wide support of the point spread function. The straight line sloping upward from left to right is the -11 dB SNR threshold discussed in Chapter 5. Note the close agreement between theoretical bounds and PGA performance using synthesized SAR data. Recall that to the right of the knee of the combined bound, performance is determined by SNR. To the left of the knee, performance is determined by width of support.

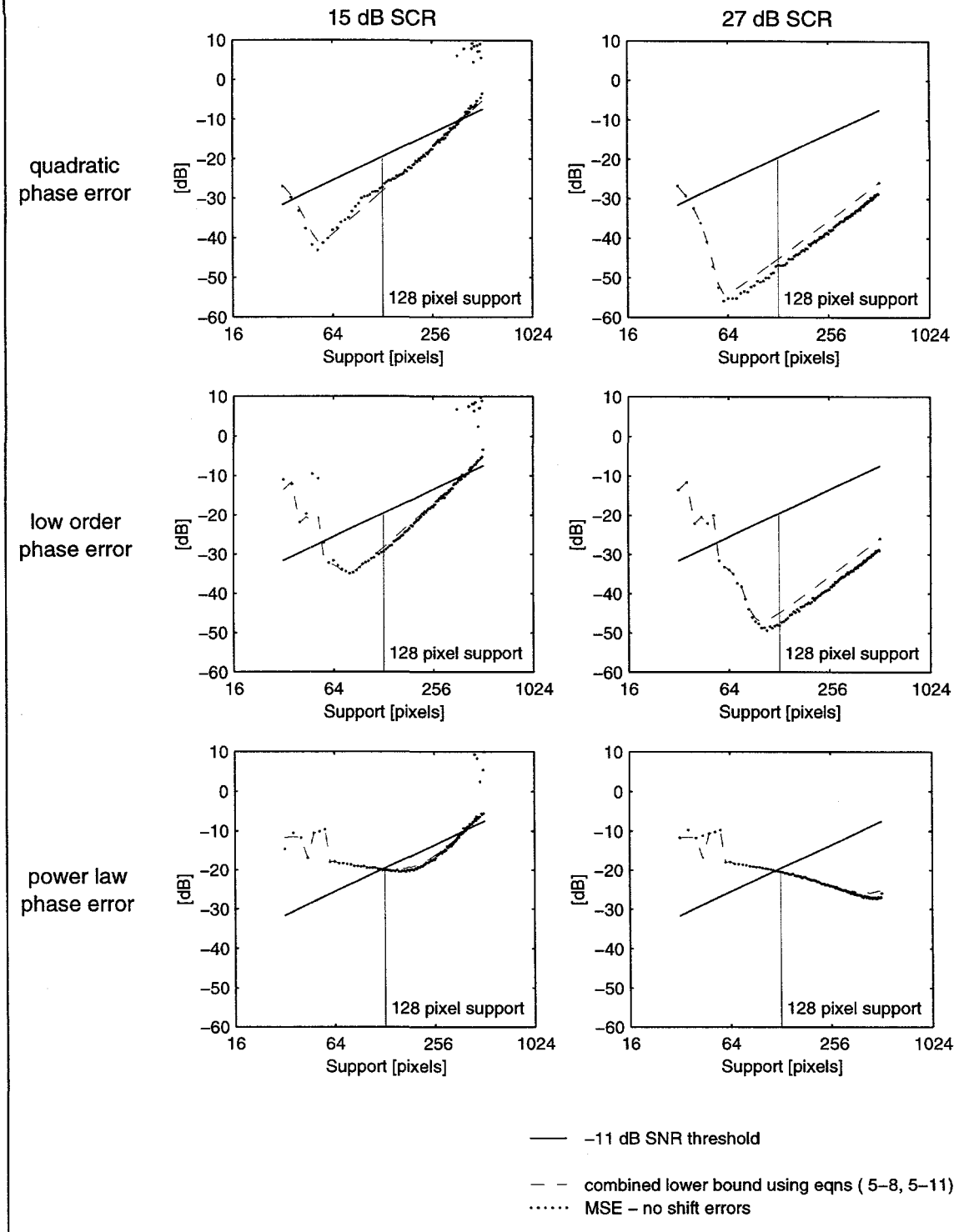

Figure 6-17. Theoretical and actual MSE for SCR = 15 dB and 27 dB and three aberrating phase errors.

These same measures are shown for the real SAR data in Figure 6-18. In addition to the CRLB computed using equations (5-8) and (5-10), the CRLB computed using equations (5-12) and (5-13) is also shown. Recall that equation (5-12) uses the signal and clutter values computed from the SAR data. Performance of PGA using real SAR data does not agree with the model as well as performance using synthesized data. This suggests that the real SAR data are not fully represented by the model. Note that the data with low SNR (Rural-3) deviate from the bound to the left of the knee. This deviation is consistent with results generated from data with correlated noise. We will not, however, draw that conclusion at this point.

6.3.2 Plots of Estimates and Truth, and Distributions of Estimation Error Relative to Truth

In the next four figures (Figure 6-19 through Figure 6-22) we compare plots of truth to plots of estimated and interpolated phase gradients. We also examine scattergrams of estimation errors relative to truth for correlation. The selected data are for the 128 pixel-wide support of the point spread function. Plots of estimates and truth in the first column of these figures show interpolated data. Scattergrams in the second column show the errors in gradient estimates prior to interpolation. Truth in the scattergrams was determined from the first differences of truth down-sampled to 128 data points. Theory indicates that, for the quadratic and low order phase errors, the bound is determined by SNR. This is not the case for the power law phase error but we will, nonetheless, display those results for the same 128 pixel-wide support. Data for the 15 dB and 27 dB SCR

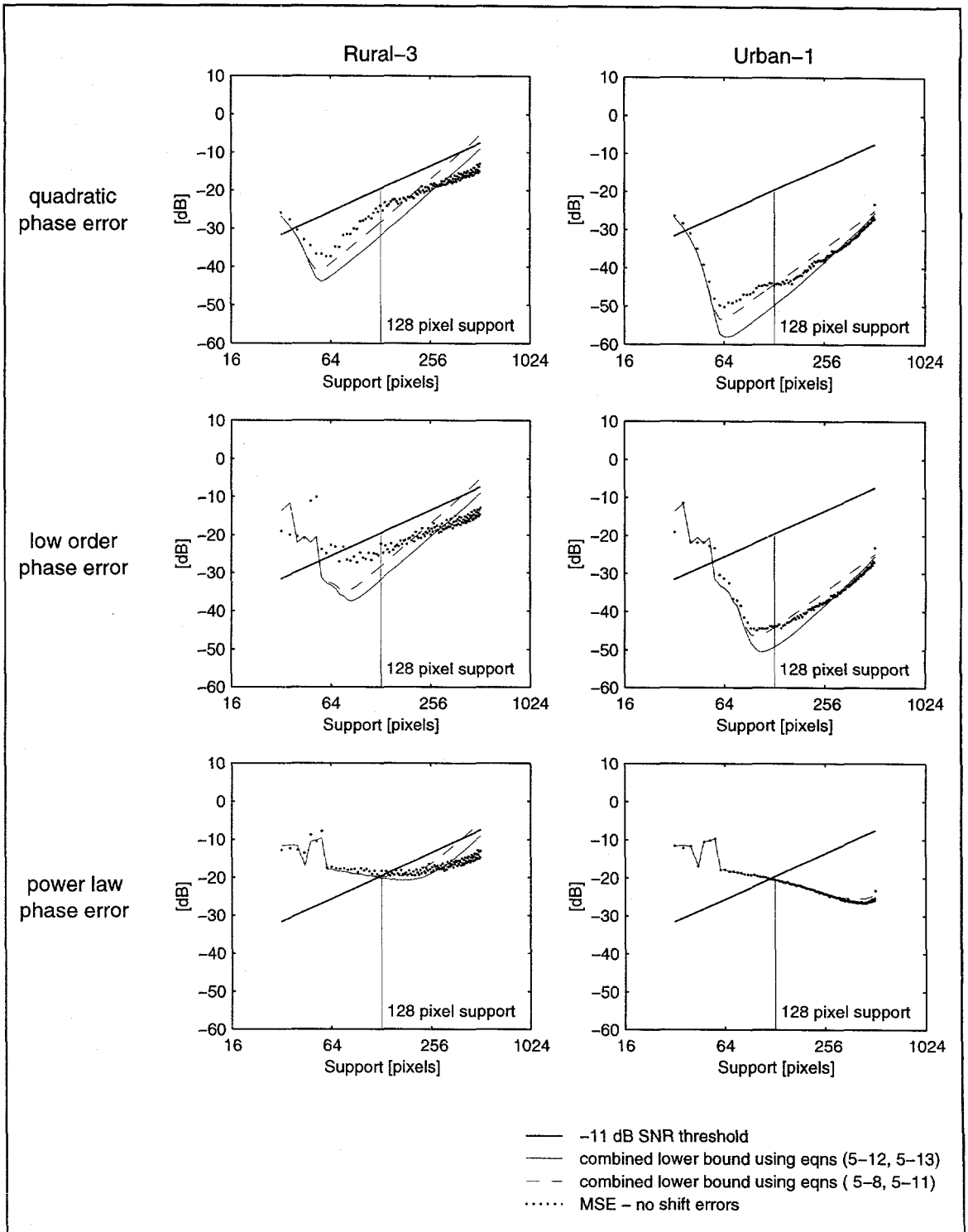

Figure 6-18. Theoretical and actual MSE for scenes Rural-3 and Urban-1 and three aberrating phase errors -- no shift errors.

synthesized SAR data are shown in Figure 6-19 and Figure 6-20 respectively. Data for Rural-3 and Urban-1 are shown in Figure 6-21 and Figure 6-22 respectively.

Any trend of zero slope indicates a constant error in phase-gradient estimation. This represents a linear phase error which shifts, but does not blur, the image. Such trends are of no interest here. Any trend with non-zero slope represents a gradient-dependent estimation error or estimation bias and is of interest here.

The distributions of phase-gradient errors versus truth are most interesting. For the quadratic and low order phase errors these distributions are similar for the 15 dB SCR data and Rural-3 and indicate a non-zero trend. This suggests gradient-dependent estimation bias (refer to the first two plots in the second column of Figure 6-19 and Figure 6-21). Likewise, for these two phase errors, the distributions are similar for the 27 dB SCR data and the Urban-1 data (refer to the first two plots in the second column of Figure 6-20 and Figure 6-22), but no deductions can be made about estimator bias from these data. The distributions for the power law phase error are the same for all four data sets. However, since the 128 pixel-wide support is to the left of the knee of the combined lower bound, these estimation errors may be due to bandlimiting and no conclusions should be drawn.

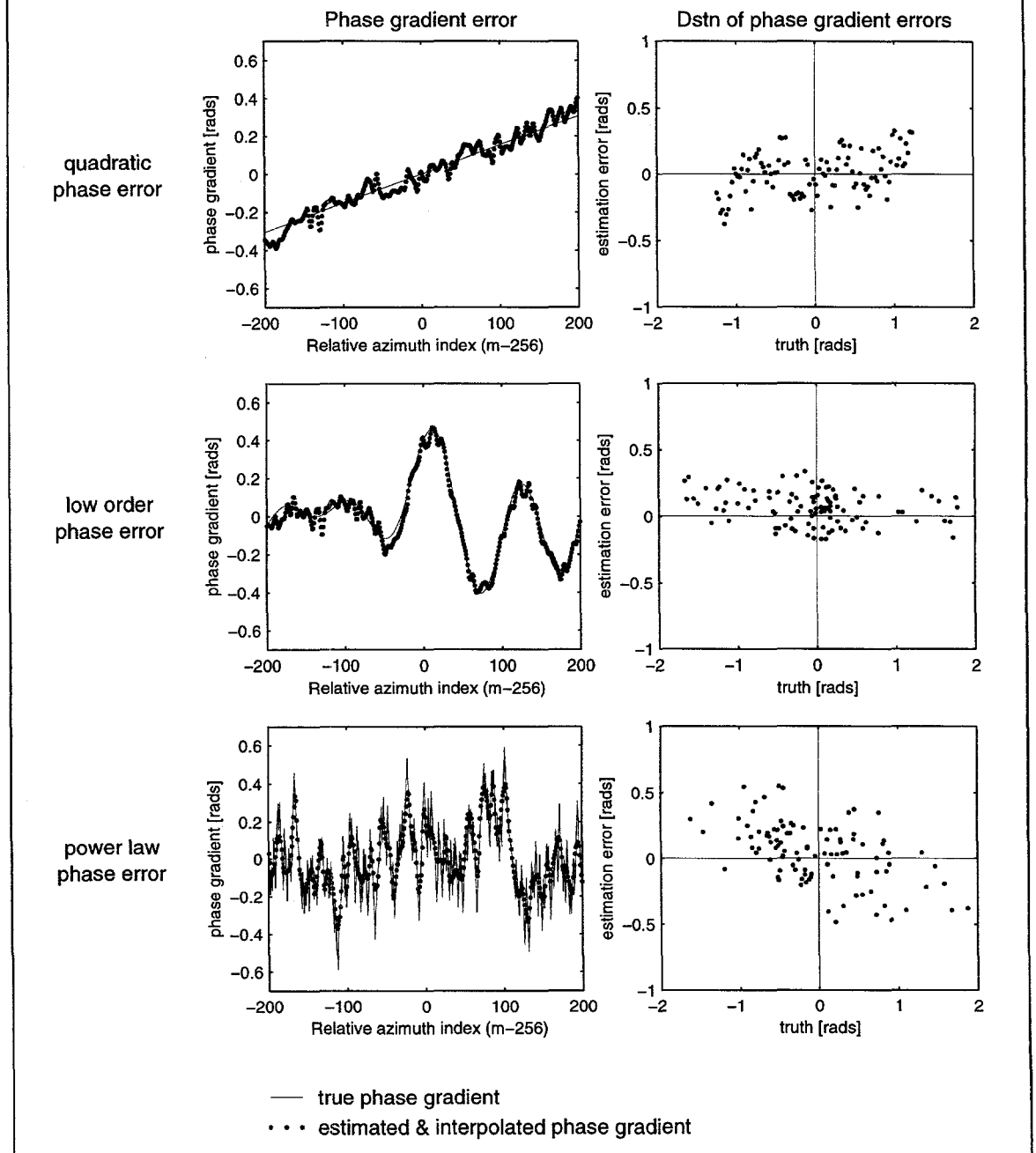

Figure 6-19. Measures of residual phase errors for $N_{support}$ = 128 pixels; synthesized data with SCR = 15 dB; no shift errors.

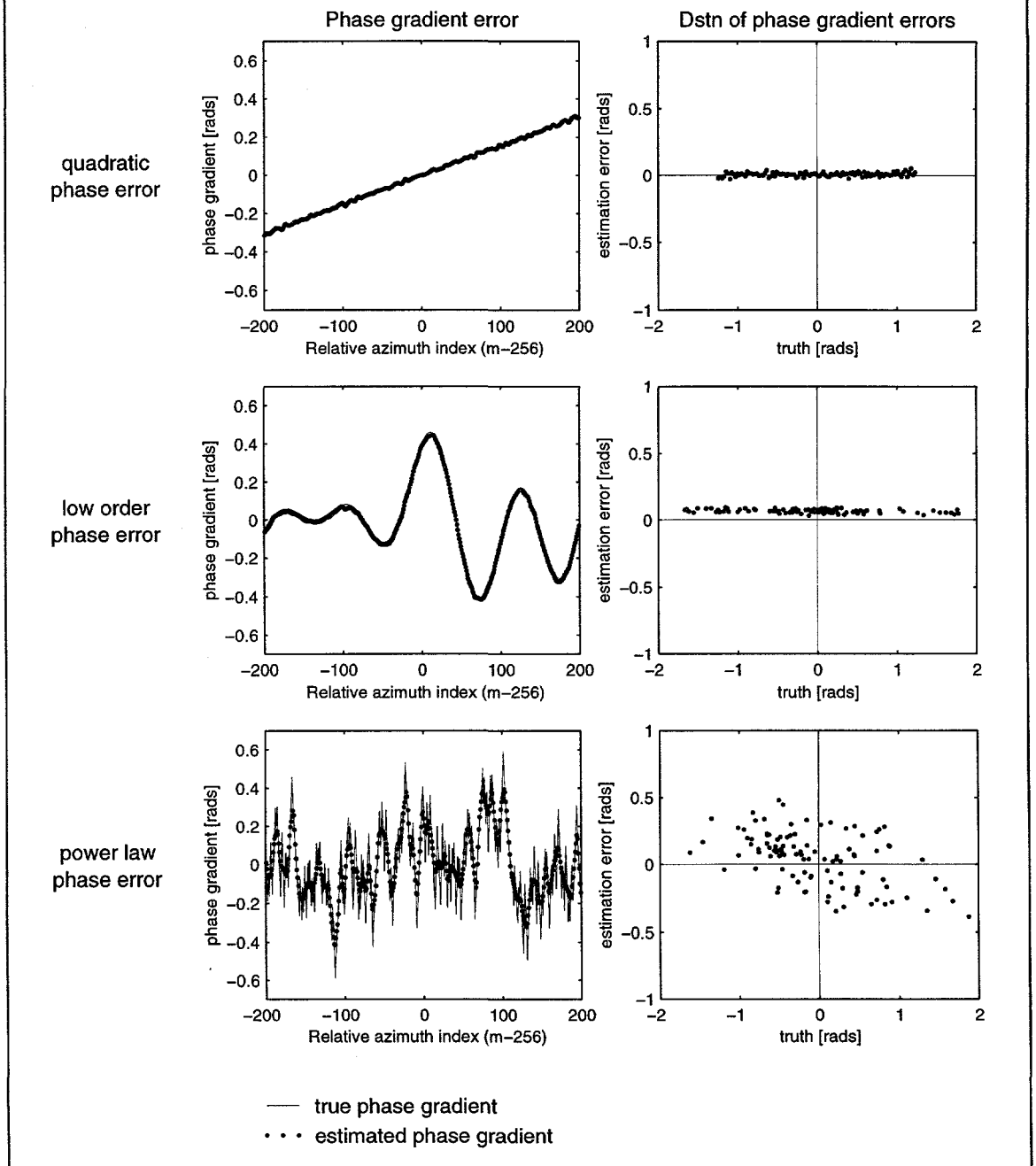

Figure 6-20. Measures of residual phase errors for $N_{support}$ = 128 pixels; synthesized data with SCR = 27 dB; no shift errors.

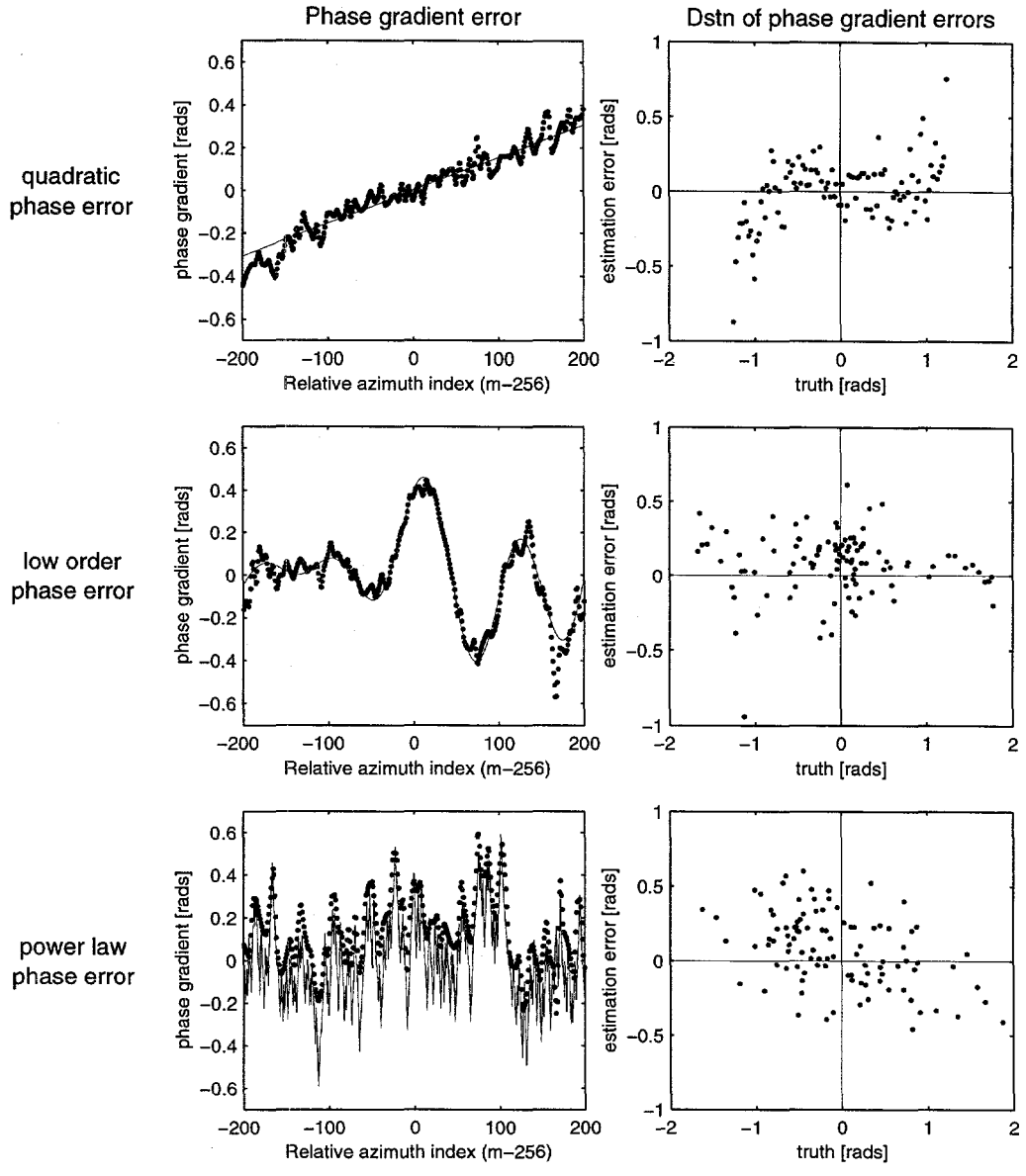

Figure 6-21. Measures of residual phase errors for $N_{support}$ = 128 pixels. Scene = Rural-3 no shift errors.

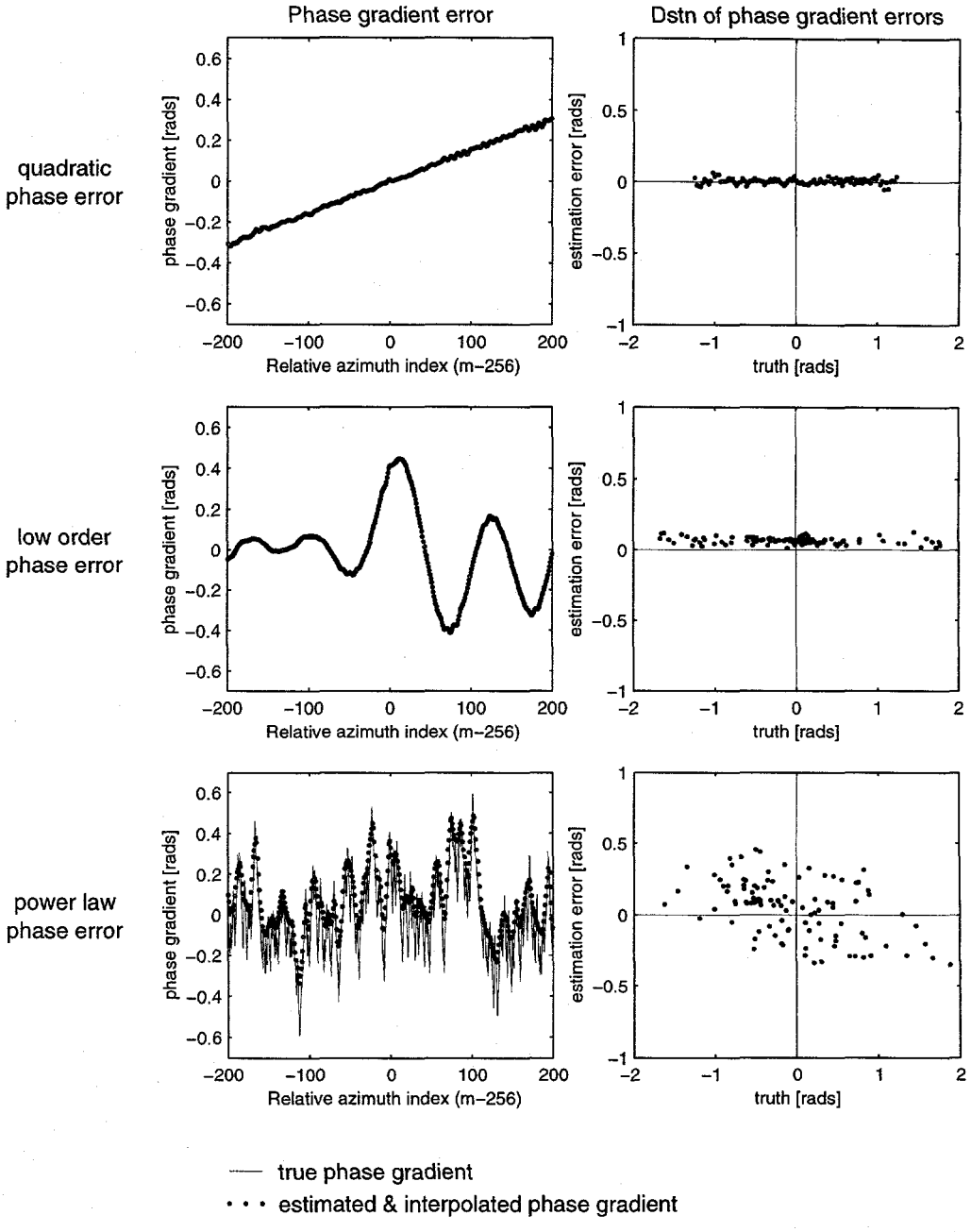

Figure 6-22. Measures of residual phase errors for $N_{support}$ = 128 pixels. Scene = Urban 1 no shift errors.

6.3.3 Summary, Conclusions and Recommendations

We have compared measures of PGA performance for real and synthesized data aberrated by three phase errors. Performance using synthesized data agrees closely with theoretical bounds. Performance using real SAR data does not agree as closely with theoretical bounds. We have considered the data to the left of the knee of the combined lower bound. In this region, for data with uncorrelated noise, performance is determined by support width. We note from Figure 6-3 that correlated noise results in degraded performance. We hypothesize that the noise in real SAR data is correlated.

6.4 Effect of Shift Errors on Estimator Performance

Three approaches were used to examine the effect of shift errors on estimator performance. The first approach was to expand the data model to include shift errors as multiplicative noise, calculate the CRLB and then verify that calculation with simulations in the phase-history domain. The second approach was to process simulated data with three known distributions of shift errors through PGA. The third approach was to process the real SAR data with unknown shift distributions; that is, the loci of the brightest points were determined from the aberrated image. Presentation of results for simulations with synthesized and real SAR data are the same as the presentations for the previous section.

6.4.1 Modeling of Shift Errors

Consider modifying the original data model from equation (3-1) where

$$x_{k,m} = a_k e^{j\phi_m} + n_{k,m}$$

to include shift errors as multiplicative noise. Then

$$x_{k,m} = a_k e^{j\phi_m} e^{j\omega_k m} + n_{k,m} \tag{6-6}$$

where ω_k is the radian frequency associated with the shift error at the k^{th} range,

m is the azimuth index with the time step normalized to unity, and

all other parameters are as defined in Chapter 3.

Using the data model for zero-mean data; that is, equation (5-6), the CRLB for data with shift errors and SNR < 0 dB is

$$\sigma_{\hat{\psi}}^2 \geq \frac{\beta^2\left(1-\zeta^2\right)+1+2\beta}{2N_R\beta^2\zeta^2} \tag{6-7}$$

where $\zeta = E\left\{e^{j\omega_k}\right\}$. $E\left\{e^{j\omega_k}\right\} = E\left\{e^{-j\omega_k}\right\} = E\left\{\cos\omega_k\right\}$ if the probability density of ω_k is symmetric and zero mean. We will assume this to be the case. Details of this derivation are provided in Appendix E. Note that this model is valid only for SNR < 0 dB. The simulation using phase-history data aberrated by the low order phase was used to verify equation (6-7). Recall that for the phase history simulations, the equivalent support of the point spread function was 64 pixels. Three distributions of shift errors were considered, and two scale factors — 0.5 and 1.0 — were used to adjust the amplitude of the low order phase. The shift errors for this experiment were determined using the following distribution attributed to Viterbi (see Appendix E for greater detail):

$$p_\omega(\omega \mid \Lambda) = \frac{\exp(\Lambda\cos\omega)}{2\pi\, I_o(\Lambda)} \tag{6-8}$$

where $I_o(\Lambda)$ is a modified Bessel function of the first kind and Λ controls the spread of the distribution.

The values of Λ, the associated standard deviations (determined numerically) and the width of uniform distributions (relative to 64 pixels) with equivalent variances are given in Table 6-1.

Table 6-1. Parameters of shift error distributions

Λ	Standard Deviation[rads]	Relative width of uniform dstn
20.0	0.2	0.125
6.0	0.4	0.25
1.9	0.9	0.50
0.8	1.4	0.75
0.1	1.8	0.97

Five distributions are shown in Figure 6-23(a). The point spread functions for 0.5 and 1 times the low order phase error are shown in Figure 6-23(b) and (c) relative to the distributions of shift errors. The vertical lines on either side of the point spread functions indicate the width of the 64 pixel-wide support. Simulation outputs are compared to theoretical bounds in Figure 6-24. The heavy, solid line is the CRLB for data without shift errors. In the plots, the distribution of the simulation outputs are shown by box plots. Box plots are a condensed form of data histograms. The line in the middle of the box marks the median of the data. The box itself extends over the two center quartiles of the data. The whiskers extend to the lesser of the outermost data point or to 1.5 times the inter-quartile range. Data outliers are shown as individual points. Simulation output and CRLBs are shown only for the three widest shift error distributions; that is for $\Lambda = 1.9$, 0.8 and 0.1. The worst performance is due, of course, to the widest distribution with

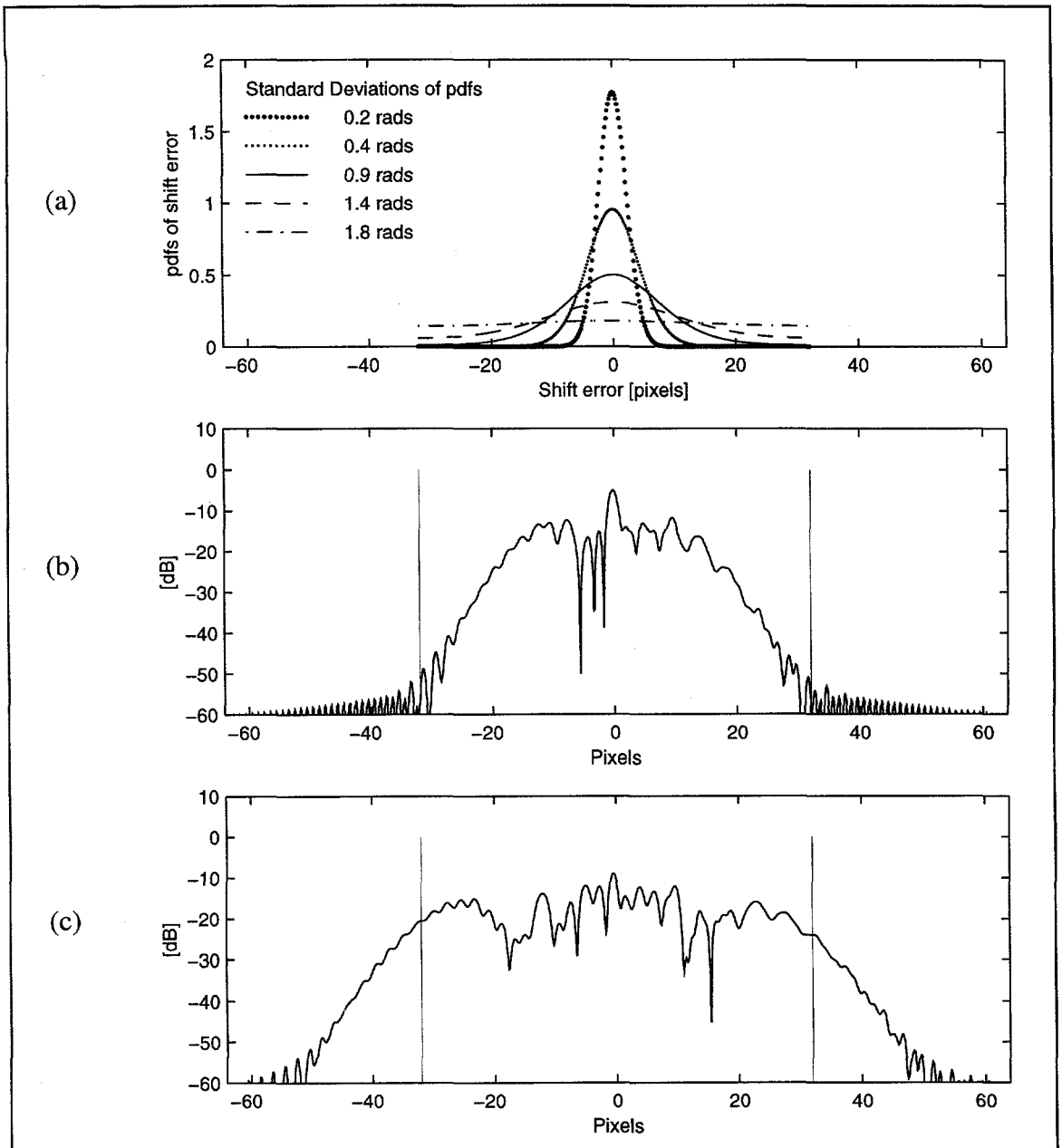

Figure 6-23. Conditions of experiment with phase-history domain data to study the effect of shift errors on ML phase-gradient estimator performance.

(a) Distributions of shift errors used for experiment.
(b) Point spread function due to low order phase error scaled by 0.5 shown relative to distibution of shift error.
(c) Point spread function due to low order phase error scaled by 1.0 shown relative to distibution of shift error.
Vertical lines indicate width of support of point spread function used for this experiment.

(a)

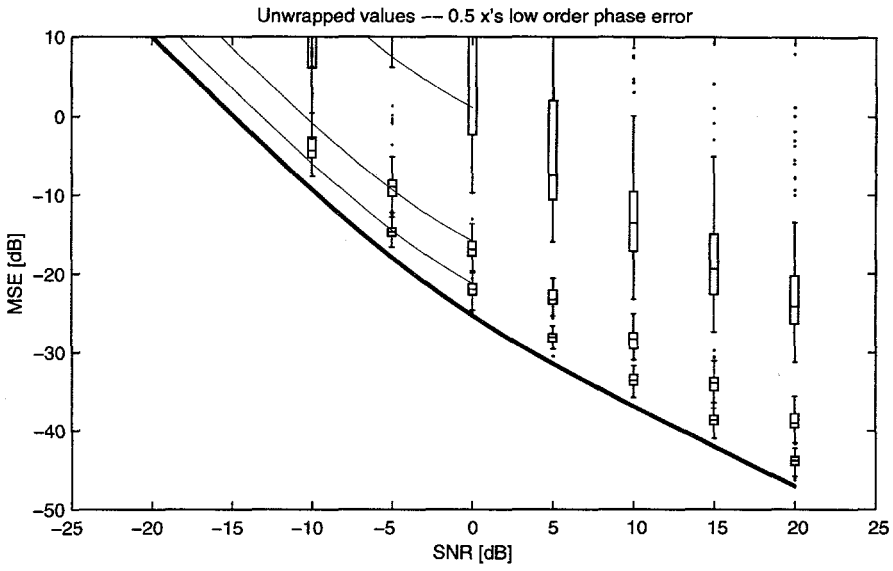

(b)

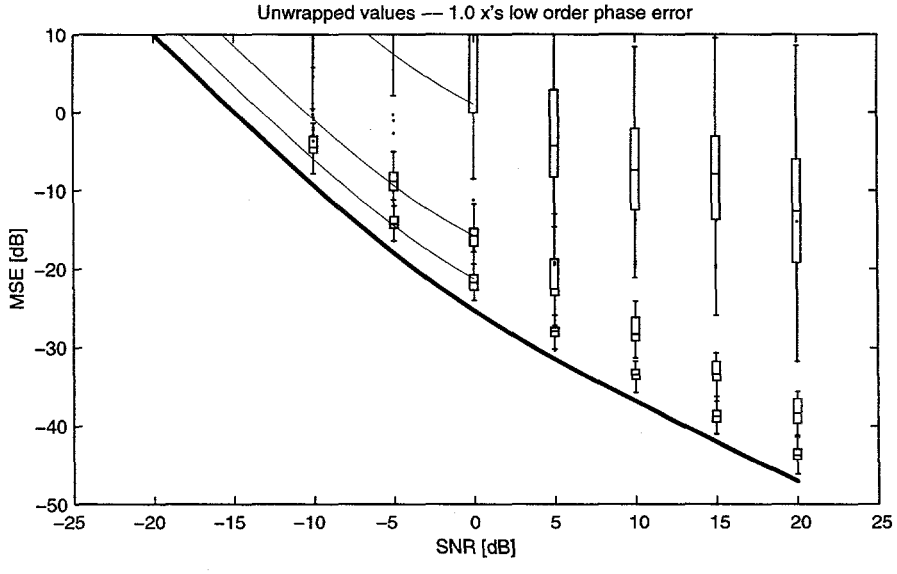

Figure 6-24. Results of experiment with phase-history domain data to study the effect of shift errors on ML phase-gradient estimator performance.

(a) Unwrapped phase-gradient errors for low order phase scaled by 0.5. (b) Unwrapped phase-gradient errors for low order phase scaled by 1.0. The heavy solid line indicates the CRLB without shift errors. Moving upward, light lines indicate CRLBs for σ_{shift} = 0.9, 1.4 and 1.8 rads respectively. Boxes indicate distributions of data from Monte-Carlo simulations.

$\Lambda = 0.1$. Simulations using the two narrowest shift error distributions showed changes of less than 3 dB in MSE and are not shown on the plots in Figure 6-24. For SNR < 0 dB, the simulations agree with the theory. The trends of the MSE for shifted data follow nearly the same shape as the CRLB curve for unshifted data. This suggests that shift errors effectively reduce the SNR. This concept is illustrated by the phasor diagram in Figure 6-25. As illustrated on the left, the signal difference angle is no longer constant with range but varies with ω. As illustrated on the right, in the absence of shift errors, the signal is the coherent sum of vectors, but in the presence of shift errors, the signal is the sum of partially coherent vectors. The shifted component normal to the signal vector contributes to noise.

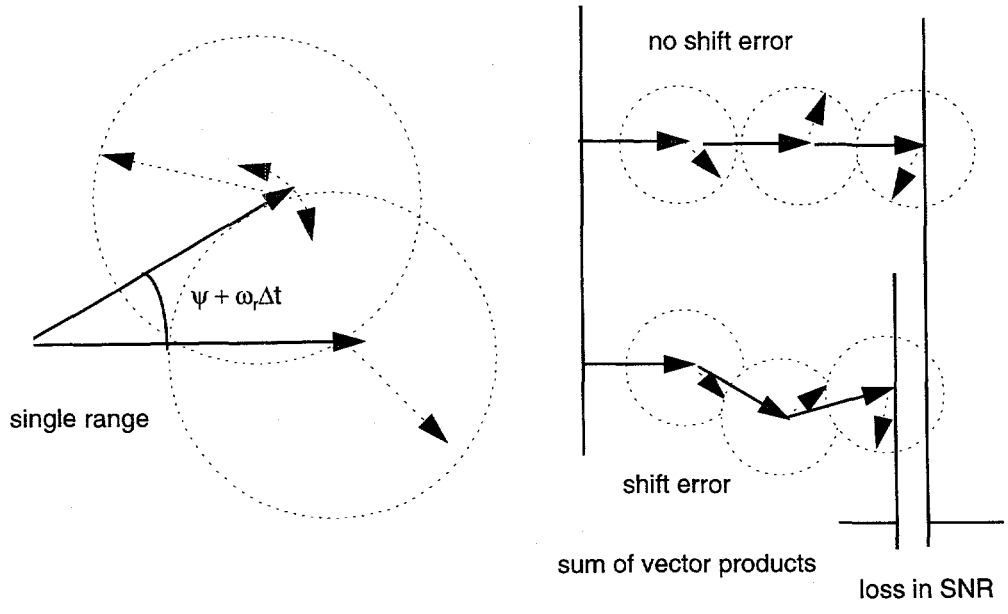

Figure 6-25. Phasor diagram illustrating the loss in SNR due to shift errors.

Solid vectors indicate signal, dotted line vectors indicate noise. The dotted line arc indicates the variation in gradient angle across ranges due to shift errors.

If the model in (6-7) is accurate, then, using the synthesized data with 15 dB SCR (- 3 dB SNR for a 64 pixel-wide support), we would expect shift errors to raise the level of the lower bound to the right of the knee of the combined bound by a constant amount. That is, we believe that performance to the right of the knee is driven by SNR and our theory indicates that shift errors effect a decrease in SNR.

6.4.2 Simulations with Shift Errors

We proceed now to examine the output of our simulations using synthesized data with known distributions of shift errors. We considered a slightly different set of shift distributions. We used the narrowest, the middle and the widest distribution with $\Lambda = 20$, 1.9 and 0.1 respectively. Results are shown in Figure 6-26 through Figure 6-28. (Data for no shift errors were shown in Figure 6-17). The narrow distribution with $\Lambda = 20$ has no noticeable affect on MSE. The two larger distributions do have a noticeable affect. The results, however, conflict with our expectations. We were expecting an increase in MSE to the right of the knee of the combined bound. But we see no significant change here. Instead, we see a definite shift of the bound to the left of the knee. In fact, for the data from the quadratic and low order phases, the knee is shifted to the right by an amount approximated by the width of an equivalent uniform distribution, that is, for $\Lambda =$ 1.9, the equivalent uniform distribution is 0.5×64 pixels or 32 pixels wide. This is indicative of a bandlimiting effect associated with the width of the window, not an increase in signal-to-noise ratio. The model used to derive the CRLB clearly does not represent reality! The data for the power law phase error provides little insight.

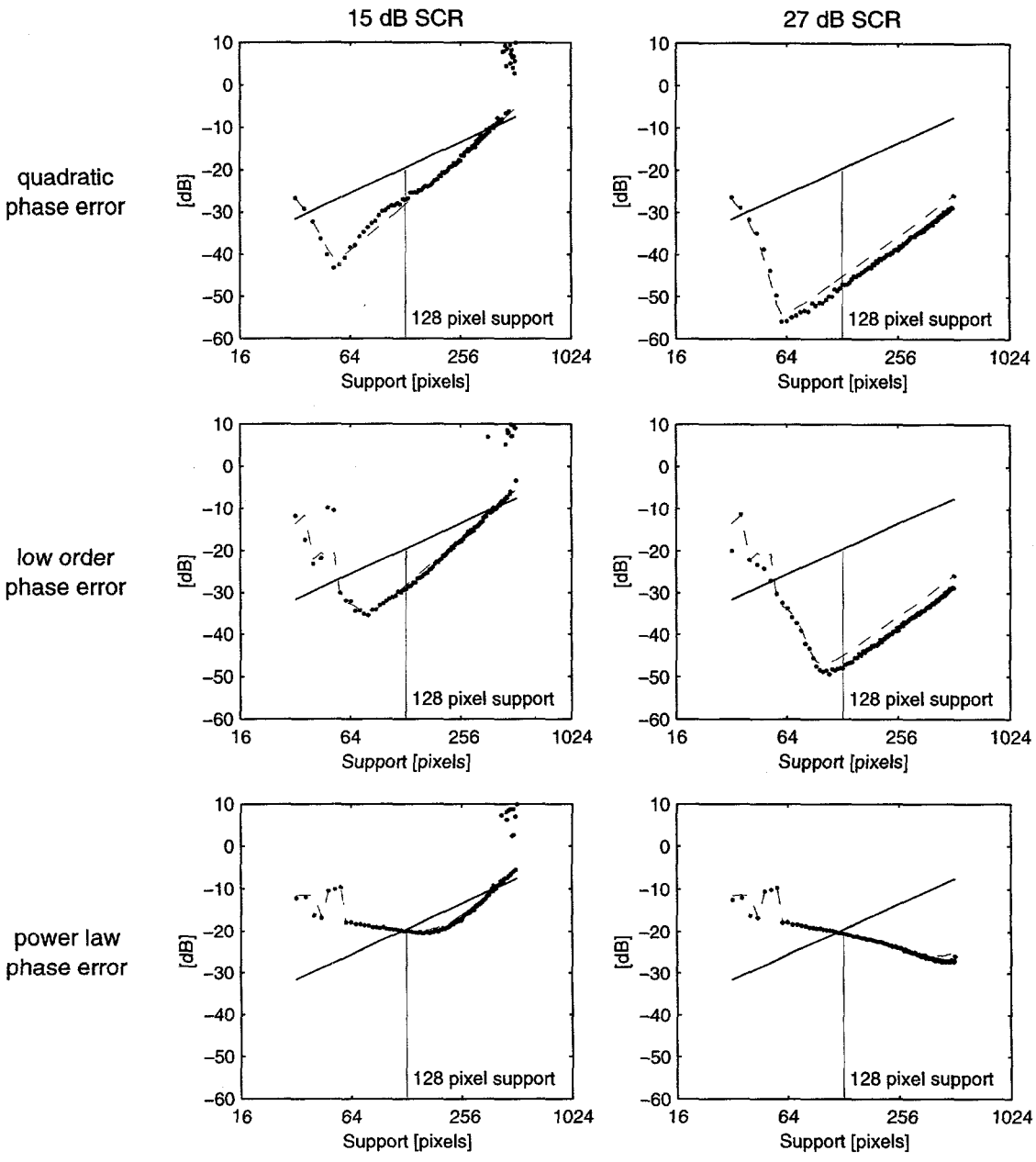

Figure 6-26. MSE for synthesized data with shift errors. $\Lambda = 20.0$

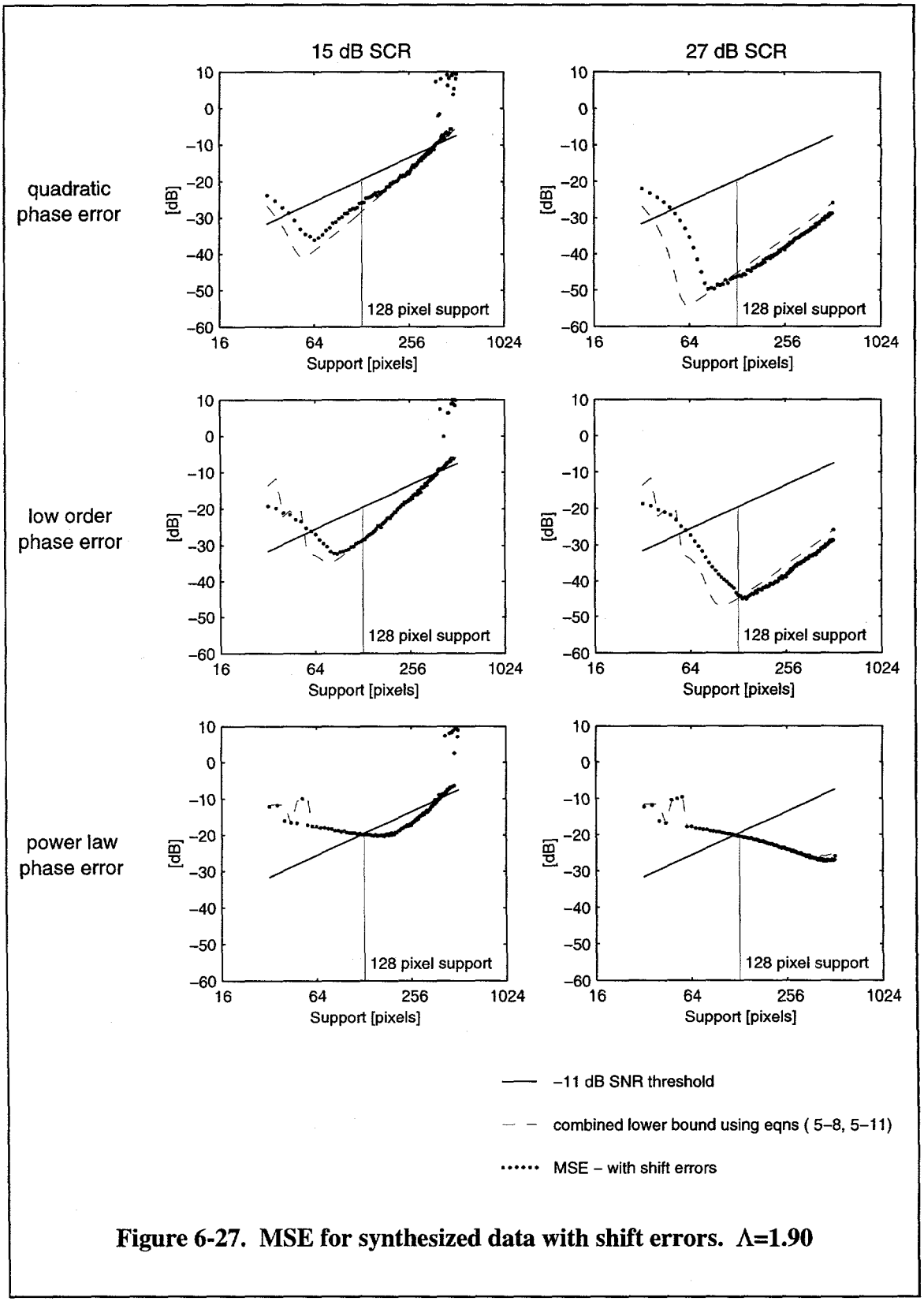

Figure 6-27. MSE for synthesized data with shift errors. Λ=1.90

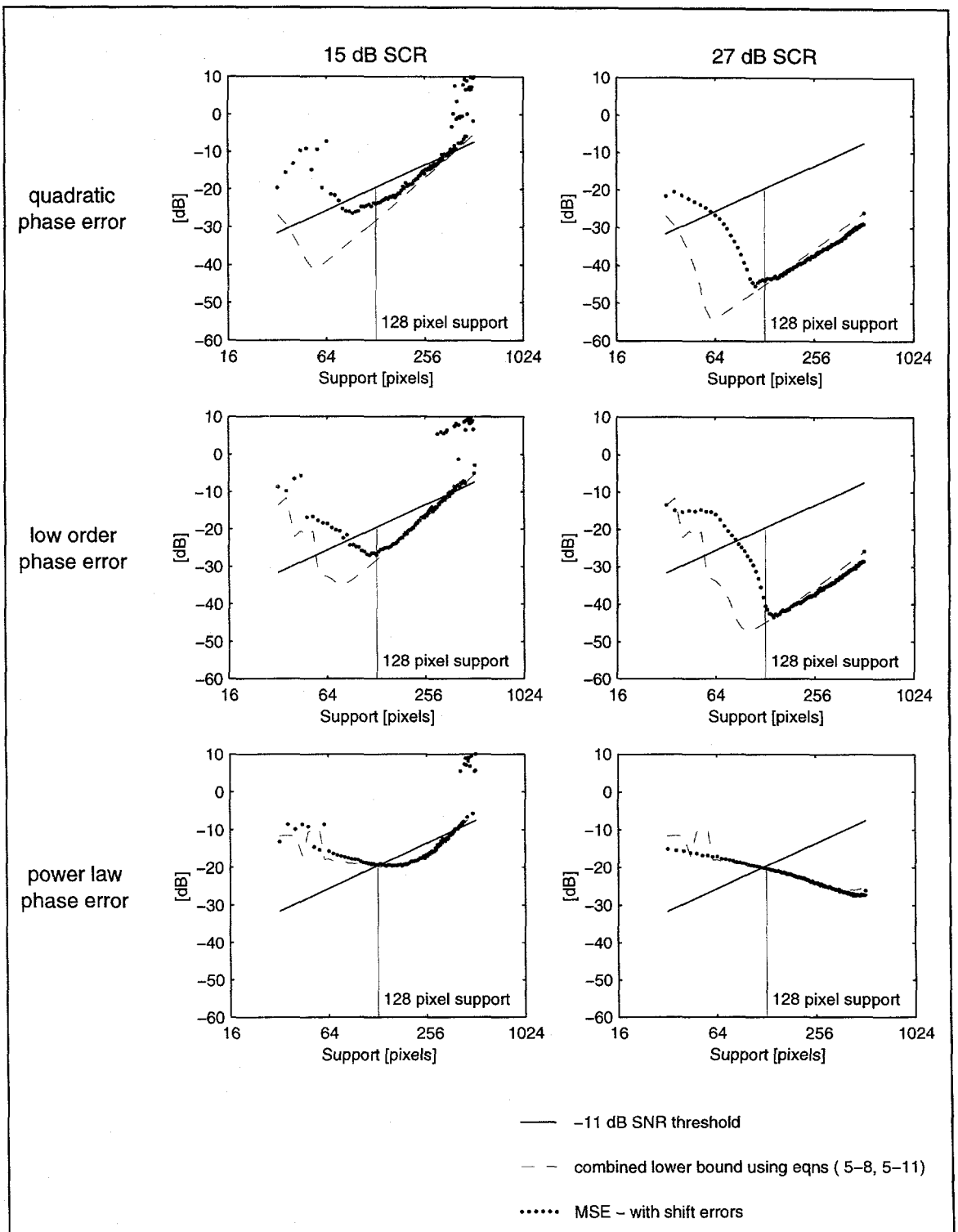

Figure 6-28. MSE for synthesized data with shift errors. Λ=0.10.

For that phase error the shift errors do not extend beyond the region where limited support width dominates estimation error.

Figure 6-29 shows simulation results using the real SAR data. Data with and without shift errors are shown. The trends for the real SAR data with shift errors are the same as for the synthesized data. There is no noticeable effect to the far right where our CRLB tells us to expect an increase in MSE. The knee of the data is shifted to the right.

We will complete the study of the effects of shift errors with an examination of plots comparing truth to estimates and distributions of estimation error relative to truth. These are the same types of data we saw in the previous section where we compared output from unshifted synthesized and real data.

Referring to Figure 6-26 through Figure 6-28 we see that the 128 pixel-wide support is very close to the right of the knee for the synthesized SAR data aberrated by the quadratic and low order phase functions. There is little value in examining further data for that 128 pixel-wide support; we have already seen these data in Figure 6-19 and Figure 6-20. However, for the real SAR data, there is some notable difference in MSE between the unshifted and shifted data, particularly for the Urban-1 scene. Plots of true and estimated gradients and scattergrams of true and error gradients for the shifted real SAR data are shown in Figure 6-30 and Figure 6-31. Shifting errors magnify the trends seen in the scattergrams of gradient errors versus true gradient for the quadratic and low order phase errors.

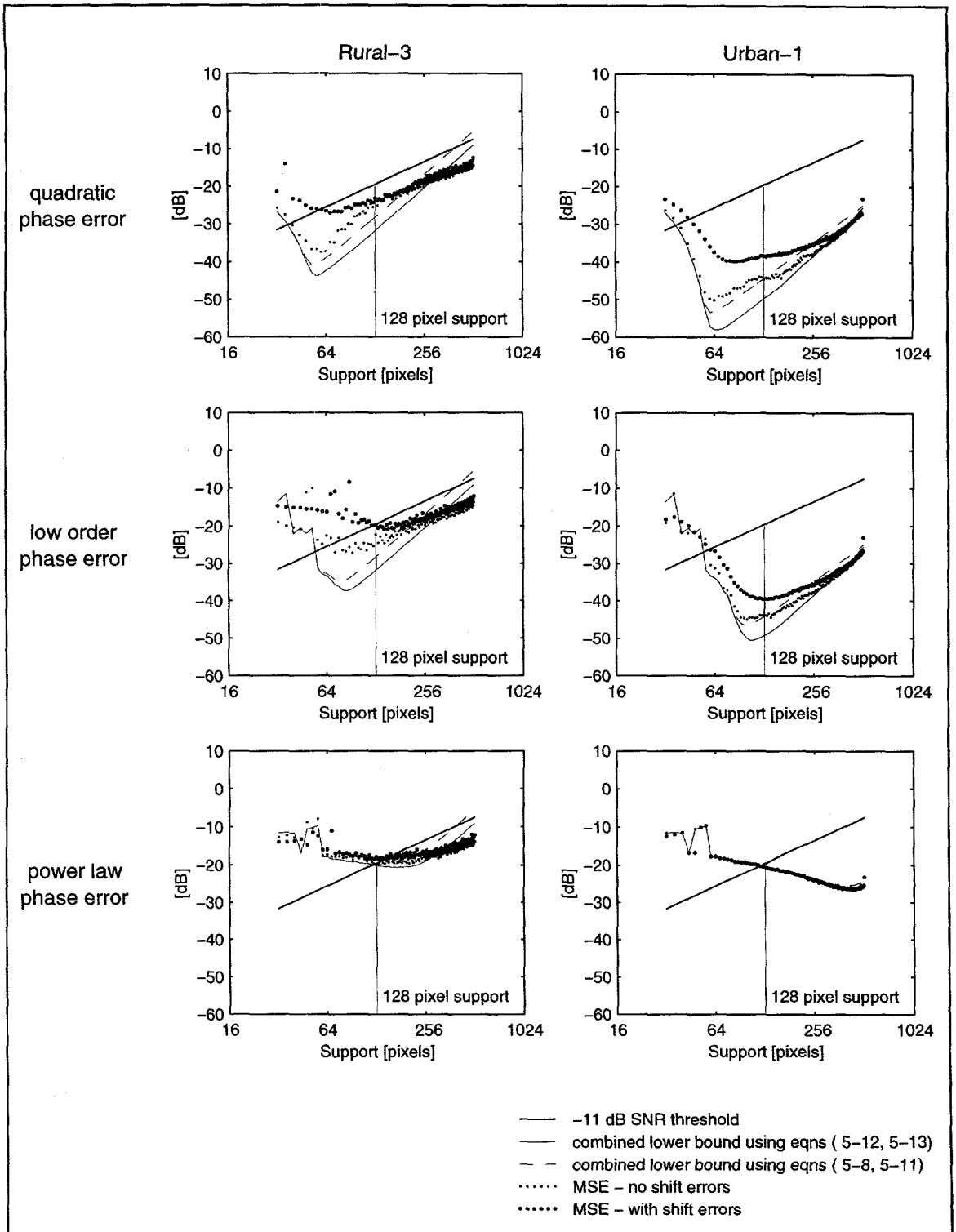

Figure 6-29. MSE for data with shift errors compared to MSE for data without shift errors as shown in Figure 6-18 for scenes Rural-3 and Urban-1 and three aberrating phase errors.

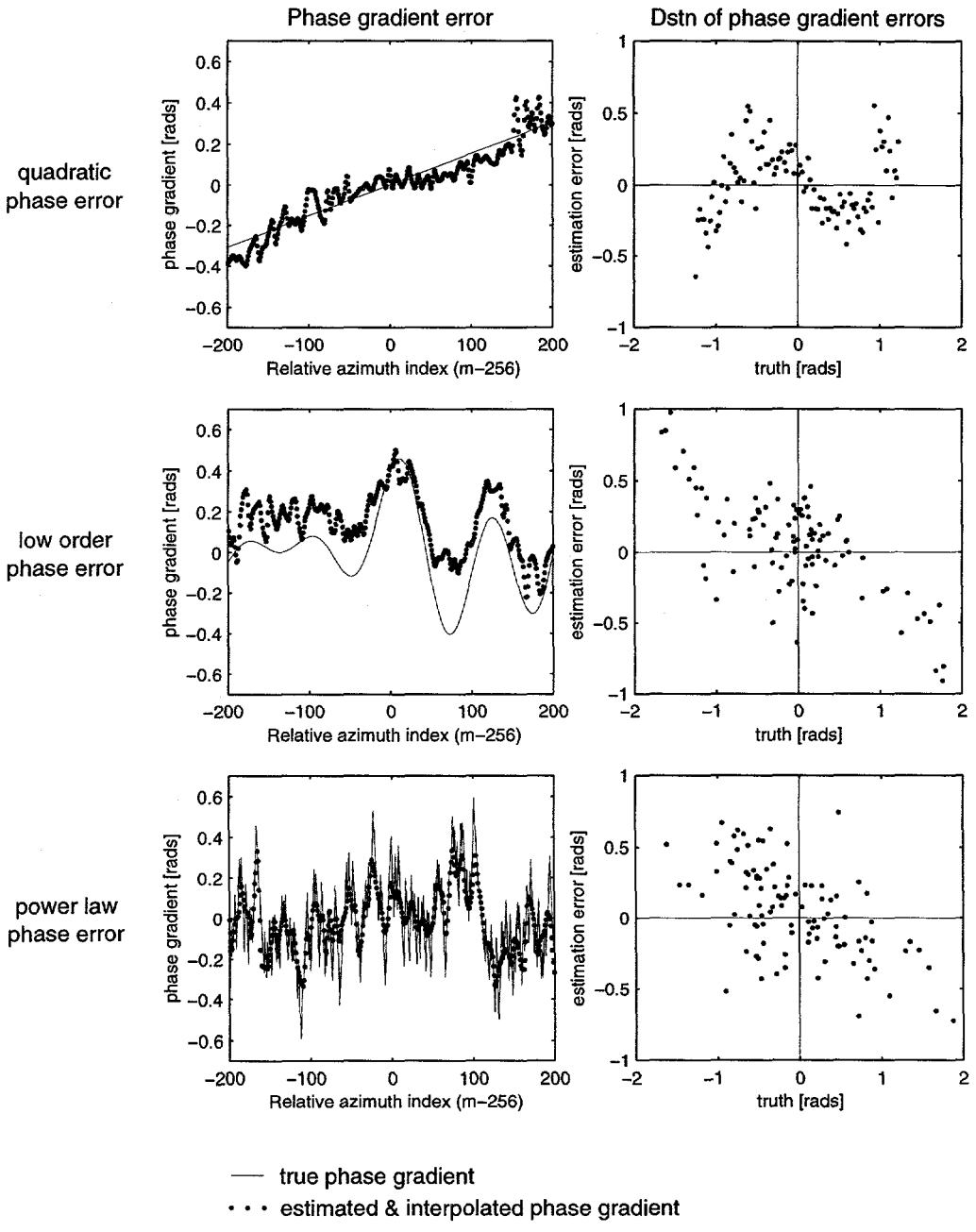

Figure 6-30. Measures of residual phase errors for $N_{support}$ = 128 pixels. Scene = Rural 3 shift errors.

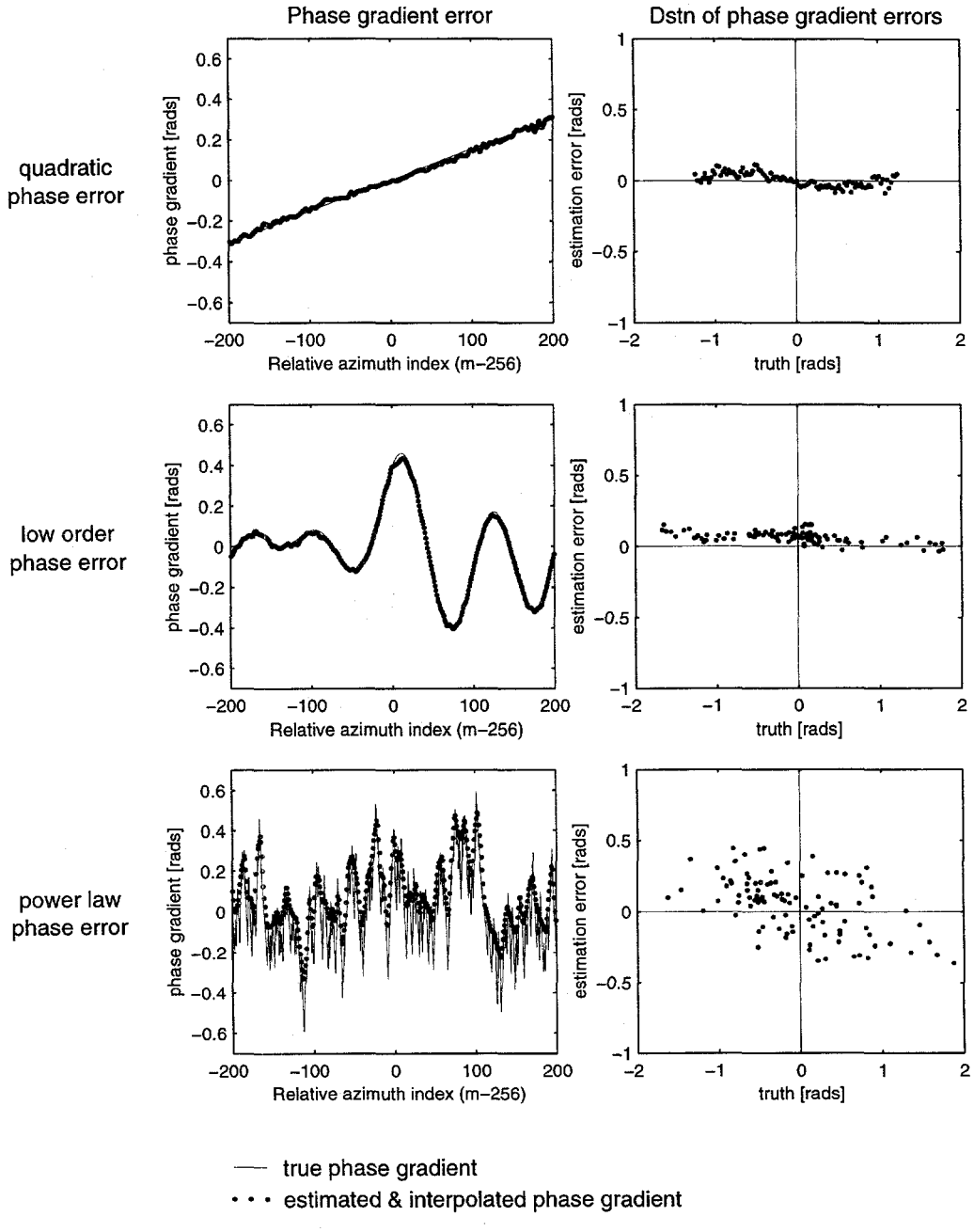

Figure 6-31. Measures of residual phase errors for $N_{support}$ = 128 pixels. Scene = Urban 1 shift errors .

6.4.3 Summary, Conclusions and Recommendations

We have used synthesized SAR data to show that our data model and derived CRLB do not represent the performance of the PGA algorithm for shifted data. To make further progress in this area of mathematically modeling PGA performance, it appears necessary to expand the data model to explicitly include 1) the transfer function of the support of the point spread function, and 2) the amplitude and spatial frequency of clutter. The second recommendation is based both on the analysis of the SAR data in Chapter 4 and the PGA performance analysis in this and the previous section. In Chapter 4 we saw that signal-to-maximum clutter statistics for real SAR data are lower than for synthesized SAR data with the same signal-to-clutter statistics. In this and the previous section we have seen indications that correlated noise may be influencing PGA performance.

We propose the following data model be considered. This model uses spatial frequency, ω, normalized over $\pm\pi$ and SAR pulse repetition period normalized to unity.

$$x_{m,k} = h_m \otimes \left[e^{j\phi_m} \int_{-\pi}^{\pi} a_k(\omega) e^{jm\omega} d\omega \right] \tag{6-9}$$

where h_m is the discrete-time transfer function of the support of the point spread function,

$\otimes$ is used here to denote discrete-time convolution,

ϕ_m is the familiar aberrating phase function at the m^{th} sample, and

$a_k(\omega)$ is the spatially continuous complex envelope of both signal and clutter echoes as a function of spatial frequency.

The modulation of both signal and clutter by the aberrating phase is expressed explicitly in this model. Any inhomogeneous distribution of clutter will likely result in a small but certainly non-zero correlation of clutter noise. Evaluation of the CRLB using this data model may well produce the explanation for observed behavior.

6.5 Definition of the Support for the Point Spread Function

The current practice with the PGA algorithm is to set the width of the support for the point spread function to 1.5 times the -10 dB width of the mainlobe of the non-coherent sum of the circularly shifted data. The -10 dB width is determined by searching inward from the outer edges. This procedure is used only for scenes with high signal-to-clutter ratios such as the two urban scenes used here. For rural scenes with low signal-to-clutter ratios, the contrast between the peak value of the non-coherent sum and the non-coherent sum of clutter is often less than 10 dB. For these cases the current practice is to set the width of the support to the maximum anticipated value based on the conditions of operation. This may be the full width of the detected image. The support is then successively narrowed by 20% with each iteration.

6.5.1 Definition of the New Algorithm

We propose an alternative approach to setting the support threshold using the same non-coherent data sum. Recall that this non-coherent sum is the sum over range dimension k of the magnitude squared of the detected image

$$S_m = \sum_{k=1}^{N_{range}} \left| I_{k,m} \right|^2 . \tag{6-10}$$

This new approach shows considerable promise for establishing appropriate support widths for rural scenes with low signal-to-clutter ratios. The thresholding criterion is set

at the points at which the non-coherent sum first drops below its mean value. The mean value is the arithmetic average of the non-coherent sum; that is,

$$\overline{S} = \frac{1}{N_{az}} \sum_{m=1}^{N_{az}} S_m . \tag{6-11}$$

Because this average is proportional to the total power in the scene, it does not change with phase aberration. However, the distribution of this power across the azimuth dimension of the image does change with phase aberration.

Before beginning a review of the data, we will first discuss general findings using this approach. Results using this thresholding algorithm indicate that, in general, the required support of the point spread function is overestimated for low signal-to-clutter scenes and underestimated for high signal-to-clutter scenes. However, these results do compare favorably to those produced by the current practice. For scenes with low signal-to-clutter ratios, the new algorithm produces meaningful thresholds where the current practice defaults to the full width of the image.

6.5.2 Assessment of Algorithm Performance

Algorithm performance and resultant image quality were assessed using five graphic formats.

1. Plots of the non-coherent sum and the threshold illustrate the algorithm but prove to be a poor format for comparing performance over a variety of conditions.

2. Plots comparing peak-sidelobe ratios (PSLR) outside the support (as a function of support width), image contrast, and the thresholds selected using both the new algorithm and current practice provide a much more condensed presentation of data. These plots provide a visual basis for comparing the thresholds selected using the two algorithms.
3. Final product is illustrated in figures showing the detected image after each iteration.
4. Plots of initial and residual point spread functions and image peak responses complement the image data and provide insights into the properties of the residual phase errors for the selected windows.
5. Plots displaying the menu of metrics defined and illustrated in Section 5.3 of Chapter 5 provide the most condensed display of residual phase error and resultant image quality.

6.5.2.1 Plots of Non-Coherent Sums Illustrating Threshold Selection

The plots in Figure 6-32 through Figure 6-35 illustrate the new thresholding algorithm using the real SAR data from Rural-3 and Urban-1, and the three classes of phase error functions: quadratic, low order and power law. To complete this part of the investigation, each of the three phase error functions were scaled by four scale factors; 0.25, 0.50, 1.0, and 1.5. The non-coherent sums used here were generated from data with shifting errors. The horizontal line indicates the arithmetic mean, $\overline{S}$. The two vertical lines mark the first crossing of the non-coherent sum below $\overline{S}$. Direction of search is outward from the

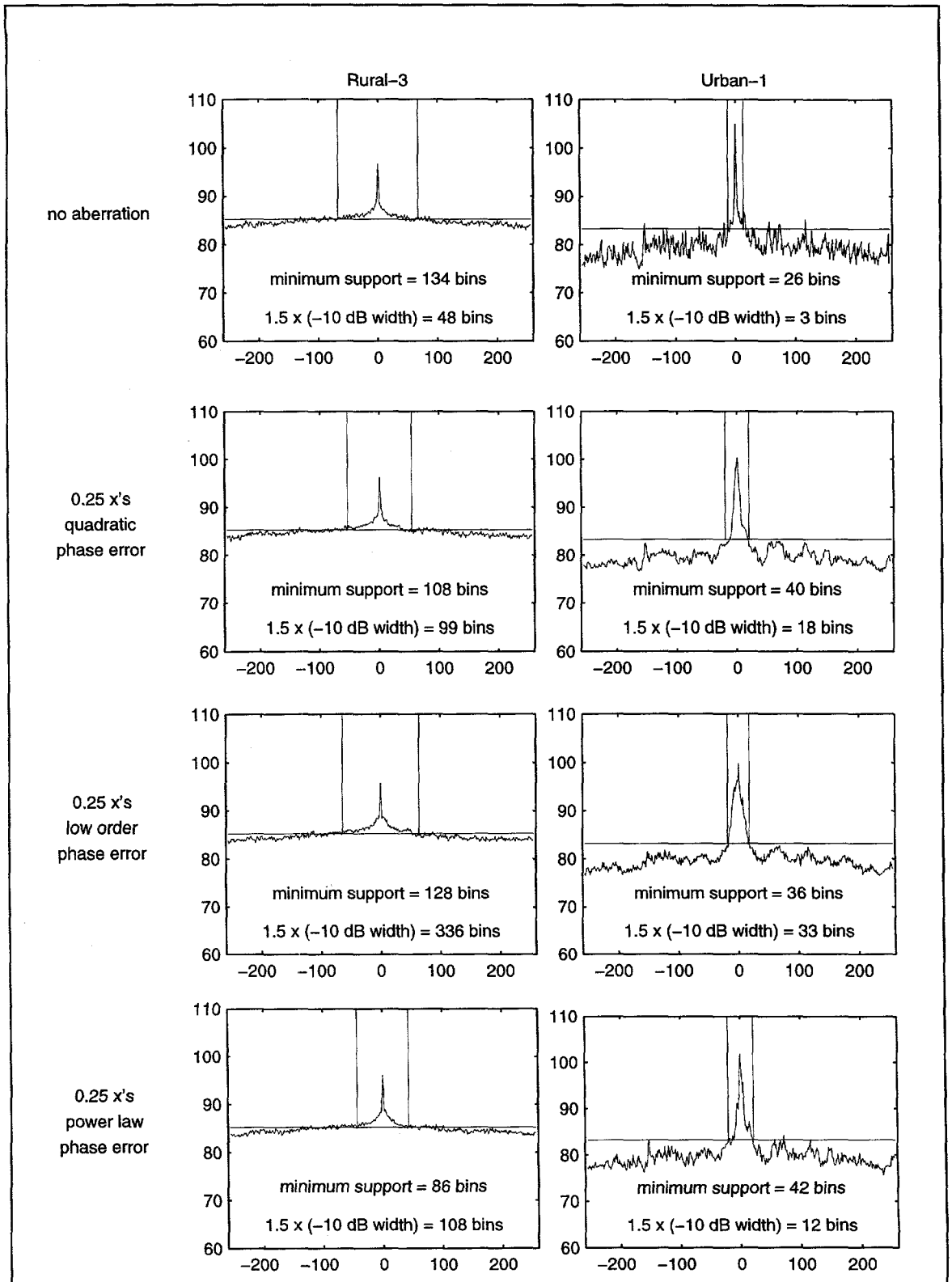

Figure 6-32. Illustration of support threshold algorithm, phases scaled by 0.25.

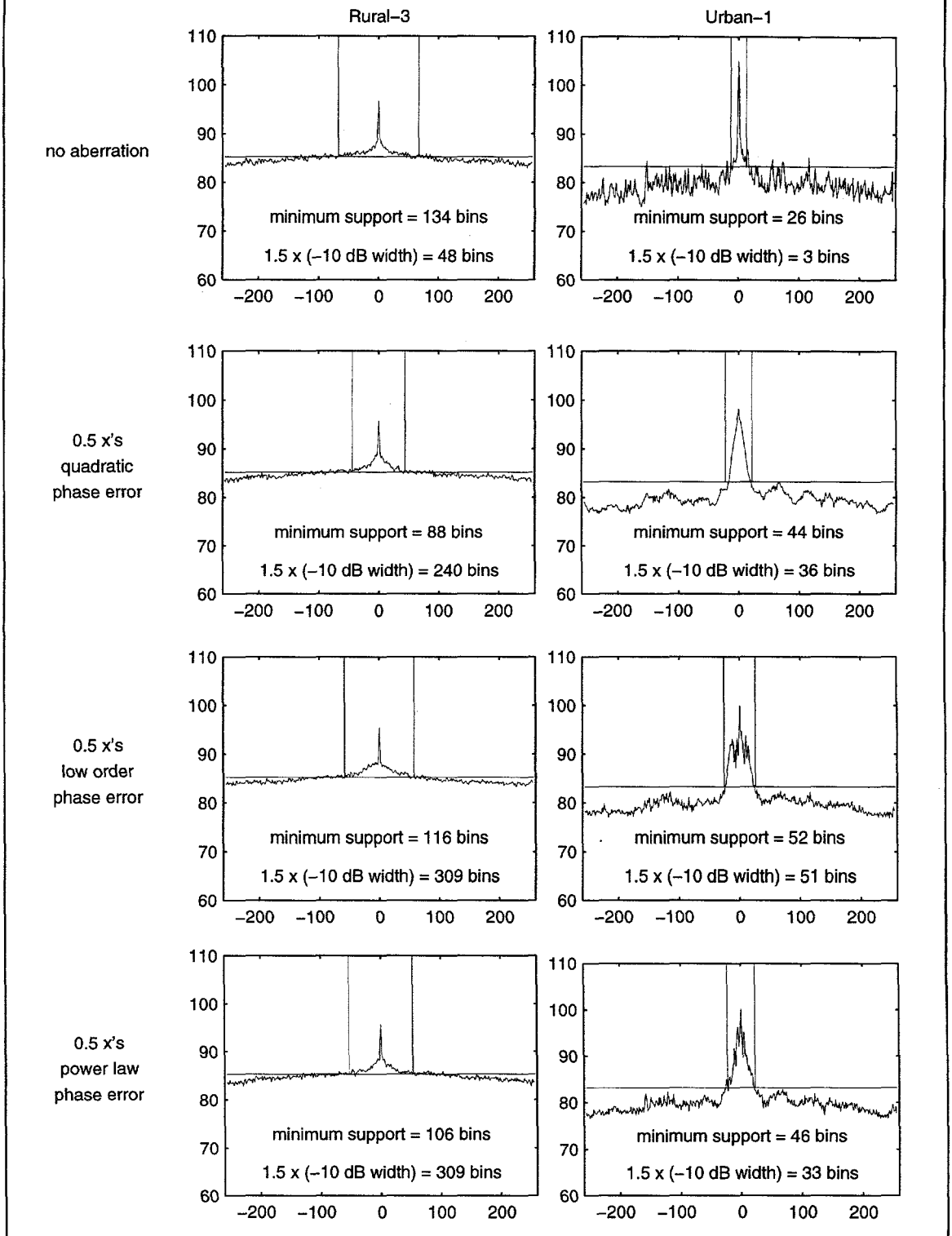

Figure 6-33. Illustration of support threshold algorithm, phases scaled by 0.50.

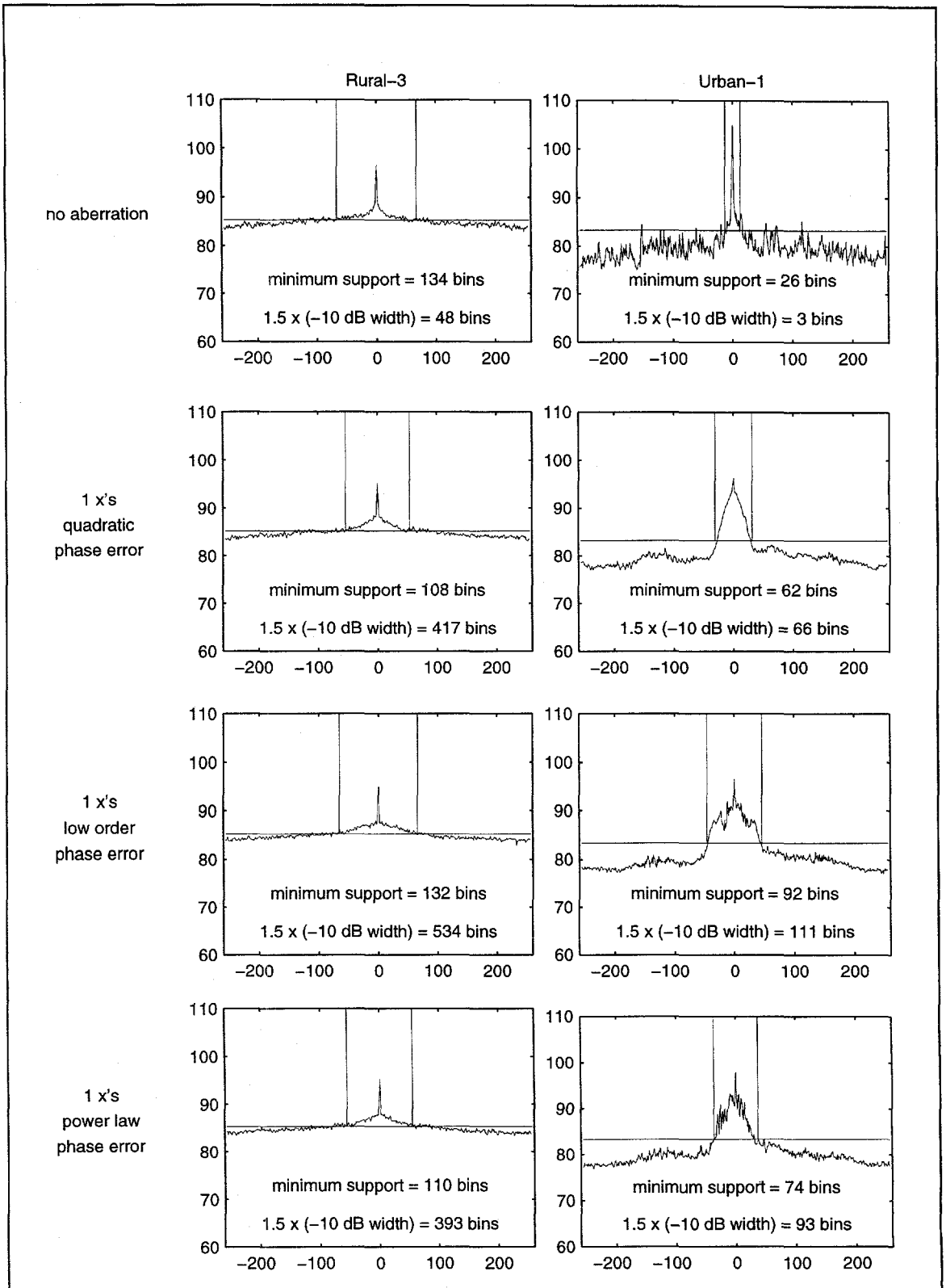

Figure 6-34. Illustration of support threshold algorithm, phases scaled by 1.00.

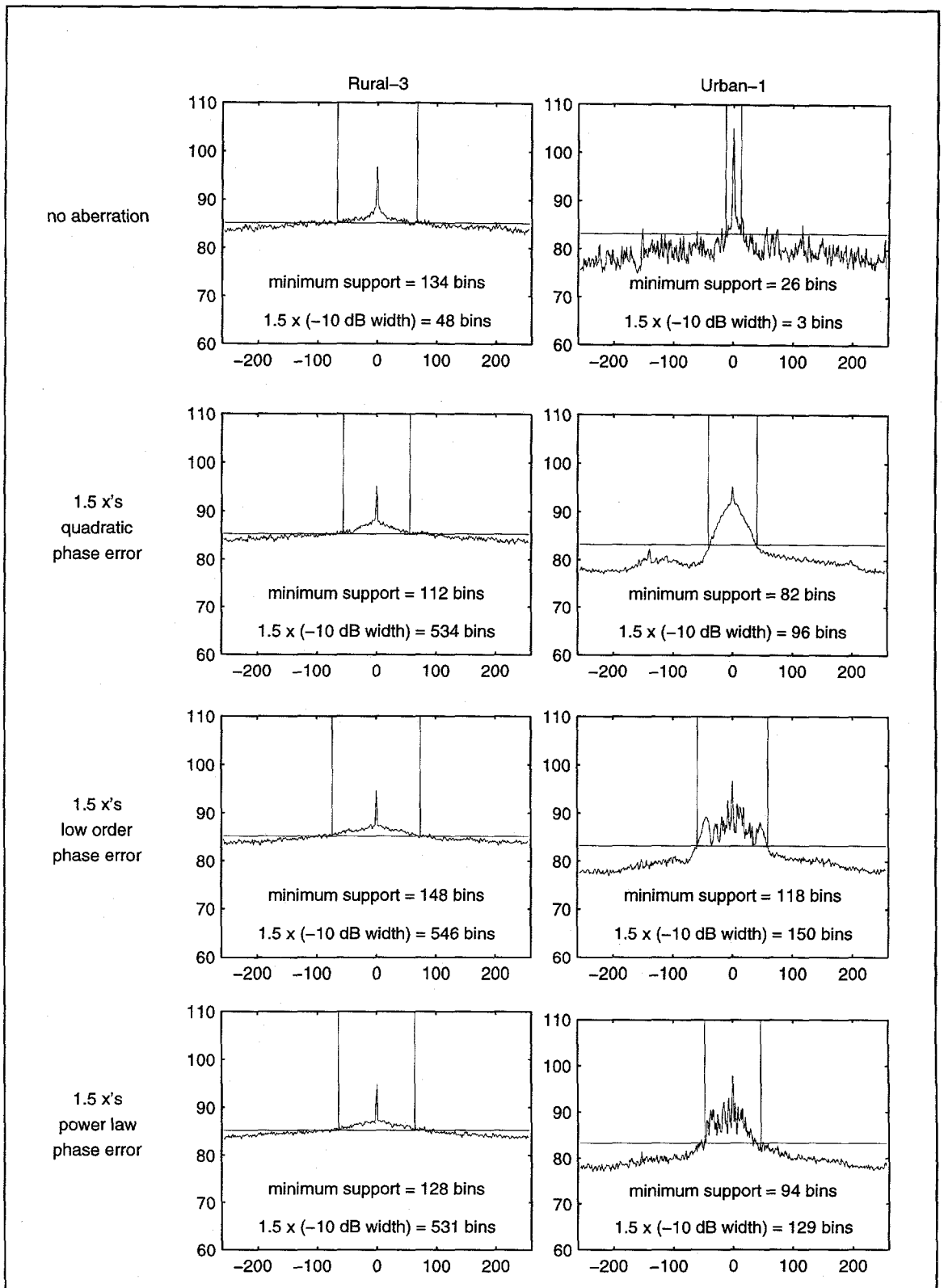

Figure 6-35. Illustration of support threshold algorithm, phases scaled by 1.50.

maximum value at the center. The value for minimum support is the greater of two times the distance (*m* pixels) from center to first crossing. This value is tabulated in the lower portion of each plot. It is called, "minimum support" because support scale factors will be considered later. Below that is 1.5 times the detected -10 dB width, the current practice. The four figures show data for no aberration and aberration by each of the phase quadratic, low order and power law. While these four figures illustrate the process, they do not provide a convenient basis for comparison.

6.5.2.2 Thresholds Compared to Residual Peak Sidelobes and Image Contrast

The data shown in the four pages of plots just discussed are condensed into four plots, one plot for each phase scale factor. These four plots of condensed data are shown in Figure 6-36 and Figure 6-37. These are complicated but very informative plots. The horizontal axis is the width of the support in pixels. The scale is log base 2. The y axis is peak sidelobe level in dB normalized to an ideal point spread function with mainlobe peak of 0 dB. The three downward sloping curves are the peak sidelobe levels of the point spread functions *outside the support of the point spread function* due to the three aberrating phase errors: quadratic, low order and power law. The horizontal lines mark the maximum values of the ratio of mean clutter signal for the Rural-3 and Urban-1 scenes. The ratio of mean clutter to signal is a measure of image contrast. The black dots mark the support width thresholds along the horizontal axis selected by the new algorithm. Phase identifiers associated with the black dots are in upper case alpha

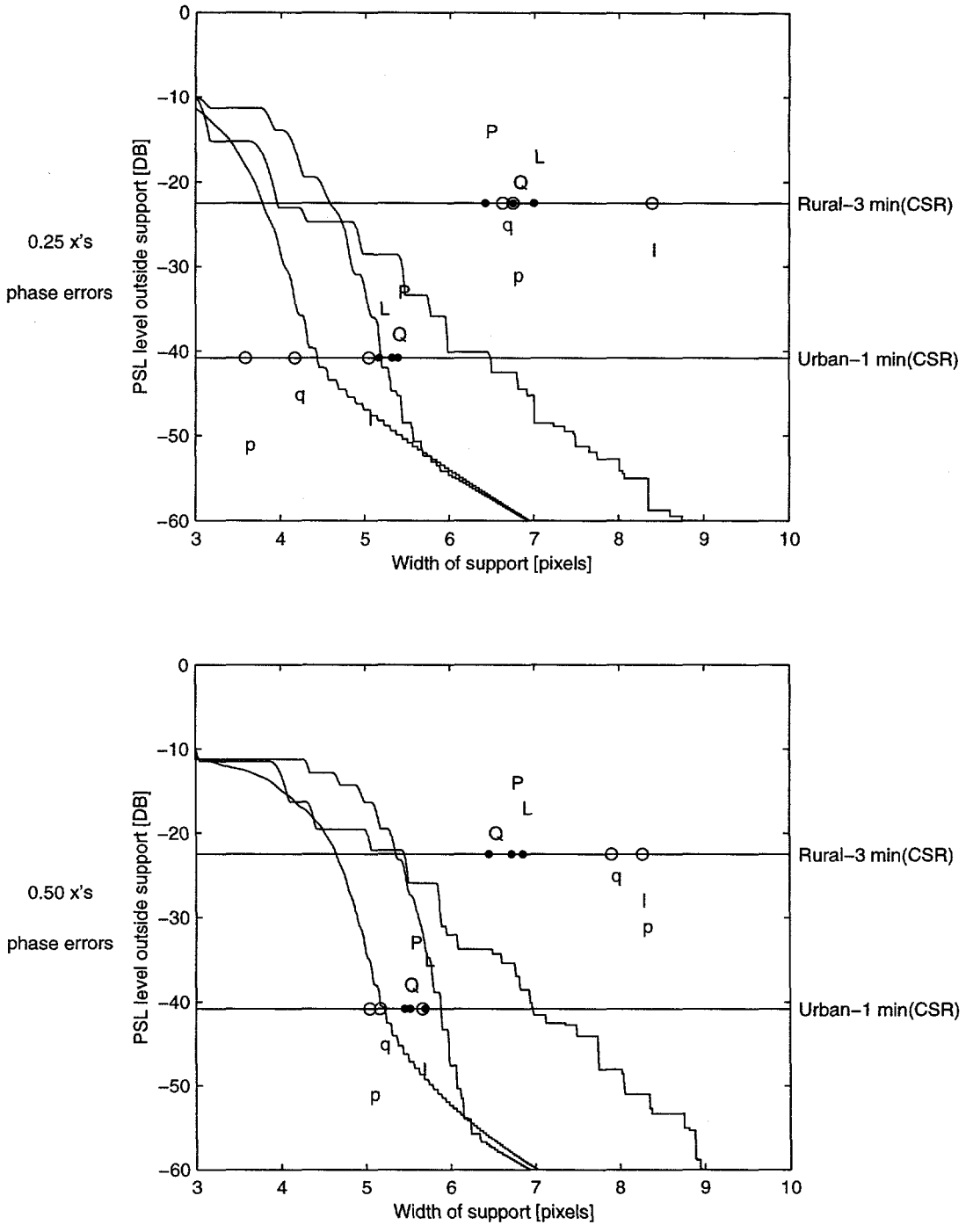

Figure 6-36. Selected threshold relative to maximum SCR in the scene and maximum sidelobe of point spread function outside threshold.

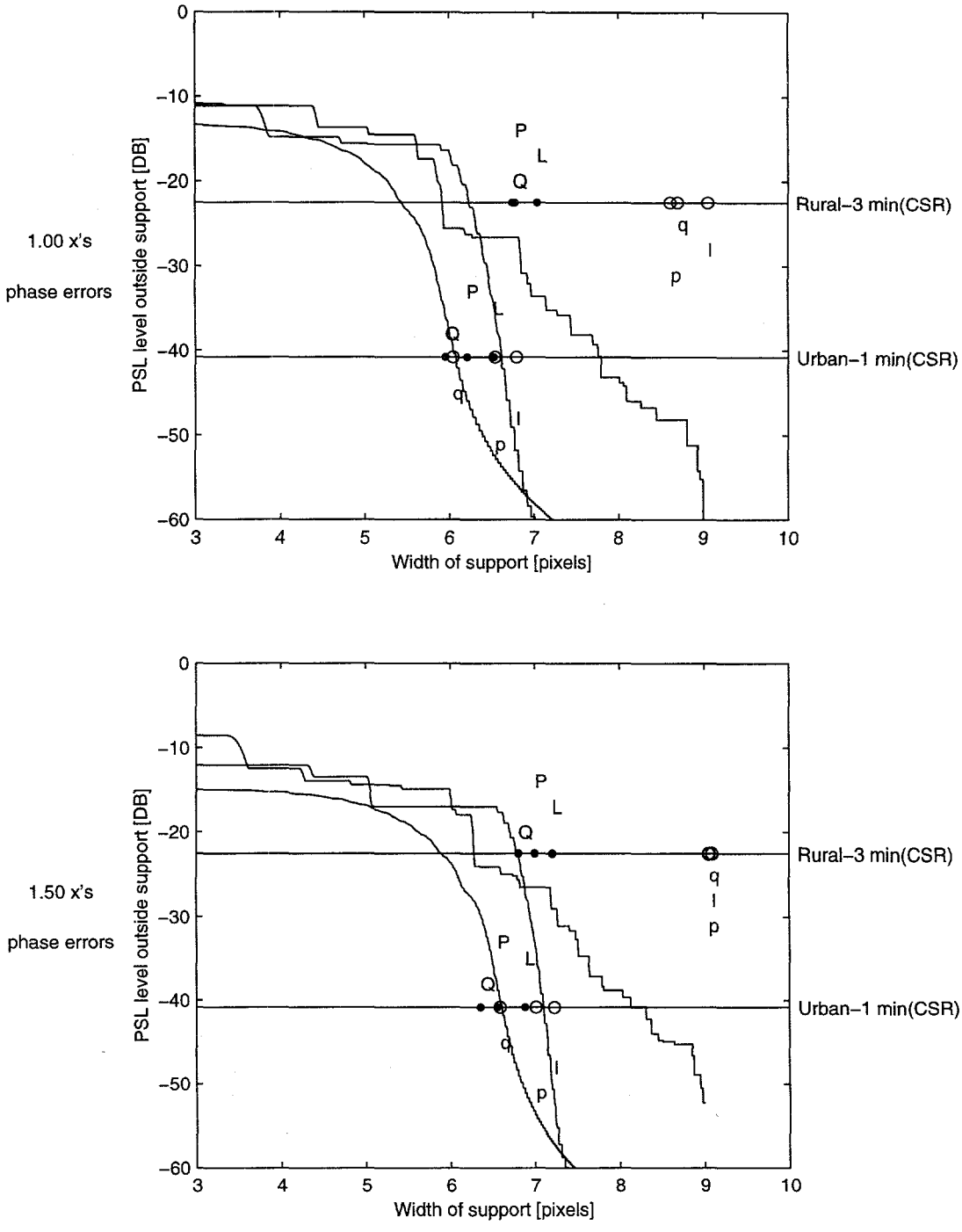

Figure 6-37. Selected threshold relative to maximum SCR in the scene and maximum sidelobe of point spread function outside threshold.

characters: "Q" for quadratic, "L" for low pass and "P" for power law and appear above the horizontal lines. The vertical offset of these alpha identifiers was arbitrarily set to make them readable. The open circles indicate the thresholds selected by current practice. Associated phase identifiers are in lower case below the horizontal lines: "q" for quadratic, "l" for low pass and "p" for power law. In order to capture all the phase sidelobes greater than the maximum CSR, the threshold needs to be to the right of the intersection of the horizontal maximum CSR line and the peak sidelobe curve for the phase of interest. If the threshold is too far to the right of this intersection, then more clutter than necessary is captured by the support window. More clutter means more noise into the ML estimator.

Let's consider some of the data shown in the two plots in Figure 6-36. In the upper plot, for phases scaled by 0.25, current practice, indicated by open circles, consistently underestimates required support for all these phase errors aberrating Urban-1. Current practice consistently overestimates required support for all three phase errors aberrating Rural-3. In contrast, the minimum thresholds for the new algorithm are more closely grouped. For the Urban-1 data the order is L, Q, P. The minimum thresholds for the low order phase is right at the intersection of maximum scene contrast and peak sidelobe outside the support. The quadratic phase threshold is overestimated and the power law phase is underestimated.

6.5.2.3 Aberrated and Detected Images

Examples of the focused and defocused images and detected images after one, two and three iterations using the new threshold algorithm are included. The selected data are Rural-3 aberrated by the low order phase and Urban-1 aberrated by the power law phase. The initial and defocused images and image peak responses are shown in Figure 6-38. The detected image after one, two and three iterations using the proposed thresholding algorithm are shown in Figure 6-39.

6.5.2.4 Initial and Residual Point Spread Function and Image Peak Responses

In Figure 6-40 and Figure 6-41 we see the associated point spread functions and peak image responses for the three iterations of PGA on Rural-3 and Urban-1 respectively. The threshold widths are noted in these figures. The Rural-3 thresholds were the minimum thresholds. The Urban-1 thresholds were twice the minimum thresholds. These selections represent the *worst* cases selected from the three dimensional array of options: five real SAR scenes, three aberrating phases (at full scale) and three threshold scale factors (1.0, 1.4 and 2.0). The threshold does not narrow significantly after the second iteration for the rural scenes with low signal-to-clutter ratios. This results in wider than desired mainlobe widths. The threshold is too narrow on the first iteration for urban scenes with high signal-to-noise ratios. This results in a well defined mainlobe but high sidelobes that produce an image with sidelobe streaking, which are noticeable in the areas of the scene with high contrast.

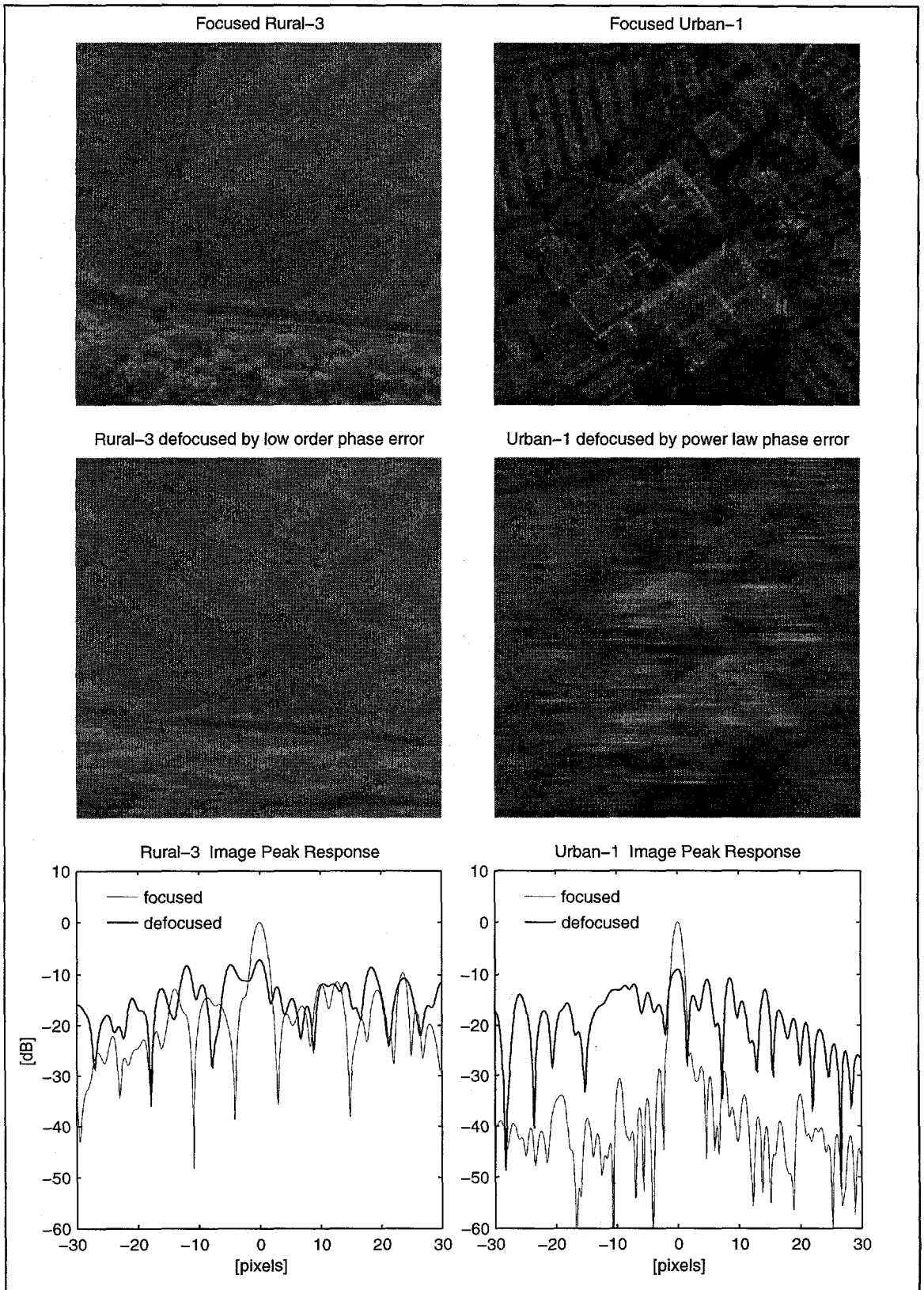

Figure 6-38. Focused and defocused images and image peak responses.

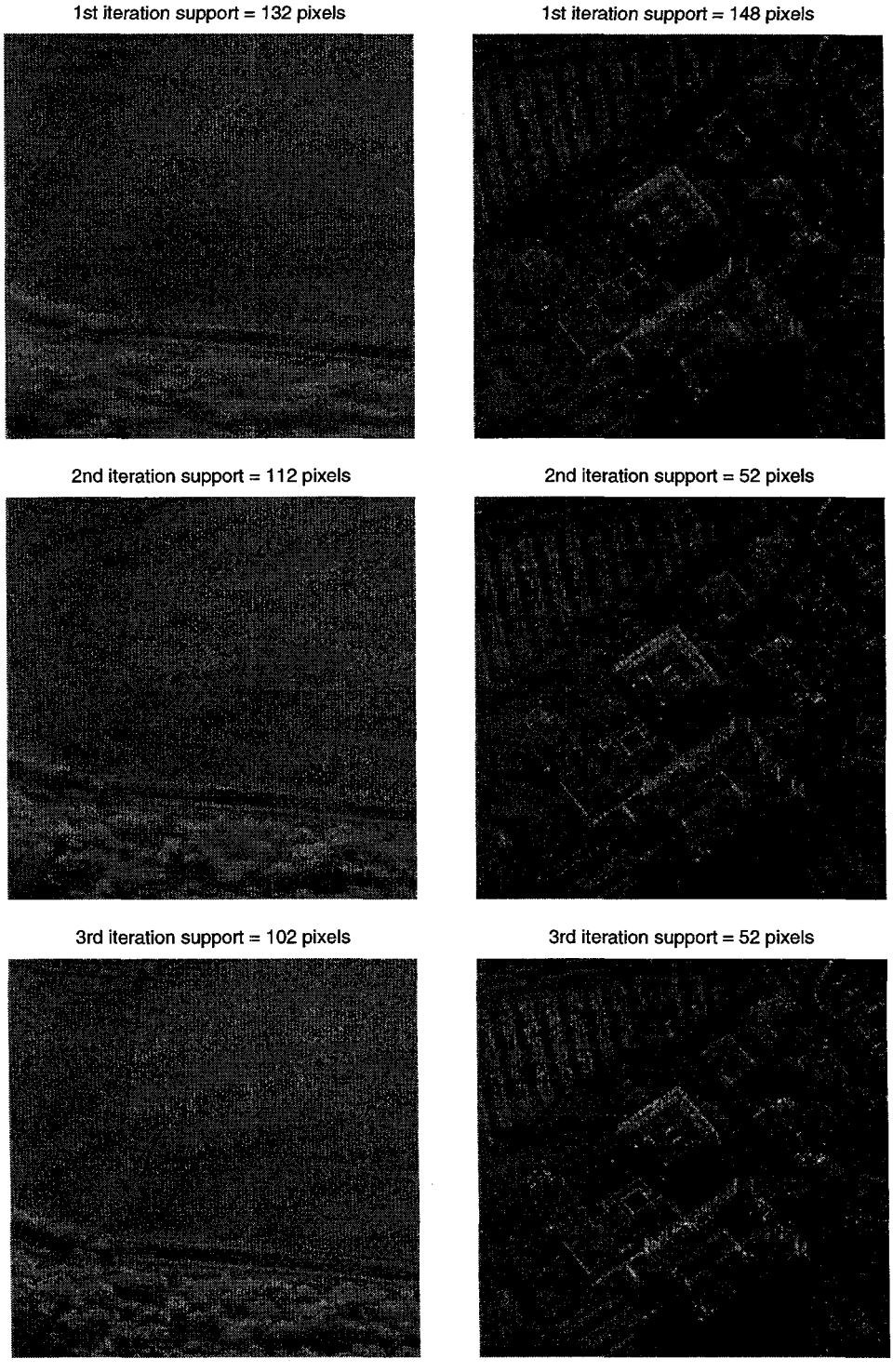

Figure 6-39. Detected images for 3 iterations of PGA using the new thresholding algorithm without scaling.

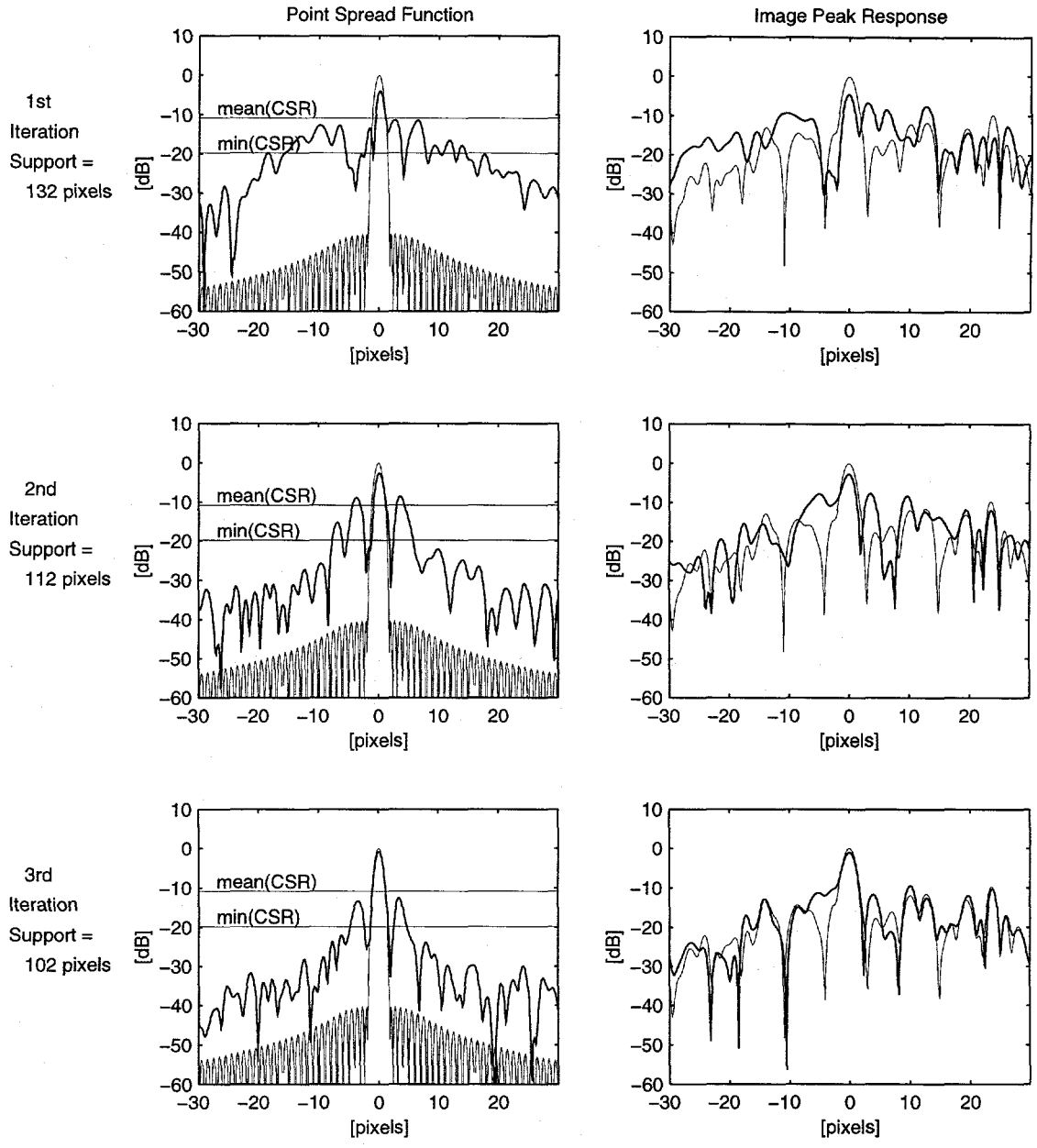

Figure 6-40. Point spread functions and image peak responses for Rural-3.

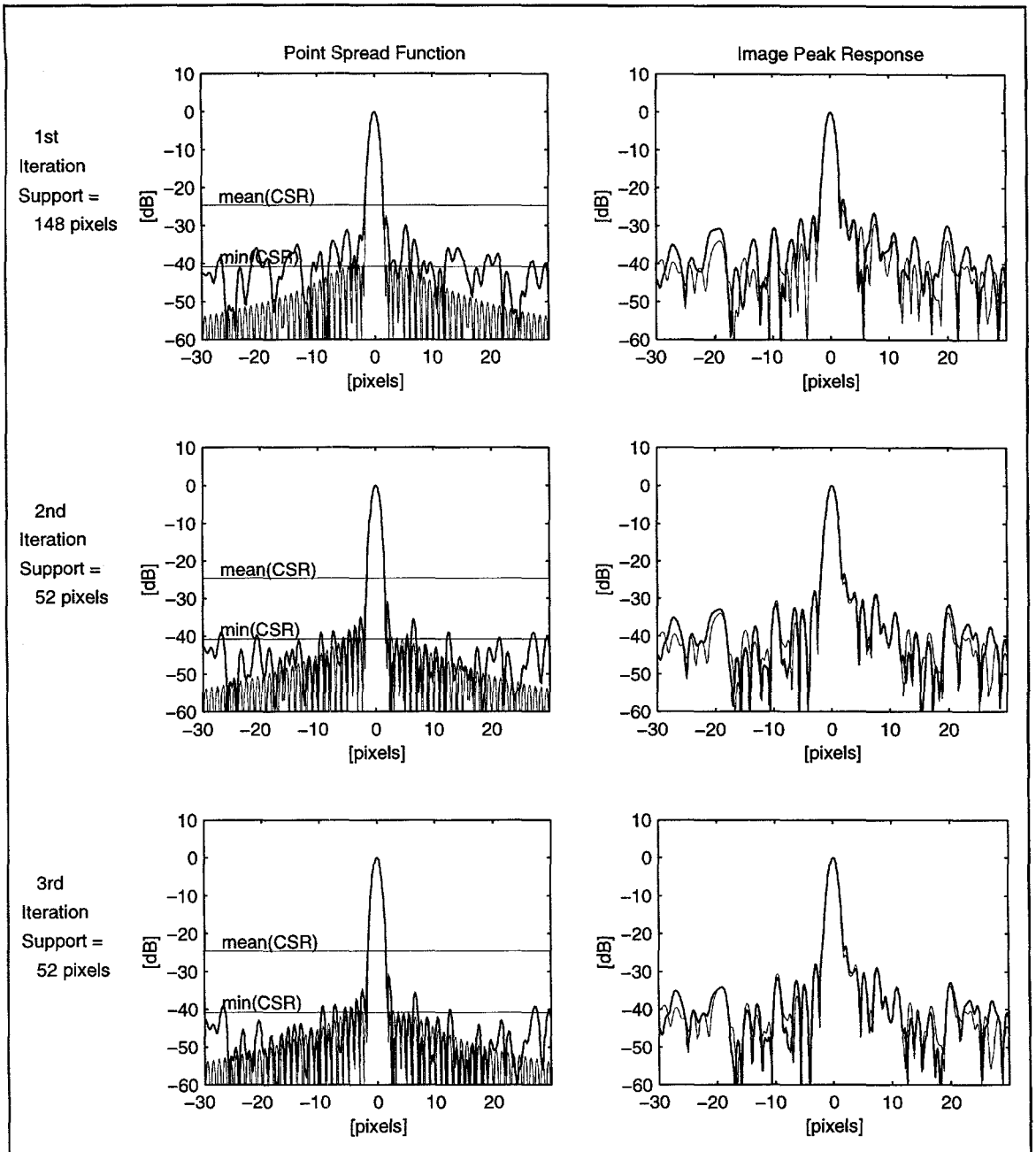

Figure 6-41. Point spread functions and image peak responses for Urban-1.

6.5.2.5 Menu of Metrics of PGA Performance for Three Iterations

For completeness the menu of metrics defined and illustrated in Section 5.3 of Chapter 5 are included for all three iterations of the two cases studied here. Those metrics are displayed in Figure 6-42 through Figure 6-44 for the Rural-3 example and in Figure 6-45 through Figure 6-47 for the Urban-1 example. The vertical lines indicate the window selected for that iteration. The phase error used for the second and third iterations was, of course, the residual phase error after the preceding iteration for the selected window.

Graph (a) in Figure 6-42, residual MSE after the first iteration, shows the selected window to be slightly to the left of the knee of the data. This indicates that the selected support was slightly too narrow. The improvement seen in the point spread functions after the second and third iterations is clearly reflected in graphs (d) and (e) of Figure 6-42, Figure 6-43 and Figure 6-44, which show the Strehl ratio and integrated-sidelobe ratio (ISLR) respectively. The improvement is not so obvious in graphs (a), (b), and (c), which show MSE, bandwidth of the residual phase gradients and modulation index, respectively. These results for Rural-3 contrast sharply with the results for Urban-1. The selected window for the first iteration shown in graph (a) of Figure 6-45 is clearly to the left of the knee of the data. This is the cause of the sidelobe streaking visible in the detected images shown in Figure 6-39. The sidelobe level determined by the first iteration is shown in graph (h) of Figure 6-45. In graphs (e) one can detect a slight improvement in ISLR between the first iteration shown in Figure 6-45 and the second iteration shown in Figure 6-46.

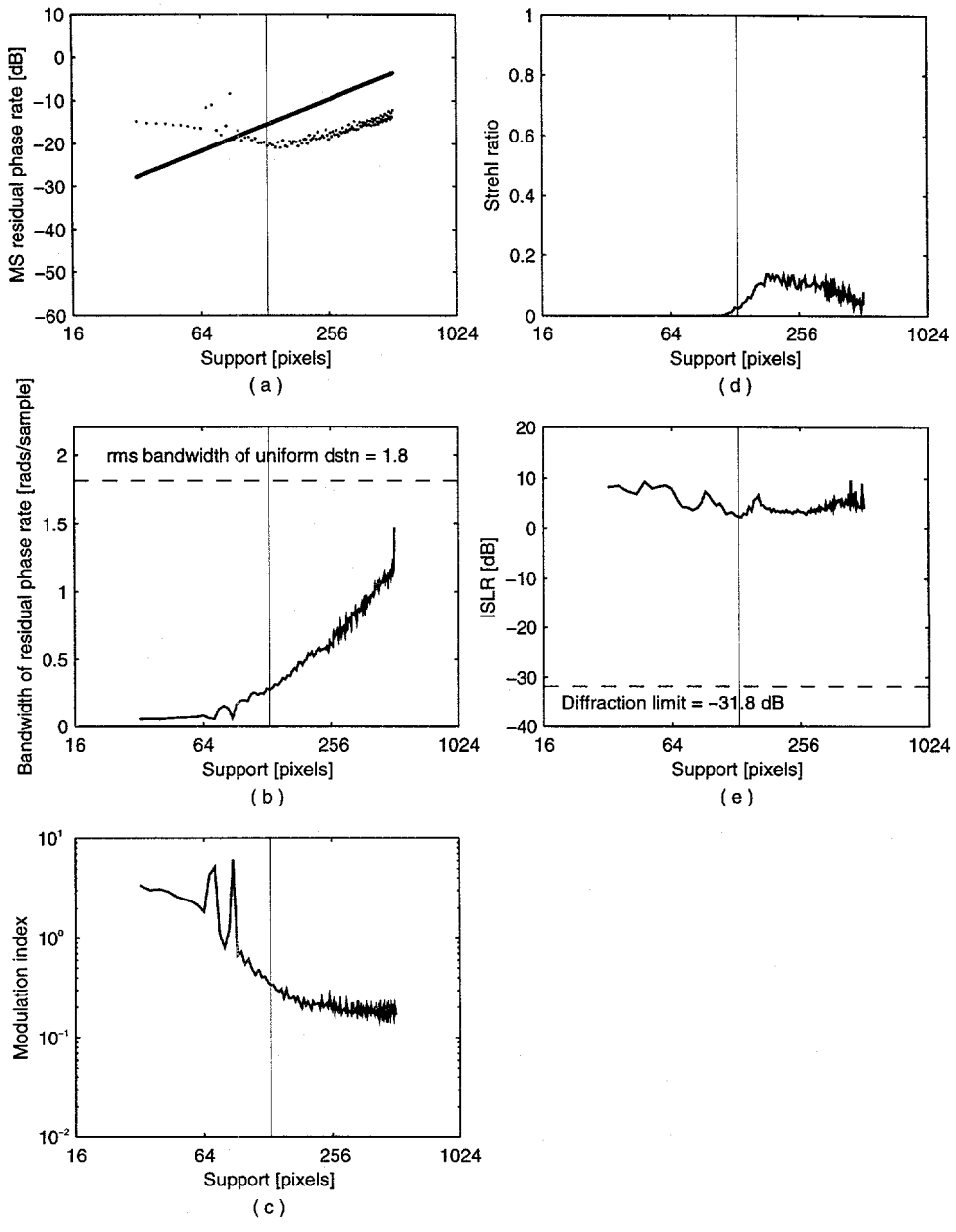

1st iteration window = 132 bins

Rural–3
shift errors
1.0 x low order phase
Part 1

Figure 6-42. Menu of metrics of PGA performance after 1st iteration for Rural-3 aberrated by the low order phase.

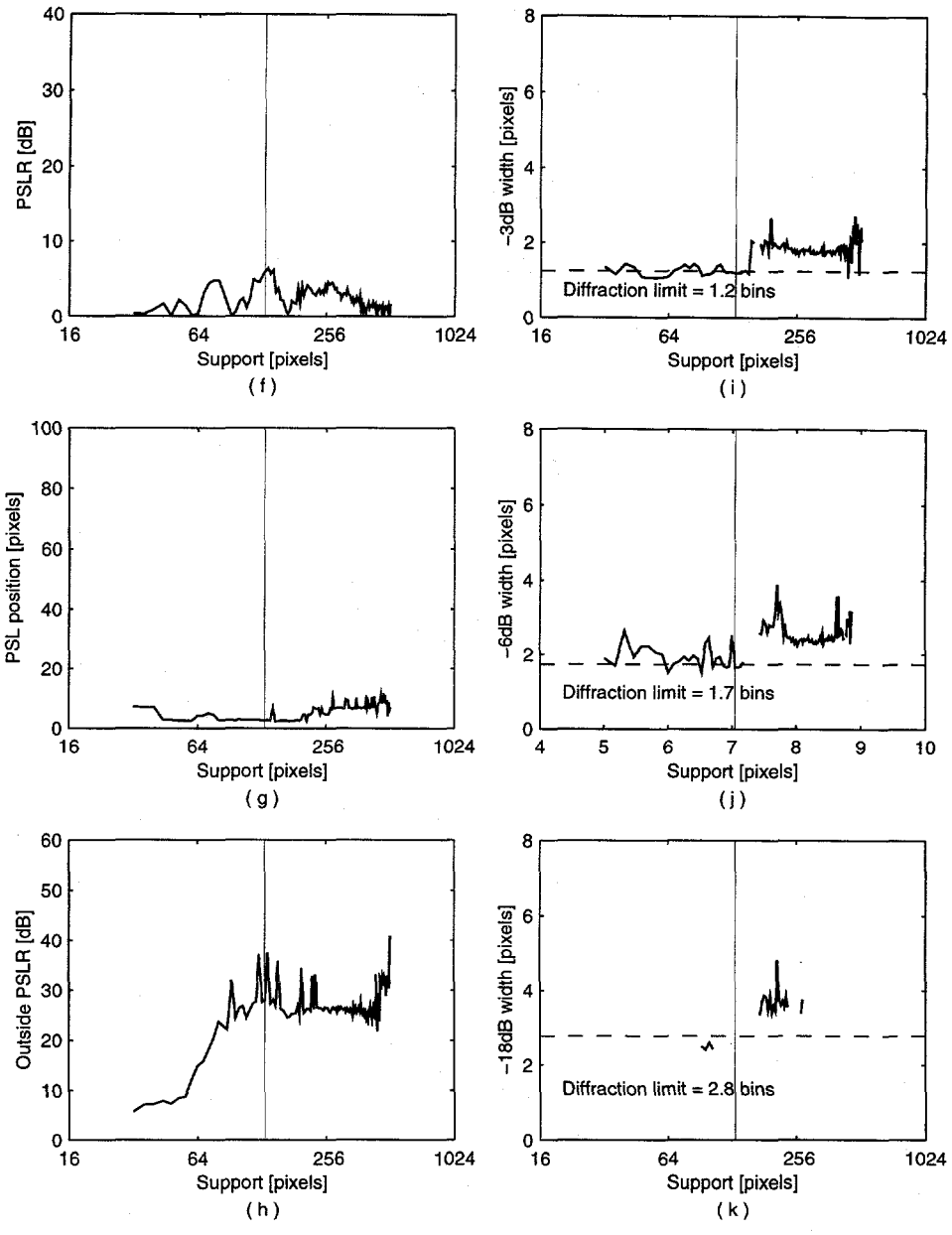

Figure 6-42 (con't). Menu of metrics of PGA performance after 1st iteration for Rural-3 aberrated by the low order phase.

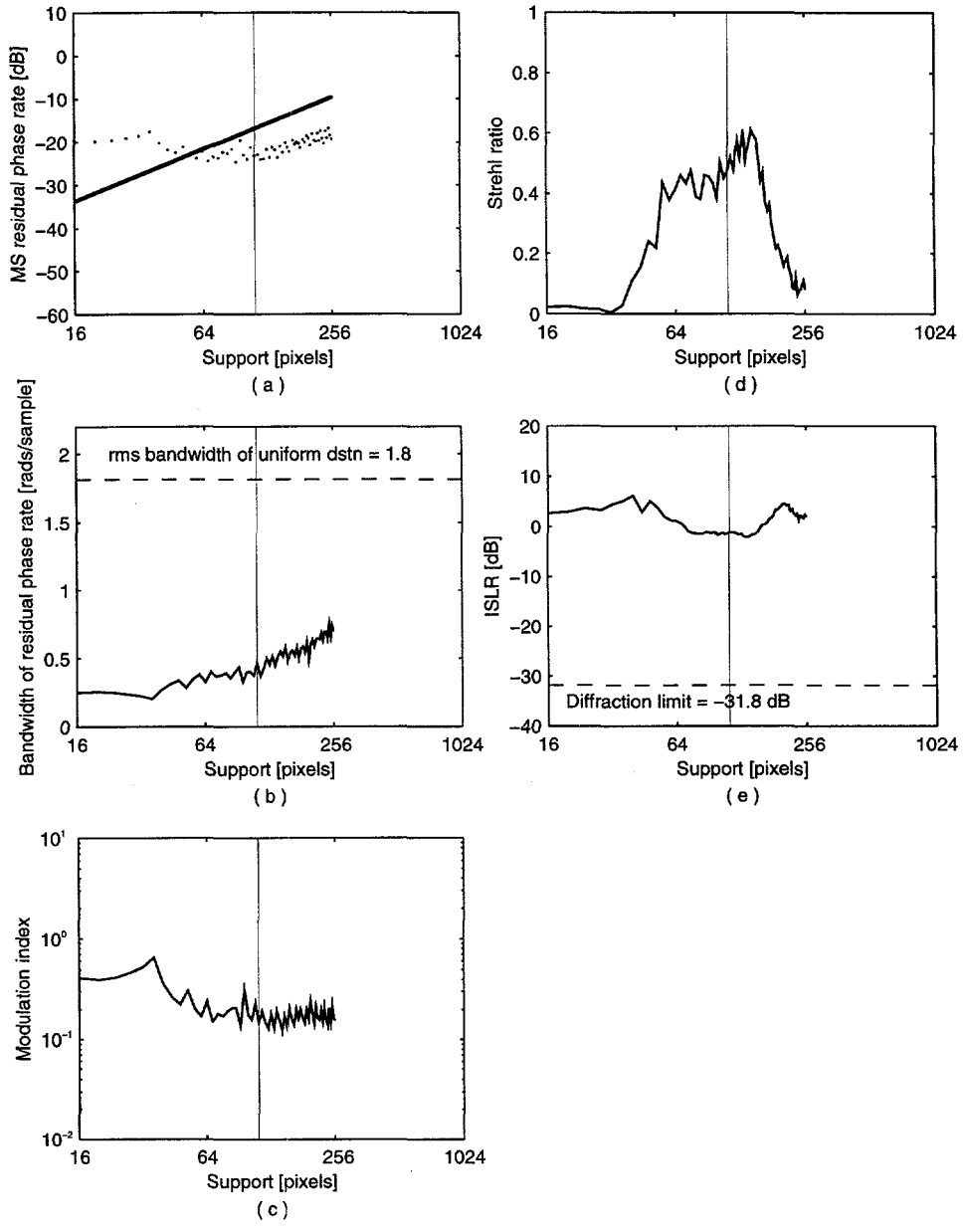

Figure 6-43. Menu of metrics of PGA performance after 2nd iteration for Rural-3 aberrated by the low order phase.

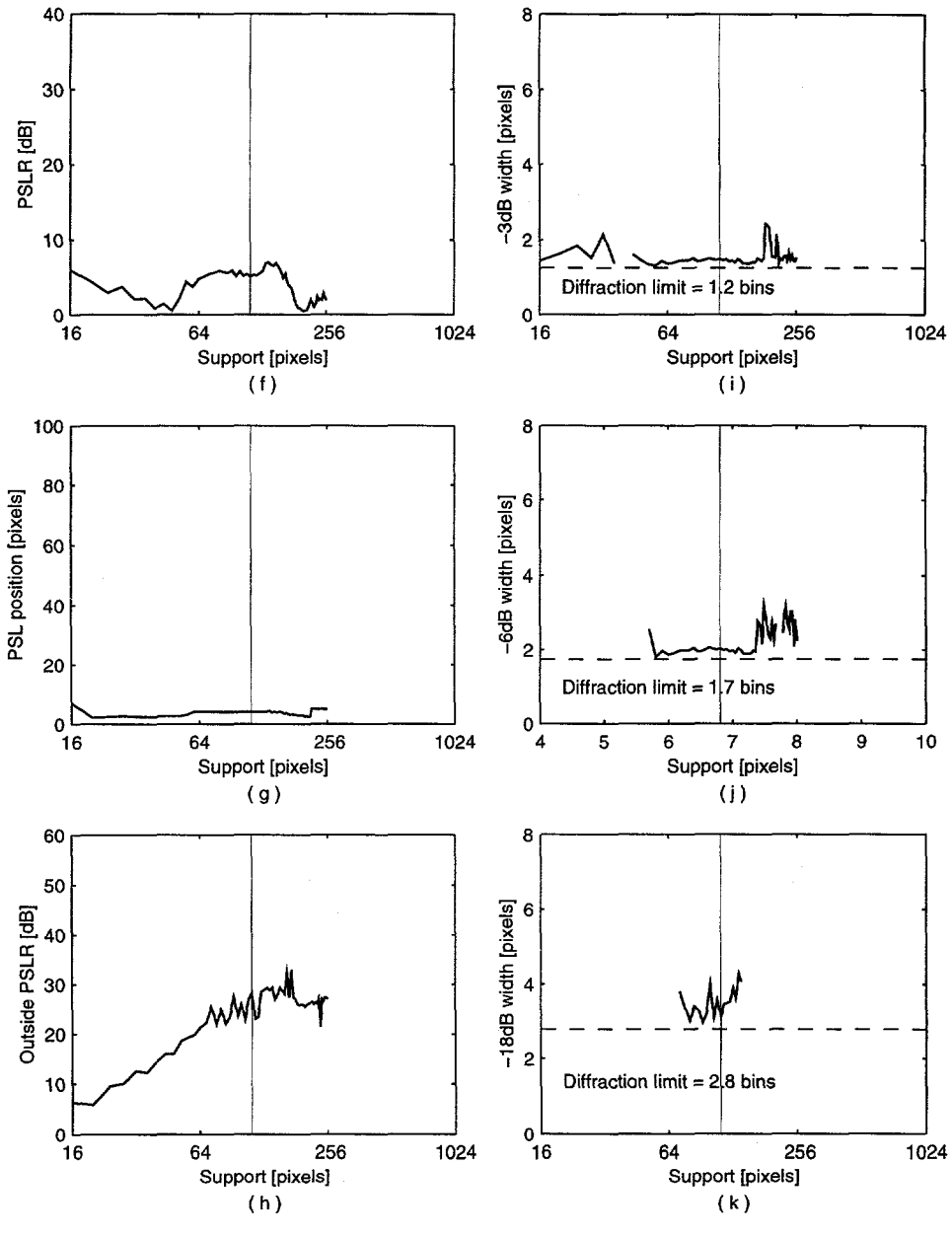

Figure 6-43(con't). Menu of metrics of PGA performance after 2nd iteration for Rural-3 aberrated by the low order phase.

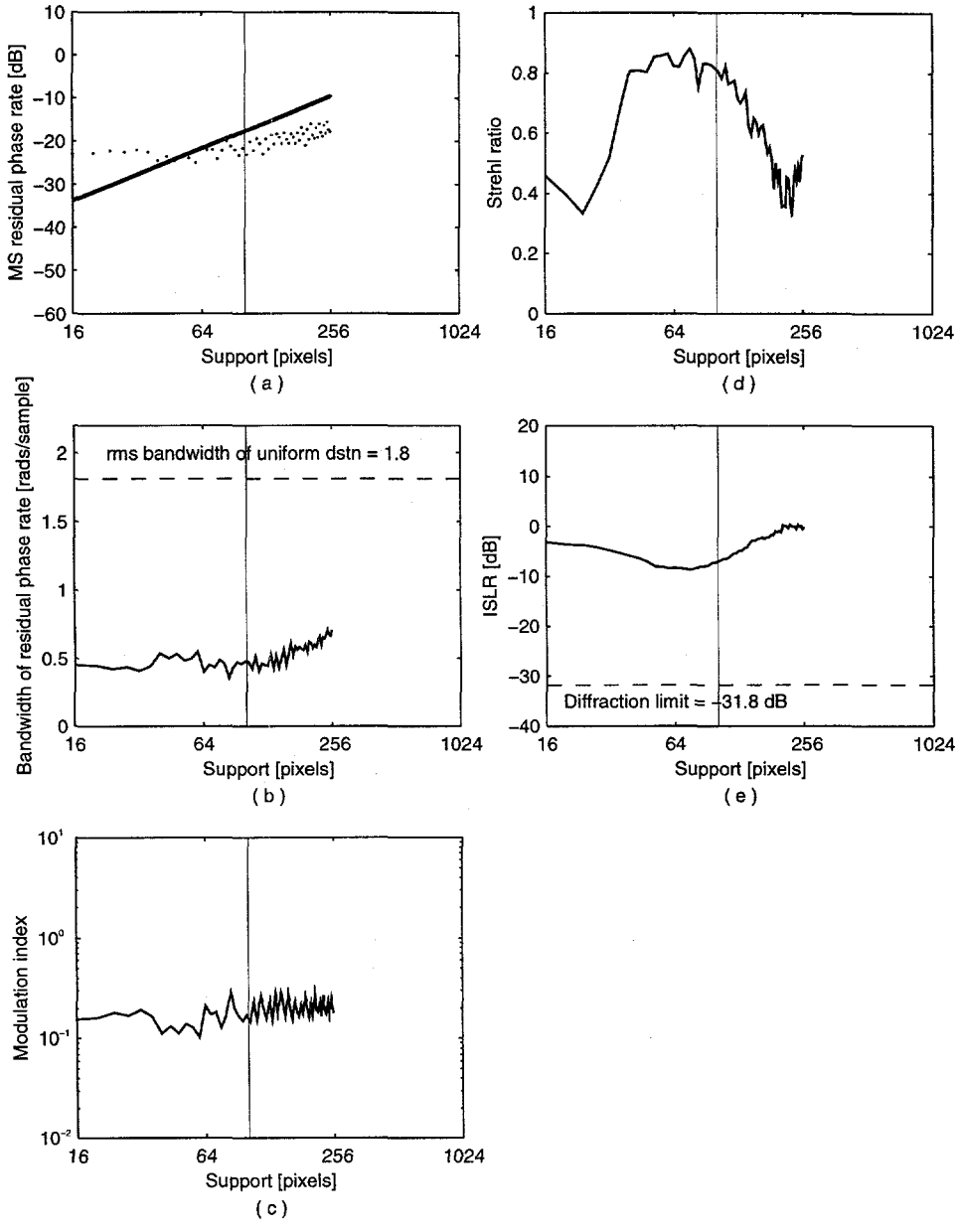

3rd iteration window = 102 bins

Rural–3
shift errors
1.0 x low order phase
Part 1

Figure 6-44. Menu of metrics of PGA performance after 3rd iteration for Rural-3 aberrated by the low order phase.

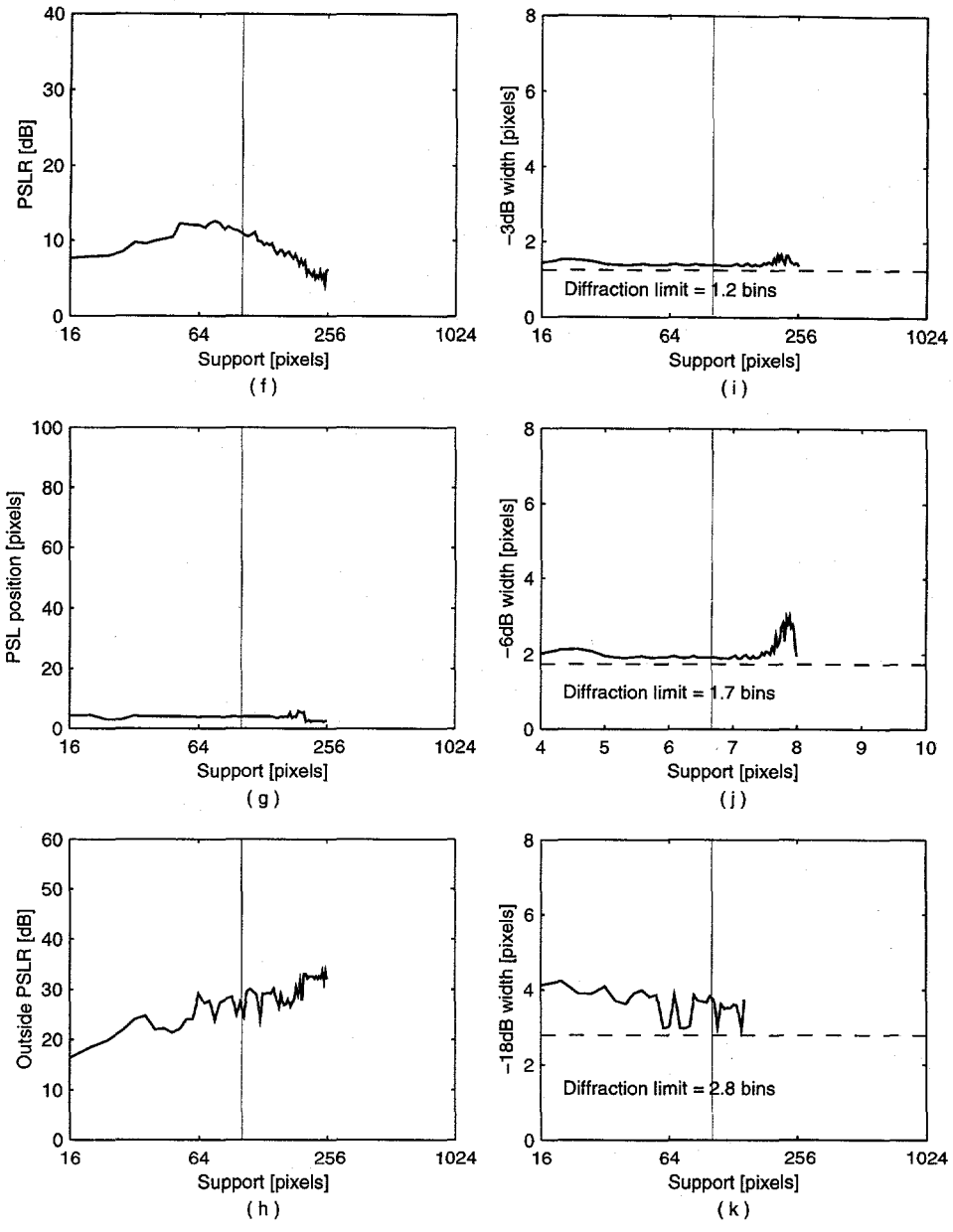

Figure 6-44 (con't). Menu of metrics of PGA performance after 3rd iteration for Rural-3 aberrated by the low order phase.

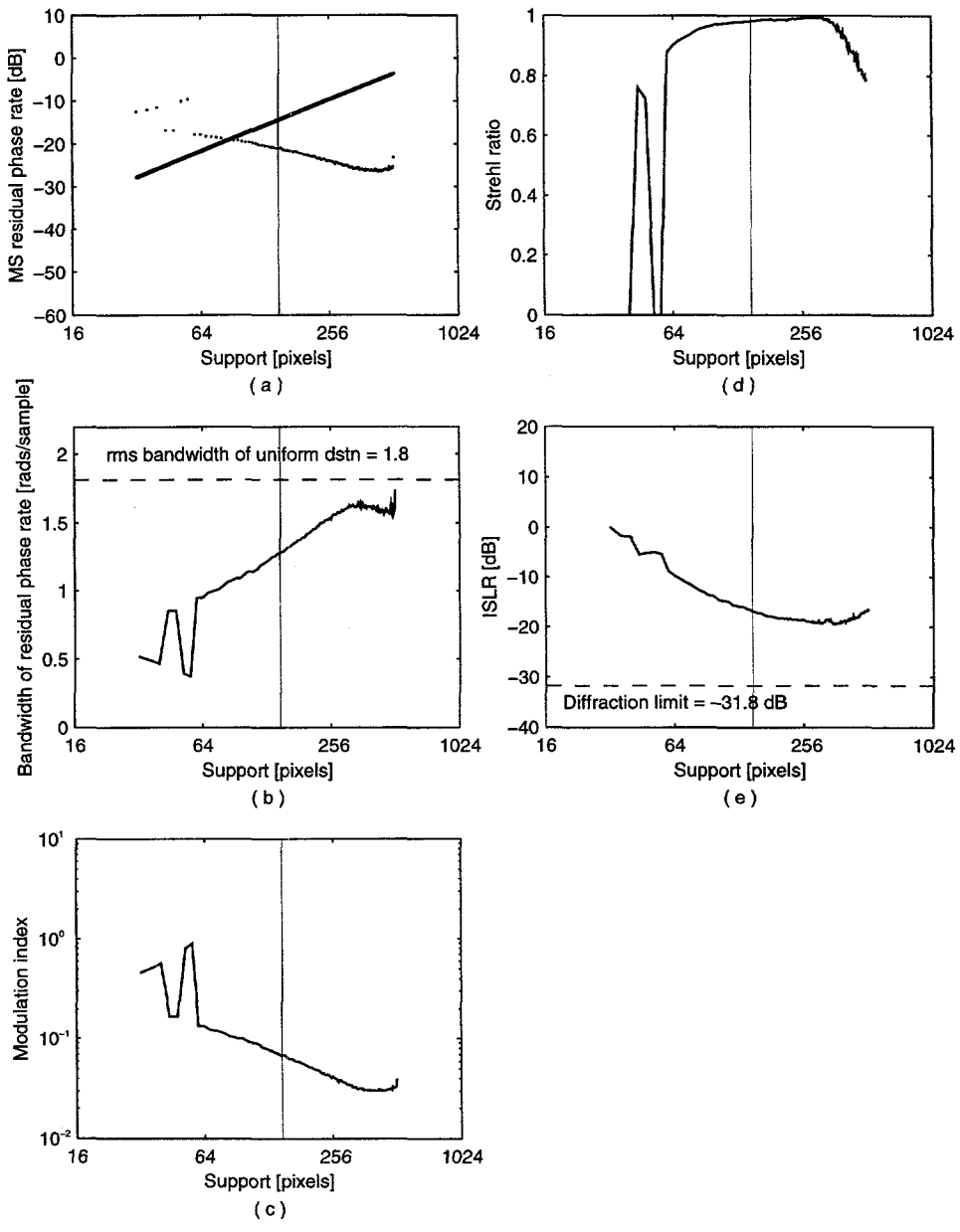

Figure 6-45. Menu of metrics of PGA performance after 1st iteration for Urban-1 aberrated by the low order phase.

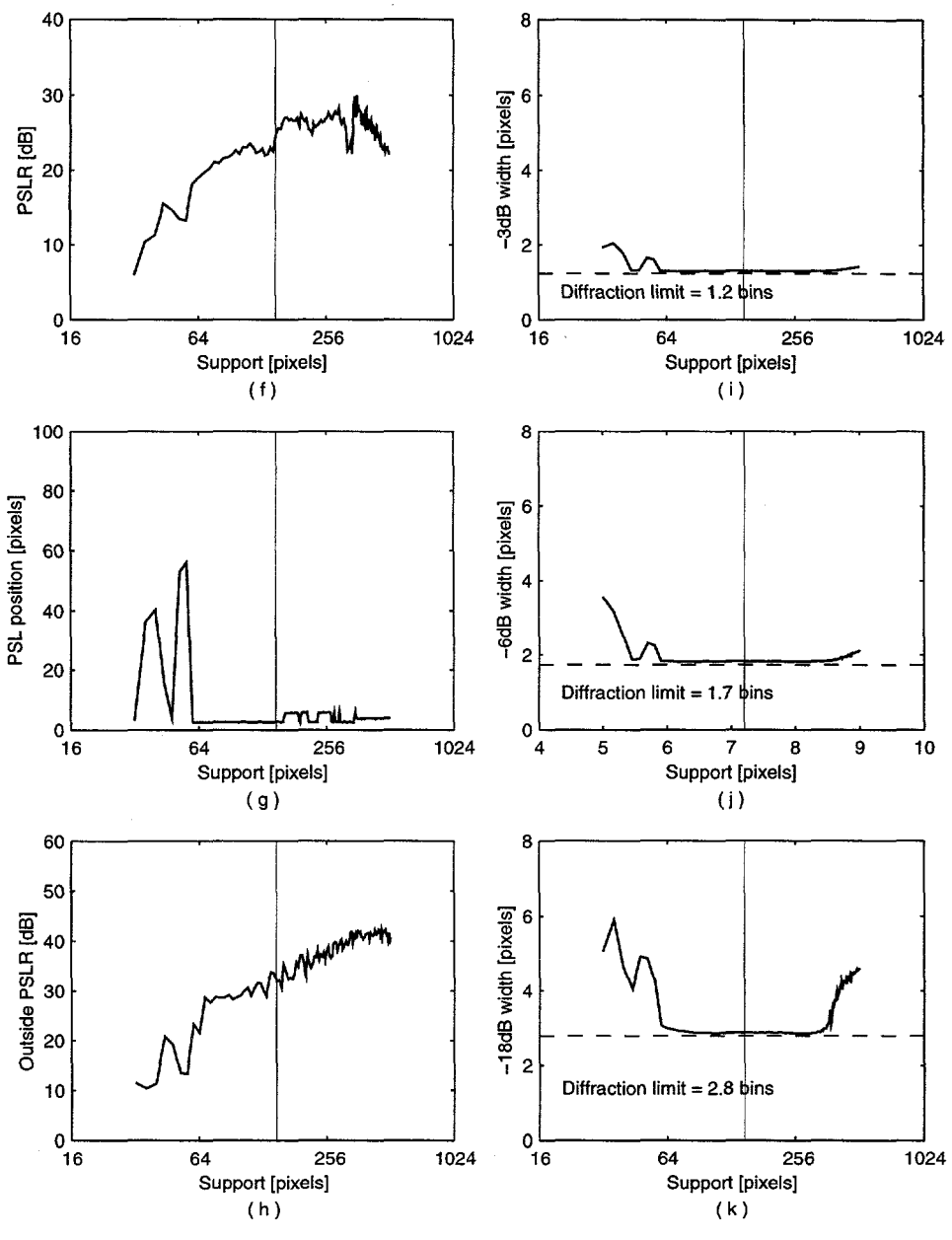

Figure 6-45 (con't). Menu of metrics of PGA performance after 1st iteration for Urban-1 aberrated by the low order phase.

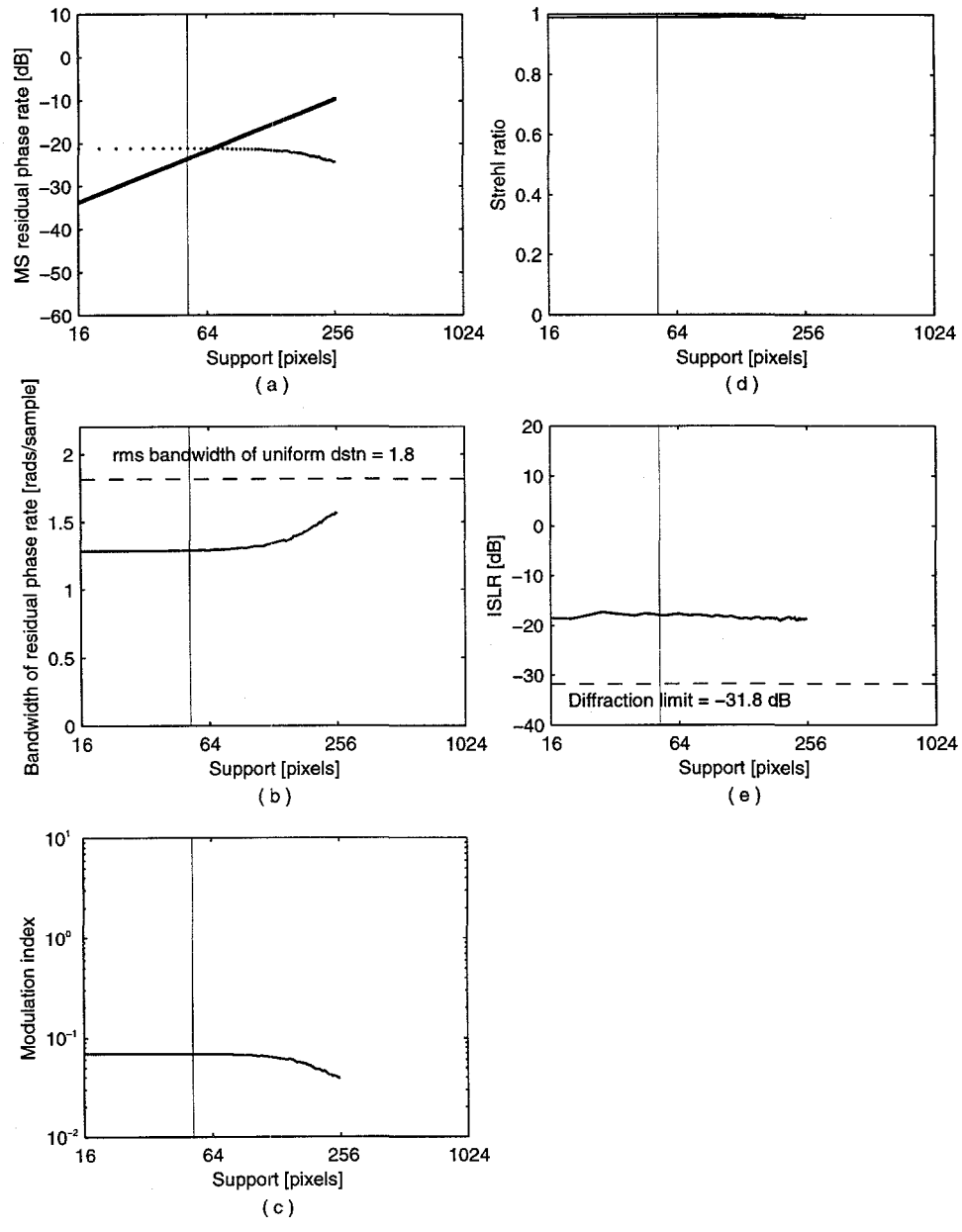

2nd iteration window = 52 bins

Urban–1
shift errors
1.0 x power law phase
Part 1

Figure 6-46. Menu of metrics of PGA performance after 2nd iteration for Urban-1 aberrated by the low order phase.

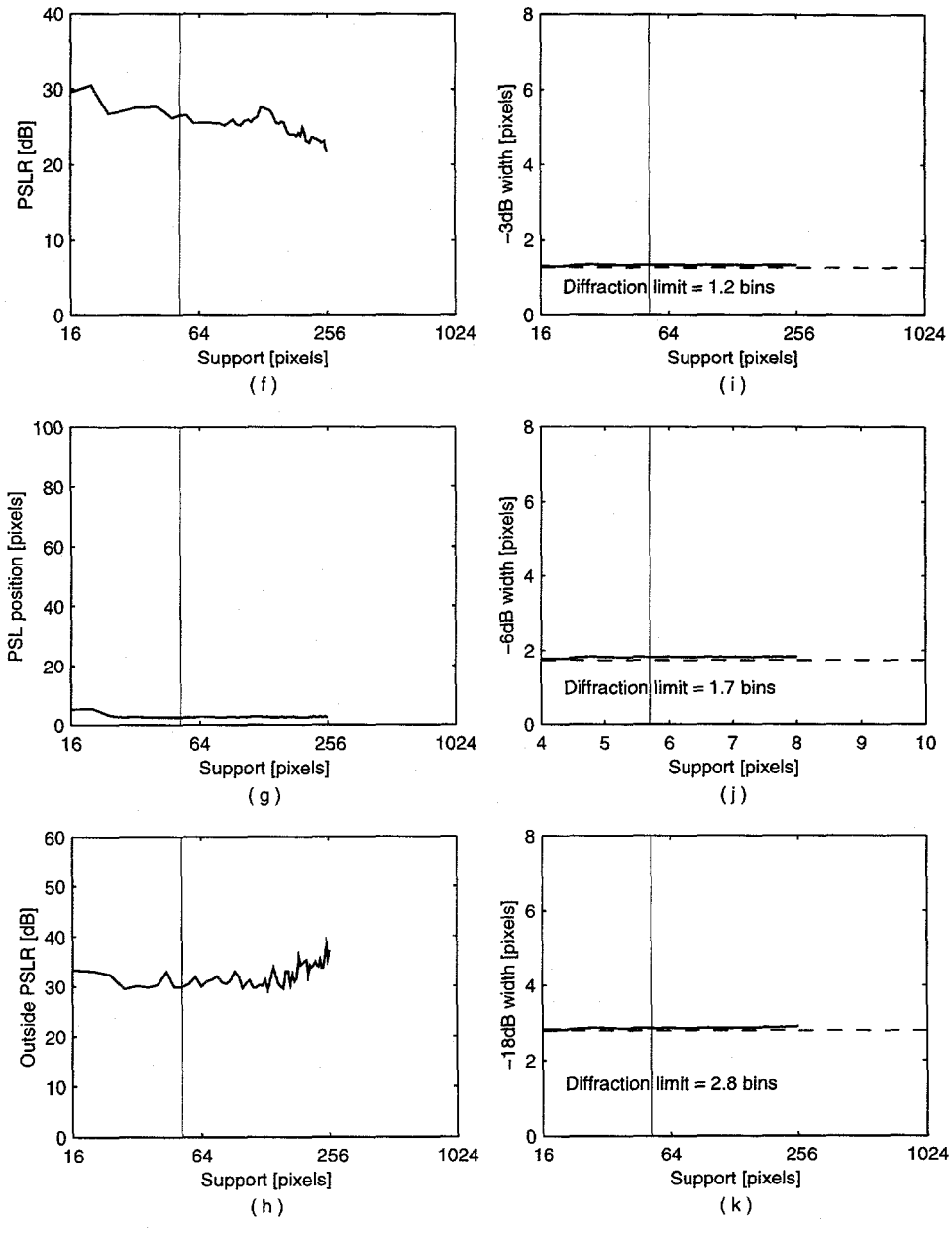

Figure 6-46 (con't). Menu of metrics of PGA performance after 2nd iteration for Urban-1 aberrated by the low order phase.

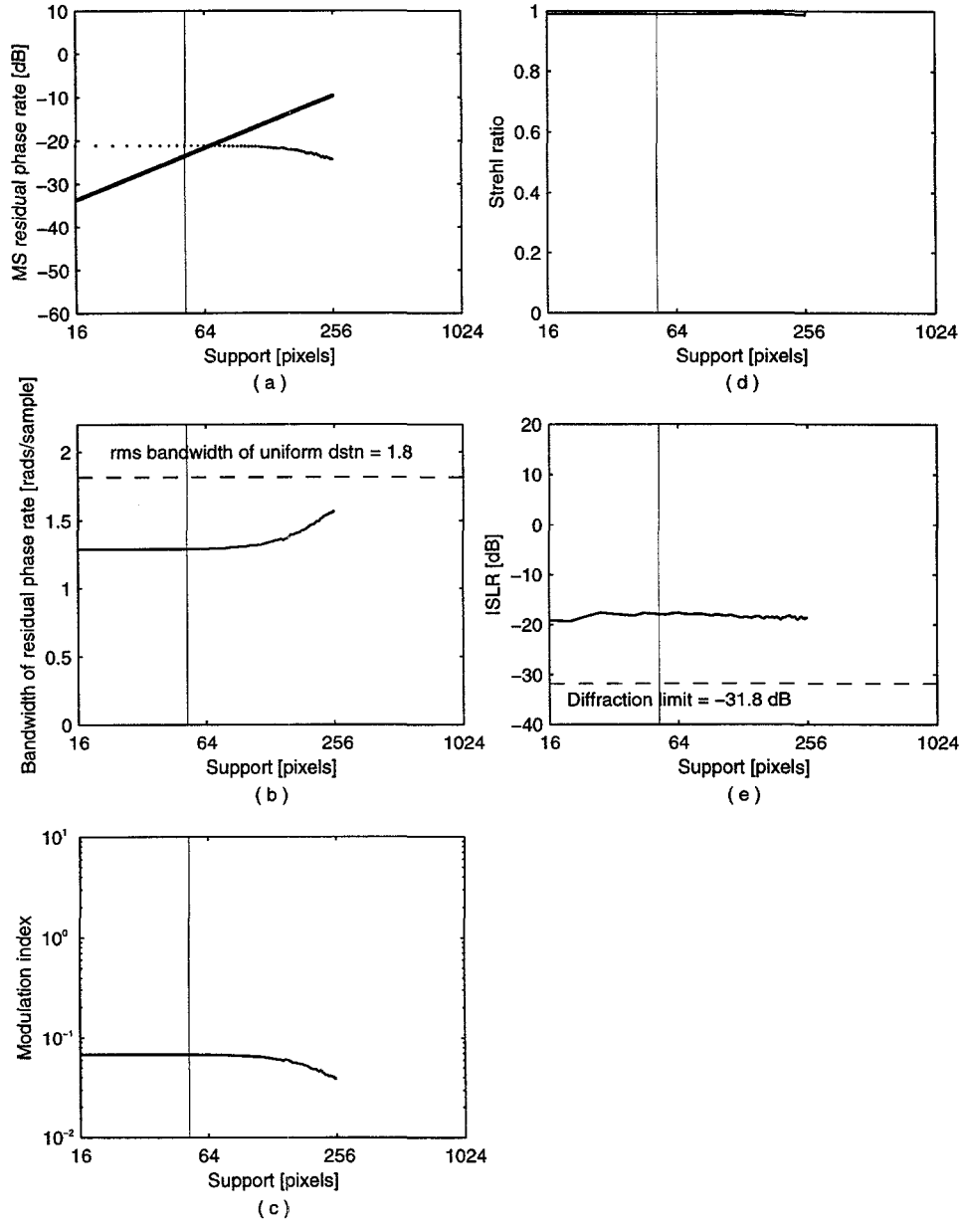

Figure 6-47. Menu of metrics of PGA performance after 3rd iteration for Urban-1 aberrated by the low order phase.

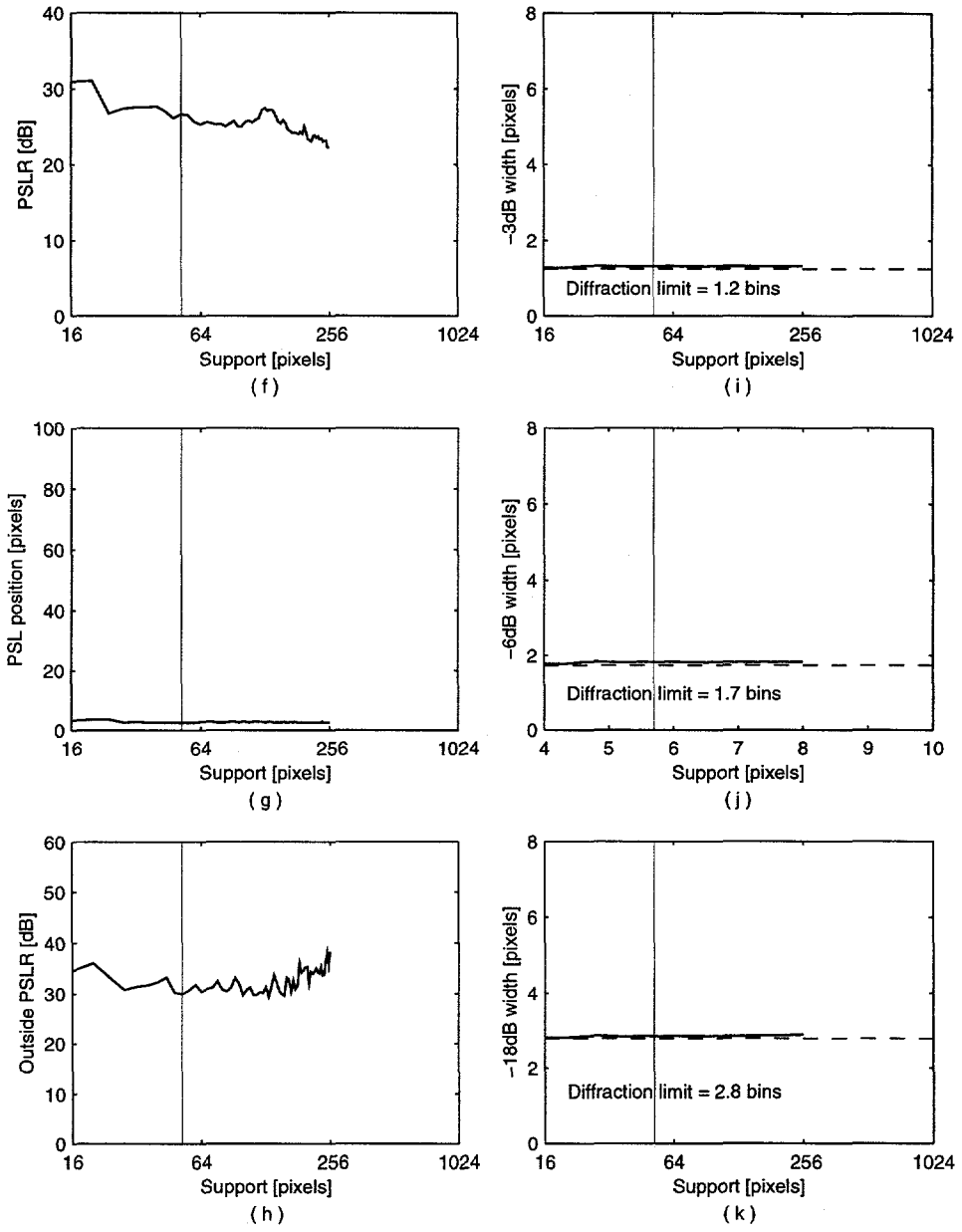

Figure 6-47 (con't). Menu of metrics of PGA performance after 3rd iteration for Urban-1 aberrated by the low order phase.

A topic not addressed in this dissertation concerns a small, but possibly significant, detail; that is, the method of extrapolating phase gradients or integrated phase errors to the edges of the aperture. As the width of the support gets small, the interval requiring extrapolation gets large. If data are extrapolated inappropriately across a large interval, extrapolation could introduce a residual phase error significant to image quality.

6.5.3 Summary, Conclusions and Recommendations

These results show that the new thresholding algorithm compares favorably with the current practice. They indicate that this new algorithm, properly scaled, could provide better performance. The minimum and maximum values of the coherent sum used to develop the threshold might provide data useful for developing meaningful threshold scaling factors. The methods of analysis used in this section are, perhaps, a contribution as significant as the new thresholding algorithm. These methods provide a means of visually inspecting large amounts of data over a complex matrix of control variables.

Chapter 7

Conclusions and Recommendations

The research described in this dissertation has addressed five areas of investigation pertaining to the implementation and the performance of the Phase Gradient Autofocus (PGA) algorithm. This research was conducted using three classes of aberrating phase errors, synthesized SAR data and a set of five real SAR image data. Method of analyses were both numerical and theoretical. Results have

1. identified a subprocess that can introduce angle-dependent estimator bias and have shown how this bias can be avoided;
2. identified an angle dependent bias inherent in the non-linearity of the estimation problem;
3. found indications of clutter correlation in real SAR data that is not present in the synthesized data;
4. identified limitations of the current data model to represent the effect of shift errors on algorithm performance and,
5. offered a new approach to defining the support of the point spread function supported by results. This new approach promises a reduction in the number

of iterations required for scenes with low signal-to-clutter ratios such as the rural scenes used for this research.

7.1 Review of Methods of Analyses

In Chapter 4 we introduced the phase data and real SAR image data used for this research. We considered the properties of random modulation and associated metrics of mean squared phase-gradient error (MSE), bandwidth, and modulation index. We used the signal-to-clutter ratio of real SAR data to synthesize SAR data with homogeneous clutter. We considered a number of distributions of real and synthesized SAR signal and clutter relationships and made comparisons between the real and synthesized SAR data. As a result we identified potentially significant differences in the clutter distributions between the real and synthesized SAR data.

In Chapter 5 we reviewed the theoretical and numerical methods of analysis used for this research. We presented the general form of the Cramér-Rao lower bound (CRLB) for both unbiased and biased estimators. We showed how the CRLB for functions of the basic parameters is calculated. We showed the importance of the formulation of the data model to the validity of the CRLB and emphasized the importance of verifying the equivalence of results using the two methods of computing the Fisher information matrix. This verification is of particular importance 1) when the parameter of interest is a non-linear function of the observations, as is the case with phase-gradient estimation; and

2) when the data model is predicated on simplifying assumptions, as is the case with the currently published data model.

The numerical methods reviewed in Chapter 5 were divided into two groups:
1) simulations conducted entirely in the phase-history domain, which do not model the transfer function of the limited support of the point spread function; and 2) full processing of data through the PGA process using scene, aberrating phase and support width as control variables. These simulations generated a menu of nine types of performance metrics for a total of eleven metrics of algorithm performance. That menu of nine types of metrics was further divided into metrics of phase residual phase error and metrics of image quality. They were:

- Metrics of residual phase error:
    1) MSE of the residual phase gradients averaged across the aperture
    2) rms bandwidth of the residual phase gradients; and
    3) modulation index, which is a function of the first two
- Metrics of image quality:
    4) Strehl ratio;
    5) ISLR (integrated sidelobe ratio);
    6) PSLR (peak sidelobe ratio);
    7) relative position of the peak side lobe;
    8) PSLR outside the support of the point spread function; and
    9) -3, -6,-18 dB width of the point spread function.

This catalogue of metrics was supported by examples. Although these metrics provide a very condensed presentation of a large amount of data, there are situations when a graphic presentation of the estimated phase gradient or gradient error is most revealing, as we showed in Chapter 6, Section 6.1, where the display of the gradient error exposed a clear estimator bias.

7.2 Review of Research Results

In Chapter 6 we used the data, findings and methods from Chapter 4 and 5 to address five areas of investigation. We will review those results and recommendations and then summarize the recommendations in the final section.

7.2.1 Method of Interpolating and Integrating Phase Gradient Estimates

A subprocess of the PGA algorithm not addressed in the literature has been examined here in detail. Four implementations of this subprocess were considered. Only one of the four implementations, Method 4 (DFT with phase rate interpolation), produces results that equal the combined lower bound. For applications where the increased computational burden of DFTs is unacceptable and FFTs must be used, we have shown that increasing the width of the support to the next highest power of two is preferable to zero padding. Only Method 4 was used for the analyses presented here.

7.2.2 Improvement with Iteration

The experimental results show that there is improvement with iteration if the width of the support of the point spread function is reduced with iteration. For improvement to occur, the residual phase gradient must have some detectable low pass structure with bandwidth less than the bandwidth associated with the support used on that iteration. This is consistent with the Taylor series expansion, which shows an angle-dependent bias inherent in maximum-likelihood phase-gradient estimator. The magnitude of this bias is shown in Appendix D to be inversely proportional to the number of data samples used in the estimate. Development of a full convergence model using the expression for estimator bias, requires a well-defined relationship between scene SCR, point spread, and selected support of the point spread.

7.2.3 Differences Between Synthesized and Real SAR Data

Measures of PGA performance for real and synthesized data aberrated by three phase errors have been compared. Performance using synthesized data agrees closely with theoretical bounds. Performance using real SAR data does not agree as closely with theoretical bounds. We have considered the data to the left of the knee of the combined lower bound. In this region, for data with uncorrelated noise, performance is determined by support width. We note from Figure 6-3 that correlated noise results in degraded performance. We hypothesize that the noise in real SAR data is correlated.

7.2.4 Effect of Shift Errors on Estimator Performance

We have used synthesized SAR data to show that our data model and derived CRLB do not represent the performance of the PGA algorithm for shifted data. To make further progress in this area of mathematically modeling PGA performance, it appears necessary to expand the data model to explicitly include 1) the transfer function of the support of the point spread function, and 2) the amplitude and spatial frequency of clutter. The second recommendation is based both on the SAR data analysis in Chapter 4 and the PGA performance analysis in this and the previous section. In Chapter 4 we saw that signal-to-maximum clutter statistics for real SAR data are lower than for synthesized SAR data with the same signal-to-clutter statistics. In this and the previous section we have seen indications that correlated noise may be influencing PGA performance.

The following data model was proposed in equation (6-9). This model uses spatial frequency, ω, normalized over $\pm\pi$ and SAR pulse repetition period normalized to unity.

$$x_{m,k} = h_m \otimes \left[e^{j\phi_m} \int_{-\pi}^{\pi} a_k(\omega) e^{jm\omega} d\omega \right]$$

where h_m is the discrete-time transfer function of the support of the point spread function,

$\otimes$ is used here to denote discrete-time convolution,

ϕ_m is the familiar aberrating phase function at the m^{th} sample, and

$a_k(\omega)$ is the spatially continuous complex envelope of both signal and clutter echos as a function of spatial frequency.

The modulation of both signal and clutter by the aberrating phase is expressed explicitly in this model. Any inhomogeneous distribution of clutter will likely result in a small but certainly non-zero correlation of clutter noise. Evaluation of the CRLB using this data model may well produce the explanation for observed behavior.

7.2.5 Definition of the Support for the Point Spread Function

These results show that the new thresholding algorithm compares favorably with the current practice. They indicate that this new algorithm, properly scaled, could provide better performance. The minimum and maximum values of the coherent sum used to develop the threshold might provide data useful for developing meaningful threshold scaling factors.

7.3 Review of Recommendations

Through the study of Area 1 the Method of Interpolating and Integrating Phase Gradient Estimates), we have shown that the method used to transition from bandlimited estimates of phase gradients to integrated estimates of phase error interpolated across the full aperture can introduce a significant bias to the estimate. We recommend that zero-padding be avoided completely. The recommended method is to use discrete Fourier

transforms (DFT) to transform shifted, support-limited, complex image data to the phase-history domain. If DFTs are computationally too burdensome, then we have shown that the slight increase in MSE due to increased clutter included in the next power-of-two FFT is far preferable to a biased estimate associated with zero-padded FFTs.

Through the study of Area 2 (Improvement with Iteration), Area 3 (Differences Between Synthesized and Real SAR Data) and Area 4 (Effect of Shift Errors on Estimator Performance) we have identified:

1. an angle-dependent bias inherent in the estimator due to the non-linear relationship between the parameter of interest and the observations; and
2. limitations in representation of real SAR data by the current data model.

We have recommended that the data model be expanded to include explicit representation of:

1. the transfer function of the support of the point spread function; and
2. the amplitude, spatial frequency and phase modulation of the scene clutter.

As as a starting point, an equation was suggested at the conclusion of the investigation of Area 4 in Section 6.4. The problem of developing the full Cramér-Rao lower bound for this expanded data model is outlined in Appendix D.

Finally, in the study of Area 5 (Definition of the Support for the Point Spread Function) we have proposed a new method of estimating the required support of the point spread function. In order to compare current practice to the new proposal, we developed a

condensed visualization of the selected support relative to peak sidelobes of the aberrated point spread function outside the selected support.

The results presented here provide the insights necessary and identify the directions of research required to develop a complete model of the convergence of the Phase Gradient Autofocus algorithm. As such, they provide information pertinent to the application of this algorithm to other coherent image applications.

Appendix A

Historical Overview of the Development of Non-Parametric SAR Autofocus Algorithms

This appendix provides a chronological summary of the evolution of non-parametric SAR autofocus algorithms and the development of the PGA algorithm addressed here.

The development of synthetic aperture radar originated with Carl Wiley in 1951. He postulated that azimuth resolution could be achieved through detection of Doppler shift. The first SAR image was produced in 1958 at the University of Michigan, using optical processing [30]. At that time, photographic film was the only data storage medium having the necessary bandwidth and dynamic range for SAR imaging [17, p. 512]. Focusing and autofocusing concepts were developed within this optical imaging constraint. In the early 1970's with the advent of off-line non-real time digital signal process capabilities, the options for SAR autofocus algorithms broadened.

A number of the references are from the literature on optical/stellar imaging where problems of image blur due to aberrations in the signal path length are similar to those of SAR imaging.

The definition and the performance of PGA, as applied to SAR imaging, has been documented in the literature in a series of papers beginning in 1989 submitted by researchers at Sandia National Laboratories, Albuquerque, New Mexico. Those researchers names are indicated by boldface type.

October 1974	In [37] Knox & Thompson, researchers in optical imaging, introduce their algorithm for determining the object transfer function from the statistical autocorrelation of the image transform.
January 1986	In [3], Aitken, Johnson and Houtman introduce the LUMV phase-gradient estimator to optical astronomical imaging through turbulent media. Related publications are Aitken and Johnson [1] and [2], Johnson and Aitken [35] and Aitken [4].
1988	In [6] Ayers, Northcott and Dainty compare Knox-Thompson to triple-correlation (optical) imaging through atmospheric turbulence. They show that the phase gradient method of Aitken, Johnson and Houtman [3] is a subset of the more general Knox-Thompson method.

January 1989 — In [5] Attia & Steinberg introduce the ML phase-gradient estimator within the context of self-cohering large antenna arrays. See also Steinberg & Subbaram [52].

January, March 1989 — In [34], **Jakowatz**, **Eichel** and **Ghiglia** introduced the four essential steps of the algorithm: 1) shift, 2) window, 3) estimate, and 4) iterate. In [18], the same authors introduced the name "Phase-Gradient Autofocus" in recognition of the use of the same phase-gradient estimation kernel by Aitken, Johnson and Houtman in optical astronomy for imaging through turbulent media [1] and [3].

1989 — In [24], **Ghiglia** and **Mastin** extended PGA to two-dimensions. This research considers only the one-dimensional problem of azimuth autofocus.

October 1989 — In [19], **Eichel** and **Jakowatz** showed the phase-gradient estimation kernel in [18] to be a linear unbiased minimum variance estimator (LUMV) for large signal-to-noise ratios.

In [14], **Calloway, Jakowatz, Thompson** and **Eichel** compared performance of the PGA algorithm to that of a conventional subaperture cross-correlation approach.

June 1989 — In [21], Fienup provides an historical perspective and introduces "shear averaging", a phase-gradient estimation algorithm equivalent to the ML kernel of PGA (but without the essential four steps). He attributes the initial invention to Attia and Steinberg [5] in the context of beamforming with large arrays. Fienup makes the connection with shearing interferometry.

1989 — In [26] Gray, Wolfe and Riley present an eigenvector method for estimating the positions of the elements of an array of receivers. This is followed in 1990 by Gray and Riley [27] with an ML estimator and CRLB for a complex signal vector.

1990 — In [64], **Wahl, Eichel** and **Jakowatz** presented a near real-time hardware implementation of PGA algorithm.

December 1993 — In [33], **Jakowatz** and **Wahl** made a significant modification to the algorithm. The LUMV phase-gradient estimation kernel was replaced with a maximum likelihood (ML) phase-gradient estimation kernel. This new estimator was shown to compare favorably to the derived Cramér-Rao lower bound for phase-gradient estimation. Gray et al [26] and [27] are referenced.

Summer 1993 — In [39], **Mastin, Plimpton** and **Ghiglia** documented the implementation of digital spotlight SAR processing, including PGA autofocus, on the commercially available massively parallel computers.

1991 — This was preceded by [38], in which the same authors presented details of the implementation of PGA on two of those computers.

1991 — In [66], **Wahl, Jakowatz, Ghiglia** and **Eichel** considered application of SONAR self-survey techniques to SAR autofocus and compared results to those achieved using PGA on SAR imagery. This work formed an important bridge between the signal processing methodologies for SAR and SONAR applications.

July 1994 — Most recently, in [65], **Wahl, Eichel, Ghiglia** and **Jakowatz** demonstrated the necessity of the four steps of PGA over a variety of scene content and phase-error-function structures. They also showed that the computational demands of the PGA algorithm did not represent a large fraction of the computational demands of the full SAR image formation process.

1994 In [51] Snarski considers the problem of range-Doppler imaging with phase errors that are uncorrelated from pulse to pulse. The algorithm studied is the Rank One Phase Estimation (ROPE) algorithm attributed to Dyson et al [16]. This algorithm is very similar to PGA in that it is a shift, ML estimate, and iterate algorithm without the windowing step of PGA.

July 1994 In [36] Just and Bamler consider the phase statistics of interferograms with applications to synthetic aperture radar. The estimation kernel here is the same ML estimation kernel of PGA. Rodriguez and Martin [49] are cited as the source for the estimator and the stated Cramér-Rao lower bound.

Appendix B

Characterization of Scene Signal-to-Clutter Ratios

In Chapter 4, Section 4.2, the results of exploratory analysis of the SAR data used in this dissertation were summarized. The detected images were shown in Figure 4-6 of that chapter. This appendix offers more detailed discussion of those data and the methods of analysis.

B.1 Description of the SAR Image Data

Eight images were studied: one synthesized image using Rayleigh statistics is included as a baseline, three images of rural scenes, two images of urban scenes and two data sets synthesized from the sample distributions of signal-to-clutter ratios of scenes Rural-3 and Urban-1 with mean SCR of 15 dB and 27 dB respectively. The Rayleigh image was generated using Matlab® software, which defaults to double precision floating point numbers. At each pixel the real and imaginary parts were determined by random draw from independent but identical Gaussian distributions. The Rayleigh scene clutter power is, therefore, exponentially distributed. At each range the signal was defined as the pixel with the largest squared magnitude. The signal of the Rayleigh scene is Gumbel or

extreme-value distributed [44]. The mean signal-to-clutter ratio (SCR) of the Rayleigh data is 11.2 dB and is 3 dB less than the mean SCR of the three rural scenes. The remaining five images are those that appear in [65] and are offered to researchers by the authors of that reference. The image names used here and the associated filenames from the data set provided through [65] are catalogued in Table B-1. The detected images have a dynamic range of 93 dB. All images are displayed in Figure 4-6 of Chapter 4, using a gray scale of 256 values. The scale is weighted to produce a visually pleasing display. These corrected SAR images are assumed to be unaberrated and are used to estimate the scene signal-to-clutter ratios.

The PGA algorithm locates the brightest point at each range in the aberrated image and assumes it to be 'signal'. The range and azimuth indices of an isolated bright point in each scene are catalogued in Table B-1. The positions of these brightest points at each range were determined from the unaberrated image. These data are used in Chapter 6 to assess PGA performance with the new algorithm offered here for estimating the required support for the point spread function.

Consider some of the problems of dealing with real SAR data where truth is not known but is assumed to be closely approximated by the data. Although the complex image data sets were 512 by 512 pixels, examination of the range-compressed phase histories reveal stop bands, or bands of data with very low total power, at the beginning and end of the phase histories. Among the five images, these stop bands vary in width from 30 to 50

Table B-1. Catalogue of indices to an isolated bright point in each scene.

Scene	Data file name from [65]	Range index	Azimuth index
Synthesized Rayleigh image	N/A		
Rural-1	fig1a.iq	153 299	130 225
Rural-2	fig_2_corrected.iq	312	63
Rural-3	fig_4_corrected.iq	474	276
Urban-1	fig_3_corrected.iq	462	278
Urban-2	fig_5_corrected.iq	343	131

Table B-2. Numbers of data domain azimuth and range samples for six SAR data sets.

Scene	Data file name from [65]	No. of azimuth samples	No. of range samples
Synthesized Rayleigh image	N/A	512	512
Rural-1	fig1a.iq	432	512
Rural-2	fig_2_corrected.iq	452	512
Rural-3	fig_4_corrected.iq	412	512
Urban-1	fig_3_corrected.iq	452	512
Urban-2	fig_5_corrected.iq	452	512

pixels on each side. These stop bands suggest that the original phase histories were either zero padded to achieve 512 azimuth pixels in the image, or were severely attenuated at the edges of the aperture. There is also an obvious but unknown taper across the aperture. The stop band and the aperture taper indicate that azimuth resolution is somewhat greater than a single FFT bin or pixel. Neither the aperture taper nor the size of the stop bands were provided with the data. The number of azimuth samples determined by examination of the data are catalogued in Table B-2. Although there also appeared to be stop bands in the range dimension, it is not an issue as critical to the analysis of the performance of the PGA algorithm as the stop bands in the azimuth dimension. Stop bands in the range dimension simply reduce the number of range samples over which phase gradients are estimated to a number less than 512. For the results presented here the range dimension was assumed to be the full 512 samples.

B.2 Exploratory Analysis of the SAR Data

Examination of isolated bright points in the data, as illustrated in Figure B-1 and later experience with the data, indicate that the total power in the seven pixels centered at the brightest point renders a reasonable estimation of total signal power. It can be argued that if seven points are too many, then the contribution to total power from the outer pixels is insignificant. This approach to determining total signal power is meaningful when considering signal-to-noise ratio (SNR) into the maximum likelihood (ML) estimation kernel of the PGA algorithm. Measures of scene contrast, however, require ratios of peak signal to mean clutter.

Comparisons of non-coherent sums shown in Figure 4-8 of Chapter 4 suggest differences in clutter statistics that may be a function of the width of the support of the point spread function. For this reason, analyses were repeated using the clutter data in the 1/4, 1/8, 1/16 of the total remaining image pixels surrounding the signal, as illustrated in Figure B-2.

Measures considered were ratios of signal-to- mean, median and maximum clutter. At each range, the ratio of signal-to- mean, median and maximum clutter was computed, producing 512 measures for each SAR data set. The arithmetic mean of clutter was used to calculate signal-to-mean-clutter. All results are expressed in dB. The arithmetic mean,

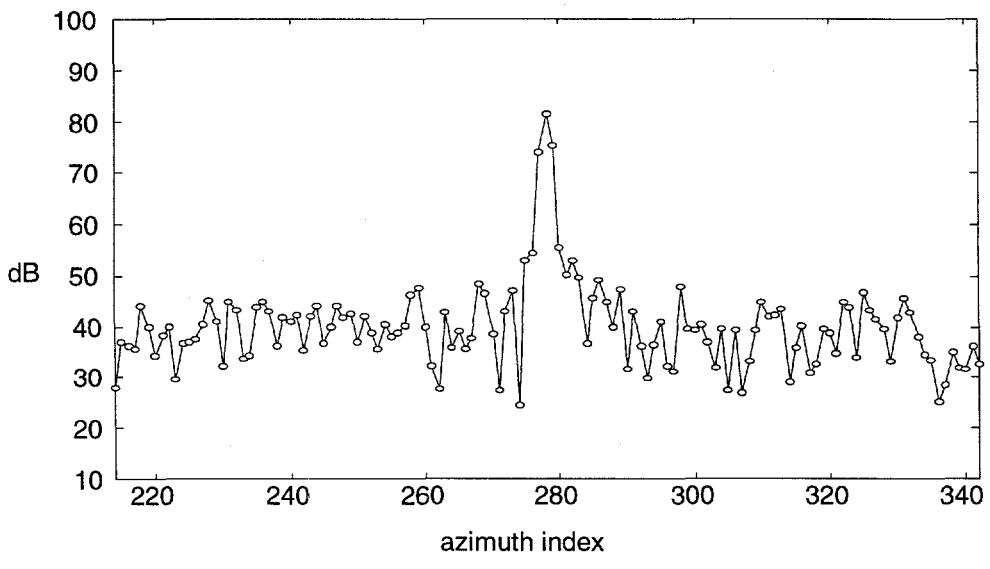

Figure B-1. Exploded view of detected image at range index 462 of scene Urban-1.

minimum, and maximum values for each data set are tabulated in Table B-3 through Table B-6 for the three selected supports of the point spread function. Mean values are tabulated in Table B-3 and Table B-4 for peak and total signal power respectively. Minimum and maximum values are tabulated in Table B-5, and Table B-6 again for peak and total signal power respectively. Note that there is little difference in the data among the three rural scenes and likewise little difference in the data between the two urban scenes. The mean values for the Rayleigh data are at least 3 dB less than those for the rural scenes. Mean total SCR for the three rural scenes is about 15 dB and about 27 dB for the two urban scenes.

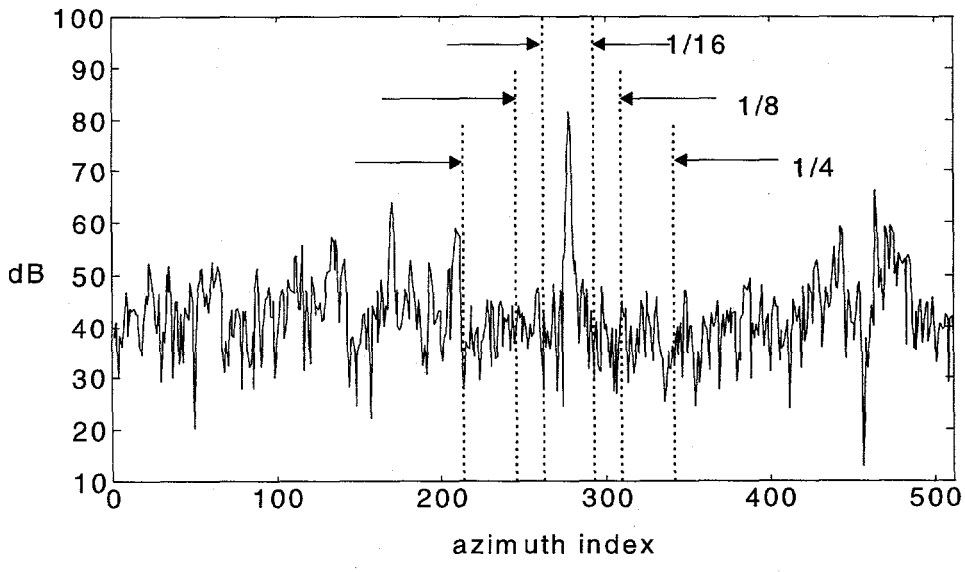

Figure B-2. Illustration of three windows used to calculate mean, median and maximum clutter surrounding brightest points. Data shown are from range index 462 of scene Urban 1. Maximum is at azimuth index 278.

Table B-3. Measures of scene contrast — summary of mean values using *peak* signal [dB].

Scene	Width of clutter window	Signal-to-mean clutter [dB] mean	Signal-to-median clutter [dB] mean	Signal-to-maximum clutter [dB] mean
Rayleigh	1/4	8.5	10.0	1.5
	1/8	8.5	10.1	2.2
	1/16	8.6	10.2	3.0
Rural 1	1/4	12.6	18.5	2.8
	1/8	11.7	16.2	3.5
	1/16	11.	14.4	4.7
Rural 2	1/4	11.3	14.5	2.8
	1/8	10.7	13.7	3.3
	1/16	10.4	13.1	4.3
Rural 3	1/4	10.8	14.5	2.3
	1/8	10.4	13.7	3.1
	1/16	10.1	12.8	4.2
Urban 1	1/4	24.6	31.8	12.8
	1/8	24.7	30.6	14.8
	1/16	24.9	29.2	17.6
Urban 2	1/4	23.6	30.5	12.2
	1/8	21.2	28.8	13.9
	1/16	23.3	27.4	16.3

Table B-4. Measures of signal and clutter power — summary of mean values using *total* signal [dB].

Scene	Width of clutter window	Signal-to-mean clutter [dB]		Signal-to-median clutter [dB]		Signal-to-maximum clutter [dB]	
		mean	median	mean	median	mean	median
Rayleigh	1/4	11.2		12.8		4.3	
	1/8	11.2		12.8		4.9	
	1/16	11.3		12.9		5.7	
Rural 1	1/4	16.7		22.6		6.9	
	1/8	15.7		20.3		7.6	
	1/16	15.0		18.4		8.7	
Rural 2	1/4	15.4		18.6		6.8	
	1/8	14.7		17.8		7.3	
	1/16	14.3		17.0		8.2	
Rural 3	1/4	15.0		18.7		6.5	
	1/8	14.5		17.9		7.2	
	1/16	14.2		16.9		8.3	
Urban 1	1/4	26.9		34.2		15.0	
	1/8	27.0		33.0		16.9	
	1/16	27.1		31.4		19.8	
Urban 2	1/4	26.0		33.0		14.6	
	1/8	25.6		31.2		16.2	
	1/16	25.7		29.8		18.6	

Table B-5. Measures of scene contrast — summary of minimum and maximum values using *peak* signal[dB].

Scene	Width of clutter window	Signal-to-mean clutter [dB]		Signal-to-median clutter [dB]		Signal-to-maximum clutter [dB]	
		min	max	min	max	min	max
Rayleigh	1/4	6.2	11.2	7.1	13.6	0.0	5.0
	1/8	5.8	12.0	6.5	13.9	0.0	5.6
	1/16	5.6	12.6	6.2	15.4	0.0	7.8
Rural 1	1/4	7.0	22.6	7.6	28.3	0.0	11.7
	1/8	6.1	20.6	7.6	26.4	0.0	11.7
	1/16	4.6	24.0	4.8	25.8	0.0	17.9
Rural 2	1/4	6.3	19.3	7.4	23.2	0.0	9.8
	1/8	5.9	18.4	7.3	22.7	0.0	11.3
	1/16	4.7	20.0	5.6	23.0	0.0	13.9
Rural 3	1/4	6.0	19.8	7.0	25.9	0.0	10.8
	1/8	5.4	22.4	6.2	25.9	0.0	15.8
	1/16	4.9	22.5	5.6	25.9	0.0	16.6
Urban 1	1/4	10.6	40.8	13.7	43.9	0.0	29.8
	1/8	8.9	39.2	12.0	42.2	0.0	29.8
	1/16	6.6	38.0	9.2	41.6	0.0	30.9
Urban 2	1/4	10.9	36.4	14.0	45.2	0.0	27.1
	1/8	8.6	35.1	11.0	41.0	0.0	27.7
	1/16	6.9	36.1	10.0	38.5	0.0	30.2

Table B-6. Measures of signal and clutter power — summary of minimum and maximum values using *total* signal[dB].

Scene	Width of clutter window	Signal-to-mean clutter [dB]		Signal-to-median clutter [dB]		Signal-to-maximum clutter [dB]	
		min	max	min	max	min	max
Rayleigh	1/4	7.9	13.6	9.5	15.4	1.8	7.8
	1/8	7.3	14.3	8.0	16.2	1.8	8.5
	1/16	7.4	14.4	8.0	17.7	1.8	9.4
Rural 1	1/4	10.1	23.2	11.7	30.9	2.6	14.9
	1/8	9.9	22.9	11.4	28.0	2.5	15.8
	1/16	8.1	26.5	9.12	28.3	2.8	20.4
Rural 2	1/4	9.0	22.8	11.0	27.0	2.4	14.2
	1/8	9.0	22.9	10.0	26.3	2.5	16.6
	1/16	8.6	23.0	9.0	26.6	2.6	16.9
Rural 3	1/4	8.5	24.3	9.6	29.1	1.2	15.3
	1/8	7.9	25.4	8.7	29.3	1.2	18.7
	1/16	7.7	25.4	8.6	29.1	2.9	19.6
Urban 1	1/4	13.1	42.4	16.6	45.4	1.9	31.4
	1/8	12.1	40.8	15.7	44.6	2.1	31.4
	1/16	8.9	39.6	13.6	43.6	2.1	33.1
Urban 2	1/4	26.8	37.9	17.2	47.2	2.1	29.0
	1/8	11.4	37.6	13.7	43.1	2.1	29.3
	1/16	10.7	37.6	13.3	40.9	2.4	31.7

B.3 Histograms and Scattergrams of Data for 1/4 Wide Support

Data for the 1/4 image wide clutter are displayed in histograms and scattergrams in Figure B-3 through Figure B-8 for the Rayleigh data and the five sets of real SAR data. The histograms and scattergrams in the left columns are for the Rayleigh or real SAR data. With the exception of the Rayleigh data, where the columns on the right are for synthesized data with 15 dB SCR, the histograms and scattergrams in the right column are for synthesized data with the same distributions of signal to clutter. The data synthesis procedure was described in Chapter 4, Section 4.2.1.

These histograms and scattergrams display the following, using total signal (as opposed to peak signal):

Distributions of:

1. Signal-to-mean, -median, and -maximum clutter ratios are shown in rows 1, 2, and 3 of parts (a).
2. Position of maximum clutter pixel relative to signal pixel is shown in row 4 of part (a).

Correlations between the following are in rows 1 through 4 respectively of parts (b) of the figures:

1. Position of maximum clutter and signal-to-clutter ratios.
2. Position of maximum clutter and maximum-clutter-to-mean-clutter ratios.
3. Signal-to-maximum clutter ratio and signal-to-mean clutter ratio.
4. Maximum-to-mean clutter ratio and signal-to-mean clutter ratio.

The data were visually inspected and the findings are summarized in Table B-7.

Table B-7. Summary of exploratory analyses of real and synthesized SAR data.

Distributions	Real SAR data	Synthesized SAR data
1. Signal-to-mean -median and -maximum clutter ratios.	The range of values is consistent with measured RCS reported in the literature. Monotonic increase in SCR with increase in width of support. Calculation of SNR for a given width of support of the point spread function may require special numerical handling.	No change in SCR as a function of width of the support. $SNR = SCR/N_{support}$
2. Maximum clutter position relative to signal.	Slightly less than uniform. May be significant to data model.	Uniformly distributed.
Correlations		
3. Maximum clutter position and signal-to-clutter ratios.	Uncorrelated.	Uncorrelated.
4. Maximum clutter position and maximum-clutter-to-mean-clutter ratios.	Uncorrelated.	Uncorrelated.
5. Signal-to-maximum clutter ratio and signal-to-mean-clutter ratio.	Linearly correlated. Y-intercept is significantly less than for synthesized data than for real SAR data.	Linearly correlated.
6. Maximum-to-mean clutter ratio and signal-to-mean clutter ratio.	May be correlated and significant to data model.	Uncorrelated.

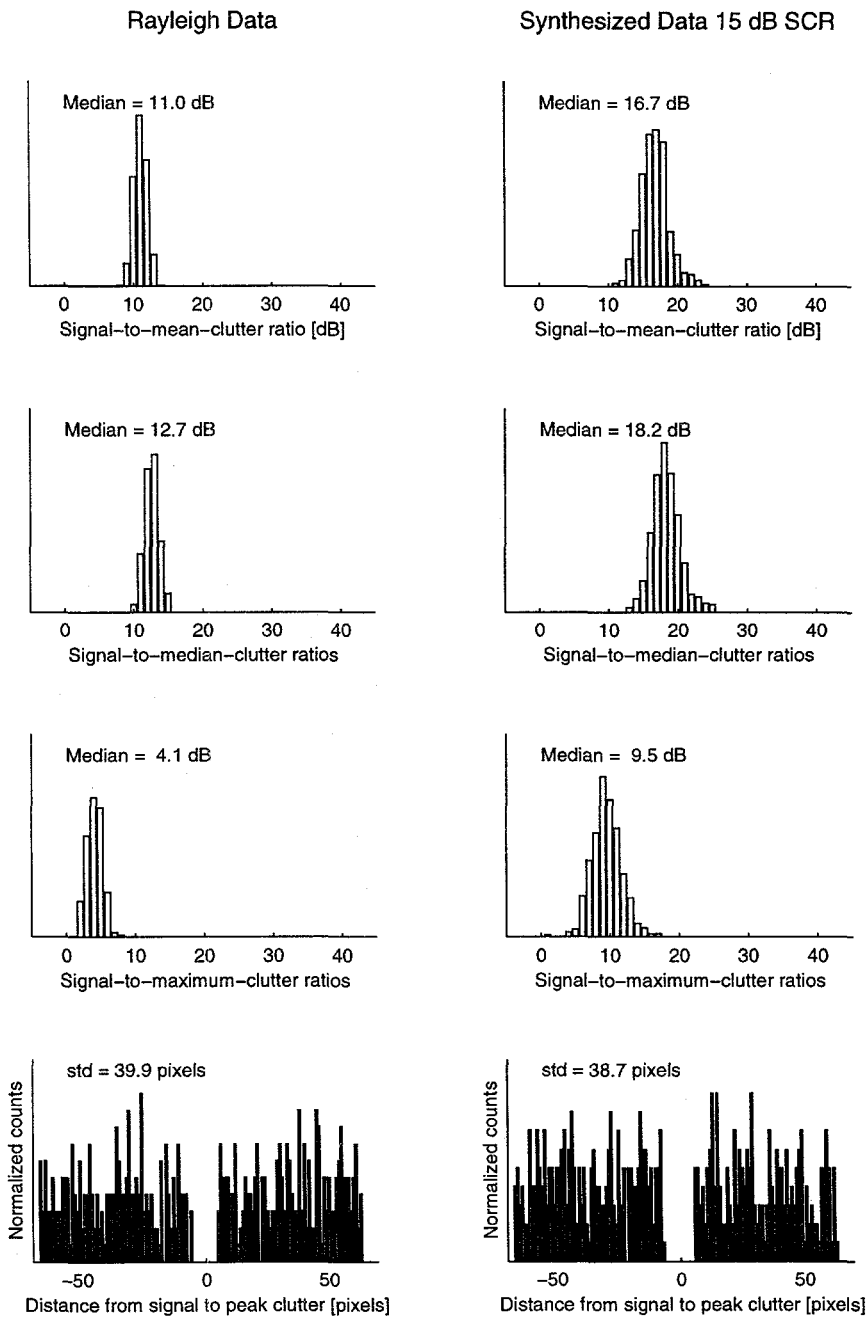

Figure B-3a. Comparison of metrics of synthesized Rayleigh data and synthesized SAR data with 15 dB SCR.

The differences in the distributions of signal-to-maximum clutter and the position of maximum clutter relative to signal suggest differences between the real and synthesized SAR data.

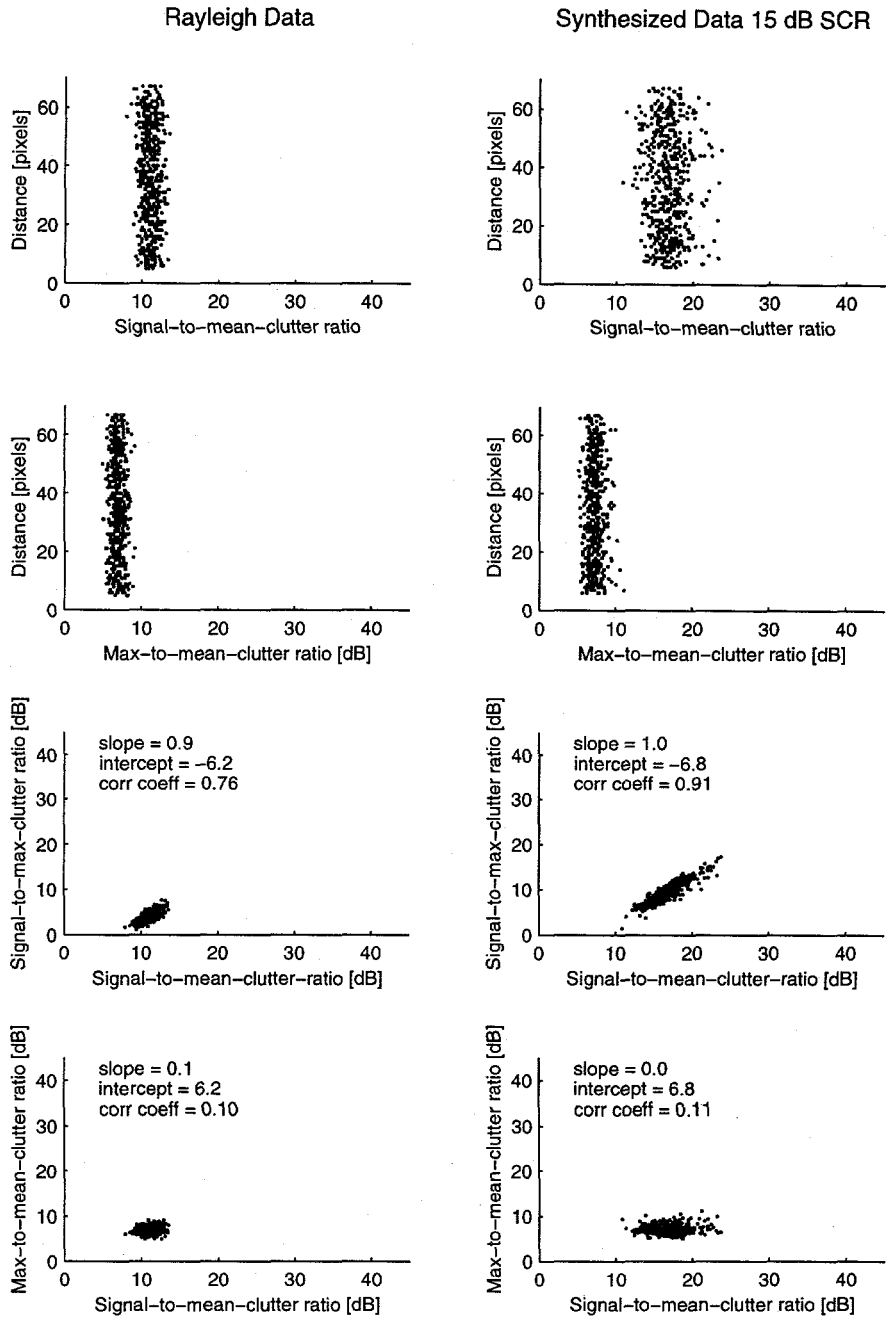

Figure B-3b. Comparison of metrics of synthesized Rayleigh data and synthesized SAR data with 15 dB SCR.

The differences in the distributions of signal-to-maximum clutter and the position of maximum clutter relative to signal suggest differences between the real and synthesized SAR data.

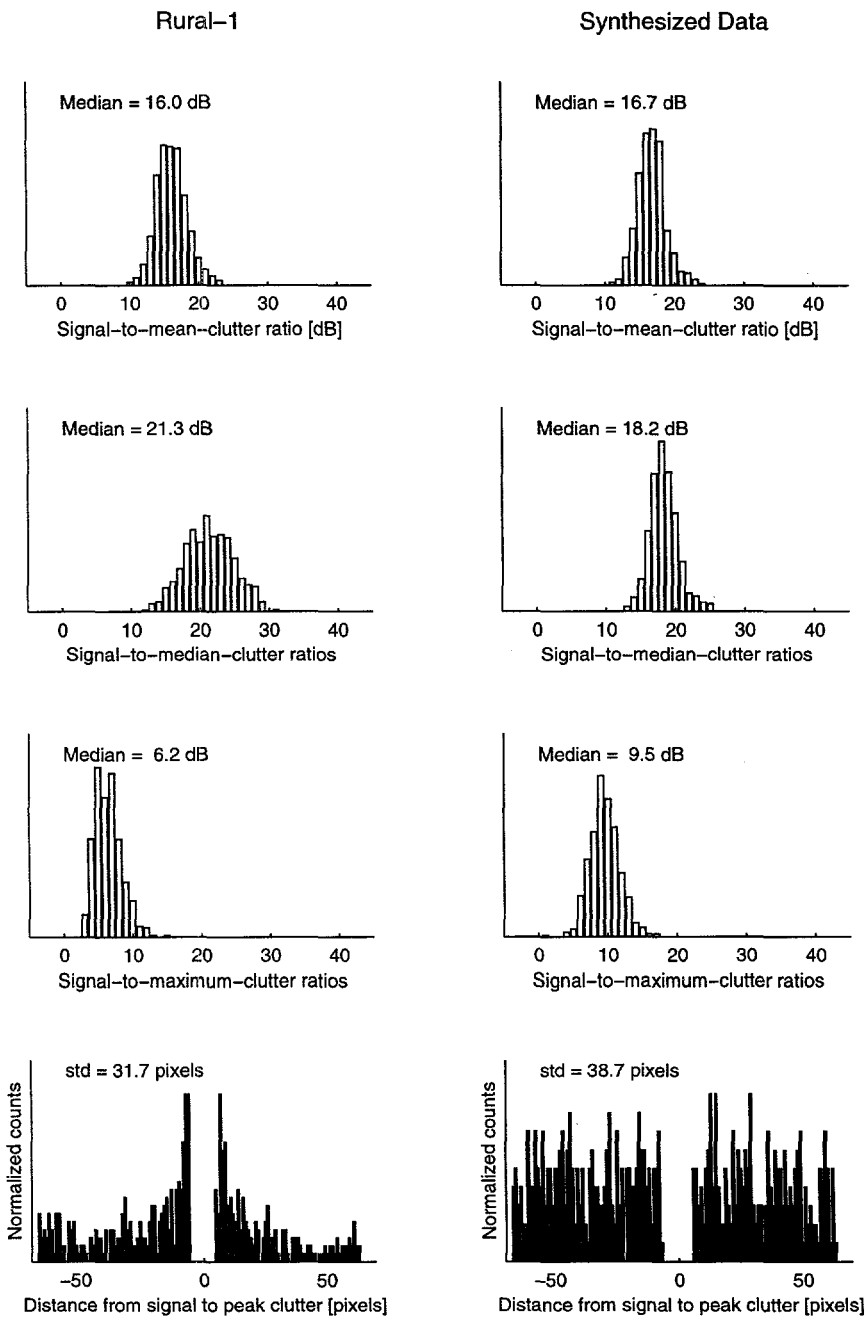

Figure B-4a. Comparison of metrics of Rural-1 and synthesized SAR data.

The differences in the distributions of signal-to-maximum clutter and the position of maximum clutter relative to signal suggest differences between the real and synthesized SAR data.

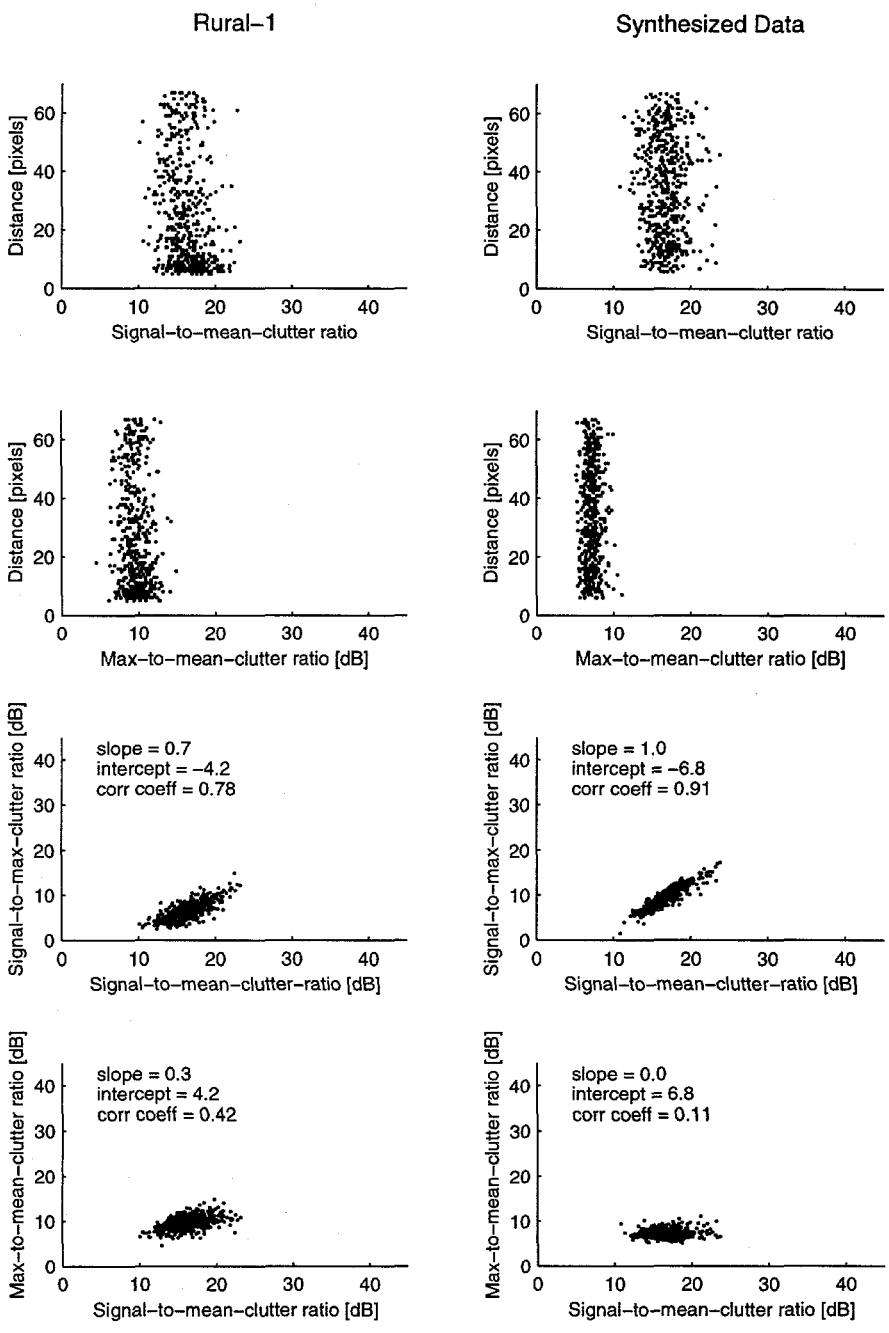

Figure B-4b. Comparison of metrics of Rural-1 and synthesized SAR data.

The four upper scattergrams show no correlation between signal-to-clutter ratio and signal-to-clutter position. The four lower scattergrams indicate some differences in clutter distributions between real and synthesized SAR data.

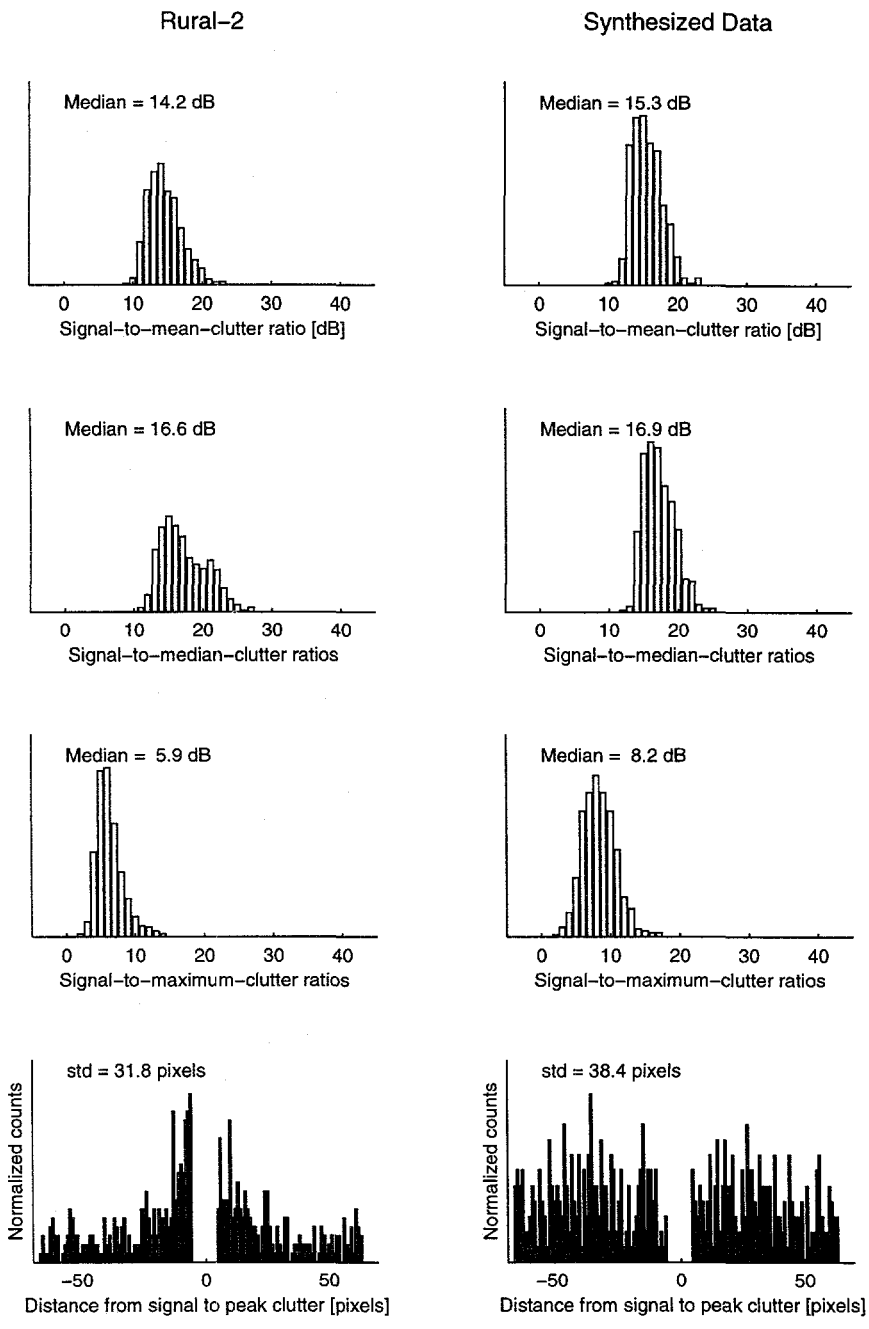

Figure B-5a. Comparison of metrics of Rural-2 and synthesized SAR data.

The differences in the distributions of signal-to-maximum clutter and the position of maximum clutter relative to signal suggest differences between the real and synthesized SAR data.

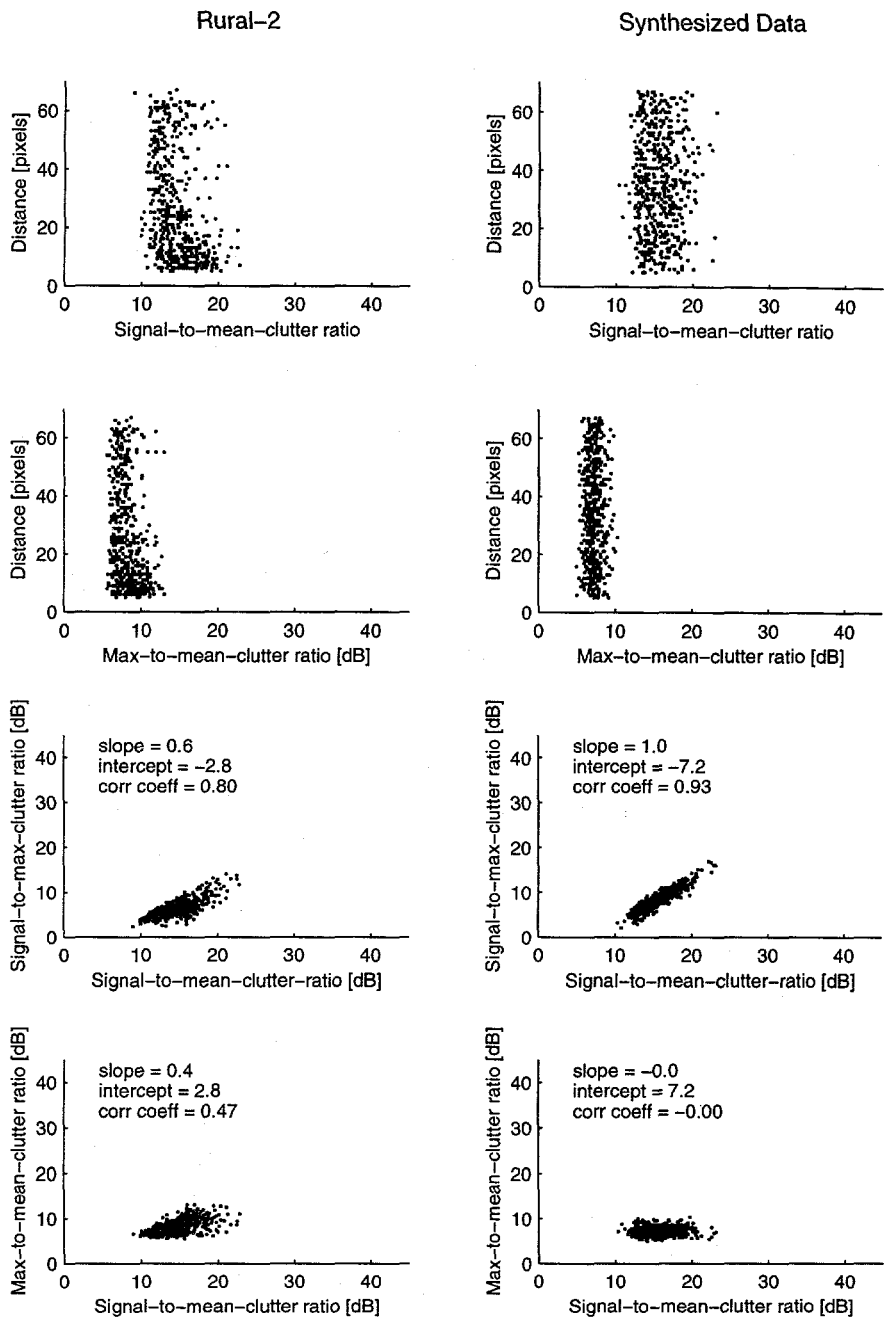

Figure B-5b. Comparison of metrics of Rural-2 and synthesized SAR data.

The four upper scattergrams show no correlation between signal-to-clutter ratio and signal-to-clutter position. The four lower scattergrams indicate some differences in clutter distributions between real and synthesized SAR data.

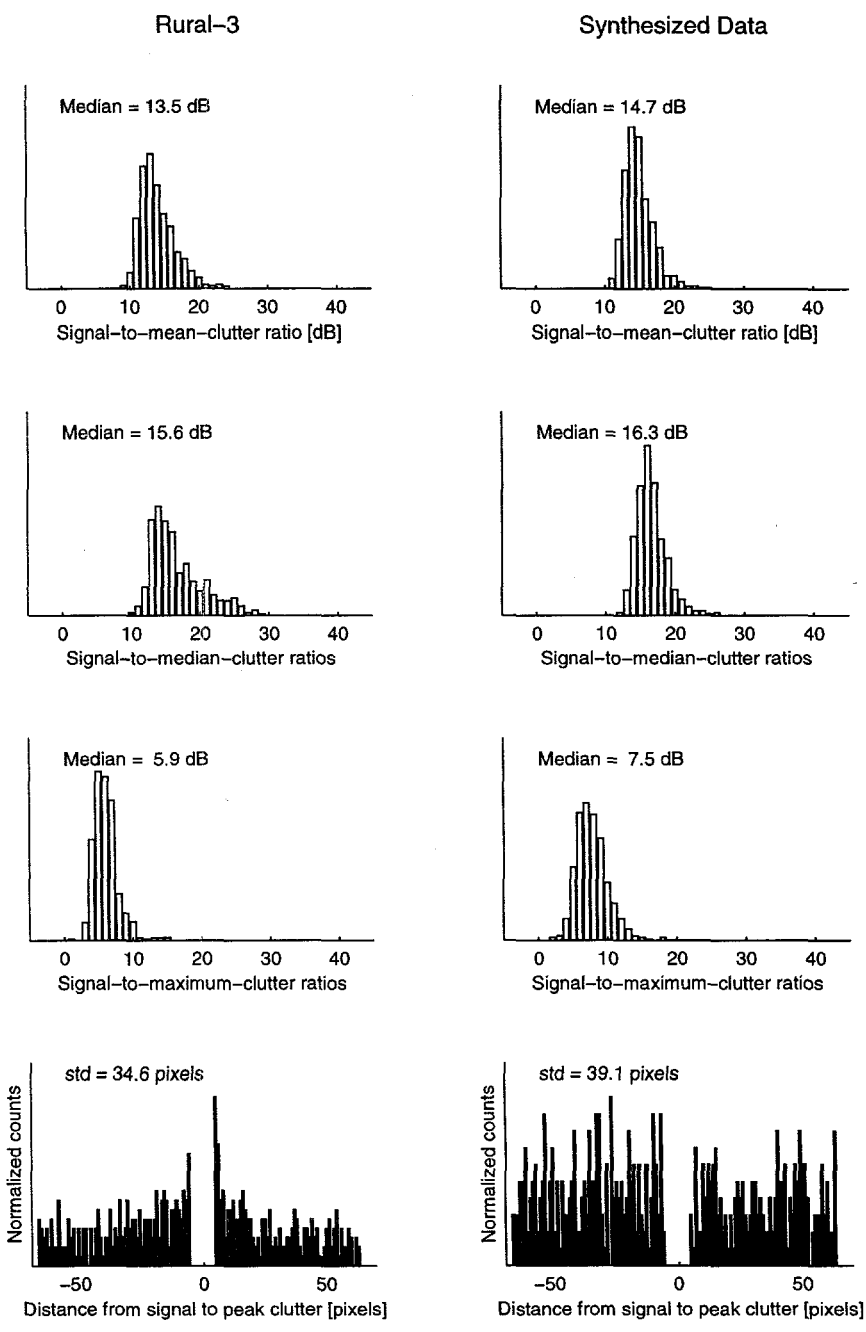

Figure B-6a. Comparison of metrics of Rural-3 and synthesized SAR data.

The differences in the distributions of signal-to-maximum clutter and the position of maximum clutter relative to signal suggest differences between the real and synthesized SAR data.

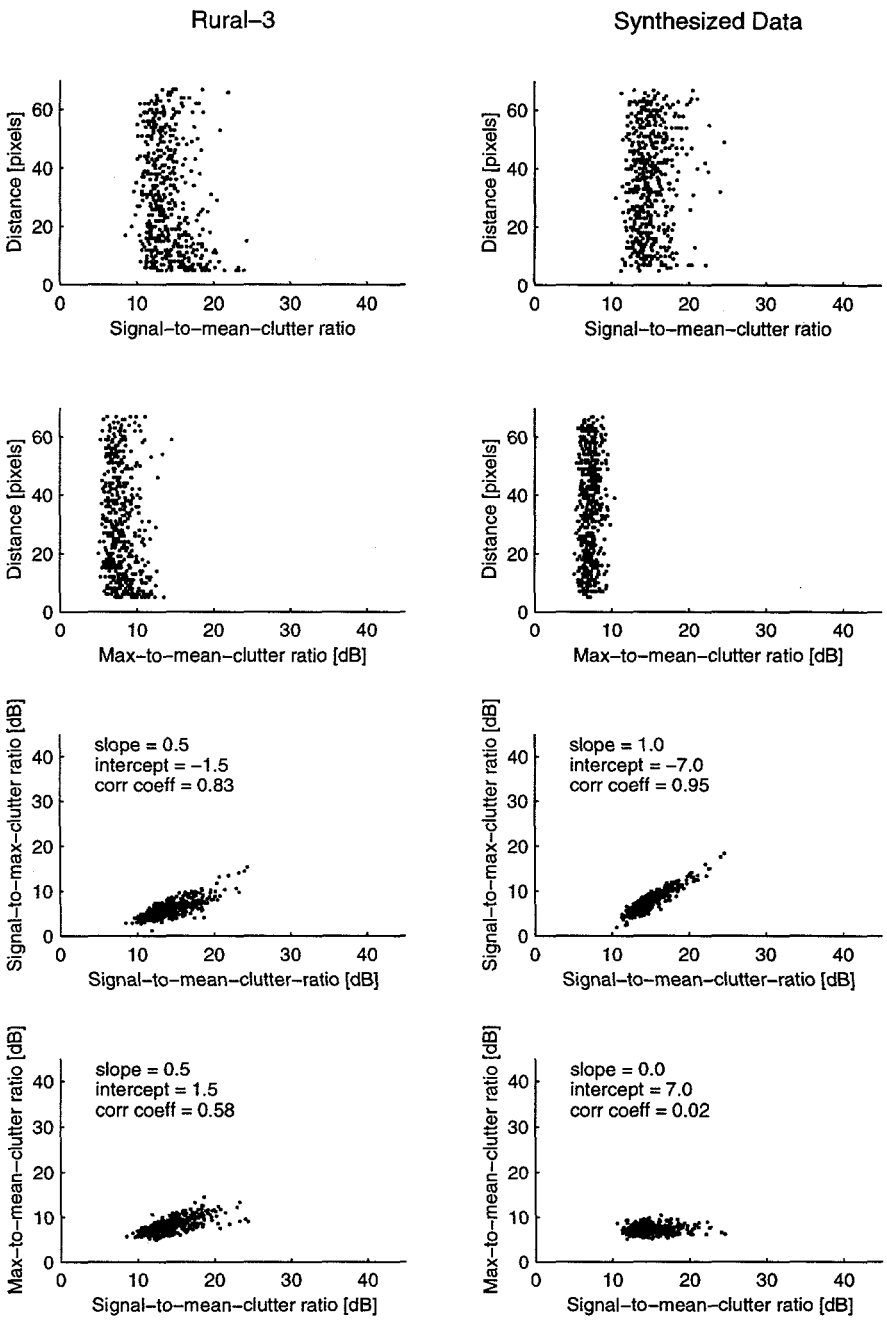

Figure B-6b. Comparison of metrics of Rural-3 and synthesized SAR data.

The four upper scattergrams show no correlation between signal-to-clutter ratio and signal-to-clutter position. The four lower scattergrams indicate some differences in clutter distributions between real and synthesized SAR data.

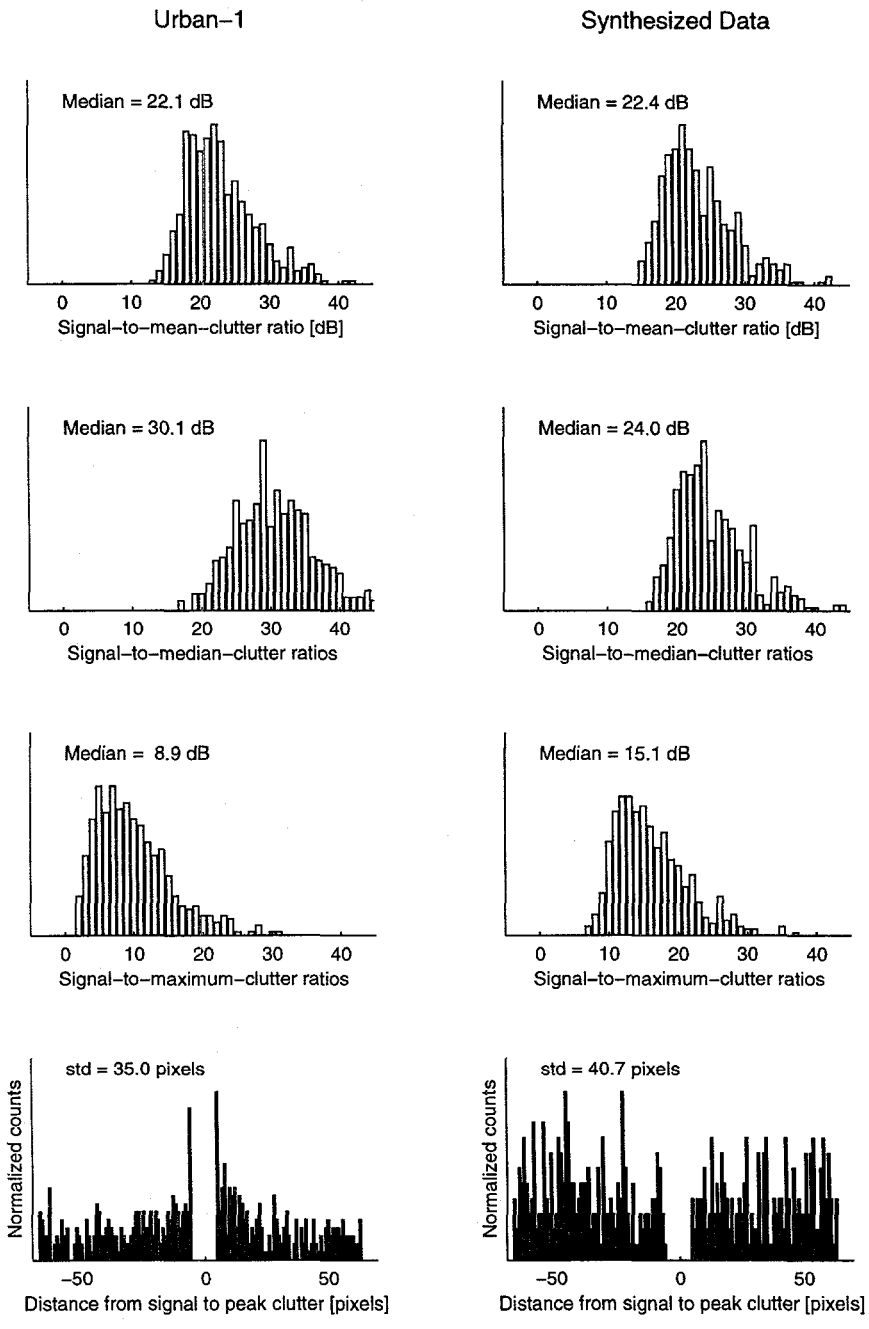

Figure B-7a. Comparison of metrics of Urban-1 and synthesized SAR data.

The differences in the distributions of signal-to-maximum clutter and the position of maximum clutter relative to signal suggest differences between the real and synthesized SAR data.

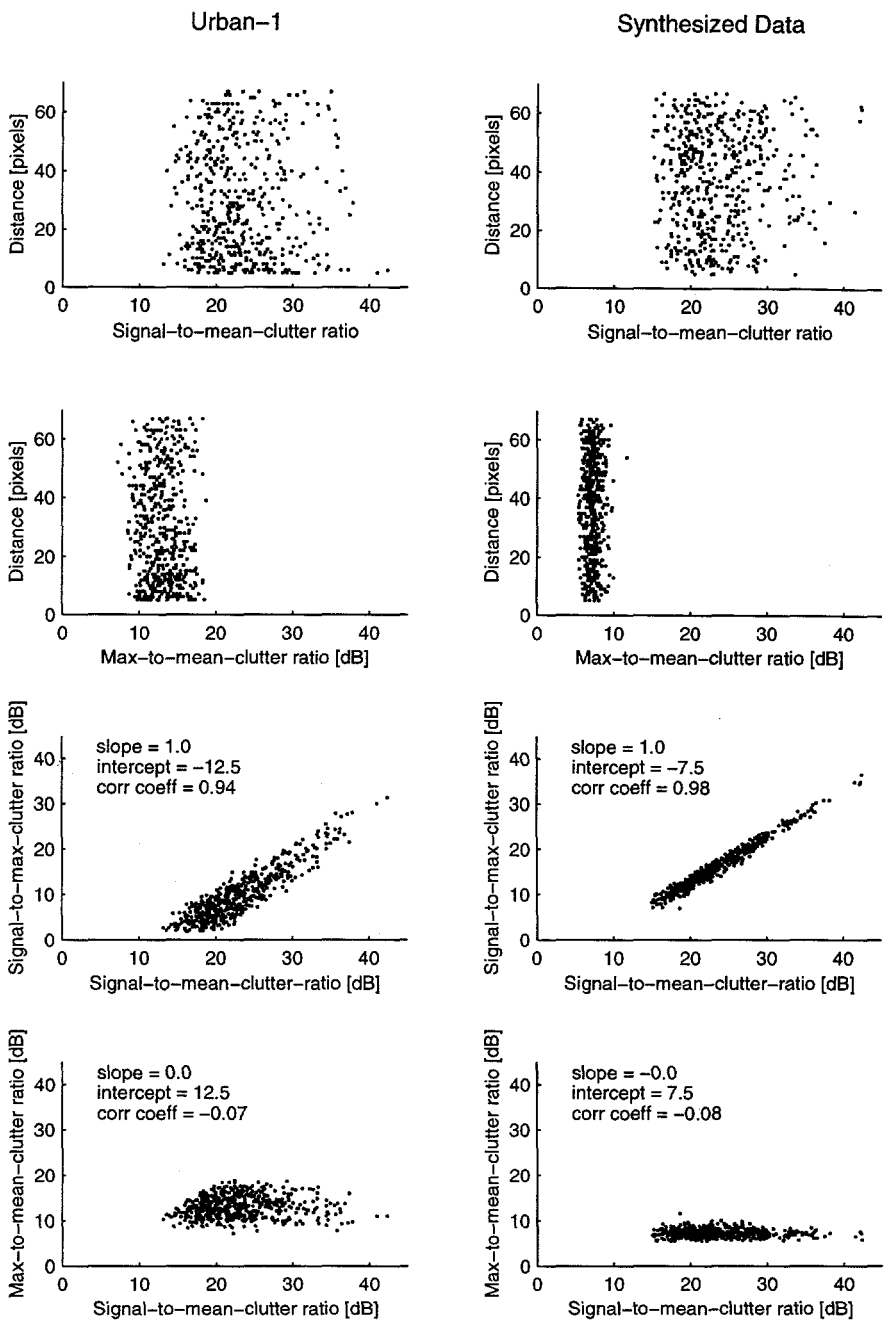

Figure B-7b. Comparison of metrics of Urban-1 and synthesized SAR data.

The four upper scattergrams show no correlation between signal-to-clutter ratio and signal-to-clutter position. The four lower scattergrams indicate some differences in clutter distributions between real and synthesized SAR data.

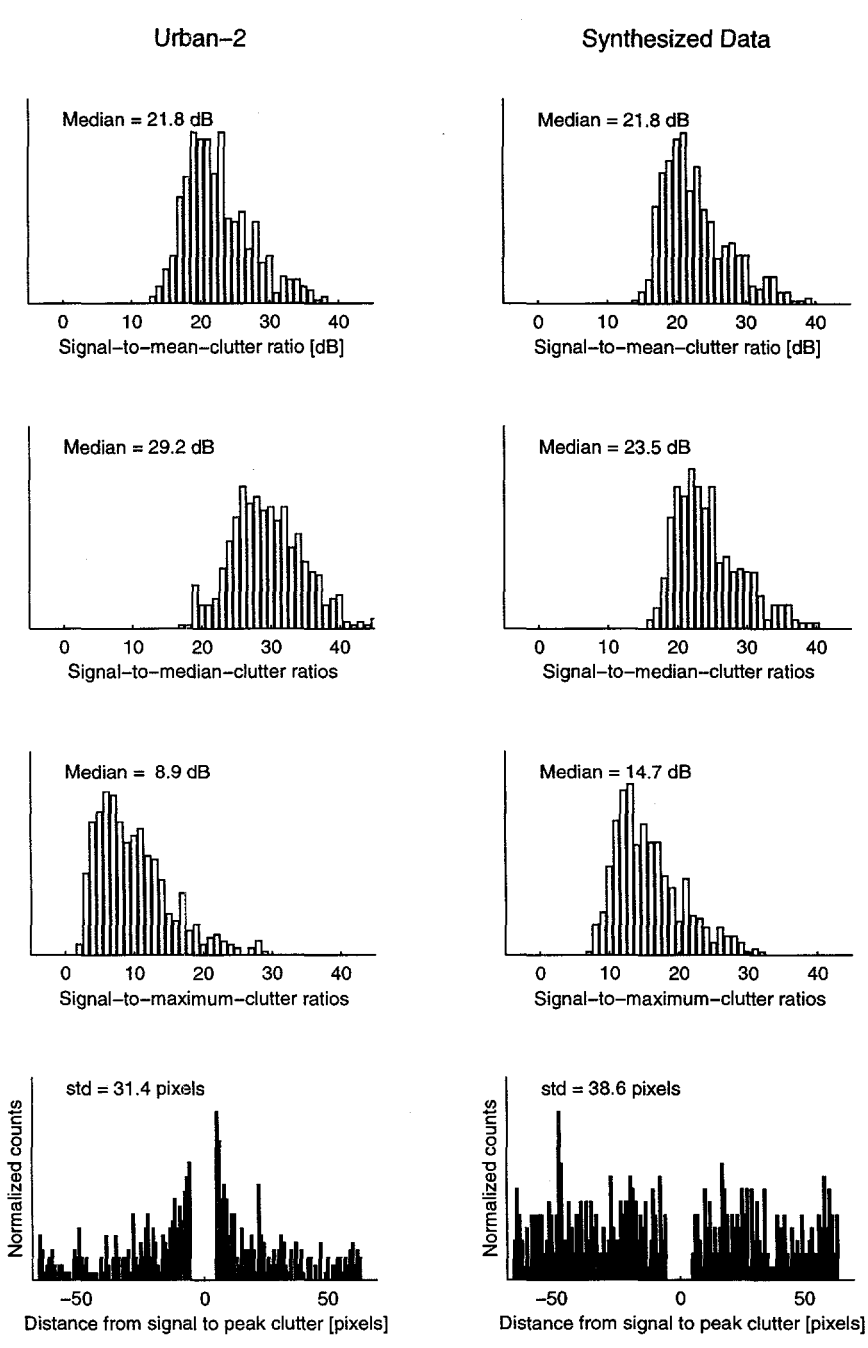

Figure B-8a. Comparison of metrics of Urban-2 and synthesized SAR data.

The differences in the distributions of signal-to-maximum clutter and the position of maximum clutter relative to signal suggest differences between the real and synthesized SAR data.

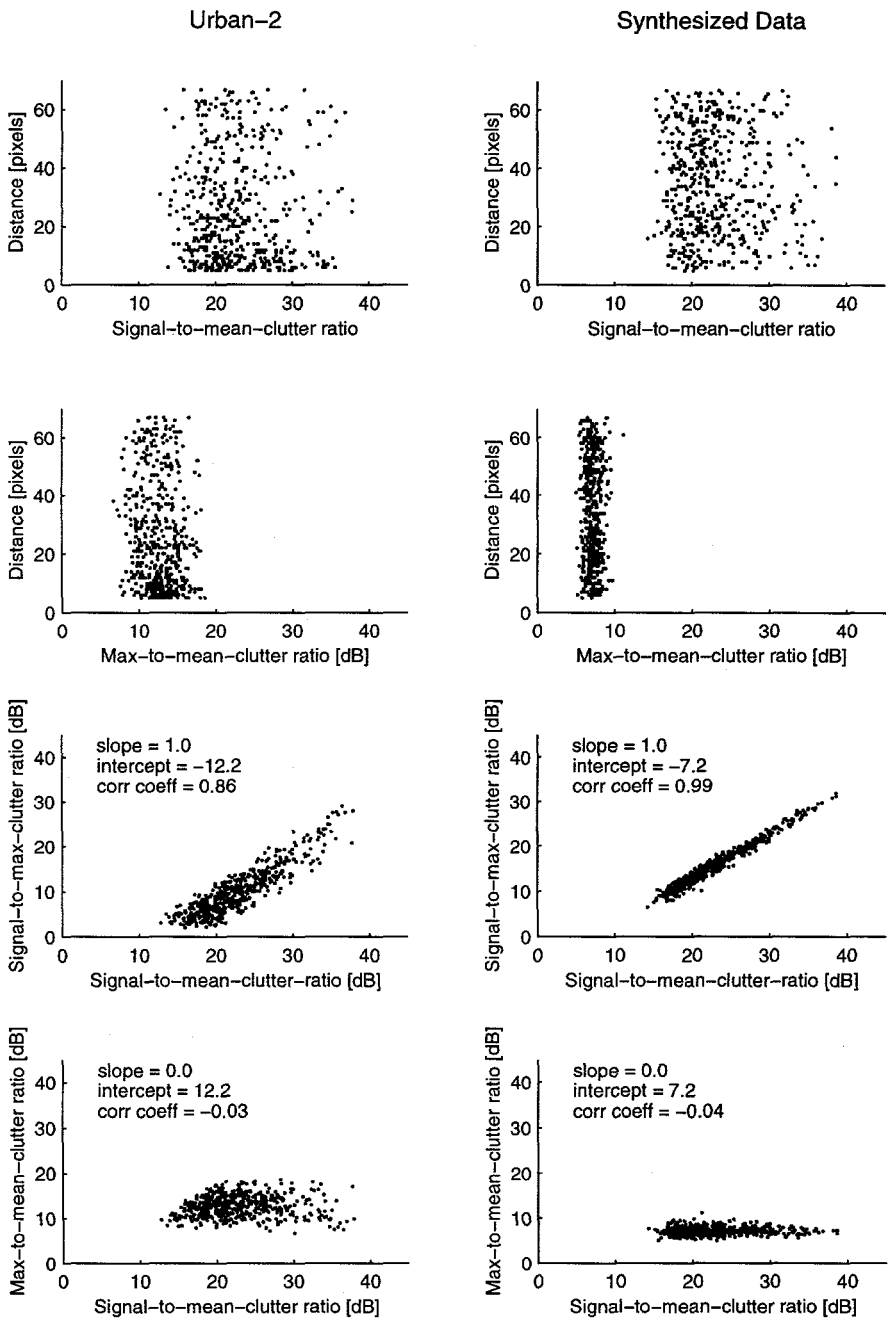

Figure B-8b. Comparison of metrics of Urban-2 and synthesized SAR data.

The four upper scattergrams show no correlation between signal-to-clutter ratio and signal-to-clutter position. The four lower scattergrams indicate some differences in clutter distributions between real and synthesized SAR data.

Appendix C

Derivation of Cramér Rao Lower Bound for Unbiased Estimators

In this appendix the Cramér Rao lower bound is derived for the two data models (zero mean and non-zero mean) discussed in Chapter 5. In Chapter 3 the model for the observations, $x_{k,m}$, was given as

$$x_{k,m} = a_k e^{j\phi_m} + n_{k,m} \tag{C-1}$$

where

$a_k = |a_k| e^{j\theta_k}$ is the complex envelope of the signal at the k^{th} range. The expected value of the magnitude squared of a_k, $E\{|a_k|^2\} = \sigma_a^2$ and $|a_k|$ are assumed to be independent and identically distributed across ranges, but invariant across azimuth at any single range. Similarly θ_k, a target dependent phase is assumed to be independent and identically and uniformly distributed across ranges, but invariant across azimuth at any single range.

ϕ_m is the aberrating phase of interest at the m^{th} azimuth sample and is assumed to be invariant across ranges for any given azimuth index.

$n_{k,m}$ is complex circularly Gaussian noise, assumed to be independent and identically distributed for all range samples indexed by k and all azimuth samples indexed by m. Noise power is defined as $E\left\{\left|n_{k,m}\right|^2\right\}=\sigma_n^2$.

In Chapter 5 the general form of the Cramér Rao lower bound for an unbiased estimator was given in equation (5-3) as

$$E\left\{\left(\hat{\psi}-\psi\right)^2|\mathbf{x}\right\}\geq\left[-E\left\{\frac{\partial^2 \ln p(\mathbf{x}|\psi)}{\partial\psi^2}\right\}\right]^{-1} \tag{C-2}$$

where the Fisher information matrix, $\mathbf{J}=-E\left\{\frac{\partial^2 \ln p(\mathbf{x}|\psi)}{\partial\psi^2}\right\}$.

In Chapter 5 equation (5-7), it was shown that the log likelihood function for circularly Gaussian data is

$$\sum_{k=1}^{N_{ranges}}\ln p(\mathbf{x}_k|\psi)=-\left(\sum_{k=1}^{N_{ranges}}\ln\left[\pi^2|\mathbf{C}_k|\right]+\mathbf{x}_k^H\mathbf{C}_k^{-1}\mathbf{x}_k\right). \tag{C-3}$$

For pair-wise estimates of zero mean data, the covariance matrix

$$\mathbf{C}=\begin{bmatrix}\sigma_a^2+\sigma_n^2 & \sigma_a^2e^{-j\psi}\\ \sigma_a^2e^{j\psi} & \sigma_a^2+\sigma_n^2\end{bmatrix} \tag{C-4}$$

and the determinant $|\mathbf{C}|=\left(\sigma_a^2+\sigma_n^2\right)^2-\left(\sigma_a^2\right)^2=\left(\sigma_n^2\right)^2+2\sigma_n^2\sigma_a^2$, which is not a function of ψ. The log likelihood function for identically distributed complex envelop, a, and noise, n, then reduces to

$$N_{ranges}\ln p(\mathbf{x}_k|\psi)=-N_{ranges}\mathbf{x}_k^H\mathbf{C}_k^{-1}\mathbf{x}_k. \tag{C-5}$$

where

$$\mathbf{C}^{-1} = \frac{1}{|\mathbf{C}|}\begin{bmatrix} \sigma_a^2 + \sigma_n^2 & -\sigma_a^2 e^{-j\psi} \\ -\sigma_a^2 e^{j\psi} & \sigma_a^2 + \sigma_n^2 \end{bmatrix}. \tag{C-6}$$

The Fisher information matrix $\mathbf{J} = -E\left\{\frac{\partial^2 \ln p(\mathbf{x}|\psi)}{\partial \psi^2}\right\}$

$$= N_{ranges} E\left\{\mathbf{x}_k^H \frac{d^2 \mathbf{C}_k^{-1}}{d\psi^2}\mathbf{x}_k\right\}$$

$$= N_{ranges} \frac{1}{|\mathbf{C}|} E\left\{\mathbf{x}_k^H \begin{bmatrix} 0 & \sigma_a^2 e^{-j\psi} \\ \sigma_a^2 e^{j\psi} & 0 \end{bmatrix}\mathbf{x}_k\right\}$$

$$= N_{ranges} \frac{1}{|\mathbf{C}|} E\left\{x_{m-n} x_m^* \sigma_a^2 e^{j\psi} + x_{m-n}^* x_m \sigma_a^2 e^{-j\psi}\right\}$$

$$= \frac{1}{|\mathbf{C}|} 2N_{ranges}\left(\sigma_a^2\right)^2. \tag{C-7}$$

$\mathbf{J}^{-1} = \frac{\left(\sigma_n^2\right)^2 + 2\sigma_n^2\sigma_a^2}{2N_{ranges}\left(\sigma_a^2\right)^2}$. Substituting signal-to-noise ratio $\beta = \frac{\sigma_a^2}{\sigma_n^2}$ produces

$$\mathbf{J}^{-1} = \frac{1+2\beta}{2N_{ranges}\beta^2}. \tag{C-8}$$

Consider now data that are not zero mean but with noise that is zero mean, complex, circularly Gaussian. Then the log-likelihood function is

$$\sum_{k=1}^{N_{ranges}} \ln p(\mathbf{x}_k|\phi, a_k) = -\left(\sum_{k=1}^{N_{ranges}} \ln\left[\pi^2|\mathbf{C}_k|\right] + \left(\mathbf{x}_k^H - \boldsymbol{\mu}_{\mathbf{x}_k}^*\right)\mathbf{C}^{-1}\left(\mathbf{x}_k - \boldsymbol{\mu}_{\mathbf{x}_k}\right)\right) \tag{C-9}$$

where the covariance matrix

$$\mathbf{C} = \begin{bmatrix} \sigma_n^2 & 0 \\ 0 & \sigma_n^2 \end{bmatrix} \tag{C-10}$$

and is determinant $|\mathbf{C}| = \left(\sigma_n^2\right)^2$, which is not a function of ψ. The log likelihood function for identically distributed complex envelope, a, and noise, n, then reduces to

$$N_{ranges} \ln p(\mathbf{x}_k|\psi) = -N_{ranges}\left(\mathbf{x}_k^H - \boldsymbol{\mu}_{\mathbf{x}_k}^*\right)\mathbf{C}^{-1}\left(\mathbf{x}_k - \boldsymbol{\mu}_{\mathbf{x}_k}\right). \tag{C-11}$$

The Fisher information matrix $J_{m,n} = -E\left\{\dfrac{\partial^2 \ln p(\mathbf{x}|\psi)}{\partial\phi_{m-n}\phi_m}\right\}$

$$= N_{ranges} E\left\{\frac{\partial^2}{\partial\phi_{m-n}\phi_m}\left(\mathbf{x}_k - \boldsymbol{\mu}_{\mathbf{x}_k}\right)^H \mathbf{C}^{-1}\left(\mathbf{x}_k - \boldsymbol{\mu}_{\mathbf{x}_k}\right)\right\}$$

$$= N_{ranges}\frac{1}{\sigma_n^2} E\left\{\frac{\partial^2}{\partial\phi_{m-n}\phi_m}\left(\mathbf{x}_k - \boldsymbol{\mu}_{\mathbf{x}_k}\right)^H \left(\mathbf{x}_k - \boldsymbol{\mu}_{\mathbf{x}_k}\right)\right\}$$

$$= N_{ranges}\frac{1}{\sigma_n^2} E\left\{\frac{\partial^2}{\partial\phi_{m-n}\phi_m}\left(x_{m-n}x_{m-n}^* + x_m^* x_m\right)\right\}$$

$$= \frac{\sigma_a^2}{\sigma_n^2} 2N_{ranges} \text{ for } m = n \tag{C-12}$$

$$= 0 \text{ otherwise.}$$

Thus $\mathbf{J} = \dfrac{\sigma_a^2}{\sigma_n^2} 2N_{ranges}\begin{bmatrix} 1 & 0 \\ 0 & 1 \end{bmatrix}$ and

$$\mathbf{J}^{-1} = \frac{1}{2N_{ranges}\beta}\begin{bmatrix} 1 & 0 \\ 0 & 1 \end{bmatrix}. \tag{C-13}$$

On page 83 of [61], Van Trees provides the following general form for determining the CRLB for unbiased estimates of functions, $g(\mathbf{A})$, of the basic parameters, $\mathbf{A}$.

$$E\left\{\left(\hat{g}(\mathbf{A}) - g(\mathbf{A})\right)^2 |\mathbf{x}\right\} \geq \left[\nabla\left(g^H(\mathbf{A})\right)\right]^H \mathbf{J}^{-1}\left[\nabla\left(g^H(\mathbf{A})\right)\right], \tag{C-14}$$

where $\mathbf{x}$ is the observation vector,

A is the vector of basic parameters,

g(**A**) is a column vector of the functions of **A** that are of interest,

∇ is the gradient operator,

the superscript H is the Hermitian or complex conjugate transpose, and

J is the Fisher information matrix.

For this application $g(A) = \psi = \phi_m - \phi_{m-n}$ and $\nabla g(A) = [-1 \quad 1]^T$, thus

$$CRLB = E\left\{\left(\hat{g}(\mathbf{A}) - g(\mathbf{A})\right)^2 | \mathbf{x}\right\}$$

$$\geq \frac{1}{2N_{ranges}\beta}[-1 \quad 1]\begin{bmatrix}1 & 0\\ 0 & 1\end{bmatrix}\begin{bmatrix}-1\\ 1\end{bmatrix}$$

$$= \frac{1}{N_{ranges}\beta}. \qquad \text{(C-15)}$$

This completes the derivation of the CRLB for two data models. Results illustrate Swerling's point in [56] that the formulation of the data model affects the computed CRLB. Equations (C-8) and (C-15) are given in Chapter 5 as equations (5-8) and (5-10).

Appendix D

Taylor Series Expansion of

Maximum Likelihood Estimator

In this appendix the issue of phase-gradient estimator bias is addressed. This appendix is subdivided into three topics.

1. Derivation of estimator bias using nested Taylor series expansions.
2. Calculation of $\left(\frac{dE\{\hat{\psi}\}}{d\psi}\right)^2$, the numerator in the expression for the Cramér-Rao lower bound (CRLB) of a biased estimator.
3. Calculation of the Fisher information matrix, the inverse of which completes the derivation of the CRLB.

The critical expressions necessary to gain insight into the behavior of both noise-induced and inherent estimator bias are developed. The full expressions for the Cramér Rao lower bounds are not developed, however, the solution to these problems is outlined.

D.1 Derivation of Estimator Bias

The data model as given in Chapter 3 is:

$$x_{k,m} = a_k e^{j\phi_m} + n_{k,m}$$

where

$a_k = |a_k| e^{j\theta_k}$ is the complex envelope of the signal at the k^{th} range. The expected value of the magnitude squared of a_k, $E\{|a_k|^2\} = \sigma_a^2$ and $|a_k|$ are assumed to be independent and identically distributed across ranges, but invariant across azimuth at any single range. Similarly θ_k, a target-dependent phase at the k^{th} range, is assumed to be independent and identically and uniformly distributed across ranges, but invariant across azimuth at any single range.

ϕ_m is the aberrating phase of interest at the m^{th} azimuth sample and is assumed to be invariant across ranges for any given azimuth index.

$n_{k,m}$ is complex circularly Gaussian noise, assumed to be independent and identically distributed for all range samples indexed by k and all azimuth samples indexed by m. Noise power is defined as $E\{|n_{k,m}|^2\} = \sigma_n^2$.

Here we will consider the case where the correlation between the real parts, and similarly the correlation between the imaginary parts of the noise, is non-zero; that is, $E\{n_{k,m}^{(R)} n_{k,m-n}^{(R)}\} = E\{n_{k,m}^{(I)} n_{k,m-n}^{(I)}\} = \rho_n \frac{\sigma_n^2}{2}$ for $|n| > 0$. The superscripts (R) and (I) denote the real and imaginary parts and ρ_n is the noise correlation coefficient at the n^{th} separation. We will continue to assume that the cross correlations between real and imaginary parts of the noise are all zero.

The maximum likelihood (ML) phase-gradient estimator is defined in Chapter 3 equation (3-6) as

$$\hat{\psi}_{n,m} = \angle \sum_{k=1}^{N_{ranges}} x_{k,n} x_{k,m}^{*}. \tag{D-1}$$

We are interested in the expected value of the estimator $E\{\hat{\psi}_{m,n}\}$. Equation (D-1) can be restated as

$$\hat{\psi}_{n,m} = \arctan\left(\frac{\frac{1}{N_{ranges}} \sum_{k=1}^{N_{ranges}} \mathrm{Im}\left(x_{k,n} x_{k,m}^{*}\right)}{\frac{1}{N_{ranges}} \sum_{k=1}^{N_{ranges}} \mathrm{Re}\left(x_{k,n} x_{k,m}^{*}\right)} \right). \tag{D-2}$$

By using the rectangular notation for complex numbers $X + jY = \frac{1}{N_{ranges}} \sum_{k=1}^{N_{ranges}} x_{k,n} x_{k,m}^{*}$ where

$$X = \frac{1}{N_{ranges}} \sum_{k=1}^{N_{ranges}} \mathrm{Re}\left(x_{k,n} x_{k,m}^{*}\right) \tag{D-3}$$

and

$$Y = \frac{1}{N_{ranges}} \sum_{k=1}^{N_{ranges}} \mathrm{Im}\left(x_{k,n} x_{k,m}^{*}\right), \tag{D-4}$$

(D-2) can be re-expressed as

$$\hat{\psi}_{n,m} = \arctan(Y / X). \tag{D-5}$$

On page 181 of [44] Mood, Graybill and Boes give the following general expression for the expected value of a function of two random variables. This expression uses the Taylor series expansion of the function $g(X,Y)$ expanded about μ_X and μ_Y.

$$E\{g(X,Y)\} \approx g(\mu_X,\mu_Y)+\frac{1}{2}\sigma_X^2\frac{\partial^2}{\partial X^2}g(X,Y)\Big|_{\mu_X,\mu_Y} + \frac{1}{2}\sigma_Y^2\frac{\partial^2}{\partial Y^2}g(X,Y)\Big|_{\mu_X,\mu_Y} + \sigma_{XY}\frac{\partial^2}{\partial X\partial Y}g(X,Y)\Big|_{\mu_X,\mu_Y} \quad \text{(D-6)}$$

For the phase-gradient estimator $g(X,Y)=\arctan(Y/X)$. Expressions for the means, variances, covariances, and second partial derivatives are required to evaluate equation (D-6). The expressions for the variances and covariance are quite complicated to develop and will be addressed last.

D.1.1 Evaluation of μ_X and μ_Y

Referring back to (D-3) and (D-4) we see that

$$\mu_X = E\{X\} = E\left\{\mathrm{Re}\left(x_{k,n}x^*_{k,m}\right)\right\} \quad \text{(D-7)}$$

and

$$\mu_Y = E\{Y\} = E\left\{\mathrm{Im}\left(x_{k,n}x^*_{k,m}\right)\right\} \quad \text{(D-8)}$$

where

$$x_{k,m}x^*{}_{k,m-n} = \left(a_k e^{j\phi_m}a^*{}_k e^{-j\phi_{m-n}} + a_k e^{j\phi_m}n^*{}_{k,m-n} + a^*{}_k e^{-j\phi_{m-n}}n_{k,m} + n_{k,m}n^*{}_{k,m-n}\right). \quad \text{(D-9)}$$

If the noise, $n_{k,m}$, is uncorrelated for n ≠ 0, then the expected value of (D-9) reduces to $E\left\{|a_k|^2 e^{j\phi_m-\phi_{m-n}}\right\} = \sigma_a^2 e^{j\psi_m}$. If the noise, $n_{k,m}$, is correlated for n ≠ 0 then $E\left\{n_{k,m}n^*{}_{k,m-n}\right\} = \rho_n\sigma_n^2$ with $-1<\rho_n<1$, then the expected value of (D-9) becomes $\sigma_a^2 e^{j\psi_{m,n}} + \rho_n\sigma_n^2$. Thus

$$\mu_X = \rho\sigma_n^2 + \sigma_a^2\cos\psi \quad \text{(D-10)}$$

and

$$\mu_Y = \sigma_a^2\sin\psi\,. \quad \text{(D-11)}$$

D.1.2 Substituting μ_X and μ_Y into the First Term in the Taylor Series

Using only the first term of the Taylor series expansion in (D-6) we see that the expected value of the gradient estimate

$$E\{\hat{\psi}\} = \arctan\left\{\frac{\sigma_a^2 \sin\psi}{\rho\sigma_n^2 + \sigma_a^2 \cos\psi}\right\} + \quad \cdots$$

$$E\{\hat{\psi}\} = \arctan\left\{\frac{\beta \sin\psi}{\rho + \beta \cos\psi}\right\} + \quad \cdots \qquad \text{(D-12)}$$

is biased if the noise is correlated, where the signal-to-noise ratio $\beta = \frac{\sigma_a^2}{\sigma_n^2}$. The conditions under which noise is correlated are addressed in Chapter 6, Section 6.1.

D.1.3 Evaluating the Second Partial Derivatives in the Second Order Terms

Given the mean value of X and Y, the second partial derivatives in (D-6) can now be evaluated.

$$\frac{\partial^2}{\partial X^2} g(X,Y)\Big|_{\mu_X,\mu_Y} = \frac{\partial}{\partial X} \frac{-1}{1+(Y/X)^2} Y/X^2 \Big|_{\mu_X,\mu_Y},$$

$$= \frac{\partial}{\partial X} \frac{-Y}{X^2+Y^2}\Big|_{\mu_X,\mu_Y}$$

$$= \frac{2XY}{\left(X^2+Y^2\right)^2}\Big|_{\mu_X,\mu_Y}$$

$$= \frac{2}{\left(\sigma_a^2\right)^2} \cos\psi \sin\psi \qquad \text{(D-13)}$$

$$\left.\frac{\partial^2}{\partial Y^2} g(X,Y)\right|_{\mu_X,\mu_Y} = \left.\frac{\partial}{\partial Y} \frac{1}{1+(Y/X)^2} 1/X^2\right|_{\mu_X,\mu_Y},$$

$$= \left.\frac{\partial}{\partial X} \frac{X}{X^2+Y^2}\right|_{\mu_X,\mu_Y}$$

$$= \left.\frac{-2XY}{\left(X^2+Y^2\right)^2}\right|_{\mu_X,\mu_Y}$$

$$= \frac{2}{\left(\sigma_a^2\right)^2} \cos\psi \sin\psi \qquad \text{(D-14)}$$

$$\left.\frac{\partial^2}{\partial X \partial Y} g(X,Y)\right|_{\mu_X,\mu_Y} = \left.\frac{\partial}{\partial Y} \frac{Y}{X^2+Y^2}\right|_{\mu_X,\mu_Y},$$

$$= \left.\frac{\left(X^2+Y^2\right)-2Y^2}{\left(X^2+Y^2\right)^2}\right|_{\mu_X,\mu_Y}$$

$$= \left.\frac{X^2-Y^2}{\left(X^2+Y^2\right)^2}\right|_{\mu_X,\mu_Y}$$

$$= \left(\sigma_a^2\right)^2 \left(\cos^2\psi - \sin^2\psi\right)$$

$$= \frac{-1}{\left(\sigma_a^2\right)^2} (\cos 2\psi) \qquad \text{(D-15)}$$

Before evaluating σ_X^2, σ_Y^2 and σ_{XY}, let us consider the form of the second order terms of (D-6).

$$\frac{1}{2}\sigma_X^2\frac{\partial^2}{\partial X^2}g(X,Y)\bigg|_{\mu_X,\mu_Y}+\frac{1}{2}\sigma_Y^2\frac{\partial^2}{\partial Y^2}g(X,Y)\bigg|_{\mu_X,\mu_Y}+\sigma_{XY}\frac{\partial^2}{\partial X\partial Y}g(X,Y)\bigg|_{\mu_X,\mu_Y}$$

$$=\frac{1}{\left(\sigma_a^2\right)^2}\left[\left(\sigma_X^2+\sigma_Y^2\right)\cos\psi\sin\psi-\sigma_{XY}\cos 2\psi\right] \qquad \text{(D-16)}$$

D.1.4 Evaluation of the Variances of X, Y, and Covariance of XY

In order to evaluate the second order term of the Taylor series in equation (D-6) we need an expression for σ_X^2

$$\sigma_X^2=\frac{1}{N^2}E\sum_{k=1}^{N}\sum_{j=1}^{N}\left\{\begin{array}{l}\left(\mathrm{Re}\left(x_{k,n}x_{k,m}^*-E\left(x_{k,n}x_{k,m}^*\right)\right)-\mu_X\right)\\ \qquad\times\left(\mathrm{Re}\left(x_{j,n}x_{j,m}^*-E\left(x_{j,n}x_{j,m}^*\right)\right)-\mu_X\right)\end{array}\right\} \qquad \text{(D-17)}$$

where

$$\mathrm{Re}\left(x_{k,n}x_{k,m}^*\right)$$

$$=\mathrm{Re}\left(a_k e^{j\phi_m}a^*{}_k e^{-j\phi_{m-n}}+a_k e^{j\phi_m}n^*{}_{k,m-n}+a^*{}_k e^{-j\phi_{m-n}}n_{k,m}+n_{k,m}n^*{}_{k,m-n}\right)$$

$$=\left(\begin{array}{l}\left|a_k\right|^2\cos\left(\phi_m-\phi_{m-n}\right)+\quad\cdots\\ \qquad\left|a_k\right|\cos\left(\phi_m-\theta\right)n^{(R)}{}_{k,m-n}+\left|a_k\right|\sin\left(\phi_m-\theta\right)n^{(I)}{}_{k,m-n}+\quad\cdots\\ \qquad\left|a_k\right|\cos\left(\phi_{m-n}-\theta\right)n^{(R)}{}_{k,m-n}-\left|a_k\right|\sin\left(\phi_{m-n}-\theta\right)n^{(I)}{}_{k,m}+\quad\cdots\\ \qquad+n^{(R)}{}_{k,m}n^{(R)}{}_{k,m-n}+n^{(I)}{}_{k,m}n^{(I)}{}_{k,m-n}\end{array}\right) \qquad \text{(D-18)}$$

and $\mu_X=\left|a_k\right|^2\cos\left(\phi_m-\phi_{m-n}\right)$. The superscripts (R) and (I) denote the real and imaginary part of the complex noise. Because the estimator has already been shown to be biased if the noise is correlated, the higher order terms of (D-6) will only be evaluated for the case of uncorrelated noise. For $j = k$ the expectation of (D-17) is

$$= N \times E\left\{\begin{array}{l} |a_k|^2 \cos 2(\phi_m - \theta) n^{(R)^2}{}_{k,m-n} + |a_k|^2 \sin^2(\phi_m - \theta) n^{(I)^2}{}_{k,m-n} + \cdots \\ |a_k|^2 \cos^2(\phi_{m-n} - \theta) n^{(R)^2}{}_{k,m-n} - |a_k|^2 \sin^2(\phi_{m-n} - \theta) n^{(I)^2}{}_{k,m} + \cdots \\ + n^{(R)^2}{}_{k,m} n^{(R)^2}{}_{k,m-n} + n^{(I)^2}{}_{k,m} n^{(I)^2}{}_{k,m-n} \end{array}\right\} \quad \text{(D-19)}$$

For $j \neq k$ the expectation of (D-17) is zero. The expectation of (D-19), σ_X^2 reduces to

$$\sigma_X^2 = \frac{1}{N}\left(\sigma_a^2 \sigma_n^2 + \frac{\left(\sigma_n^2\right)^2}{2}\right). \quad \text{(D-20)}$$

Similarly

$$\sigma_Y^2 = \sigma_X^2 = \frac{1}{N}\left(\sigma_a^2 \sigma_n^2 + \frac{\left(\sigma_n^2\right)^2}{2}\right) \quad \text{(D-21)}$$

and for uncorrelated noise

$$\sigma_{XY} = 0. \quad \text{(D-22)}$$

D.1.5 Explicit Form of Bias Inherent in Estimator

Substituting (D-20), (D-21), and (D-22) into (D-16) gives the explicit form for the estimator bias, ε, for data with uncorrelated noise:

$$\varepsilon = \frac{1}{\left(\sigma_a^2\right)^2}\left[\left(\sigma_X^2 + \sigma_Y^2\right)\cos\psi \sin\psi - \sigma_{XY}\cos 2\psi\right]$$

$$= \frac{1}{N\left(\sigma_a^2\right)^2}\left[\left(2\sigma_a^2\sigma_n^2 + \left(\sigma_n^2\right)^2\right)\cos\psi \sin\psi\right]$$

$$\varepsilon = \frac{\sin 2\psi}{2N}\left(\frac{2}{\beta} + \frac{1}{\beta^2}\right) \quad \text{(D-23)}$$

Equation (D-23) is the expression for the angle-dependent bias of the phase-gradient estimator.

D.2 Calculation of $\left(\frac{dE\{\hat{\psi}\}}{d\psi}\right)^2$ for the ML Estimator With Uncorrelated Noise

To determine the Cramér Rao lower bound (CRLB) for the biased estimator we must evaluate $\left(\frac{dE\{\hat{\psi}\}}{d\psi}\right)^2 = \left(1+\frac{d\varepsilon}{d\psi}\right)^2$. We will do so only for $\rho = 0$ where

$$\varepsilon = \frac{\sin 2\psi}{2N}\left(\frac{2}{\beta}+\frac{1}{\beta^2}\right).$$

$$\frac{d\varepsilon}{d\psi} = \frac{\cos 2\psi}{N}\left(\frac{2}{\beta}+\frac{1}{\beta^2}\right) \tag{D-24}$$

and

$$\left(1+\frac{d\varepsilon}{d\psi}\right)^2 = 1+\frac{2\cos 2\psi}{N}\left(\frac{2}{\beta}+\frac{1}{\beta^2}\right)+\left[\frac{\cos 2\psi}{N}\left(\frac{2}{\beta}+\frac{1}{\beta^2}\right)\right]^2. \tag{D-25}$$

D.3 Calculation of the Fisher Information Matrix for Data with Correlated Noise

The log likelihood function

$$\sum_{k=1}^{N_{ranges}} \ln p(\mathbf{x}_k|\phi, a_k) = -\left(\sum_{k=1}^{N_{ranges}} \ln\left[\pi^2|\mathbf{C}_k|\right]+\left(\mathbf{x}_k^H-\mu_{\mathbf{x}_k}^*\right)\mathbf{C}^{-1}\left(\mathbf{x}_k-\mu_{\mathbf{x}_k}\right)\right). \tag{D-26}$$

The covariance matrix **C** for the zero-mean data model is

$$\mathbf{C} = \begin{bmatrix} \sigma_a^2 + \sigma_n^2 & \sigma_a^2 e^{-j\psi} + \rho\sigma_n^2 \\ \sigma_a^2 e^{-j\psi} + \rho\sigma_n^2 & \sigma_a^2 + \sigma_n^2 \end{bmatrix},$$

and the determinant,

$$|\mathbf{C}| = \left(\sigma_a^2 + \sigma_n^2\right)^2 - \left(\sigma_a^2 e^{-j\psi} + \rho\sigma_n^2\right)\left(\sigma_a^2 e^{-j\psi} + \rho\sigma_n^2\right),$$

is a function of the gradient, ψ. The development of the Fisher information matrix, **J**, for the zero mean data model is complicated by the dependence of |**C**| on ψ.

The data vector for the non-zero mean data is $\mathbf{X} = \begin{bmatrix} x_m - \mu_{x_m} \\ x_{m-n} - \mu_{x_{m-n}} \end{bmatrix}$ (see equation (5-8) in Chapter 5), and the covariance matrix is $\mathbf{C} = \sigma_n^2 \begin{bmatrix} 1 & \rho \\ \rho & 1 \end{bmatrix}$. The determinant of the covariance matrix $|\mathbf{C}| = \left(\sigma_n^2\right)^2\left(1-\rho^2\right)$, and is not dependent on the gradient, ψ.

Since $|C|$ is not a function of ψ, the Fisher information matrix is easily developed using the method of second derivatives and determining the CRLB for a function of the basic parameters, $\psi_m = \phi_m - \phi_{m-n}$.

$$\mathbf{C}^{-1} = \frac{1}{\sigma_n^2\left(1-\rho^2\right)} \begin{bmatrix} 1 & -\rho \\ -\rho & 1 \end{bmatrix} \qquad \text{(D-27)}$$

The log-likelihood function $L = -\left(\sum_{k=1}^{N_{ranges}} \left(\mathbf{x}_k^H - \boldsymbol{\mu}_{\mathbf{x}_k}^*\right)\mathbf{C}^{-1}\left(\mathbf{x}_k - \boldsymbol{\mu}_{\mathbf{x}_k}\right) \right)$

$$\frac{dL(\phi)}{d\phi_1} = \frac{-\sigma_n^2}{|\mathbf{C}|}\begin{bmatrix} j\mu_1^*(x_1-\mu_1) - j\mu_1(x_1-\mu_1)^* + j\rho\mu_1(x_2-\mu_2)^* \cdots \\ -j\rho\mu_1{}^*(x_2-\mu_2) \end{bmatrix}$$

$$\frac{d^2L(\phi)}{d\phi_1{}^2} = \frac{-\sigma_n^2}{|\mathbf{C}|}\begin{bmatrix} j\mu_1^*(x_1-\mu_1) + 2\mu_1^*\mu_1 + \mu_1(x_1-\mu_1)^* - \rho\mu_1(x_2-\mu_2)^* \cdots \\ -\rho\mu_1{}^*(x_2-\mu_2) \end{bmatrix}$$

$$-E\left\{\frac{d^2L(\phi)}{d\phi_1{}^2}\right\} = \frac{\sigma_n^2}{|\mathbf{C}|}\left[2\mu_1^*\mu_1\right] = \frac{2\sigma_n^2\sigma_a^2}{|\mathbf{C}|}.$$

Similarly $-E\left\{\frac{d^2L(\phi)}{d\phi_2{}^2}\right\} = \frac{\sigma_n^2}{|\mathbf{C}|}\left[2\mu_2^*\mu_2\right] = \frac{2\sigma_n^2\sigma_a^2}{|\mathbf{C}|}$, and

$$-E\left(\frac{\partial^2 L(\varphi)}{\partial\phi_1\partial\phi_2}\right) = \frac{-\sigma_n^2}{|\mathbf{C}|}\left[\rho\mu_1^*\mu_2 + \rho\mu_1\mu_2{}^*\right] = \frac{-2\sigma_n^2\sigma_a^2\rho\cos\psi}{|\mathbf{C}|}.$$

Thus $$\mathbf{J} = \frac{2\sigma_n^2\sigma_a^2}{|\mathbf{C}|}\begin{bmatrix} 1 & -\rho\cos\psi \\ -\rho\cos\psi & 1 \end{bmatrix} \text{ and}$$

$$\mathbf{J}^{-1} = \frac{|\mathbf{C}|}{2\sigma_n^2\sigma_a^2}\frac{1}{1-\rho^2\cos^2\psi}\begin{bmatrix} 1 & \rho\cos\psi \\ \rho\cos\psi & 1 \end{bmatrix}. \qquad \text{(D-28)}$$

The desired function of the basic parameters is $D = \phi_1 - \phi_2$, and $\nabla D^T = \begin{bmatrix} -1 & 1 \end{bmatrix}$.

Finally, $\mathbf{D}^T\mathbf{J}^{-1}\mathbf{D} = \frac{|\mathbf{C}|}{2\sigma_n^2\sigma_a^2}\frac{1}{1-\rho^2\cos^2\psi}\begin{bmatrix} -1 & 1 \end{bmatrix}\begin{bmatrix} 1 & \rho\cos\psi \\ \rho\cos\psi & 1 \end{bmatrix}\begin{bmatrix} -1 \\ 1 \end{bmatrix}$, and the

$$\text{unbiased portion of } CRLB \geq \frac{2|\mathbf{C}|}{2\sigma_n^2\sigma_a^2}\frac{(1-\rho\cos\psi)}{(1-\rho^2\cos^2\psi)}$$

$$= \frac{2\left(\sigma_n^2\right)^2\left(1-\rho^2\right)}{2\sigma_n^2\sigma_a^2}\frac{1}{(1+\rho\cos\psi)}$$

$$= \frac{\left(1-\rho^2\right)}{\beta(1+\rho\cos\psi)}. \qquad \text{(D-29)}$$

The algebraically tedious product of the first derivatives method has been calculated and agreement between the two methods has been verified. Details are omitted. Next, consider the values of (D-29) for $\psi = 0$ and $\psi = \pi/2$. For $\psi = 0$ (D-29) reduces to $\frac{1-\rho}{\beta}$. For $\psi = \pi/2$ (D-29) reduces to $\frac{(1-\rho^2)}{\beta}$.

D.4 Summary

Using a Taylor series expansion, we have shown that correlated noise causes an angle-dependent bias in the ML phase-gradient estimator. We have used that same Taylor series expansion to show that the estimator has an inherent angle-dependent bias and developed the expression for that second-order bias term. We have developed the Fisher information matrix and its inverse for data with correlated noise. The inverse of the Fisher information matrix is the CRLB for the unbiased estimate, that is the estimate minus the bias. Further development of these terms is required to fully derive the Cramér Rao lower bound for the biased estimators. The general form of the required equation was given in Chapter 5, equation (5-3)

$$E\left\{\left(\hat{\psi}-\psi\right)^2 | \mathbf{x}\right\} \geq \frac{\left[\frac{\partial\, E\{\hat{\psi}|\}}{\partial\psi}\right]^2}{-E\left\{\frac{\partial^2 \ln p(\mathbf{x}|\psi)}{\partial\psi^2}\right\}}. \qquad \text{(D-30)}$$

For the case of correlated noise, the numerator of (D-30) is a function of signal-to-noise ratio, β, gradient angle, ψ, noise correlation coefficient, ρ, and inherent estimation bias, ε.

The denominator is a function of ψ and ρ. For the case of uncorrelated noise, the numerator is a function of β, ψ and ε, and the denominator is a function of β. For the case of uncorrelated noise, the denominator has already been derived in Appendix C and reported in Chapter 5 as equation (5-7). The numerator was derived in this appendix in Section D-2.

Researchers who choose to pursue this derivation for correlated noise should derive the Fisher information matrix for the zero-mean data model using both the method of second derivatives and the method of products of first derivatives. The results using these two methods should be compared to identify the region over which the result is valid.

Appendix E

Expansion of Data Model and CRLB to Include Shift Errors, ω_k, Represented as Multiplicative Measurement Noise

In this appendix, the data model used by Jakowatz, Eichel and Ghiglia in [34] and [18] and later used by Jakowatz and Wahl in [33] to derive the Cramér-Rao lower bound (CRLB) for the phase-gradient estimation problem is modified to include shift errors as multiplicative noise. The Fisher information matrix is then derived for this expanded model using both the method of second derivatives and the method of products of first derivatives. The two derived forms are compared and are shown numerically to agree only for signal-to-noise ratios (SNR) of < 0 dB. The probability density used here for the numerical analysis is one derived by Viterbi to describe the steady-state distribution for phased-locked loops. A similar distribution is used in statistical optics to describe phase distributions [25]. However, this derivation of the CRLB depends only on $E\{e^{jn\omega_k}\}$, where ω_k is the shift error and n is the normalized discrete time difference between the data samples from which the gradient is estimated.

The data model assumed by Jakowatz and Wahl in [33] for the m^{th} phase-history data sample at the k^{th} range is defined as

$$x_{k,m} = a_k e^{j\phi_m} + n_{k,m} \tag{E-1}$$

where

$a_k = |a_k| e^{j\theta_k}$ is the complex envelope of the signal at the k^{th} range. The expected value of the magnitude squared of a_k, $E\{|a_k|^2\} = \sigma_a^2$ and $|a_k|$ are assumed to be independent and identically distributed across ranges, k, but invariant across azimuth, m, at any single range. Similarly θ_k, a target-dependent phase at the k^{th} range, is assumed to be independent and identically and uniformly distributed across ranges, k, but invariant across azimuth, m, at any single range.

ϕ_m is the aberrating phase of interest at the m^{th} azimuth sample and is assumed to be invariant across ranges for any given azimuth index, m.

$n_{k,m}$ is complex circularly Gaussian noise, assumed to be independent and identically distributed for all range samples indexed by k and all azimuth samples indexed by m. Noise power is defined as $E\{|n_{k,m}|^2\} = \sigma_n^2$.

Although this data model is defined in the phase-history domain, it defines related assumptions in the image domain. This data model implies that clutter in the image domain is also complex circularly Gaussian and independent and identically distributed for all range samples indexed by k and all azimuth samples indexed by m. It further

implies that signal is complex circularly Gaussian and independent and identically distributed for all ranges with only one signal per range.

We next expand (E-1) to include shift errors as multiplicative noise. Then

$$x_{k,m} = a_k e^{j\phi_m} e^{jm\omega_k} + n_{k,m} \tag{E-2}$$

where ω_k is the radial frequency associated with the shift error at the k^{th} range, and

m is the azimuth index with the time step normalized to unity.

Consider the covariance matrix for sample pairs. The off-diagonal elements are $E\{x_{k,m}x_{k,m-n}^*\}$ and $\psi_{m,n} = \phi_m - \phi_{m-n}$. Then the covariance matrix is

$$\mathbf{C}_k = E\begin{bmatrix} a_k^2 + n_{k,1}^2 & a_k^2 e^{-j\psi_{m,n}} e^{-jn\omega_k} \\ a_k^2 e^{j\psi_{m,n}} e^{jn\omega_k} & a_k^2 + n_{k,2}^2 \end{bmatrix}$$

$$= \begin{bmatrix} \sigma_a^2 + \sigma_n^2 & \sigma_a^2 e^{-j\psi_{m,n}} E\{e^{-jn\omega_k}\} \\ \sigma_a^2 e^{j\psi_{m,n}} E\{e^{jn\omega_k}\} & \sigma_a^2 + \sigma_n^2 \end{bmatrix}$$

$$= \begin{bmatrix} \sigma_a^2 + \sigma_n^2 & \sigma_a^2 e^{-j\psi_{m,n}} \zeta \\ \sigma_a^2 e^{j\psi_{m,n}} \zeta & \sigma_a^2 + \sigma_n^2 \end{bmatrix}$$

where the distribution of ω is assumed to be symmetric and zero mean. Then

$$\zeta = E\{e^{jn\omega_k}\} = E\{e^{-jn\omega_k}\}$$

and

$$\mathbf{C}_k^{-1} = \frac{1}{|\mathbf{C}|}\begin{bmatrix} \sigma_a^2 + \sigma_n^2 & -\sigma_a^2 e^{-j\psi_{m,n}} \zeta \\ -\sigma_a^2 e^{j\psi_{m,n}} \zeta & \sigma_a^2 + \sigma_n^2 \end{bmatrix}. \tag{E-3}$$

where

$$|\mathbf{C}| = \left(\sigma_a^2 + \sigma_n^2\right)^2 - \left(\sigma_a^2 \zeta\right)^2. \tag{E-4}$$

The log likelihood function is $L(\psi) = -\sum_{k=1}^{N_{ranges}} \mathbf{X}_k^H \mathbf{C}_k^{-1} \mathbf{X}_k$, where N_{ranges} is the number of data samples (number of ranges). First we will use Method 1, the second derivative method, to determine the Fisher information matrix for N_R data samples. We proceed as follows:

$$\mathbf{J} = -E\left\{\frac{\partial^2 L(\psi)}{\partial \psi^2}\right\}$$

$$= N_R \frac{1}{|\mathbf{C}|} E\left\{\begin{bmatrix} x_1^* & x_2^* \end{bmatrix} \begin{bmatrix} 0 & \sigma_a^2 e^{-j\psi_{m,n}} \zeta \\ \sigma_a^2 e^{j\psi_{m,n}} \zeta & 0 \end{bmatrix} \begin{bmatrix} x_1 \\ x_2 \end{bmatrix}\right\}$$

$$= N_R \frac{1}{|\mathbf{C}|} E\left\{x_1 x_2^* \sigma_a^2 e^{j\psi_{m,n}} \zeta + x_1^* x_2 e^{-j\psi_{m,n}} \zeta\right\} \tag{E-5}$$

where $E\left\{x_m x_{m-n}^*\right\} = \left(E\left\{x_m^* x_{m-n}\right\}\right)^* = \sigma_a^2 e^{-j\psi_{m,n}} \zeta$. Then (E-5) reduces to

$$\mathbf{J} = \frac{2N_R\left(\sigma_a^2 \zeta\right)^2}{|\mathbf{C}|} \tag{E-6}$$

Taking the inverse and collecting terms,

$$\mathbf{J}^{-1} = \frac{\left(\sigma_a^2 + \sigma_n^2\right)^2 - \left(\sigma_a^2 \zeta\right)^2}{2N_R\left(\sigma_a^2 \zeta\right)^2}$$

$$= \frac{\left\{\sigma_a^2\right\}^2 + 2\left\{\sigma_a^2\right\}\left\{\sigma_n^2\right\} + \left\{\sigma_n^2\right\}^2 - \left\{\sigma_a^2\right\}^2 \zeta^2}{2N_R\left\{\sigma_a^2\right\}^2 \zeta^2}$$

$$= \frac{\frac{\left\{\sigma_a^2\right\}^2}{\left\{\sigma_n^2\right\}^2}\left(1 - \zeta^2\right) + 1 + 2\frac{\left\{\sigma_a^2\right\}}{\left\{\sigma_n^2\right\}}}{2N_R \frac{\left\{\sigma_a^2\right\}^2}{\left\{\sigma_n^2\right\}^2} \zeta^2} \tag{E-7}$$

By substituting $\beta = \sigma_a^2 / \sigma_n^2$ for the SNR in (E-7), the CRLB for an unbiased estimator for the data model in (E-2) is thus expressed as

$$CRLB \geq \mathbf{J}^{-1} = \frac{\beta^2 \left(1-\zeta^2\right)+1+2\beta}{2N_R \beta^2 \zeta^2}. \tag{E-8}$$

Next we consider Method 2, the product of derivatives method of determining the Fisher information matrix

$$\mathbf{J} = E\left\{\left(\frac{\partial L(\psi)}{\partial \psi}\right)^2\right\}$$

$$= N_R \frac{1}{|\mathbf{C}|^2} E\left\{\left(\begin{bmatrix} x_m^* & x_{m-n}^* \end{bmatrix}\begin{bmatrix} 0 & -j\sigma_a^2 e^{-j\psi_{m,n}}\zeta \\ j\sigma_a^2 e^{j\psi_{m,n}}\zeta & 0 \end{bmatrix}\begin{bmatrix} x_m \\ x_{m-n} \end{bmatrix}\right)^2\right\}$$

$$= N_R \frac{1}{|\mathbf{C}|^2} E\left\{\left(-jx_m x_{m-n}^* \sigma_a^2 e^{j\psi_{m,n}}\zeta + jx_m^* x_{m-n}^2 e^{-j\psi_{m,n}}\zeta\right)^2\right\}$$

$$= N_R \frac{\left(\sigma_a^2\zeta\right)^2}{|\mathbf{C}|^2} E\left\{\left(x_m x_{m-n}^*\right)^2 e^{j2\psi_{m,n}} - \left(x_m^* x_{m-n}^2\right)^2 e^{-j2\psi_{m,n}} + 2x_m x_m^* x_{m-n}^2 x_{m-n}^*\right\}$$

$$= N_R \frac{\left(\sigma_a^2\zeta\right)^2}{|\mathbf{C}|^2} E\left\{\begin{array}{l} -|a|^4\left(e^{j2\psi_{m,n}} + e^{-j2\psi_{m,n}}\right) \quad \cdots \\ \qquad +2\left(|a|^4 + |a|^2|n_m|^2 + |a|^2|n_{m-n}|^2 + |n_m|^2|n_{m-n}|^2\right) \end{array}\right\}$$

$$= 2N_R \frac{\left(\sigma_a^2\zeta\right)^2}{|\mathbf{C}|^2}\left(E\left\{|a|^4\right\}\left(1 - E\left\{e^{j2\psi_{m,n}}\right\}\right) + 2\sigma_a^2\sigma_n^2 + \left(\sigma_n^2\right)^2\right). \tag{E-9}$$

If we assume that $|a|$ is Rayleigh distributed and that a^2 is consequently exponentially distributed, then $E\{|a|^4\} = 2\sigma_a^2$ and (E-9) reduces to

$$E\left\{\left(\frac{\partial L(\psi)}{\partial \psi}\right)^2\right\}$$

$$= 2N_R \frac{(\sigma_a^2 \zeta)^2}{|\mathbf{C}|^2}\left(2(\sigma_a^2)^2\left(1 - E\{e^{j2\psi_{m,n}}\}\right) + 2\sigma_a^2\sigma_n^2 + (\sigma_n^2)^2\right). \qquad \text{(E-10)}$$

For (E-10) to equal (E-6) the following must be true

$$|\mathbf{C}| = \left(2(\sigma_a^2)^2\left(1 - E\{e^{j2\psi_{m,n}}\}\right) + 2\sigma_a^2\sigma_n^2 + (\sigma_n^2)^2\right). \qquad \text{(E-11)}$$

But referring to (E-4) we see that this is not the case.

The ratio of these two scalar-valued calculations of the Fisher information matrix in dB, that is,

$$10 \times \log 10\left(-E\left\{\frac{\partial^2 L(\psi)}{\partial \psi^2}\right\} \Big/ E\left\{\left(\frac{\partial L(\psi)}{\partial \psi}\right)^2\right\}\right), \qquad \text{(E-12)}$$

is plotted in Figure E-1 for several values of σ_ω. For these calculations, the probability density assumed for shift errors was

$$p_\omega(\omega \mid \Lambda) = \frac{\exp(\Lambda \cos \omega)}{2\pi I_o(\Lambda)}. \qquad \text{(E-13)}$$

The parameter Λ controls the spread of the density and, using a linear analysis, is inversely proportional to the variance of ω. This density was derived by Viterbi [63] to

describe the steady-state probability density of phase errors for first order phased-locked loops. Van Trees [61] uses this family of distributions for the class of signal estimation problems where the data measurements include nuisance or unwanted parameters. He uses (E-13) to model the distributions of unwanted random phase angles.

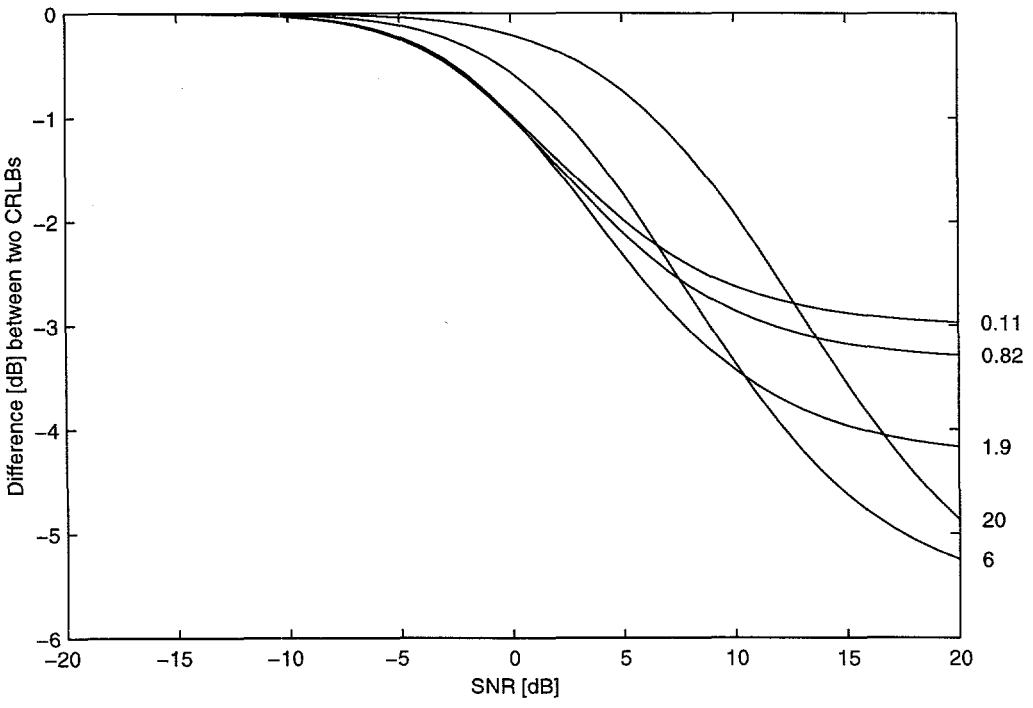

Figure E-1. Ratio [dB] of Fisher information matrix calculated using 2nd derivatives (E-8) to Fisher information matrix calculated using the product of 1st derivatives (E-10).

The values of Λ used are identified in the right margin of the plot. The values of Λ associated standard deviations and widths of uniform distributions with equivalent variances are summarized in Table 6-1 Chapter 6. That table is repeated here as Table E-1.

In Figure E-1 we see that the two computed CRLBs begin to diverge for SNRs > 0 dB. We will use (E-8) to represent CRLBs for the mean squared phase gradient estimation errors for data with shift errors as modeled in (E-2). This model is, of course, limited to SNR < 0 dB.

Table E-1. Parameters of shift error distributions

Λ	Standard Deviation [rads]	Relative width of uniform dstn
20.0	0.2	0.125
6.0	0.4	0.25
1.9	0.9	0.50
0.8	1.4	0.75
0.1	1.8	0.97

Glossary

a_k	the complex echo amplitude at the k^{th} range, assumed to be constant over azimuth -- $a_k = \lvert a_k \rvert \exp(j\theta_k)$
B_M	modulation index
B_ψ	bandwidth of phase gradient, ψ
β	signal-to-noise-ratio
c	velocity of light ~3×10^8 m/s
CRLB	Cramér-Rao lower bound
CSR	clutter-to-signal ratio, the inverse of signal-to-clutter ratio, a metric of image contrast
DFT	discrete Fourier transform
Dstn	sample distribution
dB	decibels = 10*log10 (Watts/Watt)
E{*}	expected value

FFT	fast Fourier transform
ISLR	integrated sidelobe ratio
J	the Fisher information matrix, a square matrix
j	the imaginary number $\sqrt{-1}$
J_{ij}	the i^{th}, j^{th} element of the Fisher information matrix **J**
J^{ij}	the i^{th}, j^{th} element of $\mathbf{J^{-1}}$; the variance of any unbiased estimate of ψ_i, $\sigma^2_{\psi_i} \geq J^{ii}$
k	range index, when used as a subscript when two ranges are indexed, j, k are used
ln(*)	natural logarithm
m	azimuth index, when used as a subscript when two azimuth positions are indexed, m, n are used, with $n > m$
$M_{support}$	the length of the support for the point spread function
ML	maximum likelihood
MSE	mean squared error MSE [dB] = 10*log10 ((residual phase-gradient error[rads])^2)

N_{az}	the number of azimuth samples in the image
$n_{k,m}$	the complex noise in the range-compressed phase history data sample for the k^{th} range at the m^{th} azimuth position
N_{ranges}	the number of range bins in the image
PGA	phase gradient autofocus
phase history	range-compressed phase history
psf	point spread function
PSLR	peak sidelobe ratio
ϕ_m	the aberrrating phase at the m^{th} azimuth sample
$\psi_{m,n}$	the difference in aberrating phase between the m^{th} and the m^{th}-n^{th} azimuth samples (ϕ_m - ϕ_{m-n})
radar	radio detection and ranging
rcs	radar cross section -- a measure of target reflectivity
rms	root mean squared
SAR	synthetic aperture radar

SCR	signal-to-clutter ratio, an image domain metric of image contrast
SNR	signal-to-noise ratio, a phase-history domain metric
θ_k	a target-dependent phase at the k^{th} range, assumed to independent and uniformly distributed across ranges
$\mathbf{x}^H$	hermitian or complex conjugate transpose of the complex matrix $\mathbf{x}$
$x_{k,m}$	the range-compressed phase-history data sample for the k^{th} range at the m^{th} azimuth position

Selected Bibliography

[1] Aitken, G. J. M., and R. Johnson. *Phase-Gradient Reconstruction from Photon-Limited Stellar Speckle Images.* Applied Optics, October 1, 1987, Vol. 26, No. 19.

[2] Aitken, G. J. M., and R. Johnson. *High-Resolution Reconstruction of Photon-Limited Stellar Images Using Phase Gradients.* Canada Journal of Physics, 1988, Vol. 66.

[3] Aitken, G. J. M., R. Johnson, and R. Houtman. *Phase-Gradient Stellar Image Reconstruction.* Optics Communications, January 15, 1986, Vol. 56, No. 6.

[4] Aitken, G. J. M. *Diffraction-Limited Imaging from the Ground: Measurement of Stellar Spatial Spectra.* Publications of the Astronomical Society of the Pacific, May 1989, Vol. 101, No. 639, pp. 471-488.

[5] Attia, E. H., and B. D. Steinberg. *Self-Cohering Large Antenna Arrays Using the Spatial Correlation Properties of Radar Clutter.* IEEE Transactions on Antennas and Propagation, January 1989, Vol. 37, No.1, pp. 30-38.

[6] Ayers, G. R., M. J. Northcott, and J. C. Dainty. *Knox-Thompson and Triple-Correlation Imaging Through Atmospheric-Turbulence.* Journal of the Optical Society of America, July 1988, Vol. 5, No. 7, pp. 963-985.

[7] Bakut, P. A., V. E. Kirakosyants, V. A. Loginov, C. J. Solomon, and J. C. Dainty. *Optimal Wavefront Reconstruction from Shack-Harmann Sensor by Use of a Bayesian Algorithm.* Optics Communications, June 15, 1994, Vol. 109, pp. 10-15.

[8] Bendor, G. A., and T. W. Gedra. *Single-Pass Fine-Resolution SAR Autofocus.* Proceedings of the IEEE, 1983, NAECON.

[9] Born, Max, and Emil Wolf. *Principles of Optics—Electromagnetic Theory of Propagation, Interference and Diffraction of Light* (Fifth Edition). Oxford: Pergamon Press, Ltd., 1975.

[10] Breipohl, Arthur M. *Probabilistic Systems Analysis—An Introduction to Probabilistic Models, Decisions, and Applications of Random Processes*. New York: John Wiley & Sons, Inc., 1970.

[11] Brogan, William L. *Modern Control Theory*. New York: Quantum Publishers, Inc., 1974.

[12] Brown, W. D., and G. D. Cable. *The Spatial Variance of Ionospherically-Induced Phase Errors in SAR Imagery*. Albuquerque, NM: Sandia National Laboratories, 1993, SAND-93-0976C.

[13] Brown, W. D., and D. C. Ghiglia. *Some Methods for Reducing Propagation-Induced Phase Errors in Coherent Imaging-Systems. I. Formalism*. Journal of the Optical Society of America A-Optics and Image Science, June 1988, Vol. 5, No. 6, pp. 924-941.

[14] Calloway, T. M., C. V. Jakowatz, Jr., P. A. Thompson, and P.H. Eichel. *Comparison of Synthetic Aperture Radar Autofocus Techniques—Phase Gradient vs Subaperture*. Proceedings of the SPIE (The International Society for Optical Engineering), July 1991, Vol. 1566, pp. 353-364.

[15] Cook, Charles E., and Marvin Bernfeld. *Radar Signals—An Introduction to Theory and Application*. New York: Academic Press, 1967.

[16] Dyson, F.; R. Garwin, P. Horowitz, J. Katz, R. Muller, W. Press, P. Weinerg. *Recovery of SAR Images with One Dimension of Unknown Phases*. The MITRE Corporation. McLean, VA. Jason Program Office Report No. JSR-91-175 (March 1992), DTIC AD-B164 984.

[17] Eaves, Jerry L., and Edward K. Reedy (editors). *Principles of Modern Radar*. New York: Van Nostrand Reinhold Company, 1987.

[18] Eichel, P. H., D. C. Ghiglia, and C. V. Jakowatz, Jr. *A Speckle Processing Method for Synthetic Aperture Radar Phase Correction*. Optics Letters, January 1989.

[19] Eichel, P. H., and C. V. Jakowatz. *Phase-Gradient Algorithm as an Optimal Estimator of the Phase Derivative*. Optics Letters, October 15, 1989, Vol. 14, No. 20, pp. 1101-1103.

[20] Elachi, Charles. *Spaceborne Radar Remote Sensing: Applications and Techniques*. New York: IEEE Press, 1988.

[21] Fienup, J. R. *Phase Error Correction by Shear Averaging*. Proceedings of the conference on Signal Recovery and Synthesis III — 1989 Technical Digest Series, Vol. 15, June 14-16, 1989, pp. 134-137.

[22] Fitch, J. Patrick. *Synthetic Aperture Radar.* Springer-Verlag: New York, 1988.

[23] Gardner, William A. *Introduction to Random Processes with Applications to Signals and Systems.* New York: MacMillan Publishing Company, 1986.

[24] Ghiglia, D. C., and G. A. Mastin. *Two-Dimensional Phase Correction of Synthetic Aperture Radar Imagery.* Optics Letters, 1989, Vol. 14, No. 20, pp. 1104-1106.

[25] Goodman, J. W. *Laser Speckle and Related Phenomena* (Second Enlarged Edition). J. C. Dainty (ed.). Springer-Verlag, Berlin, 1984, pp. 29-35.

[26] Gray, D. A., W. O. Wolfe, and J. L. Riley. *An Eigenvector Method for Estimating the Positions of the Elements of an Array of Receivers.* Proceedings of the Australian Symposium on Signal Processing Applications, April 17-19, 1989, pp. 391-393.

[27] Gray, D. A., and J. L. Riley. *Maximum Likelihood Estimate and Cramér-Rao Bound for Complex Signal Vector.* Gold Coast, Australia: Proceedings of the International Symposium on Signal Processing Applications, 1990, pp. 352-355.

[28] Harris, Fredric J. *On the Use of Windows for Harmonic Analysis with the Discrete Fourier Transform.* Proceedings of the IEEE, January 1978, Vol. 66, No. 1, pp. 51-83.

[29] Haykin, Simon. *Adaptive Filter Theory* (second edition). New Jersey: Prentice Hall, 1991.

[30] Hovanessian, S. A. *Introduction to Synthetic Array and Imaging Radars.* Dedham, MA: Artech House, Inc., 1980.

[31] Hung, H., and M. Kaveh. *On the Statistical Sufficiency of the Coherently Averaged Covariance Matrix for the Estimation of the Parameters of Wideband Sources.* IEEE Proceedings of the International Conference on Transactions on Acoustics, Speech and Signal Processing, March 1987, pp. 33-36.

[32] Jakowatz, Charles V., Jr., Ph.D.; Daniel E. Wahl, Ph.D.; Paul H. Eichel, Ph.D.; Dennis C. Ghiglia, Ph.D.; and Paul A. Thompson, Ph.D. *Spotlight-Mode Synthetic Aperture Radar: A Signal Processing Approach.* Boston: Kluwer Academic Publishers, 1996.

[33] Jakowatz, Charles V., Jr., and Daniel E. Wahl. *Eigenvector Method for Maximum-Likelihood Estimation of Phase Errors in Synthetic-Aperture-Radar Imagery.* Journal of the Optical Society of America A-Optics and Image Science, December 1993, Vol. 10, No. 12.

[34] Jakowatz, Charles V., Jr., Paul H. Eichel, and Dennis C. Ghiglia. *Autofocus of SAR Imagery Degraded by Ionospheric-Induced Phase Errors.* SPIE Symposium on Aerospace Sensing, March 1989.

[35] Johnson, R., and G. J. M. Aitken. *Statistical Properties of the Photon-Address, Phase-Gradient Algorithm.* Journal of the Optical Society of America A-Optics and Image Science, January 1989, Vol. 6, No. 1, pp. 56-61.

[36] Just, Dieter, and Richard Bamler. *Phase Statistics of Interferograms with Applications to Synthetic Aperture Radar.* Applied Optics, July 10, 1994, Vol. 33, No. 20.

[37] Knox, K. T., and B. J. Thompson. *Recovery of Images from Atmospherically Degraded Short-Exposure Photographs.* The Astrophysical Journal, October 1, 1974, Vol. 193:L45-L48.

[38] Mastin, G. A., S. Plimpton, D. C. Ghiglia. *Massively Parallel Synthetic Aperture Radar Autofocus.* Proceedings of the SPIE - The International Society for Optical Engineering, 1991, Vol. 1566, p. 341-52.

[39] Mastin, G. A., S. Plimpton, and D. C. Ghiglia. *A Massively Parallel Digital Processor for Spotlight Synthetic Aperture* Radar. The International Journal of Supercomputer Applications, Summer 1993, Vol. 7, No. 2, pp. 97-112.

[40] Melsa, James L., and David L. Cohn. *Decision and Estimation Theory.* New York: McGraw Hill, 1978.

[41] Mensa, Dean L. *High Resolution Radar Imaging.* Dedham, MA: Artech House, Inc., 1981.

[42] Mensa, Dean L. *Radar Imaging.* International Journal of Imaging Systems and Technology, 1992, Vol. 4, pp. 148-163.

[43] Mrazek, Charmaine P., and Samuel W. McCandless. *A Multi-Look Correlation Auto-Focus Technique for Synthetic Aperture Radar Data.* Proceedings of the IEEE, 1983, pp. 118-122.

[44] Mood, Alexander M., and Franklin A. Graybill, Duane C. Boes. *Introduction to the Theory of Statistics,* (3rd Edition). New York: McGraw Hill, 1974.

[45] Nahi, Nasser E. *Estimation Theory and Applications.* New York: John Wiley & Sons, 1969, pp. 246-271.

[46] Oliver, C. J., D. Belcher, A. Blake, and R. G. White. *Algorithms for Focused Linear Synthetic Aperture Radar Imaging.* Proceedings of the SPIE (The International Society for Optical Engineering), Vol. 2230, pp. 60-71.

[47] Papoulis, Athanasios. *Random Modulation: A Review.* IEEE Transactions on Acoustics, Speech and Signal Processing, February 1983, Vol. ASSP-31, No.1.

[48] Papoulis, Athanasios. *Probability, Random Variables, and Stochastic Processes* (Second edition). McGraw-Hill Book Company, New York, 1986.

[49] Rodriguez, E., and J. J. Martin. *Theory and Design of Interferometric Synthetic Aperture Radars.* IEEE Proceedings-F, April 1992, Vol. 139, No. 2.

[50] Schwartz, Mischa. *Information Transmission, Modulation and Noise—A Unified Approach to Communication Systems* (Third Edition). New York: McGraw-Hill Book Company, 1980.

[51] Snarski, C. A. *A Phase Error Estimation Algorithm: Theory, Applications and Examples.* Proceedings of the SPIE (The International Society for Optical Engineering), 1994, Vol. 2230, pp. 72-86.

[52] Steinberg, Bernard D., Harrish M. Subbaram. *Microwave Imaging Techniques.* New York: John Wiley & Sons, Inc., 1991, ch. 8-9, pp. 181-276.

[53] Stimson, George W. *Introduction to Airborne Radar.* El Segundo, California: Hughes Aircraft Company, 1983.

[54] Stoica, Petre, and Arye Nehorai. *MUSIC, Maximum Likelihood, and Cramér-Rao Bound.* IEEE Transactions on Acoustics, Speech and Signal Processing, May 1989, Vol. 37, No. 5.

[55] Stremler, Ferrel G. *Introduction to Communications Systems* (Second Edition). Reading, MA: Addison-Wesley Publishing Company, 1982.

[56] Swerling, P. *Parameter Estimation Accuracy Formulas.* IEEE Transactions on Information Theory, October 1964, pp. 302-313.

[57] ten Brummelaar, T. A., W. G. Bagnuolo, Jr., and S. T. Ridgway. *Strehl Ratio and Visibility in Long-Baseline Stellar Interferometry.* Optics Letters, March 15, 1995, Vol. 20, No. 6, pp. 521-523.

[58] Theil, Henri. *Principles of Econometrics.* Santa Barbara, California: John Wiley & Sons, Inc., 1971, pp. 384-397.

[59] Tyson, Robert K. *Principles of Adaptive Optics.* Boston: Academic Press, Inc., 1991.

[60] Tzannes, Nicolaos S., Ph.D. *Communication and Radar Systems.* New Jersey: Prentice-Hall, Inc., 1985.

[61] Van Trees, R., and L. Harry. *Detection, Estimation, and Modulation Theory, Part I.* New York: John Wiley & Sons, Inc., 1968.

[62] Vant, Malcolm R. *A Spatially-Variant Autofocus Technique for Synthetic-Aperture-Radar.* International Conference Radar-82, October 18-20, 1982, pp. 159-163.

[63] Viterbi, Andrew J. *Phase-Locked Loop Dynamics in the Presence of Noise by Fokker-Planck Techniques.* Proceedings of the IEEE, 1963, Vol. 51, pp. 1737-1753.

[64] Wahl, Daniel E., Paul H. Eichel, and Charles V. Jakowatz, Jr. *Implementation of the Phase Gradient Algorithm.* Proceedings of the SPIE (The International Society for Optical Engineering), July 8-13, 1990, Vol. 1348, pp. 528-535.

[65] Wahl, D. E., P. H. Eichel, D. C. Ghiglia, and C. V. Jakowatz, Jr. *Phase Gradient Autofocus—A Robust Tool for High Resolution SAR Phase Correction.* IEEE Transactions on Aerospace Electronic Systems, July 1994, Vol. 30, No. 3, pp. 827-835.

[66] Wahl, D. E., C. V. Jakowatz Jr., D. C. Ghiglia, and P. H. Eichel. *Relationships Between Autofocus Methods for SAR and Self-Survey Techniques for SONAR.* Proceedings of the SPIE (The International Society for Optical Engineering), 1991, Vol. 1567, pp. 32-40.

[67] Wu, K. H., and M. R. Vant. A SAR Focussing Technique for Imaging Targets with Random Motion. CCC, 1984, pp. 289-295.

Distribution

Copies	*Address*
1	Thomas F. Hafer Advanced Research Projects Agency 3701 N. Fairfax Drive Arlington, VA 22203
1	Phillips Laboratory PL/LIMI - D. Voelz 3550 Aberdeen Ave. S. E. Kirtland AFB, NM 87117
1	Phillips Laboratory PL/LIMI - J. Gonglewski 3550 Aberdeen Ave. S. E. Kirtland AFB, NM 87117
1	Phillips Laboratory PL/LIO - L. Sher 3550 Aberdeen Ave. S. E. Kirtland AFB, NM 87117
1	Phillips Laboratory PL/LIO - M. Cobb 3550 Aberdeen Ave. S. E. Kirtland AFB, NM 87117
1	Rockwell Int. Corp./ Rocketdyne Div. Adv. Imaging Prgrms. P. S. Idell 6633 Canoga Ave. P. O. Box 7922 Canoga, Park, CA 91309-7922
1	ERIM Attn: J. Fienup P. O. Box 134001 Ann Arbor, MI 48113-4001

Copies	*Mailstop*	*Name*	*(Department)*
1	MS 0529	A. E. Doerry	(2345)
1	MS 0529	B. L. Remund	(2345)
1	MS 0531	W. H. Hensley	(2344)
1	MS 0531	J. T. Cordaro	(2344)
1	MS 0572	C. V. Jakowatz, Jr.	(5912)
1	MS 0759	M. K. Snell	(5845)
5	MS 0759	M. J. Hicks	(5845)
1	MS 0842	C. M. Hart	(9100)
1	MS 0843	P. H. Eichel	(9136)
1	MS 1110	D. C. Ghiglia	(1423)
1	MS 9018	Central Technical Files	(8523-2)
5	MS 0899	Technical Library	(7141)
1	MS 0619	Technical Publications	(7151)
10	MS 0100	Document Processing for DOE/OSTI	(7613-2)